

Comprehending the Aggregation Aptitude through Structural Variation within Small Molecular Framework: Comparative Analysis and Interaction Studies

A Dissertation

*Submitted in partial fulfillment for the degree of
Doctor of Philosophy*



SENJUTI HALDER

(Roll No. 166122037)

Thesis Supervisor: Prof. Gopal Das

Department of Chemistry

Indian Institute of Technology Guwahati

Assam -781039, India

Comprehending the Aggregation Aptitude through Structural Variation within Small Molecular Framework: Comparative Analysis and Interaction Studies

A Dissertation

*Submitted in partial fulfillment for the degree of
Doctor of Philosophy*



SENJUTI HALDER
(Roll No. 166122037)

Thesis Supervisor: Prof. Gopal Das

Department of Chemistry
Indian Institute of Technology Guwahati
Assam-781039, India

Dedicated to My Parents



INDIAN INSTITUTE OF TECHNOLOGY GUWAHATI

Department of Chemistry

STATEMENT

I do hereby declare that the matter embodied in this thesis is the result of investigations carried out by me in the Department of Chemistry, Indian Institute of Technology Guwahati, India, under the guidance of Prof. Gopal Das, Department of Chemistry, Indian Institute of Technology Guwahati, India.

In keeping with the general practice of reporting scientific observations, due acknowledgements have been made wherever this work is based on the findings of other investigators.

May, 2021
IIT Guwahati

Senjuti Halder

Senjuti Halder



INDIAN INSTITUTE OF TECHNOLOGY GUWAHATI

Department of Chemistry

CERTIFICATE

This is to certify that Miss Senjuti Halder has been working under my supervision since July, 2016 as a regular registered Ph. D. student. Her thesis entitled “**Comprehending the Aggregation Aptitude through Structural Variation within Small Molecular Framework: Comparative Analysis and Interaction Studies**” is authentic record of the results obtained from the research work carried out under my supervision in the Department of Chemistry, Indian Institute of Technology Guwahati, Assam, India. I am forwarding her thesis to submit for the award of degree of Doctor of Philosophy, from this institute. I hereby certify that she has fulfilled all the requirements, according to the rules of this institute regarding the investigations embodied in her thesis and this work has not been submitted elsewhere for a degree.

Prof. Gopal Das

(Thesis Supervisor)

Professor

Department of Chemistry

IIT Guwahati

Assam - 781039, India

Acknowledgement

I would like to take this opportunity for acknowledging some very special people who are the integral parts of my journey this far. Here it goes-

At the very outset, I want to mention my parents (Biswajit Halder and Sebika Halder) for their unwavering support and unbreakable belief in me throughout the long path towards my intellectual destination until this day and days to come. Any word of gratitude will fall short for them. Their eternal blessing and unconditional love has always been strength for me.

I would like to express my deepest gratitude to my thesis supervisor Prof. Gopal Das for his constant guidance, insightful advice and freedom to work. Apart from the efforts of me, the success of this thesis depends entirely on him. His kind supervision and unique style of giving inspirations always reflect in the happy faces of our group members.

Besides my supervisor, I am highly indebted to my doctoral committee members, Prof. A.S. Achalkumar, Dr. S. P. Biswas and Dr. D. Srimani, for their valuable suggestions and careful evaluation of my thesis work. I would also like to thank former (Prof. B. K. Patel and Prof. T. Punniyamurthy) and present (Prof. Gopal Das) HODs, all the faculty members, Scientific officers, technical and non-technical staffs of the Department of Chemistry, IIT Guwahati. I sincerely appreciate all the staffs and instrument operators of Central Instrument Facility, for providing necessary instrumental facilities required during my research work.

My extraordinary Lab-mates deserve a special thanks for their friendly cooperation and invaluable helps whenever required. I can not express in words how much fortunate I am to have talented lab-members like Soham Da (S. Samanta), Nilotpall Da (N. Borah), Utsab Da (U. Manna), Rupinder Bhaiya (R. Singh), Bisu Da (B. Nayak), Arnab Da (Arnab Ghosh), Jayakrishnan U., Santanu Da (S. Kayal), Deepa (D. Sachan), Aresh (A. Das), Debojit (D. Paul), Megha (M. Basak), Sagnik (S. De), Debolina (D. Ghosh) and Biswajit Da (B. Roy). From sharing evening snacks to partying in the city, from cracking jokes to debating over silly topics, from exploring new YouTube videos to capturing funny snapchat pictures for blackmailing, it was really great to work and spend times with all of them being full entertainment package in the busy lab schedule. And I will always relish these memories throughout my life. I wish them great success in every aspect of their life. Special mention of my two lab seniors cum elder brothers Bisu Da and Utsab Da, who never miss a chance to irritate me, is mandatory, not only because of their spontaneous assistance from the very first day in lab but also spoiling me like their own sister.

I also owe my obligations to my other seniors, batch mates and juniors of PhD fraternity of the chemistry department for their help and support during this tenure.

I shall always be obliged to Prof. Aiyagari Ramesh and his group for admirable support throughout my research work. I would like to offer my thanks to Sandipan Da (S. Mukherjee), Poulomi Di (P. Dey), Priya Di (P. Mullick) and Basu (B. Bhattacharjee) for all the help they extended from time to time through these years.

Now it is time to thank all my IIT Guwahati friends whose contribution is worth mentioning. Of course, nothing would function properly without the care and affection of my two beloved friends Nandita and Lopamudra being my partners in crime on daily basis in this journey. A big thanks to Preetisagar and Upasana for always being there as a responsible friend. It would be an injustice if I have not mentioned Menan, Shweta and Debeni whose craziness has been the endless source of my positivity throughout this time. From gossiping in the hostel-corridor to hanging out in the weekend, I will surely miss all of them and cherish the memories of love and laughter we shared together. I sincerely wish them good luck for their future.

I would also like to extend my gratitude to my all teachers/faculties and friends from my school, bachelor's and master's. Although they were far apart during this tenure, their direct or indirect support and motivation has guided me to reach this far.

I would like to acknowledge IIT Guwahati for the fellowship, the Microsoft Corporation for presenting the MS Word and Excel as well as Adobe Corporation for AI software.

As I am writing this thesis during a global pandemic (COVID-19), so a special mention to all the professionals and researchers who are fighting at the forefront and risking their lives.

It is difficult to weave all the names in a single piece of writing. So, any omission in this brief acknowledgement does not mean lack of gratitude.

Finally, I bow down to the Lord Almighty for his grace and blessings from the beginning of my academic life up to this doctoral level.



- *Senjuti*

The thesis entitled “**Comprehending the Aggregation Aptitude through Structural Variation within Small Molecular Framework: Comparative Analysis and Interaction Studies**” is categorized into six chapters based on the outcomes of experimental effort executed during the research period.

Chapter 1: Introduction

This chapter provides a brief introduction to the basics of Molecular self-assembly regarding the change in the characteristics properties of small molecules with the slight modification in molecular framework for providing particulars on the working principle of molecular aggregates for advanced applications. The term ‘Molecular self-assembly’ defines the process in which spontaneous organization of molecules arranges themselves into well-ordered structures. To mimic the properties of biological systems by non-living systems, many disciplines use the concept of self-assembly, which is a prevalent process in cells and a common phenomenon of nature. The beauty of self-assembly stems from the fact that it is one of the few practical strategies for fabricating various kinds of supramolecular architectures at micro- or nano-level as the prerequisite for functionalization of materials in countless areas such as optoelectronics, chemosensors, nanotechnology, biotechnology and biomedicines.

Molecules can be made to self-assemble spontaneously into multicomponent, complex structures when they are instructed to do so. The instructions exist in the form of the molecule’s shape, its chemical surfaces, and how well it fills space in the phase where the assembly takes place. These instructions are written into the molecule during its synthesis. It is reported that π -conjugated molecules permit the formation of stacked molecular arrangements, and therefore are ideal candidates for the building blocks of supramolecular assemblies where non-covalent interactions play vital roles in the creation of controlled 1, 2 and 3 dimensional superstructures, such as nanowires, nanotubes, nanoribbons, nanobelts, nanorods, nanosheets, nanospheres and nano/micro-flowers. This self-assembly process can be controlled if the spontaneous behavior is trapped by the introduction of additional components. Intensive investigations have focused on understanding and controlling self-assemblies of small molecules with non-biological stimuli in vitro (i.e., cell free setting) over the last several decades. Interestingly, the combination of controlled self-assembly of small molecule and modern bio-analytical techniques emerge as an active and promising approach to monitor the regulatory means of self-assembly of various types of biomolecules and to detect enzymatic function, metal ions, proteins or other environmentally and bio-logically important analytes. Simultaneously, modification of those supramolecular assemblies via incorporation of AIE-active unit with diverse characteristics opens up an

alternative approach to explore their vast application prospective in sensing, imaging, optoelectronics and therapeutic studies.

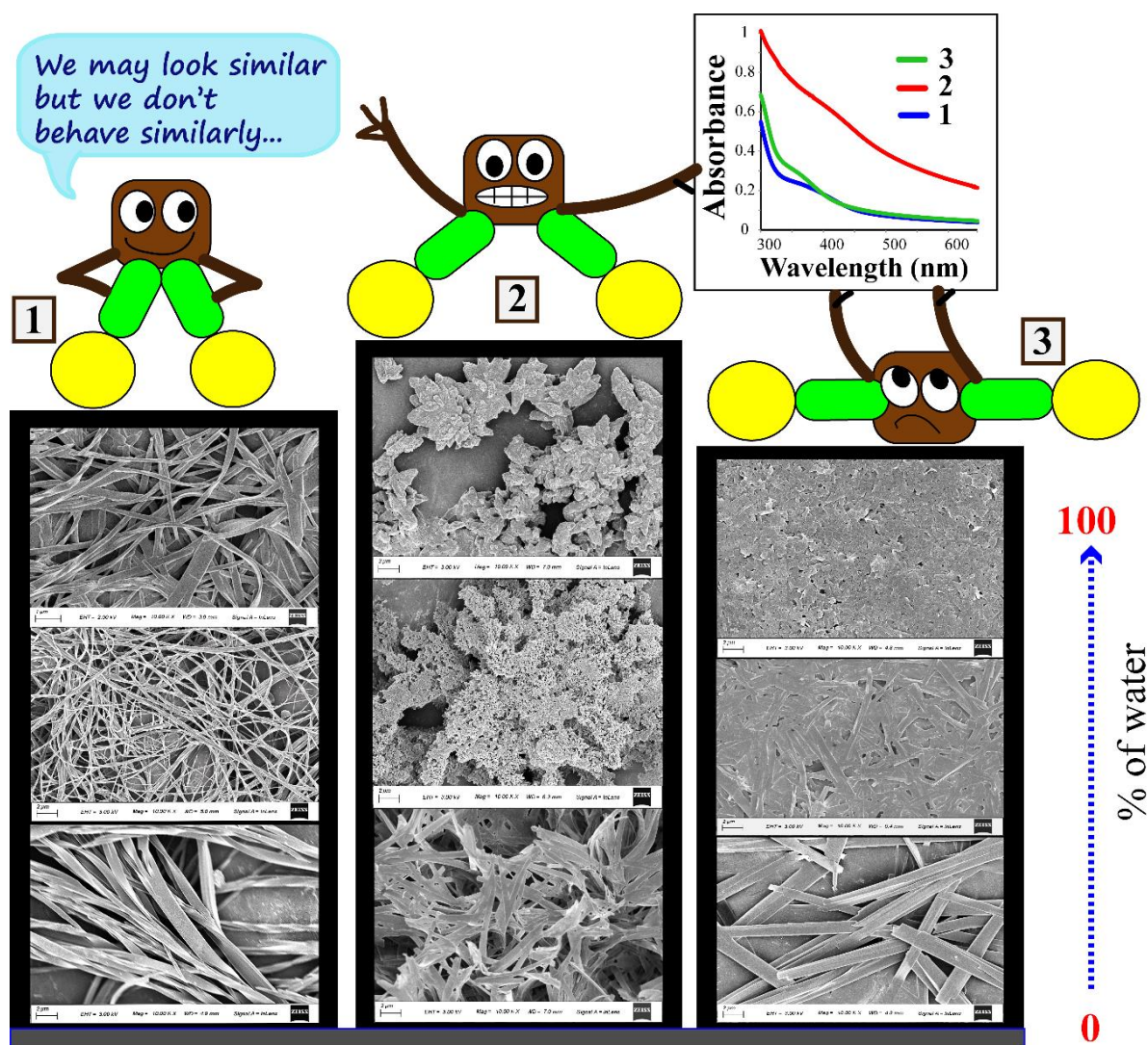
In view of recent development of nano/micro technologies, the creation of nano/micro-sized materials made of self-aggregated molecules is becoming of acute interest, as it offers a bottom-up approach to build well-defined supramolecular architectures with diverse morphologies for scrutinizing their structural property relationship in their aggregated state. However, precise control over the size, orientation, environment and photophysical properties of these self-assemblies, which is very important aspect for ensuring desired functions, still remains a major challenge and has been little explored and getting high demand and tremendous scientific importance. Working on these lines, in this thesis we have surveyed the aggregation performance of some simple urea and schiff base derivatives by varying their aromatic core as well as fluorophore unit to realize the effect of solvent tuning and presence of external analytes on their aggregation behaviour in aspect of real-life applications.

Chapter 2: Experimental Details and Characterization

This chapter covers the comprehensive information about the various materials and solvents used in the synthesis of the compounds along with synthetic procedures, specifications of analytical instruments employed as well as spectroscopic and microscopic experimental details followed for the characterization of the synthesized compounds and their aggregated form.

Chapter 3: Tuning the Aggregation Performance of Neutral Bis-Urea Derivatives with Varying the Aromatic Core: Influence of External Factors

In this chapter, we focused our intention to examine the effect of substituent position on aggregation behavior of a series of urea derivatives **1**, **2** and **3**. A set of three already reported *meta*- nitro-phenyl functionalized bis-urea derivative has been purposefully synthesized by varying the aromatic core (*ortho*-, *meta*- and *para*- position) and interestingly all three isomers exhibit substantial aggregation behavior as proved by adequate spectroscopic studies and verified by microscope imaging. Change in aromatic core revises their orientation which further controls their self-assembled architecture. The systematic survey has directed to the discovery of noteworthy isomeric effect in case of **2** in the formation and stabilization of aggregates compared with other two in the aqueous medium and the fact was also supported with the help of theoretical approach. Further we examined the outcome of external factors such as temperature, urea, salt (NaCl), pH on the aggregation characteristics to simplify molecular designing for a particular application. It was predicted that the hydrogen bonding interactions are playing the main role

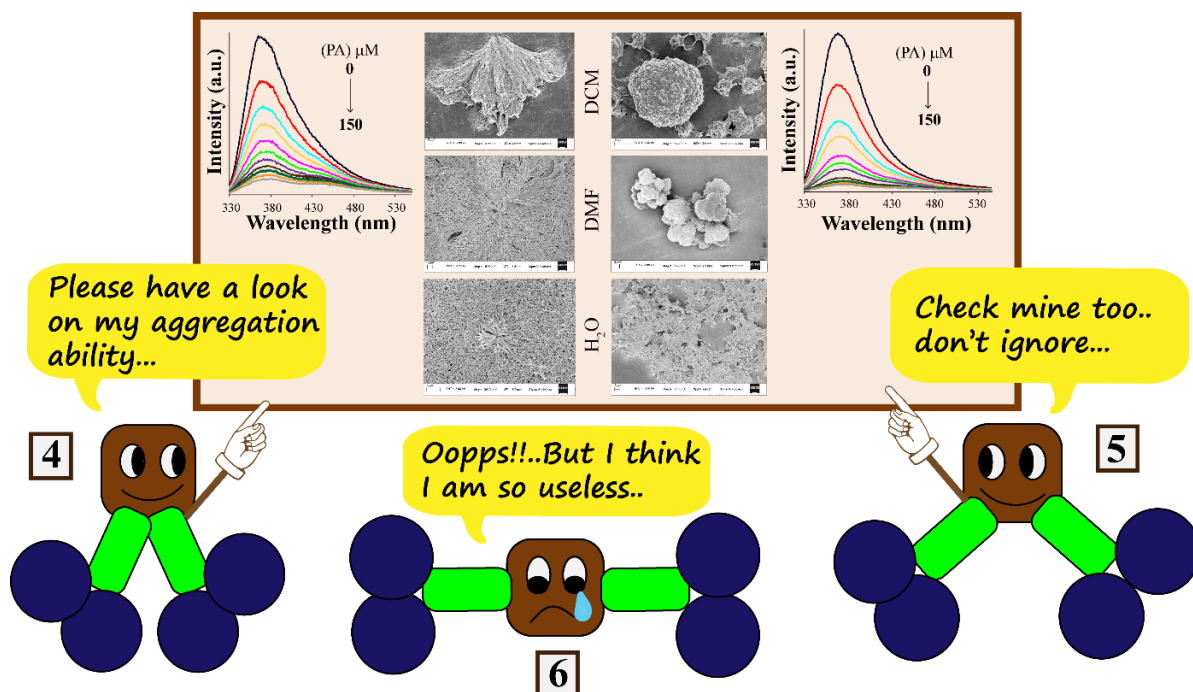


Scheme 1. A pictorial illustration of the research work covered in **chapter 3**.

among the molecules during the aggregation process and that interactions are so strong that external factors failed to interrupt the aggregation phenomenon.

Chapter 4: Probing the Aggregation Aptitude of Neutral Naphthyl bis-Urea Series with Varying the Aromatic Core: Effect of Solvent-Tuning and Response towards Nitroaromatics

In continuance of our interest in exploring the aggregation aptitude of small molecule, naphthalene functionalized bis-urea derivatives **4**, **5** and **6** with variation in aromatic core (*ortho*-, *meta*- and *para*- position) has been reported in this chapter to study their self-assembly behavior by tuning the solvent nature. Here, we tried to overcome the spectroscopic limitations of previous work by introducing naphthalene unit as a potential fluorophore and found that the change in the solvent had a visible impact on solute-solvent interaction, which further influences their aggregation pattern as supported by adequate spectroscopic studies. The ability of **4** and **5** to form a different

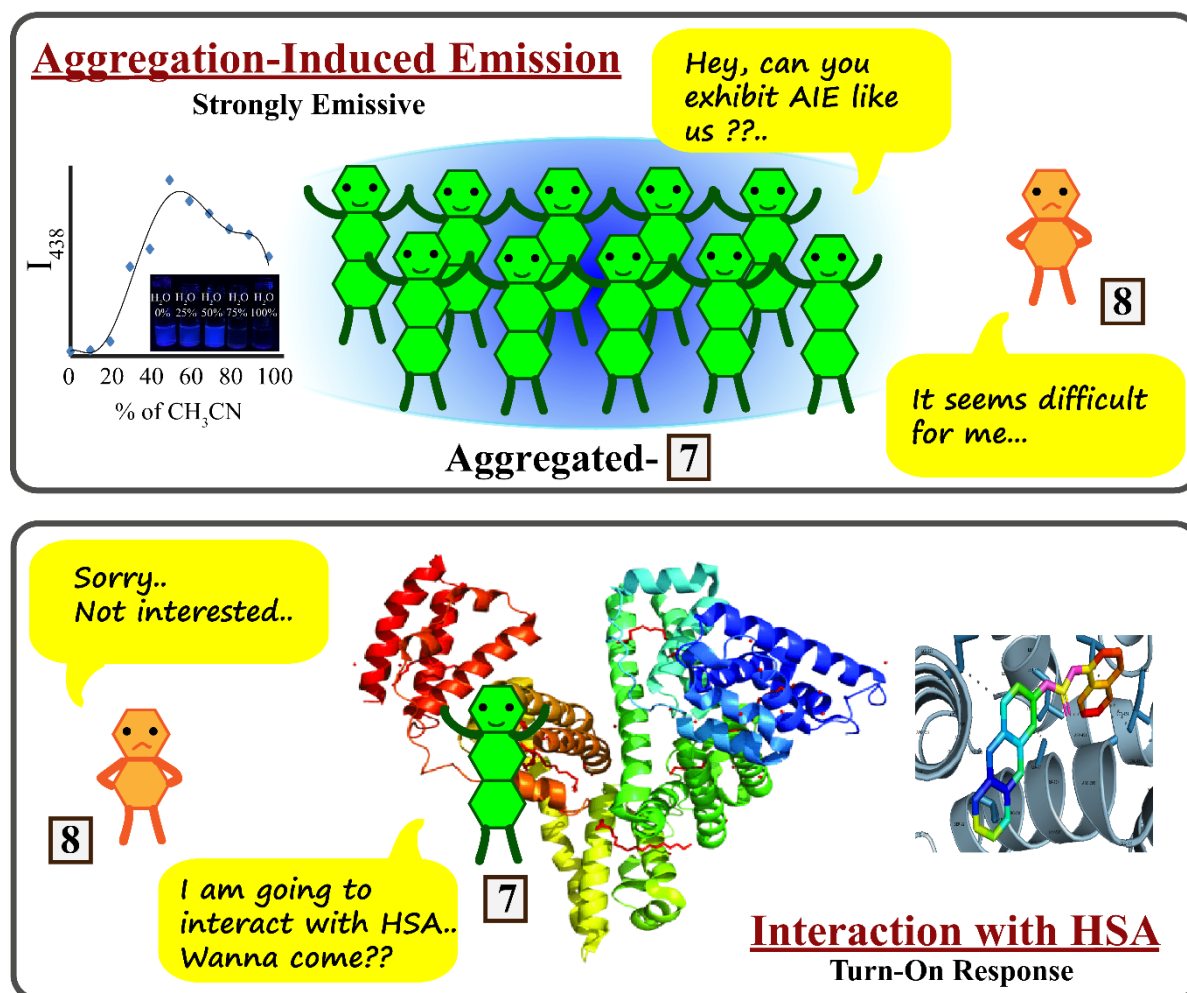


Scheme 2. A pictorial illustration of the research work covered in **chapter 4.**

type of micro/nano-structure in solvents with different polarity and H-bond donating capability was also explored with microscope imaging studies. However, compound **6** appeared to be less potent with regards to self-aggregation in the mixed solvent system as well as in aqueous medium. Moreover, we further checked the interaction with the electron-deficient nitro-phenols for the aggregated form of the compound **4** and **5** in the aqueous medium to investigate the self-aggregation tactic of small molecules in depth. And the systematic assessment encountered a significant effect in the case of PA (Picric Acid) among the nitro-phenols due to its strong electronic acceptor nature, which strikingly affects the electron transfer in fluorophore skeleton. Hence, as a result the molecular aggregation was completely disturbed in presence of PA and fluorescence quenched.

Chapter 5: Exploring the Aggregation Potential of Urea based-Luminogens with Varying the Fluorophore: AIE Activity and Interaction with Human Serum Albumin

This chapter reports a simple yet effective di-substituted urea derivative **7** which is capable of displaying interesting AIE characteristics in acetonitrile-water mixed solvent. It is worth mentioning that merely increasing the water content of the solvent mixture resulted in an exhibition of the much desired AIE characteristic in absence of any external stimuli or analyte. The AIE active **7** can also produce significant rapid change in the fluorescence behavior in real time through selective TURN-ON response towards HSA over other comparable proteins and bio-analytes in 100% aqueous medium with a very low detection limit (5 $\mu\text{g/mL}$). The interaction

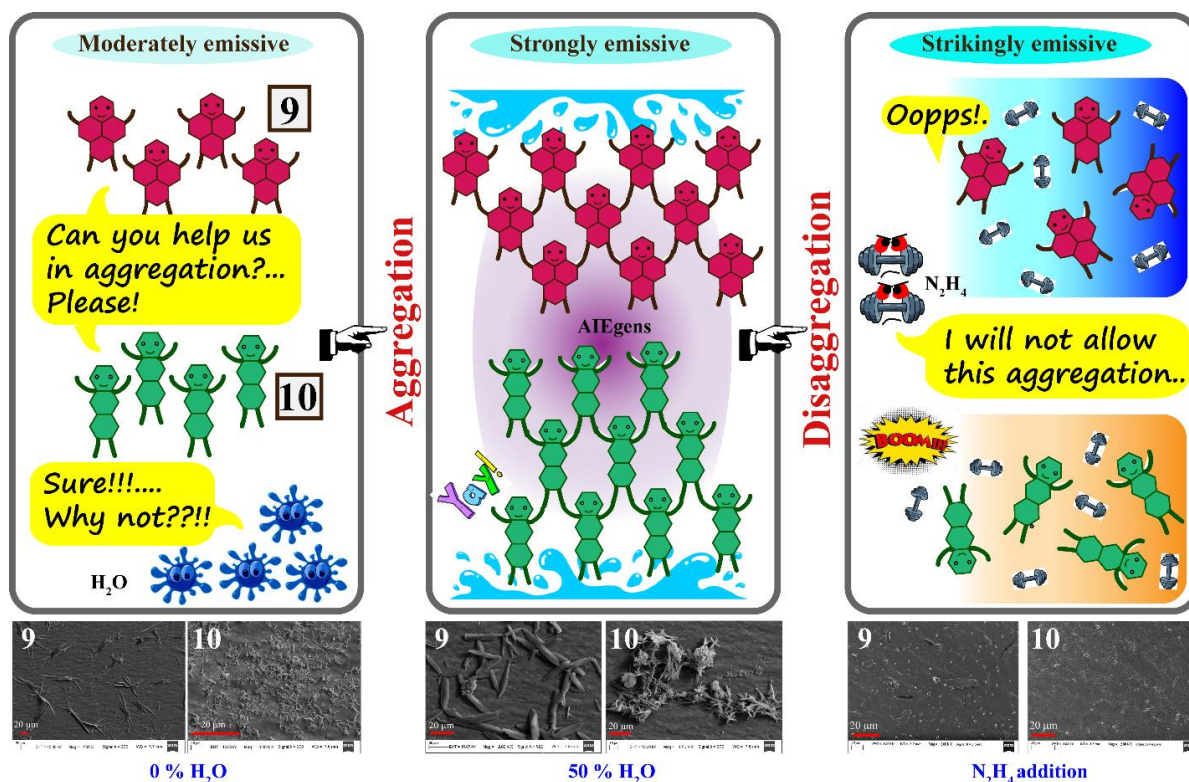


Scheme 3. A pictorial illustration of the research work covered in chapter 5.

between HSA and **7** is mainly hydrophobic in nature and has been well supported by various spectroscopic methods and molecular docking approach. Based on the drug displacement experiment, the detection of HSA by **7** can be attributed to the site-specific binding of **7** to the domain IIA and IB of HSA. In addition, **7** proved its efficient clinical utility in analytical prospects by responding to HSA in artificial urine samples as well as in bio-fluidic samples. A previously reported probe **8** was also synthesized as a control compound and studied to further understand the principles underlying the AIE behavior of **7**.

Chapter 6: Directing the Aggregation Prospective of Schiff Base-Luminogen with Varying the Fluorophore: From Classic AIEgen to Efficient Hydrazine Sensor in their Aggregated State

This chapter deals with an alternative approach to trigger both AIE and ICT by crafting both donor and acceptor moiety in two simple Schiff base compounds **9** and **10** containing pyrene and anthracene respectively as a traditional AIE core linked to 4-(N,N-diethylamino)salicylaldehyde



Scheme 4. A pictorial illustration of the research work covered in **chapter 6**.

to investigate their aggregation pattern via spectroscopic study along with microscopic support. It is worth mentioning that simply regulating the water content of the medium leads to an exhibition of the already anticipated AIE properties of the two compounds without the presence of any external stimuli. Interestingly, **9** and **10** are not only capable of acting as an effective AIE luminogen with morphological validation of aggregates formation by changing the solvent conditions but can also exhibit remarkable turn-on fluorescence responses toward hydrazine selectively. Hence, further analysis was also commenced to probe the mechanism of hydrazine interaction and its impact on the aggregation aptitude of **9** and **10**. And interestingly, the interaction between the aggregated AIEgens and hydrazine is mainly responsible for the hydrogen bonding phenomenon, which induce disaggregation of molecular aggregates. Moreover, AIEgen aggregates can show good sensitivity towards hydrazine in multiple water samples and artificial urine. Even this sensing ability was also applied in the fluorescence imaging experiment to track hydrazine in plant roots and mammalian cells.

Contents

CHAPTER 1: Introduction

1.1 Supramolecular self-assembly: macromolecule to small molecule	1
1.2 Aggregation Induced Emission(AIE): special case of supramolecular aggregates	2
1.3 Detection of analytes: aggregation/disaggregation approach	11
1.4 Objective of the thesis	17
References	18

CHAPTER 2: Experimental Details and Characterization

2.1 General Information and Materials	21
2.2 Synthesis and characterization of the compounds	22
2.2.1 Compound 1, 2 and 3	22
2.2.2 Compound 4, 5 and 6	22
2.2.3 Compound 7 and 8	22
2.2.4 Compound 9 and 10	23
2.3 UV-Vis and Fluorescence Spectral Studies	23
2.4 Detection Limit Calculations	24
2.5 Circular Dichroism measurements	25
2.6 Transmission Electron Microscopy	25
2.7 FRET and REES studies	25
2.8 Measurement of fluorescence lifetime	25
2.9 Competitive Drug Displacement Study	25
2.10 Molecular Docking Studies	26
2.11 Crystallography	26
2.12 AFM Imaging	26
2.13 Cytotoxicity Assay	27
2.14 Cell Imaging Studies	27
2.15 DFT Studies	28
References	28
Appendix-Chapter 2	29

CHAPTER 3: Tuning the Aggregation Performance of Neutral Bis-Urea Derivatives with Varying the Aromatic Core: Influence of External Factors

3.1 Objective of the Chapter	39
3.2 Outline of the Chapter	39
3.3 Structural aspiration of 1, 2 and 3	40
3.4 Aggregation outcome of 1, 2 and 3	40
3.5 Influence of external stimuli on aggregation behavior	44
3.6 Theoretical approach	46
3.7 Conclusion	47
References	48
Appendix-Chapter 3	49

CHAPTER 4: Probing the Aggregation Aptitude of Neutral Naphthyl bis-Urea Series with Varying the Aromatic Core: Effect of Solvent-Tuning and Response towards Nitro-aromatics

4.1 Objective of the Chapter	53
4.2 Outline of the Chapter	53
4.3 Structural aspects of 4, 5 and 6	54
4.4 Insights into the Aggregation Features	54
4.5 Impact of the Solvent on Aggregation	57
4.6 Interactions with nitro-aromatics	60
4.7 Conclusion	62
References	63
Appendix-Chapter 4	64

CHAPTER 5: Exploring the Aggregation Potential of Urea based-Luminogens with Varying the Fluorophore: AIE Activity and Interaction with Human Serum Albumin

5.1 Objective of the Chapter	67
5.2 Outline of the Chapter	67
5.3 Design rationale of 7 and 8	68
5.4 AIE activity of 7 and 8	68
5.5 Interaction study of 7 with HSA	72

5.6 HSA quantitation	75
5.7 Binding studies from docking results	76
5.8 Interaction of 7 with HSA in bio-fluids and artificial urine samples	76
5.9 Conclusion	76
References	77
Appendix-Chapter 5	78

CHAPTER 6: Exploring the Aggregation Potential of Urea based-Luminogens with Varying the Fluorophore: AIE Activity and Interaction with Human Serum Albumin

6.1 Objective of the Chapter	87
6.2 Outline of the Chapter	87
6.3 Design Principle of 9 and 10	88
6.4 Crystallographic evidence	89
6.5 Aggregation Prospective	89
6.6 Sensing Performance	94
6.7 Analytical Aptitude	99
6.8 Conclusion	101
References	102
Appendix- Chapter 6	103

Conclusion and Future Perspective 113

Thesis Overview 115

Curriculum Vitae 116

Crystallographic files Attached File

CHAPTER 1

Introduction



Chapter 1

1.1 Supramolecular self-assembly: macromolecule to small molecule

Nature, an unlimited source, inspires us to explore the world we live in. Researchers are all interested in discovering the mysterious veil of nature (e.g., living organisms, especially cells) at molecular levels because nature has developed elaborate machineries that largely contain supramolecular assemblies of bio macromolecules and carry out sophisticated biological tasks in all organisms. Self-assembly is a predominant process in cells and a common phenomenon of nature.^{1,1,1,2} Biological molecules like proteins, peptides, nucleic acids, lipids, and other cellular components with complementary properties self-assemble to form the basic biological unit, the cell. Cellular events like amyloid fibril formation, antigen-antibody recognition, chromatin assembly and phospholipid membrane self-assembly are brilliant examples of molecular self-assembly (Figure 1.1). Protein folding clearly elucidates the noncovalent interactions responsible in the self-assembly in aqueous solution.^{1,3} Proteins are the example of assembly of linear strands of covalently linked amino acids when regarded in a simplistic perception. So, on a much smaller scale, self-assembly principle is comprehended when two strands of DNA zip up to form the double helix that encodes our genome. Or, when cells self assemble into embryonic tissues that further develop into fully formed humans and animals. On the other hand, viruses are also examples of supramolecules based on protein and nucleic acid, with different shapes and sizes, that manifest their functionality through self-assembly. Hence, one of the most amazing aspects of life is that all living organisms are built via self assembly, an ultimate natural design process by which an organized structure apparently forms itself from a disordered association of smaller parts. But the most sophisticated biological system follow dynamic type of self assembly that repeatedly consumes energy in a never-ending cycle of assembly and disassembly to respond and adapt their environment and available components continually. This is how thousands of molecules come together to comprise cells and carry out the complex series of biochemical reactions that make life possible.

To mimic the properties of biological systems by non-living systems, many disciplines use the concept of self-assembly.^{1,4} The self-assembly of some structures can be boosted by shaking up parts and increasing their probabilities of finding corresponding connections, like a lock and key, until a stable structure appears from the sum of parts. For example, “DNA Origami” where long DNA molecules self-organize into 3D structures upon being shaken in a test tube. Thus the

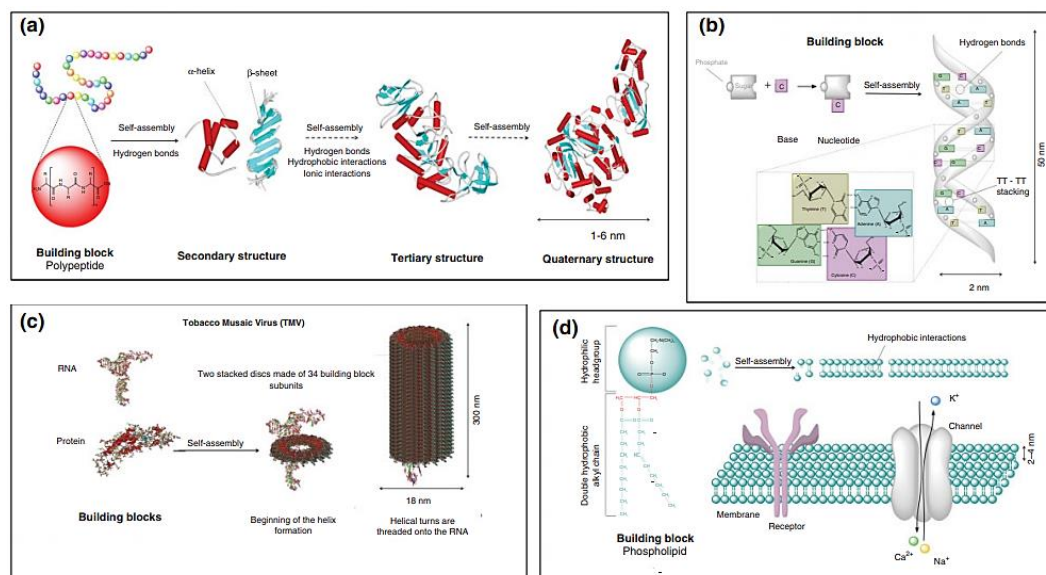


Figure 1.1 Examples of biological self-assembled structures showing the building blocks and the relevant interactions involved in the self-assembly process. (a) Protein folding; (b) ds-DNA; (c) tobacco mosaic virus (TMV); and (d) cell membrane (Reproduced with permission from ref. 1.2 Copyright 2013 Wiley).

understanding of the assemblies of bio macromolecules (e.g., DNA, RNA, and proteins) at a molecular level and the intrinsic forces for the self-assembly of small molecules of cells (e.g., lipids or cholesterol) have provided useful insights on how these simple components self-assemble to form highly ordered and precisely controlled structures in an organism,^{1,5} which has stimulated the exploration of assemblies of small molecules to mimic the properties and structures of living systems for applications in different fields to benefit humans.

The laboratory of Jean-Marie Lehn, who won the Nobel Prize three decades after Staudinger, introduced the idea of supramolecular chemistry and its link to functional structure.^{1,6} In the 1990s, George Whitesides' laboratory established the concept of self-assembly of nanoscale structures^{1,7-1,9} and the authors' laboratory developed the concept of self-assembly for functional bulk materials using designed molecules.^{1,10,1,11} Supramolecular chemistry mainly revolved around the chemical systems together with a distinct number of assembled molecular architecture or components and also refer to the chemistry beyond that of molecules. While classical chemistry deals with the coordinative bond and covalent bond formation, supramolecular chemistry focuses on the weaker and reversible noncovalent interactions between molecules such as hydrogen bonding, halogen bonding, ion-ion and ion-dipole interactions, cation- π and anion- π interactions, π - π interactions, Van der Waals forces, and hydrophobic effects (Figure 1.2). Relative to strong covalent bonds, incorporating these type of weaker interactions and make the most of on them in novel ways continues to outline the essence of the field of supramolecular chemistry. Another fascinating

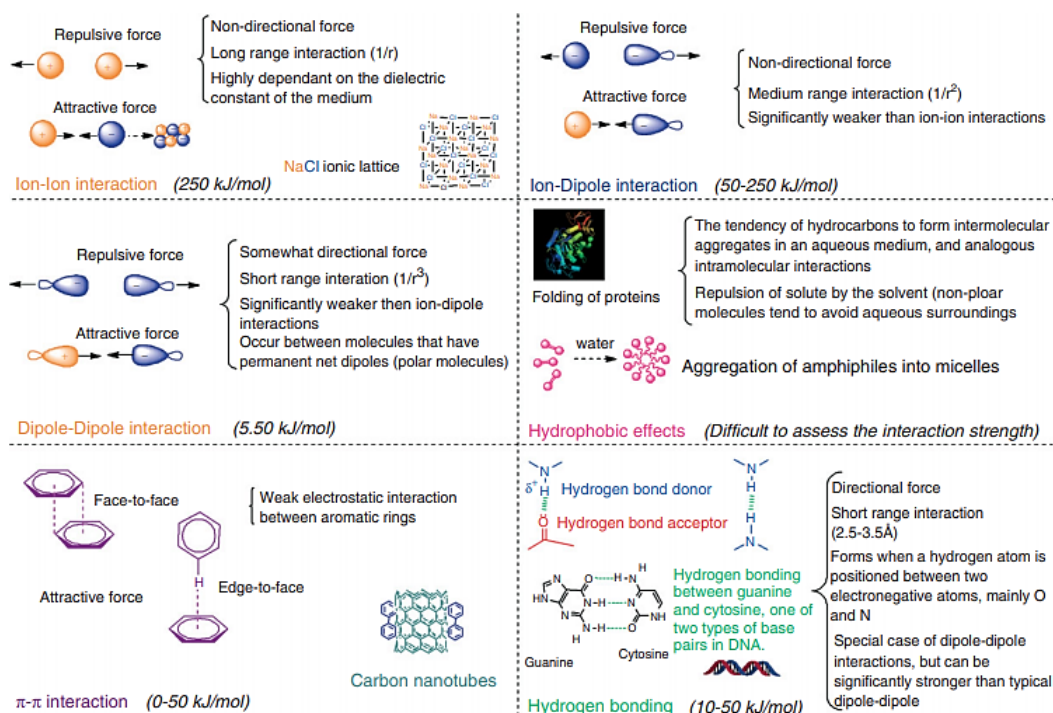


Figure 1.2 An illustration showing the noncovalent interactions involved in supramolecular chemistry and their strength (Reproduced with permission from ref. 1.2 Copyright 2013 Wiley).

description of supramolecular chemistry is as ‘lego™ chemistry’ wherein an individual lego™ brick characterises a molecular building block and there exists a reversible intermolecular interaction that holds them together to constitute a supramolecular aggregate. Hence, over the time, the definition of supramolecular chemistry extended to include any organized entity in which two or more chemical species are held together by intermolecular forces and provides the basis of self-assembly where the instructions of how to assemble larger entities are coded in the structural motifs of individual molecules.^{1,12,1.13} According to Whitesides,^{1,14} the components of a molecular self-assembling system consist of a group of molecules or segments of a macromolecule that interact with one another. These molecules, or molecular segments, may be the same or different. Their interaction starts from a less ordered state (a solution, disordered aggregate or random coil) leading to a more ordered final state (a crystal or folded macromolecule). Within the definition of self-assembly, Whitesides and Grzybowski have been considering two main classes of self-assembly: static and dynamic.^{1.15} In static self-assembly, ordered static structures are formed from the components (structure does not change in time) without any environmental exchange of energy and does not change in time. In contrast, dynamic self-assembly involves an input of energy from an external source and subsequent dissipation into the environment to form ordered nonequilibrium structures, which are maintained far from equilibrium through. Thus Supramolecular chemistry laid claim to films, gels, liquid crystals, nanostructures, polymers-all

systems that self-assemble. The field, being at the boundary of chemistry, materials science, molecular biology, engineering and polymer science, happily embodied all of these as well.

So, in the context of molecules and cells, **Molecular self-assembly** is the process in which spontaneous organization of molecules arranges themselves into well-ordered structure through different non-covalent interactions with the balance of both thermodynamic and local equilibrium. Although these forces are weak, their combined interactions can produce structurally and chemically stable arrangements.

Although the idea of self-assembly originates from molecules, its beauty lies beyond the molecular level in developing various kinds of molecular superstructures with diverse morphologies at the micro- or nano-level in countless areas.^{1.16-1.19} The design and fabrication of these functionalized materials made of self-assembled molecules rely heavily on their primary stage of synthesis. This synthesis policy focuses on manipulating the aggregation structure instead of the molecular structure, and entirely depends on the molecule's shape, size, orientation and chemical environment. So, molecules can be made to self-assemble spontaneously into multicomponent, complex structures when they are instructed to do so. And this instructions exist in the form of the molecule's shape, its chemical surfaces, and how well it fills space in the phase where the assembly takes place. These instructions are written into the molecule during its synthesis and relies heavily on chemical complementarity and structural compatibility. It is reported that π -conjugated molecules allow the formation of stacked molecular arrangements, and therefore are ideal candidates for the building blocks of supramolecular assemblies^{1.20} where non-covalent interactions play important roles in the creation of controlled 1, 2 and 3 dimensional superstructures, such as nanowires, nanotubes, nanoribbons, nanobelts, nanosheets, spheres, capsules, and nano/micro-flowers from small aromatic π -conjugated functional molecules.^{1.21-1.27} Many of these dimensionally tunable soft architectures show superior properties when compared with their individual molecular building blocks, thus offering an attractive pathway to bridge the gap between natural and artificial materials.

The success of self-assembly in a molecular system is determined by five characteristics of the system: Components-A self-assembling system comprises of a group of similar or different kind of molecules or segments that interact with one another; Interactions-Self-assembly takes place when molecules interact with one another through a balance of attractive and repulsive interactions (weak and non-covalent type); Reversibility (or Adjustability)- For self-assembly, the association either must be reversible or must allow the components to adjust their positions within an aggregate once it has formed to generate ordered structures; Environment- The self-assembly of

molecules normally occurs in solution or at an interface to allow the requisite motion of the components; Mass Transport and Agitation- For self-assembly to happen, the molecules must be in mobile phase and in solution, thermal motion plays the major role to bring the molecules into contact.

Hence, the spontaneity of this self-aggregation can be controlled externally by introducing additional stimuli. Detailed surveys have been executed to understand and monitor the controlled self-assemblies of small molecules in the presence of external components *in vitro* over the last several decades. Interestingly, the combination of controlled self-assembly of small molecules and modern bio-analytical techniques has emerged as an active and highly growing field for developing interesting supramolecular architectures.^{1.28-1.31} These self-assembled supramolecular architectures have found potential in multiple fields for high-tech applications via the interchange of concepts and various techniques (Figure 1.3).^{1.32-1.36} Although there is sufficient evidence from the recent advancement of molecular self-assembly in the case of naturally occurring materials, peptides, dendrons, surfactants, block-copolymer and amphiphiles, still the role of self-assembly of small molecules^{1.37-1.39} in revealing the natural process in aspects of chemistry remains very complicated and has been little explored.

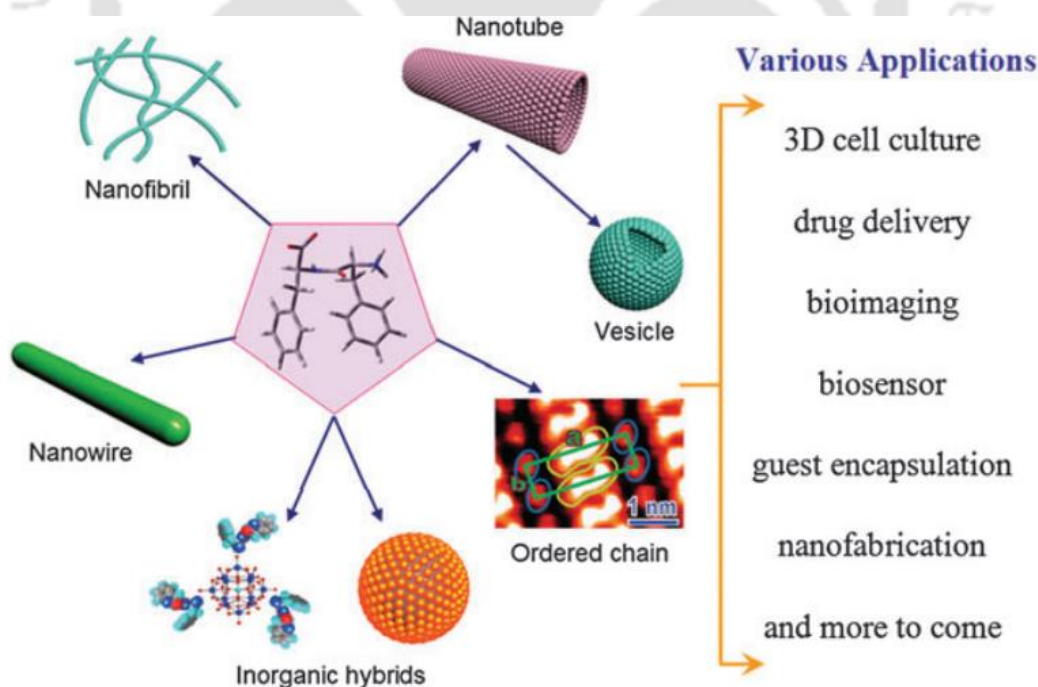


Figure 1.3 Schematic representation of various nanostructures formed by self-assembly of FF-based building blocks and their potential applications. (Reproduced with permission from ref. 1.36 Copyright 2010 RSC).

1.2 Aggregation Induced Emission(AIE): special case of supramolecular aggregates

Aggregation-induced emission (AIE) is a photophysical phenomenon related to chromophore aggregation. AIE describes the characteristics of a molecule which shows dim or no emission in dilute solution but much enhanced emission in aggregates or in the solid state. To some extent, the phenomenon of AIE is a not fresh one: Sir George Gabriel Stokes had observed a similar phenomenon in 1853 when he studied the luminescent properties of some inorganic salts.^{1.40} However, this observation and the corresponding prospective of this kind of materials for practical applications was not considered significantly until 2001, when Tang and co-workers investigated the luminescence activities of rotor-rich methyl-pentaphenylsilole, they re-discovered this phenomenon and proposed the concept of AIE.^{1.41} After the systematic analysis of the AIE phenomenon of different AIE systems (Figure 1.4), in 2003, they recognized that the active intramolecular motion of AIE luminogens (AIEgens) in the excited state possibly accelerates the non-radiative decay of the excitons to quench their emission in the solution state. Such an intramolecular rotation is restricted in the aggregated state and this results into the reduction of the non-radiative decay and an enhancement of the luminescence.^{1.42} Thus they suggested the

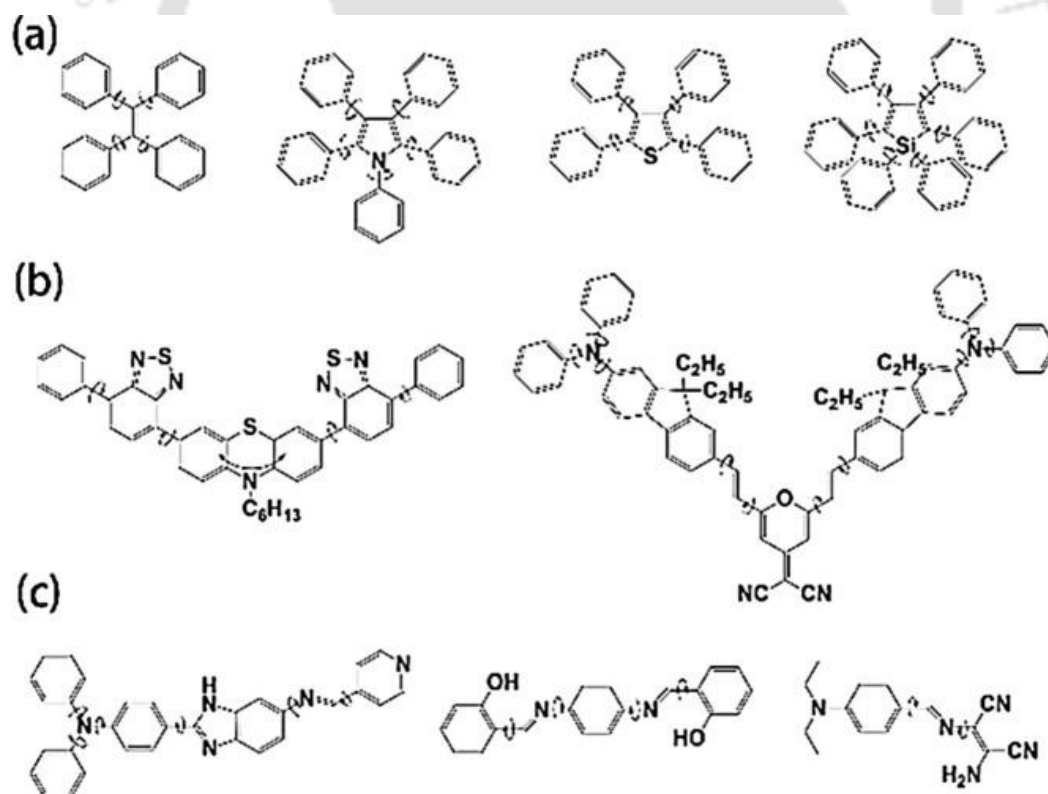


Figure 1.4 Typical molecular motifs that display aggregation-induced emission (AIE): a) propeller-shaped, b) V-shaped, and c) linear-shaped AIE motifs, respectively (Reproduced with permission from ref. 1.56 Copyright 2019 Wiley).

restriction of intramolecular rotation (RIR) as the mechanism of AIE. To rationally explain some new AIE systems without rotors, they further anticipated the restriction of intramolecular vibration (RIV) as a supplementary of RIR since intramolecular vibration can also result in non-radiative decay.^{1.43,1.44} Inclusively, RIR and RIV were combined under the new term restriction of intramolecular motion (RIM). The RIM mechanism now has been widely accepted as the mechanism of AIE and can be simply described as follows: In solution or in the mono-dispersed state, the active intramolecular motion (including rotation and vibration) boosts the non-radiative decay channels like conical intersections or dark decay processes to quench the emission, while in the aggregated state, the non-radiative decay channels are blocked due to the restriction of the intramolecular motion, leading to enhanced emission.^{1.45-1.48} Following the RIM mechanism, any manipulation that can restrict the intramolecular motion of AIEgens theoretically can lead to a stronger emission.^{1.49,1.50} The unique intramolecular motion-responsive luminescence of AIEgens and their strong solid-state emission enable their extensive applications in various fields including fluorescent imaging, bio-probes, chemical sensors, photonic drugs and optoelectronics.^{1.52-1.54} Moreover, aggregated molecular ensembles can even exhibit some new interesting features and functions that are not found in their mother molecular species. In this regard, AIE research provides an excellent platform to explore the behavior of molecular aggregates since it emphasizes the new properties achieved by molecular aggregates beyond the microscopic molecular level.^{1.55,1.56} Since Tang and co-workers introduced the concept of AIE in 2001 rapid progression and potential uses of AIE-active molecules in a vast range of scientific disciplines have encouraged researchers to modify the supramolecular assemblies with AIE activity further. Thus introducing fluorescence recognition unit and AIE active moiety in a single molecule is a promising approach for revising structural property relationship in their aggregated state. During the last 20 years, AIE research has made great advances in material development, mechanistic study and high-tech applications. These achievements validate that many behaviors and functions that are absent in molecular species can be found in molecular aggregates. In addition, since the properties of molecular ensembles are closer to those of macroscopic materials, AIE research is thus of both scientific value and technological importance for real applications.

Ben Zhong Tang et al. reported a new AIE luminogen^{1.57} consist of two units of tetraphenylethene (BTPE) and it emits more efficiently than that with one tetraphenylethene unit in the solid state (Figure 1.5) ; The emission intensity quenches as the four phenyl rings of TPE undergo an active IMR process in the solution state but the aggregation hindered the IMR process by blocking the non-radiative decay channel and hence makes TPE emissive. BTPE in the THF solution is non-fluorescent as evident from its emission spectrum which shows a flat line parallel

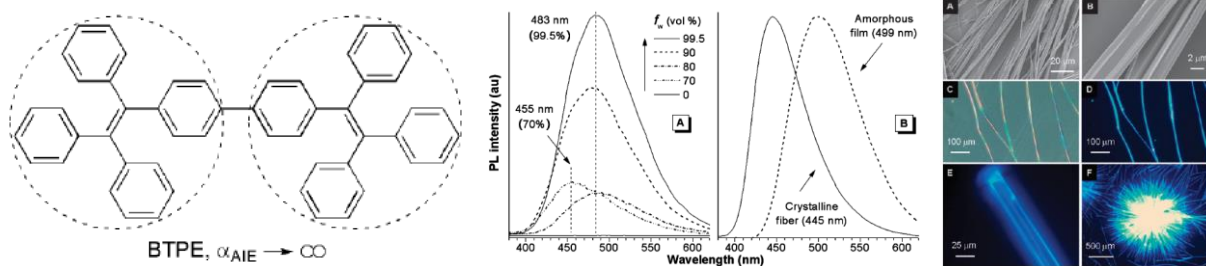


Figure 1.5 Left-Chemical structures. Middle-Emission spectra of (A) THF solution of BTPE (10 mM) and its aggregates suspended in THF/water mixtures with different fractions of water (f_w 70–99.5 vol%) and (B) its amorphous film and crystalline fibre in the solid state. Right-(A, B) SEM, (C) optical and (D–F) fluorescent images of the microfibers of BTPE obtained by slow evaporation of its THF/ethanol solutions. (Reproduced with permission from ref. 1.57 Copyright 2010 RSC).

to the abscissa. However, it started displaying clear peaks in the THF/water mixtures with high fractions of water ($f_w=70\%$). Since water is a non-solvent of BTPE, its molecules must have aggregated in the aqueous mixtures with high f_w ratios. Thus BTPE can display already anticipated AIE activity via enhancement of emission intensity due to aggregation. Self-assembly of the BTPE molecules affords crystalline microfibers that fluoresce in 100% efficiency, giving the largest effect of aggregation-induced emission. The fibres can further assemble into thicker rods, as exemplified by the optical image shown. The microwires are highly luminescent, emitting intense blue light upon photoexcitation. Its facile self-assembling and excellent EL performance make it promising for an array of technological applications.

Lang Liu and co-workers synthesized four pyrazolone phenylsemicarbazone derivatives (Figure 1.6) which do not emit in solutions.^{1.58} But the aggregates formed in nanosuspensions become highly fluorescent, exhibiting typical AIE characteristics. This AIE behavior may be attributed to the restricted intramolecular rotation mechanism based on the enhanced luminescent at low temperature. Moreover, these compounds can form 1D nanorods from 0D nanoballs with the aging

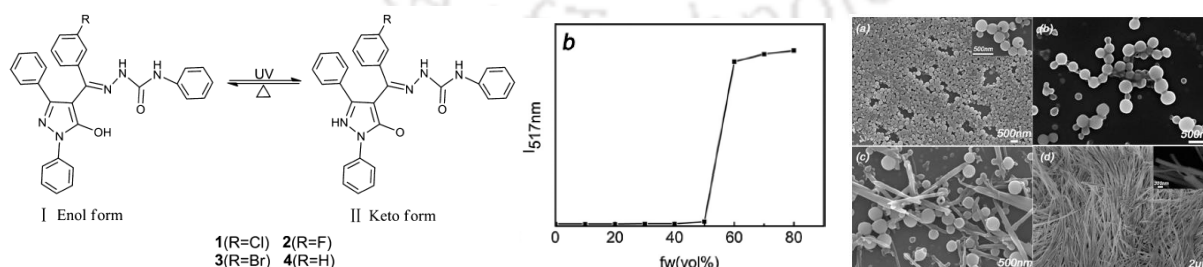


Figure 1.6 Left-Photochromic mechanism of the compound 1. Middle-Plot of emission intensity at 517 nm versus f_w for 1 in ethanol and ethanol–water mixtures. Right- SEM images of 1 aggregates in 40/60 ethanol–water mixtures (the inset is the magnified image). (a) Aging 10 min, (b) aging 1 h, (c) aging 2 h, (d) aging 10 h. (Reproduced with permission from ref. 1.58 Copyright 2014 Elsevier).

time during the aggregating process, leading to the red-shift of emission spectra.

Lallan Mishra and co-workers reported 1,8-Naphthalimide appended four benzoic acid derivatives^{1,59} that exhibit different types of nanoaggregates in water/DMF most likely assisted by complementary H-bonding besides π - π stacking interactions through their tricyclic 1,8-naphthalimide core (Figure 1.7). These aggregates can display enhanced emission and the emission intensity follows the order as LH > LMe > LCl > LN. Scanning electron and atomic force microscopy images supports the nanoaggregates formation. Several interesting supramolecular structures are formed by the weaker secondary interactions which also support the aggregation processes. They emitted intensely in both aggregated and in the solid states. Antiparallel dimeric interactions in the solid state leads to a herringbone arrangement to LH and 2D channel and stair-like arrangement for LCl and LN, respectively.

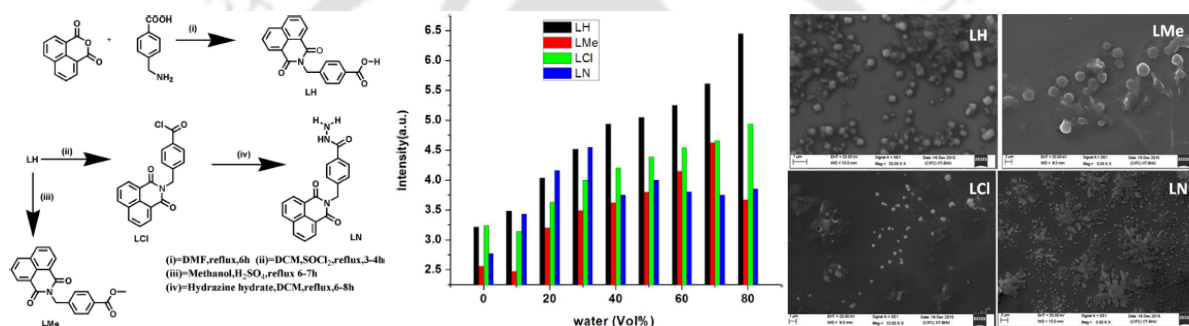


Figure 1.7 Left- Synthetic scheme of LH, LMe, LCl, and LN. Middle- Bar diagram showing variation in emission intensity of compounds on the incremental addition of water to the solution of compounds in DMF. Right- SEM images of nanoaggregates of LH, LMe, LCl, and LN (2×10^{-5} M, DMF/water 2:8 v/v for LH, 3:7 v/v for LMe, 2:8 v/v for LCl, and 4:6 v/v for LN) (Reproduced with permission from ref. 1.59 Copyright 2016 ACS).

Sheshanath V. Bhosale and co-workers became interested in the design and development of novel AIE-active TPE luminogens with supramolecular self-assembly potential to produce variety of nanostructures.^{1,60} They designed and synthesized dumbbell-shape TPE-1 and TPE-2 amphiphilic molecules which shows luminescence properties through solvophobic control (Figure 1.8). Interestingly, the variation in the water fraction in THF/water solutions results into the development of a 3D flower-shape supramolecular structure for the both TPE derivatives. SEM microscopy was used to visualise the step-wise growth of flowershape assembly. They used TPE as an extended π -conjugated moiety, amide group for a hydrogen-bonding and the alkyl chain as a segment that can introduce van der Waals interaction to the self-assembly process. These arrangements prevent crystallization and favour the directional growth of flower-shape nanostructures in a 3D fashion.

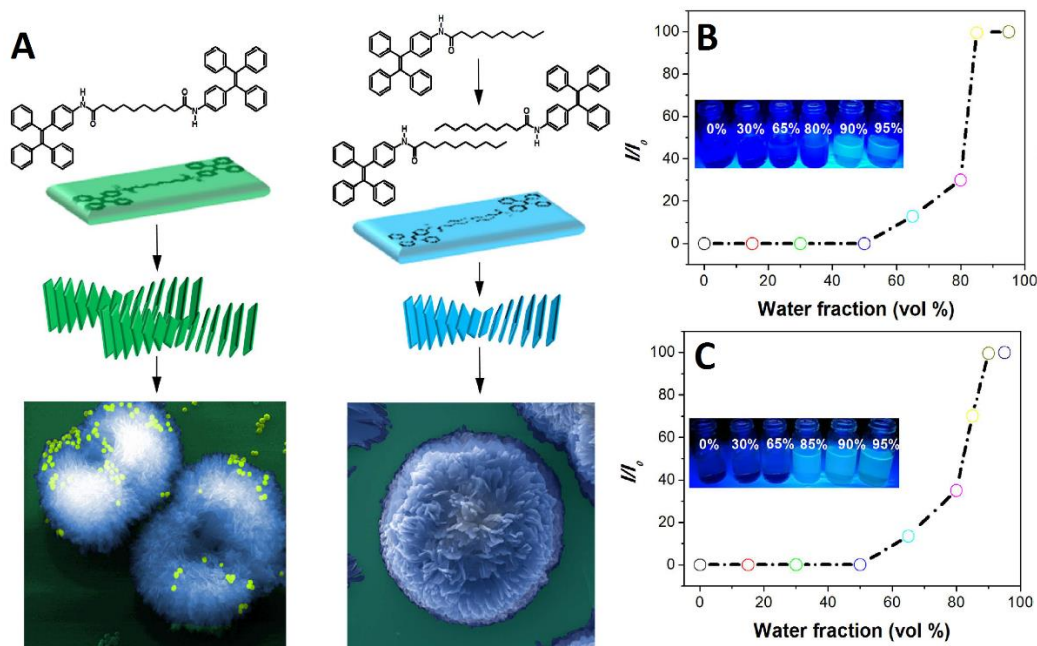


Figure 1.8 Schematic diagram illustrating flower-like assembly of TPE-1 in CHCl₃/hexane ($f_h = 95\%$) and TPE-2 in THF/water ($f_w = 85\%$). False colored SEM images used to visualize the nanospheres and flowershape assembly. (B and C) fluorescence intensity changes of TPE-2 and TPE-1 at 475 nm as a function of water fraction in THF solvent mixture and irradiation at 365 nm, respectively (Reproduced with permission from ref. 1.60 Copyright).

Ramanuj Narayan and co-workers developed a novel TPE diol amphiphile (2) with AIE property^{1,61} by mounting a hydrophilic diol moiety over hydrophobic TPE core. They confirmed the AIE behaviour of 2 by monitoring the change in PL intensity in acetonitrile-water mixture with different water fraction (f_w) (Figure 1.9). The dilute ACN solution had very weak PL intensity but a significant enhancement in the PL emission intensity was encountered for $f_w \geq 85\%$ that reached to a maximum at $f_w \approx 90\%$. The observed enhancement in PL intensity was due to the

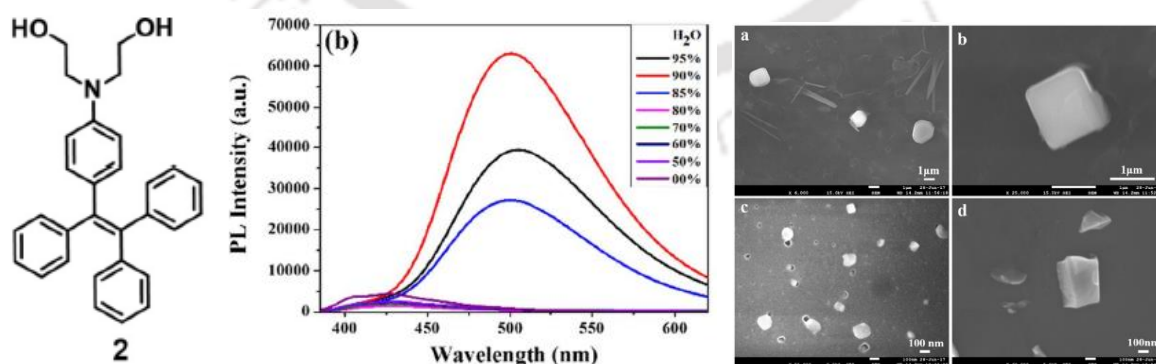


Figure 1.9 Left- TPE diol amphiphile 2. Middle-PL intensity spectra of 2 (10 μ M in CH₃CN, $\lambda_{ex} = 380$ nm) with varying % of water at constant pH 7.4. Right- FESEM morphology of 2 obtained on silicon wafer:(a, b) in ACN-water mixture ($f_w \approx 90\%$) and (c, d) in DMSO-water mixture ($f_w \approx 90\%$) (Reproduced with permission from ref. 1.61 Copyright 2017 Elsevier).

aggregate formation of **2** on the gradual increment of water fraction. Introduction of hydrophilic diol moiety in hydrophobic TPE core, successfully enhanced the intermolecular interactions between amphiphiles resulting in the stable self-assembled cubic superstructure and also improved its cellular uptake in live cells.

A pair of enantiomers, (S)-PPPtriAm and (R)-PPPtriAm, with higher optical activities and their raceme rac-PPPtriAm were synthesized via incorporation of three chiral 1-phenylethylamine pendants into the AIEE-active pentaphenylpyrrole scaffold and reported by Junge Zhi and co-workers (Figure 1.10).^{1,62} The target compounds still retained evident AIEE feature, and the chiral substituents have little influence on their AIEE behaviors. Since water is a poor-solvent for (S)-PPPtriAm, the addition of suitable amount of water would boost intermolecular aggregation, which would restrict the intramolecular motions by blocking the non-radiative decay channels, and lead to enhanced emission, signifying a typical AIEE effect for (S)-PPPtriAm. The chiral compounds (S)-PPPtriAm and (R)-PPPtriAm exhibit aggregation-induced circular dichroism (AICD) feature with mirror-image Cotton effects and chiral polarized luminescence (CPL) feature. Moreover, they can self-assemble into orderly aligned nanofibers that interlock with each other to form larger aggregates in DMSO–water mixtures, whereas their raceme rac-PPPtriAm only form nanoparticles blocks. Thus, a novel strategy has been put forward to fabricate optically-active AIEE compounds with excellent AICD and CPL features.

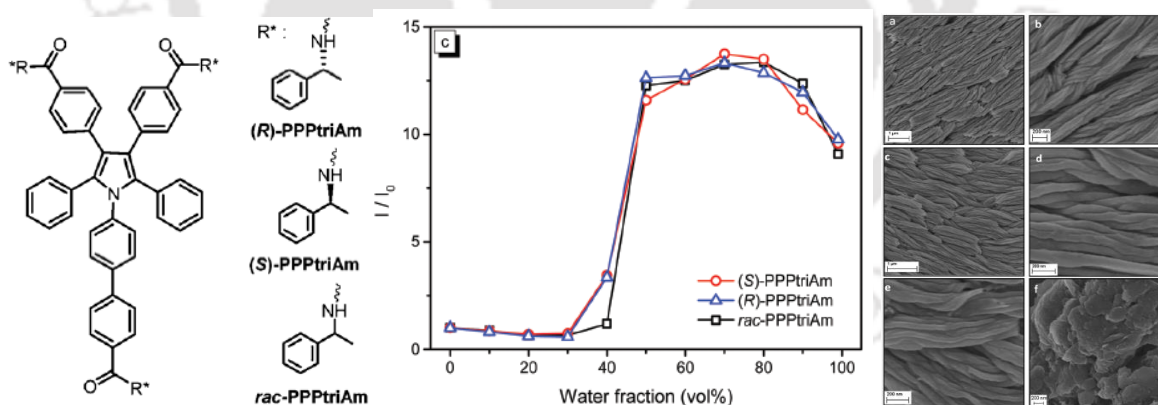


Figure 1.10 Left-chiral compounds. Middle-the comparison of I/I_0 for target compounds ($\lambda_{ex} = 290$ nm, concentration: 10 mM). Right- SEM images of the nanoaggregates obtained from DMSO–water mixtures for (S)-PPPtriAm at $f_w = 50\%$ (a and b), (R)-PPPtriAm at $f_w = 50\%$ (c and d), (S)-PPPtriAm at $f_w = 40\%$ (e), and rac-PPPtriAm at $f_w = 50\%$ (f) (concentration: 10 mM) (Reproduced with permission from ref. 1.62 Copyright 2017 RSC).

1.3 Detection of analytes: aggregation/disaggregation approach

Controlled self-assembly of molecular probes are the basis of obvious probe fluorescence signal alterations, which in turn means that the optical properties of the assembled-probe is considerably

different from that of the probe monomer. Design, manipulation and alteration of those molecular superstructures to achieve controlled photoluminescence properties and fascinating morphology in the presence or absence of external stimuli are still a challenging task. The idea of using those functional aggregates of small molecules as fluorescent sensors for the detection and imaging of important analytes and small molecules has attracted considerable attention nowadays.^{1.63-1.71} In view of the latest advancement, the involvement of AIE-active small molecule assembly in modern sensing techniques is appearing as a rapidly used functional tool for fabricating diverse supramolecular architecture through the exchange of views and practices among multiple fields for effective applications in sensing, imaging, optoelectronics and therapeutic studies. Concept of using self-assembled aggregates of small molecules as fluorescent bio-probes for the detection of analytes and imaging of protein has attracted much attention in recent years. Moreover, in comparison with conventional fluorescent sensors, AIE-active fluorescent sensors possess bonus advantages due to their bright emission with high fluorescent quantum yields, easy fabrication and broad application scope in water/high water content medium. Supramolecular aggregates as sensing ensembles are advantageous over the conventional small-molecule chemical sensors in the following aspects: (i) The building blocks are assembled by means of relatively weak and dynamic noncovalent interactions, providing easy and facile approaches for manipulating supramolecular structures. (ii) Water compatible supramolecular sensing system can be easily prepared by crafting water-soluble functionalities into the building blocks, which offers enormous prospects for such recognition systems to be employed in biological systems in the aqueous phase.^{1.72} (iii) The higher local concentration of the binding sites and the lower local concentration of water molecules around the binding sites in the aggregates substantially increase the originally weak and water-susceptible interactions, which makes those otherwise insufficient binding events in water of the corresponding molecular sensors highly sensitive. Since in many cases the building block molecules are aromatic compounds with large π -systems, strong $\pi\pi$ stacking in the aggregates would make them conjugate-polymer like, affording an additional possibility for signal amplification.^{1.73} The relative orientations among the binding sites in the aggregates can be tuned good for analyte binding,^{1.74} resulting in high selectivity. (iv) In particular, the aggregation or disaggregation process may involve cooperative interactions that also result in signal amplification, leading to higher sensitivity and selectivity as well. Therefore, using supramolecular aggregates from building blocks with easy design and facile synthesis could achieve even better sensing performance than that of molecular sensory systems that rely on sensors with delicate structures (Figure 1.11). A variety of supramolecular sensing systems have been developed. Yet, regarding analyte induced aggregation or disaggregation strategies,

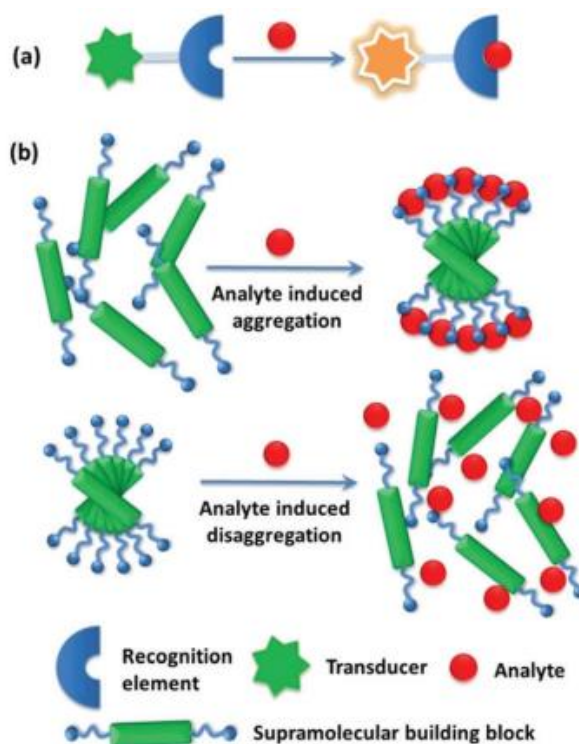


Figure 1.11 Comparison of (a) conventional sensory systems and (b) supramolecular sensory systems based on analyte induced supramolecular aggregation or disaggregation strategies (Reproduced with permission from ref. 1.71 Copyright 2016 RSC).

considerable progress has been made only with limited categories of building blocks, which operate for sensing via $\pi\pi$ stacking modulated photophysics of π -conjugated dyes, aggregation induced emission, metallophilic interactions, and more recently those emerging from highly ordered metal–organic frameworks. Although there are sufficient literature records on the recent advancement of the small molecule aggregation, still exploring the role and photophysical mechanisms of AIE-based small molecule aggregates for sensing endeavor are an active one and undoubtedly significant.

Jiang's group in 2010 reported the Hg^{2+} selective PBI derivative 1 which has an imide group similar to that in thymine (T) known to form the so-called "T– Hg^{2+} –T" binding motif.^{1.75} Thus, Hg^{2+} can specifically accelerate the aggregation of 1 and allow a highly sensitive and selective sensing of Hg^{2+} through dramatic fluorescence quenching of 1. More importantly, it afforded a non-fluorescent chemosensing ensemble "(1– Hg) n " for thiol-containing species which induce the disaggregation of the aggregates and recovery of the fluorescence. For cysteine, a detection limit of 9.6 nM was achieved. Therefore it can act as sensory system for both Hg^{2+} and thiol-containing species based on cooperative aggregation-disaggregation processes with high sensitivity and selectivity (Figure 1.12). This is the first report that shows that an imide group other than that

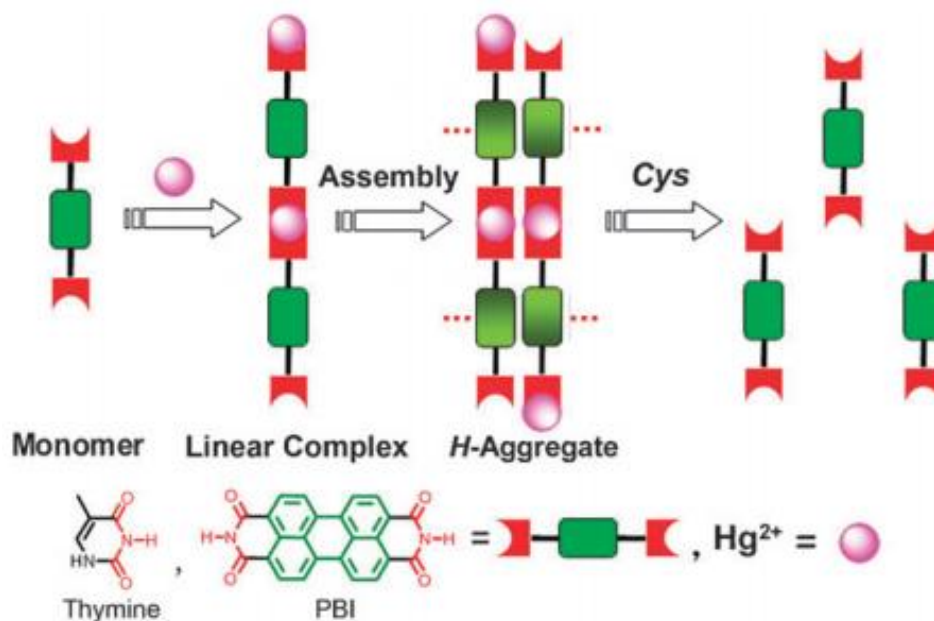


Figure 1.12 Hg^{2+} induced aggregation of 1 and dissociation of aggregates in the presence of cysteine (Reproduced with permission from ref. 1.75 Copyright 2010 RSC).

from thymine could lead to a similar “T– Hg^{2+} –T” binding motif for sensing applications.

A supramolecular amphiphilic pyrene-based boronic acid sensor for direct fluoride detection in aqueous solutions was reported by Jiang’s group (Figure 1.13).^{1,76} Binding of the fluoride anion to the boronate ester and protocatechuic acid (PCA) triggered the formation of supramolecular aggregates of ester leading to presumably lower local concentration of water and higher local density of binding sites, which enhances the fluoride affinity and therefore the selectivity against

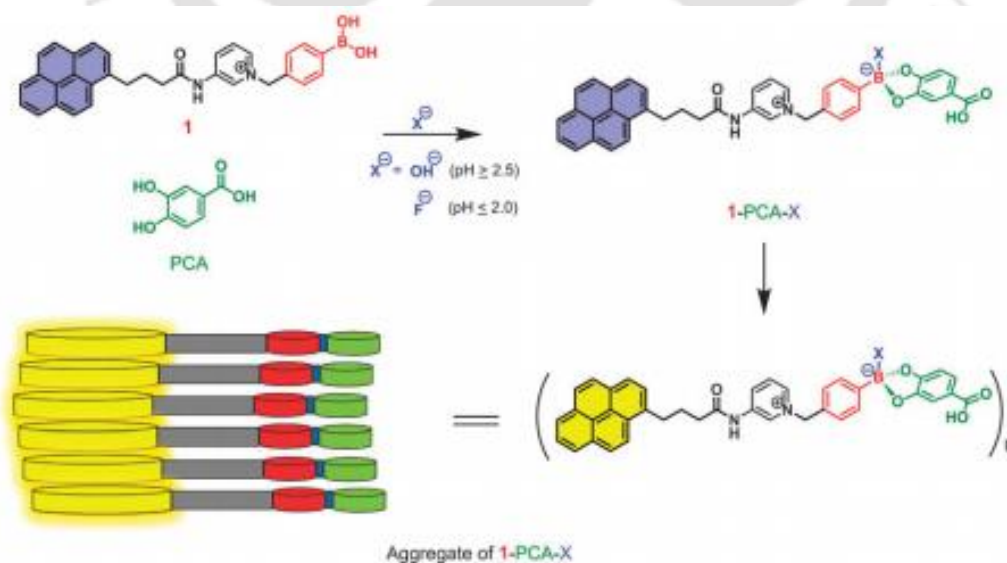


Figure 1.13 Schematic representation of fluoride sensing by the 1–PCA ensemble (Reproduced with permission from ref. 1.76 Copyright 2014 RSC).

OH. PCA was chosen to interact with 1 to enhance the Lewis acidity of boronic acid toward the fluoride ion and reduce the interference of OH. And the formed ester can aggregate under highly acidic conditions ruling out the interference of OH. Due to supramolecular aggregation the solution turned turbid when interacted with fluoride ion and a significant change in the excimer emission of 1 allows sensitive detection of fluoride at the ppm level in aqueous solutions. The fact that the addition of CTAB micelles leads to a dramatic quenching of the excimer emission supports the conclusion that aggregation strengthens the boron–fluoride interaction in aqueous solutions.

A series of AIEE active novel V-shaped naphthalimide derivatives are developed by P. K. Iyer and co-workers.^{1,77} Naphthalimide derivative functionalized with 8-hydroxyquinoline (α -NQ) can spontaneously forms highly fluorescent “nanoribbon” like structures in aqueous media irrespective of concentration and surface at room temperature. The classical head to tail π - π stacking, as revealed by the single crystal X-ray study, was found to be the main driving force for the J-type aggregation with unique self-aggregating behavior. These α -NQ nanoribbons were found to be highly sensitive and selective towards the multi-functional nonheme protein ferritin (LOD-0.33 ng mL⁻¹) under physiological conditions (Figure 1.14). On the other hand, α -NN and β -NN displayed the properties of typical AIEgens which can self-assemble into unsymmetrical nanoparticles due to the absence of strong head-to-tail π - π interactions.

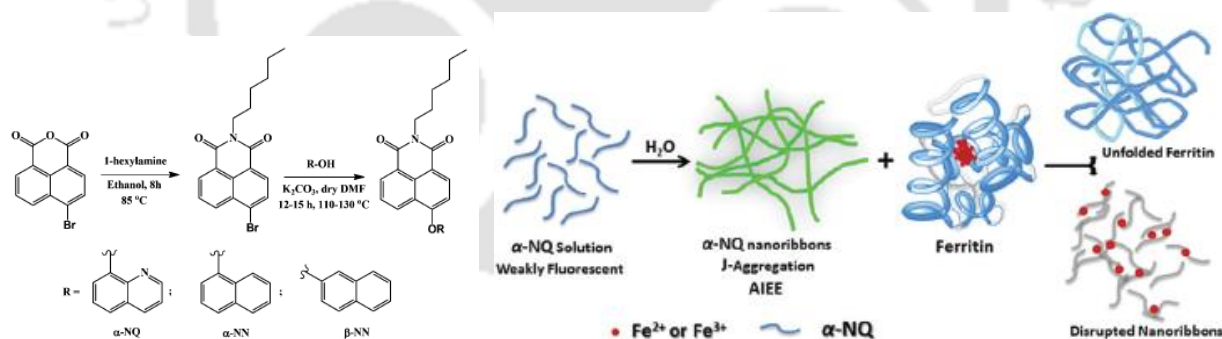


Figure 1.14 compounds α -NQ, α -NN and β -NN and illustration of the mechanism of protein unfolding and nanoribbon disruption using a fluorescent probe under physiological conditions with AIEE characteristics (Reproduced with permission from ref. 1.77 Copyright 2016 RSC).

Wenbin Zeng and co-workers designed an AIE-based bola-type small molecule 7 which is not only able to self-assemble into nanoparticles in aqueous solution but can also probe HSA (Figure 1.15).^{1,78} Nanoprobe 7 exhibits fast (15s) turn-on response to HSA with high specificity and sensitivity. Mechanism investigation discloses that noncovalent bonds including electrostatic interactions, hydrogen bonds, π - π , and cation- π interactions are responsible for trapping nanoprobe 7 into the Site I of HSA. It results into disassociation of the nanoparticle and activating the

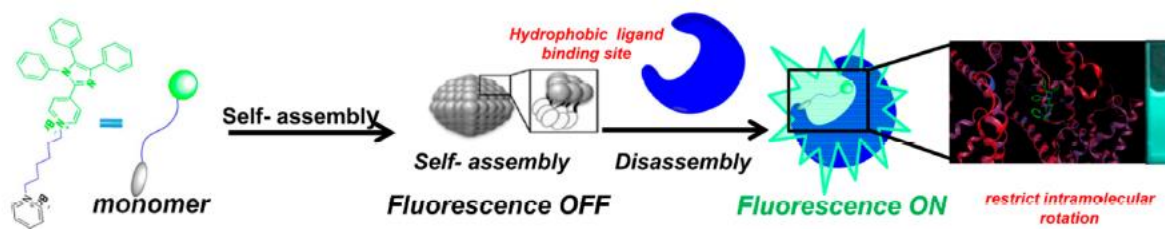


Fig 1.15 Chemical Structures of Probe Molecules and Self-Assembling Turn on Fluorescent Nanoprobe for HSA. (Reproduced with permission from ref. 1.78 Copyright 2017 ACS).

restriction intramolecular rotation. Thus, the nanoprobe 7 has good analytical potential to act as an efficient reporter for diagnosis of HSA related diseases and the molecular assembly based on AIE also opens up an alternative approach for the sensitive and selective detection for varied analytes.

Tiyanyu Han and coworkers reported a group of isomers varying the position of the carboxylic acid (para, meta- and ortho position) of an AIE core to yield positional isomers with self-assembly behavior.^{1.79} The preferential growth of the supramolecular architectures can be guided by the position of the carboxylic acid which is responsible for modulating the direction of dipole-dipole interaction. The vivid differences in morphology indicate that a minor change in chemical structure has a significant impact on the self-assembly process. In this case, carboxylic group could be visually regarded as a “rotary knob” with three gears: With the “knob” rotating, the morphology will undergo the transition from 1D to 3D supramolecular structures (Figure 1.16). These assemblies exhibited remarkable fluorescence responses toward amines, offering great

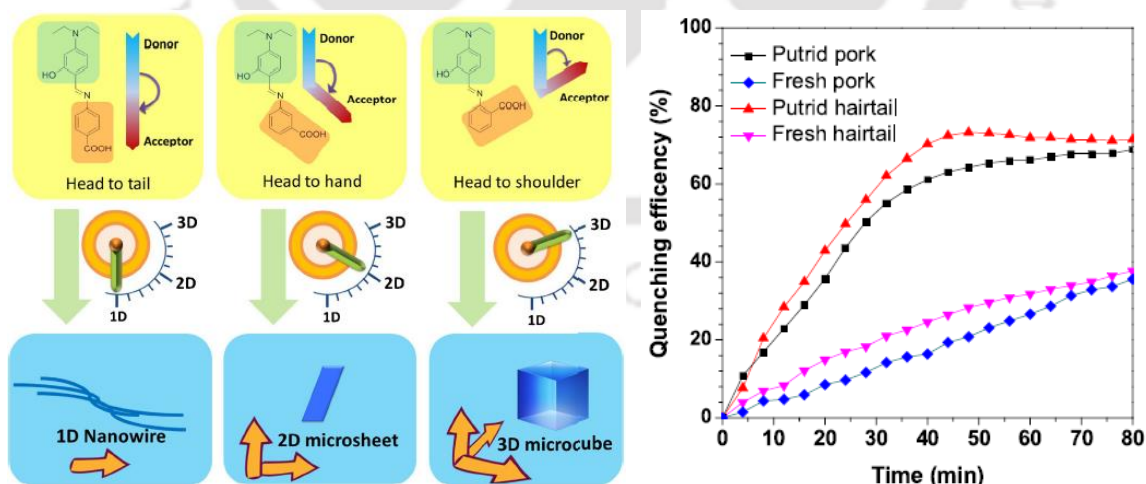


Figure 1.16 Left-Schematic illustration of the “rotary knob” with three gears that direct the 1D, 2D and 3D supramolecular self-assembly. Right-Time-dependent fluorescence quenching profile of the m-DB assemblies under the influence of meat samples. Time interval: 4 min. Excitation wavelength:430 nm. (Reproduced with permission from ref. 1.79 Copyright 2018 Elsevier).

potential to be fabricated into portable sensors for detecting meat spoilage.

K. Singh and co-workers have synthesised a benzothiazole based molecular probe which can not only exhibit maximum aggregation induced emission activity in 90% water fraction in THF solution but can also detect picric acid in their aggregated state (Figure 1.17).^{1,80} The broad emission of the compound covers a wide range of wavelength and hence reversible emission colour switching can be achieved simply by changing the excitation wave-length of the compound. In solution, the blue emission overwhelms others, whereas in dry state the emission in blue, green and red with intermediate yellow could be achieved. Furthermore the compound in its aggregated state was successfully employed for the detection of picric acid in solution, solid, as well as in human cancer cells.

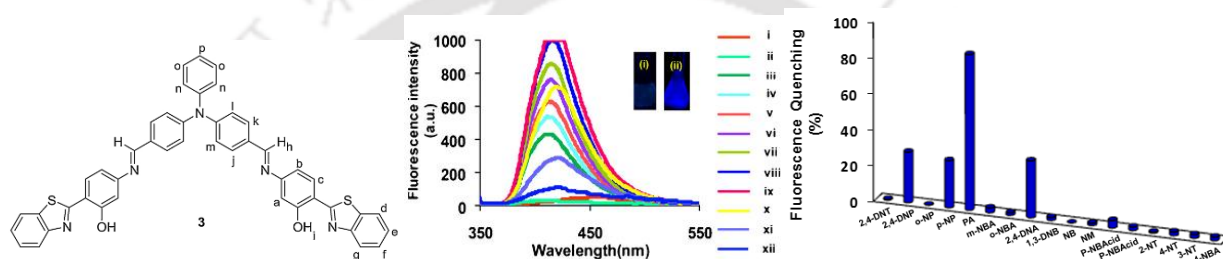


Figure 1.17 Left- The molecular probe 3. Middle- Changes in the emission behaviour of $3(5 \times 10^{-6} \text{M})$ in THF with increasing % age of water (i = 10:0, ii = 9:1, iii = 8:2, iv = 7:3, v = 6:4, vi = 5:5, vii = 4:6, viii = 3:7, ix = 2:8, x = 1:9, xi = 0.5:9.5, xii = 0.2:9.8 v/v THF:water, at $\lambda^{\text{exc.}} = 340 \text{ nm}$), inset: Photographs of 3 in (i) THF, (ii) 1:9 v/v THF:water, Under UV illumination at $\lambda = 365 \text{ nm}$. Right- Fluorescence quenching (%) at 420 nm in response to addition of solutions (9 equiv. in 1:9 v/v THF:water) of various nitroaromatics to a solution of 3 ($5 \times 10^{-6} \text{ M}$, in 1:9 v/v THF:water, at $\lambda_{\text{exc.}} = 340 \text{ nm}$) (Reproduced with permission from ref. 1.80 Copyright 2019 Elsevier).

1.4 Objective of the thesis

Though there are number of reported sensory ensemble based on small molecule, literature reports only few examples of AIE active small molecule containing neutral urea subunit or Schiff base linkage for multiple targets. Also very few of them have real application due to their working media (most of them works in organic or in mixture solvent), low selectivity, made of expensive materials or obtained after multistep reaction. So, there is still need of understanding and developing efficient AIE-active sensors based on small molecule aggregation which will works via aggregation-disaggregation approach and have good analytical prospect. Thus based on the literature review and progresses made in the field of sensing via self-assembly process, my thesis objective is:

- To design, synthesis and characterization of small biocompatible molecules via simple steps.

- To study the aggregation behavior of small biocompatible molecules in aqueous/mixed aqueous medium.
- To examine the effect of biologically and environmentally important analytes and biomolecules on the aggregation behavior of the small biocompatible molecules and vice-versa.
- To realize their sensing potential and application prospect as a sensory ensemble based on aggregation-disaggregation mechanism.

References

- 1.1 B. Alberts, D. Bray, J. Lewis, M. Raff, K. Roberts and J.D. Watson, *Molecular Biology of the Cell* (Garland, New York) 1994.
- 1.2 A.C. Mendes, E.T. Baran, R.L. Reis and H.S. Azevedo, *WIREs Nanomed. Nanobiotechnol.*, 2013, **6**, 582-612.
- 1.3 E.H.C. Bromley, K. Channon, E. Moutevelis and D.N. Woolfson, *ACS Chem. Biol.*, 2008, **3**, 38-50.
- 1.4 G.M. Whitesides and B. Grzybowski, *Science*, 2002, **295**, 2418-2421.
- 1.5 A.C. Steven, W. Baumeister, L.N. Johnson and R.N. Perham, *Molecular Biology of Assemblies and Machines*, Garland Science, 2016.
- 1.6 J.M. Lehn, *Angew. Chem., Int. Ed. Engl.*, 1988, **27**, 89-112.
- 1.7 G. Whitesides, J.P Mathias and C.T. Seto, *Science*, 1991, **254**, 1312-1319.
- 1.8 C.T Seto and G.M. Whitesides, *J. Am. Chem. Soc.*, 1993, **115**, 905-916.
- 1.9 J.P. Mathias, E.E Simanek, C.T. Seto and G. Whitesides, *Angew. Chem., Int. Ed.*, 1993, **32**, 1766-1769.
- 1.10 S.I. Stupp, S. Son, H.C. Lin and L.S. Li, *Science* 1993, **259**, 59-63.
- 1.11 S.I Stupp, V. LeBonheur, K. Walker, L.S Li, K.E.Huggins, M. Keser and A. Amstutz, *Science*, 1997, **276**, 384-389.
- 1.12 J.W. Steed and J.L. Atwood, *Supramolecular chemistry*, John Wiley and Sons Ltd., 1997, 1-6.
- 1.13 J.W. Steed, D.R. Turner and K.J. Wallace, *Core concepts in supramolecular chemistry and nanochemistry*, John Wiley & Sons, Chichester, 2007, 1-4, 52-53.
- 1.14 G.M. Whitesides and M. Boncheva, *Proc. Nat. Acad. Sci. USA*, 2002, **99**, 4769-4774.
- 1.15 K.J.M Bishop, C.J. Campbell, G. Mahmud, B.A. Grzybowski, *Biomimetic Design of Dynamic Self-Assembling Systems*; Editor(s): N. Krasnogor, S. Gustafson, D.A. Pelta, Jose L. Verdegay, *Studies in Multidisciplinarity, Elsevier*, 2008, **5**, 21-48.
- 1.16 S.I. Stupp and L.C. Palmer, *Chem. Mater.*, 2014, **26**, 507-518.
- 1.17 G. Boobalan, P. M. Imran, S. G. Ramkumar and S. Nagarajan, *J. Lumin.*, 2014, **146**, 387-393.
- 1.18 Y.J. Li, T.F. Liu, H.B. Liu, M.Z. Tian and Y.L. Li, *Acc. Chem. Res.*, 2014, **47**, 1186-1198.
- 1.19 C.H. Cai, J.P. Lin, Y.Q. Lu, Q. Zhang and L.Q. Wang, *Chem. Soc. Rev.*, 2016, **45**, 5985-6012.
- 1.20 B.K. An, J. Gierschner and S.Y. Park, *Acc. Chem. Res.*, 2012, **45**, 544
- 1.21 M.A. Kobaisi, S.V. Bhosale, K. Latham, A.M. Raynor and S.V. Bhosale, *Chem. Rev.*, 2016, **116**, 11685.

- 1.22 W. Jiang, Y. Zhou, H. Geng, S. Jiang, S. Yan, W. Hu, Z. Wang, Z. Shuai and J. Pei, *J. Am. Chem. Soc.*, 2010, **133**, 1.
- 1.23 R. Charvet, Y. Yamamoto, T. Sasaki, J. Kim, K. Kato, M. Takata, A. Saeki, S. Seki and T. Aida, *J. Am. Chem. Soc.*, 2012, **134**, 2524.
- 1.24 Y. Yamamoto, T. Fukushima, Y. Suna, N. Ishii, A. Saeki, S. Seki, S. Tagawa, M. Taniguchi, T. Kawai and T. Aida, *Science*, 2006, **314**, 1761.
- 1.25 K. P. Nandre, S.V. Bhosale, K.R. Krishna, A. Gupta and S. V. Bhosale, *Chem. Commun.*, 2013, **49**, 5444.
- 1.26 S. S. Babu, H. Mohwald and T. Nakanishi, *Chem. Soc. Rev.* 2010, **39**, 4021.
- 1.27 L. Li, R. Sun and R. Zheng, *Mater. Des.*, 2021, **197**, 109209.
- 1.28 L.F. Peng, Y. N. Chen, Y.Q. Dong, C.C. He and H.L. Wang, *J. Mater. Chem. C*, 2017, **5**, 557-565.
- 1.29 H. Huang, D. Xu, M. Liu, R. Jiang, L. Mao, Q. Huang, Q. Wan, Y. Wen, X. Zhang and Y. Wei, *Mater. Sci. Eng., C*, 2017, **78**, 862-867.
- 1.30 L.L. Zhang, K.C. Liang, L.C. Dong, P.P. Yang, Y.Y. Li, X. Feng, J.G. Zhi, J.B. Shi, B. Tong and Y.P. Dong, *New J. Chem.*, 2017, **41**, 8877-8884.
- 1.31 J.Q. Han, Y.P. Li, J. Yuan, Z.F. Li, R.X. Zhao, T.Y. Han and T.D. Han, *Sens. Actuators B Chem.*, 2018, **258**, 373-380.
- 1.32 A.R. Hirst, B. Escuder, J.F. Miravet and D.K. Smith, *Angew. Chem., Int. Ed.*, 2008, **47**, 8002-8018.
- 1.33 C. Ren, J. Zhang, M. Chen and Z. Yang, *Chem. Soc. Rev.*, 2014, **43**, 7257-7266.
- 1.34 R. Liu, P. Vairaprakash and J.S. Lindsey, *New J. Chem.*, 2019, **43**, 9711-9724.
- 1.35 Y. Xing, D. Li, B. Dong, X. Wang, C. Wu, L. Ding, S. Zhou, J. Fan and B. Song, *New J. Chem.*, 2019, **43**, 8059-8066.
- 1.36 X. Yan, P. Zhua and J. Li, *Chem. Soc. Rev.*, 2010, **39**, 1877-1890.
- 1.37 Q. Zhang, Y.X. Deng, H.X. Luo, C.Y. Shi, G.M. Geise, B.L. Feringa, H. Tian and D.H. Qu, *J. Am. Chem. Soc.*, 2019, **141**, 12804-12814.
- 1.38 C. Ren, J. Zhang, M. Chen and Z. Yang, *Chem. Soc. Rev.*, 2014, **43**, 7257.
- 1.39 C.Y. Shi, Q. Zhang, H. Tian and D.H. Qu, *SmartMat.* 2020, **1**, e1012.
- 1.40 G.G. Stokes, *Philos.Trans.R.Soc.London*, 1852, **142**, 463-562.
- 1.41 J. Luo, Z.Xie, J.W.Y. Lam, L. Cheng, H. Chen, C. Qiu, H.S. Kwok, X. Zhan, Y. Liu, D. Zhu and B. Z. Tang, *Chem. Commun.*, 2001, 1740-1741.
- 1.42 J. Chen, C.C. W. Law, J.W.Y. Lam, Y. Dong, S.M.F. Lo, I.D. Williams, D. Zhu and B.Z. Tang, *Chem. Mater.*, 2003, **15**, 1535-1546.
- 1.43 N.L.C. Leung, N. Xie, W. Yuan, Y. Liu, Q. Wu, Q. Peng, Q. Miao, J.W.Y. Lam and B.Z. Tang, *Chem. Eur. J.*, 2014, **20**, 15349-15353;
- 1.44 Z. Zhao, X. Zheng, L. Du, Y. Xiong, W. He, X. Gao, C. Li, Y. Liu, B. Xu, J. Zhang, F. Song, Y. Yu, X. Zhao, Y. Cai, X. He, R.T.K. Kwok, J.W.Y. Lam, X. Huang, D. Lee Phillips, H. Wang and B.Z. Tang, *Nat. Commun.* 2019, **10**, 2952.
- 1.45 S. Yin, Q. Peng, Z. Shuai, W. Fang, Y.H. Wang and Y. Luo, *Phys. Rev. B*, 2006, **73**, 205409.
- 1.46 Q. Li and L. Blancafort, *Chem. Commun.*, 2013, **49**, 5966-5968.
- 1.47 Y.J. Gao, X. P. Chang, X.Y. Liu, Q.S. Li, G. Cui and W. Thiel, *J. Phys. Chem. A*, 2017, **121**, 2572-2579.
- 1.48 Y. Tu, J. Liu, H. Zhang, Q. Peng, J.W.Y. Lam and B. Z. Tang, *Angew. Chem. Int. Ed.*, 2019, **58**, 14911-14914.

- 1.49 Y. Cheng, J. Dai, C. Sun, R. Liu, T. Zhai, X. Lou and F. Xia, *Angew. Chem. Int. Ed.*, 2018, **57**, 3123-3127.
- 1.50 Z. He, P. Liu, S. Zhang, J. Yan, M. Wang, Z. Cai, J. Wang and Y. Dong, *Angew. Chem.* 2019, **131**, 3874-3877.
- 1.51 J. Mei, N.L.C. Leung, R.T.K. Kwok, J.W.Y. Lam and B.Z. Tang, *Chem. Rev.*, 2015, **115**, 11718-11940.
- 1.52 C. Zhu, R.T.K. Kwok, J.W.Y. Lam and B. Z. Tang, *ACS Appl. Bio Mater.*, 2018, **1**, 1768-1786.
- 1.53 Y. Chen, J.W.Y. Lam, R.T.K. Kwok, B. Liu and B. Z. Tang, *Mater. Horiz.*, 2019, **6**, 428-433.
- 1.54 X. He, L.H. Xiong, Z. Zhao, Z. Wang, L. Luo, J.W.Y. Lam, R.T.K. Kwok, B.Z. Tang, *Theranostics*, 2019, **9**, 3223-3248.
- 1.55 Z. Zhao, H. Zhang, Jacky W. Y. Lam and Ben Zhong Tang, *Angew. Chem. Int. Ed.*, 2020, **59**, 9888-9907.
- 1.56 T. Wu, J. Huang and Y. Yan, *Chem. Asian J.*, 2019, **14**, 730-750.
- 1.57 Z. Zhao, S. Chen, X. Shen, F. Mahtab, Y. Yu, P. Lu, Jacky W.Y. Lam, H.S. Kwok and B.Z. Tang, *Chem. Commun.*, 2010, **46**, 686-688.
- 1.58 T. Ninga, L. Liua, D. Jiaa, X. Xie and D. Wu, *J. Photochem. Photobiol. A*, 2014, **291**, 48-53.
- 1.59 A.K. Srivastava, A. Singh and L. Mishra, *J. Phys. Chem. A*, 2016, **120**, 4490-4504.
- 1.60 M. Salimimarand, D.D. La, M. Al Kobaisi and S.V. Bhosale, *Sci. Rep.*, 2017, **7**, 42898.
- 1.61 R. Kumara, S. Das, S. Mukherjee, R.S. Bhosale, C.R. Patra and R. Narayan, *Mater. Sci. Eng. C*, 2017, **81**, 580-587.
- 1.62 L. Zhang, K. Liang, L. Dong, P. Yang, Y. Li, X. Feng, J. Zhi, J. Shi, B. Tong and Y. Dong, *New J. Chem.*, 2017, **41**, 8877-8884.
- 1.63 Y. Wang, J. Weng, X. Wen, Y. Hu and D. Ye, *Biomater. Sci.*, 2021, **9**, 406-421.
- 1.64 H. Wang, Z. Feng and B. Xu, *Chem Soc Rev.*, 2017, **46**, 2421-2436.
- 1.65 I. Kaur, V. Sharma, S. M. Mobin, P. Kaur and K. Singh, *Sens. Actuators: B Chem.*, 2019, **281**, 613-622.
- 1.66 J. Han, Y. Li, J. Yuan, Z. Li, R. Zhao, T. Han and T. Han, *Sens. Actuators B Chem.*, 2018, **258**, 373-380.
- 1.67 V. Bhalla, H. Singh, M. Kumar and S. K. Prasad, *Langmuir*, 2011, **27**, 15275-15281.
- 1.68 T. Han, W. Wei, J. Yuan, Y. Duan, Y. Li, L. Hu and Y. Dong, *Talanta*, 2016, **150**, 104-112.
- 1.69 X. Wen and Z. Fan, *Sens. Actuators B Chem.*, 2017, **247**, 655-663.
- 1.70 Qi. Wang, X. Wen and Z. Fan, *J. Photochem. Photobiol. A*, 2018, **358**, 92-99.
- 1.71 Q. Wang, Z. Li, D.D. Tao, Q. Zhang, P. Zhang, D.P. Guo and Y.B. Jiang, *Chem. Commun.*, 2016, **52**, 12929.
- 1.72 D. Gohl, X. Zhang and F. Wurthner, *Angew. Chem., Int. Ed.*, 2012, **51**, 6328-6348.
- 1.73 S. Rochat and T. M. Swager, *ACS Appl. Mater. Interfaces*, 2013, **5**, 4488-4502.
- 1.74 Z. Chen, Q. Wang, X. Wu, Z. Li and Y.B. Jiang, *Chem. Soc. Rev.*, 2015, **44**, 4249-4263.
- 1.75 Y.B. Ruan, A.F. Li, J.S. Zhao, J.S. Shen and Y.B. Jiang, *Chem. Commun.*, 2010, **46**, 4938-4940.
- 1.76 X. Wu, X.X. Chen, B.N. Song, Y.J. Huang, W.J. Ouyang, Z. Li, T. D. James and Y.B. Jiang, *Chem. Commun.*, 2014, **50**, 13987-13989.
- 1.77 N. Meher, S. Roy Chowdhurya and P.K. Iyer, *J. Mater. Chem. B*, 2016, **4**, 6023-6031.
- 1.78 T. Gao, S. Yang, X. Cao, J. Dong, N. Zhao, P. Ge, W. Zeng and Z. Cheng, *Anal. Chem.*, 2017, **89**, 10085-10093.
- 1.79 J. Hana, Y. Lia, J. Yuana, Z. Lia, R. Zhaoa, T. Hana and T. Han, *Sens. Actuators B Chem.*, 2018, **258**, 373-380.
- 1.80 I. Kaur, V. Sharma, S.M. Mobin, P. Kaur, K. Singh, *Sens. Actuators B Chem.*, 2019, **281**, 613-622.

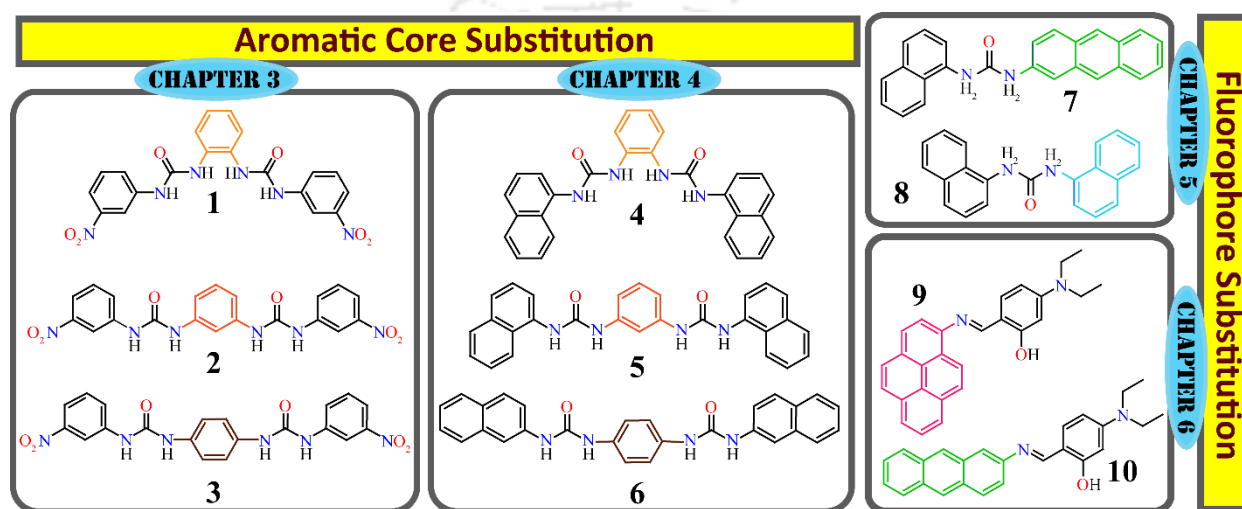
CHAPTER 2

Experimental Details and Characterization



Chapter 2

This chapter provides comprehensive information about the various materials and methodology followed for the synthesis and characterization of the molecule (1-10) involved. Specification of analytical instruments used along with different experimental conditions and calculations followed to study their aggregated form and interaction with other analytes are elaborately described.



Scheme 2.1 Molecules surveyed.

2.1 General Information and Materials

All of the reagents and solvents were commercially available and used henceforth without further purification. Absorption measurements were carried out on a Perkin-Elmer Lambda-750 UV-Vis Spectrophotometer using 10 mm path length quartz cuvettes in the wavelength range of 250–700 nm, while the fluorescence spectra were recorded on a Horiba Fluoromax-4 Spectrofluorometer using 10 mm path length quartz cuvettes with a slit width of 3 nm at 298 K. The particle sizes were measured by dynamic light scattering (DLS) experiments on Malvern Zetasizer Nano ZS instrument equipped with a 4.0 mW He–Ne laser operating at a wavelength of 633 nm. The samples and the background were measured at room temperature (25 °C). The solution was equilibrated for 60 minutes before taking the measurements. The FT-IR spectra of air-dried compounds and their aggregated form were recorded on a PerkinElmer-Spectrum One FT-IR spectrometer with KBr disks in the range 4000–450 cm^{-1} . Mass spectrum were obtained using Waters Q-ToF Premier mass spectrometer. Nuclear magnetic resonance (NMR) spectra were recorded on a Bruker Advance 600 MHz instrument. The chemical shifts were recorded in parts

per million (ppm) on the scale. The following abbreviations are used to describe spin multiplicities in ^1H NMR spectra: s = singlet; d = doublet; t = triplet; q = quartet, m = multiplet.

The morphology of the aggregated species were investigated by using FESEM imaging studies by drop (2 μl) cast method on glass plates covered with Al-foil using Gemini 300 FESEM (Carl Zeiss). For fluorescence microscope imaging, the samples (1 mM) were prepared freshly by casting all preparation drops (5 μl) on a glass slide and were dried completely at room temperature followed by image acquisition using a fluorescence microscope (Eclipse Ti-U, Nikon, USA) with respective filter. Atomic Force Microscopy images were observed from a dried drop-cast (5 μl) solution on cover-slip using Asylum Research Cypher (Oxford Instruments).

2.2 Synthesis and Characterization of the Compounds

2.2.1 Compound 1, 2 and 3:

A set of three already reported bis-urea derivatives^{2.1-2.3} **1**, **2** and **3** have been synthesized by the reaction of *ortho*, *meta* and *para*-phenylenediamine with 2.0 equiv of meta-nitrophenyl isocyanate respectively in the individual dry acetonitrile medium by following the earlier reported protocol and then subsequently characterized by ESI-MS, NMR and FT-IR studies.

2.2.2 Compound 4, 5 and 6:

A set of three already reported bis-urea derivatives^{2.4} **4**, **5** and **6** have been synthesized in good yield by the reaction of *ortho*, *meta* and *para*-phenylenediamine with 2.0 equiv of 1-naphthyl isocyanate respectively in the dry acetonitrile medium by following the earlier reported protocol and then subsequently characterized by ESI-MS, NMR and FT-IR studies (Figure A2.1).

2.2.3 Compound 7 and 8:

To a stirred solution of 2-aminoanthracene in 15 mL dry THF, a 10 mL solution of 1-naphthyl isocyanate in THF was added dropwise at room temperature. The yellow precipitate, obtained after overnight stirring, was filtered and washed several times with THF to afford pure **7**. Yield = 73%. M.P: 291–294 °C. **7** was well characterized by FT-IR, ^1H NMR, ^{13}C NMR and ESI-MS analysis (Figure A2.2-A2.5). ^1H NMR [600 MHz, DMSO- d_6 , δ (ppm)]: 9.36 (1H, s), 8.91 (1H, s), 8.49 (1H, s), 8.42 (1H, s), 8.35 (1H, s), 8.19–8.17 (1H, d), 8.10–8.01 (4H, m), 7.96–7.94 (1H, d), 7.68–7.53 (2H, m), 7.51–7.42 (5H, m). ^{13}C NMR [150 MHz, DMSO- d_6], δ (ppm): 153, 136, 134, 133, 132, 131, 130, 129, 128, 128, 128, 127, 126, 125, 125, 125, 125, 125, 124, 124, 123, 121, 120, 117, 111. ESI-MS (positive mode, m/z) calculated [**7**+ H^+]: 363.1453, obtained: 363.1425. FT-IR (KBr pellets, cm^{-1}): 3283(N–H), 3051(C–H), 1644(C=O), 1568(N–H bend).

Already reported **8**^{2.5-2.6} was similarly synthesized by drop-wise addition of a 10 ml solution of 1-naphthyl isocyanate in THF to a 15 mL solution of 1-naphthylamine in THF at room temperature. The off-white precipitate obtained after overnight stirring was filtered and washed several times with THF to obtain pure **8**. Yield = 88%. **8** was subsequently characterized by ESI-MS analysis only (Figure A2.6). ESI-MS (positive mode, m/z) calculated [**8** + H⁺]: 313.1296, obtained: 313.1301.

2.2.4 Compound 9 and 10:

4-(diethylamino)-2-hydroxybenzaldehyde was added dropwise to dehydrated methanolic solution of 1-aminopyrene (**1'**) and 2-aminoanthracene (**2'**) taken in two separate round-bottomed flasks and stirred overnight at room temperature followed by reflux for 2 h at 50 °C. A dark-yellow (**1**) and bright yellow (**2**) solid product was obtained from the two separate sets of reaction, respectively. The products were then filtered, washed several times with methanol, and dried in a desiccator to afford two pure compounds. Calculated yield: 83% (**1**) and 79% (**2**). **1** and **2** were well characterized by ¹H NMR, ¹³C NMR, ESI-MS analysis and FT-IR (Figures A2.7-2.14). For **9**, ¹H NMR [600 MHz DMSO-d₆, δ (ppm)]: 14.03 (OH, 1H, s), 8.99 (CH, 1H, s), 8.43-8.46 (Ar-H, 1H, d, J=9.2), 8.33-8.35 (Ar-H, 1H, d, J=8.3), 8.24-8.29 (Ar-H, 3H, dd, J=11.0), 8.17-8.19 (Ar-H, 1H, d, J=9.0), 8.11-8.13 (Ar-H, 1H, d, J=8.9), 8.05-8.09 (Ar-H, 2H, m), 7.47-7.49 (Ar-H, 1H, d, J=8.9), 6.40-6.42 (Ar-H, 1H, d, J=2.2), 6.20 (Ar-H, 1H, s), 3.42-3.47 (4H, q, J=6.9), 1.14-1.18 (6H, t, J=7.0). ¹³C NMR [150 MHz, DMSO-d₆], δ (ppm): 163, 163, 152, 143, 134, 131, 131, 129, 128, 127, 127, 126, 125, 125, 125, 124, 124, 122, 116, 109, 104, 97, 44, 13. ESI-MS (positive mode, m/z) calculated [**1** + H⁺]: 393.1922, obtained: 393.2236. FT-IR (KBr pellets, cm⁻¹): 1574(C=N).

For **10**, ¹H NMR [600 MHz, DMSO-d₆, δ (ppm)]: 13.78 (OH, 1H, s), 8.92 (CH, 1H, s), 8.54-8.57 (Ar-H, 2H, d, J=11.2), 8.13-8.15 (Ar-H, 1H, d, J=9.2), 8.05-8.08 (Ar-H, 2H, t, J=7.3), 7.91 (Ar-H, 1H, s), 7.64-7.66 (Ar-H, 1H, d, J=9.1), 7.49-7.55 (Ar-H, 2H, m), 7.38-7.41 (Ar-H, 1H, d, J=8.9), 6.35-6.37 (Ar-H, 1H, d, J=8.9), 6.11 (Ar-H, 1H, s), 3.39-3.44 (4H, q, J=7.0), 1.12-1.16 (6H, t, J=7.0). ¹³C NMR [150 MHz, DMSO-d₆], δ (ppm): 164, 161, 152, 145, 134, 132, 132, 131, 130, 130, 128, 128, 126, 126, 126, 121, 117, 109, 104, 104, 97, 44, 13. ESI-MS (positive mode, m/z) calculated [**2** + H⁺]: 369.1922, obtained: 369.2030. FT-IR (KBr pellets, cm⁻¹): 1578 (C=N).

2.3 UV-Vis and Fluorescence Spectral Studies

Stock solutions of **1**, **2** and **3** (5×10^{-3} mol L⁻¹) was prepared in DMF and then diluted to 10×10^{-6} mol L⁻¹ for various spectral studies for aggregation phenomenon in Millipore water and

acetonitrile. To investigate the effect of external factor on aggregation behavior of all three compounds individually, the concentration of the respective compound was maintained at 50 μM in final solutions of **1**, **2** and **3** for all spectral studies.

Stock solutions of **4**, **5** and **6** ($5 \times 10^{-3} \text{ mol L}^{-1}$) was prepared in DMF and then diluted to $10 \times 10^{-6} \text{ mol L}^{-1}$ for various spectral studies for aggregation phenomenon in Millipore water and acetonitrile. To investigate the interaction with nitro-phenols on aggregation behavior of **4** and **5** individually, the concentration of the respective compound was maintained at 50 μM and nitro-phenols at 100 μM in final solutions for all spectral studies.

Stock solutions of various anions ($1 \times 10^{-3} \text{ mol L}^{-1}$) and HSA/ BSA (10 mg mL^{-1}) were prepared in Millipore water. Stock solutions of **7** and **8** ($1 \times 10^{-3} \text{ mol L}^{-1}$) were prepared in DMF and then diluted to $2 \times 10^{-6} \text{ mol L}^{-1}$ for various spectral studies. For fluorescence selectivity experiments, the test samples were prepared by placing appropriate amounts of the stock solutions of the respective proteins/analytes into 2.0 mL of ligand solution ($2 \times 10^{-6} \text{ mol L}^{-1}$). For fluorescence quantitation experiments, another set of HSA standard solution was prepared with a concentration of 5 mg mL^{-1} by half-diluting the earlier prepared stock solution (10 mg mL^{-1}) in Millipore water. For the fluorescence measurements, **7** was excited at 380 nm and the emission was monitored between 390 and 650 nm.

Stock solutions of **9** and **10** ($5 \times 10^{-3} \text{ mol L}^{-1}$) was prepared in DMSO and then diluted to $10 \times 10^{-6} \text{ mol L}^{-1}$ for various spectral studies for aggregation behavior and sensing phenomenon in Millipore water and acetonitrile. Selectivity experiments were performed by adding 10 eqv. of hydrazine and other comparable amine, metal and anion solutions prepared in Millipore water. For the fluorescence measurements, **9** and **10** was excited at 380 nm and 420 nm respectively.

2.4 Detection Limit Calculations:

The detection limit was calculated on the basis of the fluorescence titration. The fluorescence emission spectrum of respective compound was measured 10 times, and the standard deviation of blank measurement was estimated. To measure the slope, the corresponding fluorescence emission was plotted as a function of the concentration of analyte from the titration experiment. The detection limit was then calculated using the following equation:

$$\text{Detection limit} = 3\sigma/k \text{ ..(1)}$$

where σ is the standard deviation of blank measurement, and k is the slope between the fluorescence emission intensity versus [analyte].

2.5 Circular Dichroism Measurements:

CD spectra of aqueous solutions of **7** (0.02 μM), only HSA (15 $\mu\text{g/mL}$) and HSA in presence of **7** were recorded by using a 2 mL quartz cuvette of 10 mm path length with a J-1500 (Jasco) spectropolarimeter at room temperature. Spectra were collected at 1 nm intervals and 1 nm bandwidth from 190 to 450 nm.

2.6 Transmission Electron Microscopy:

The size and morphology of the **7/8**-aggregates on increasing acetonitrile fraction in aqueous medium and **7** in presence of HSA in aqueous solution were determined by transmission electron microscopy (TEM) using a JEM-2100 (JEOL) microscope. The samples [**7/8**(2 μM) in 50% acetonitrile/water solution), HSA (0.15 mg/mL), HSA(0.15 mg/mL)+**7**(2 μM) in water] were prepared freshly by casting one preparation drop (5 μl) on carbon coated copper grids and the sample was dried completely at room temperature and images were observed under TEM.

2.7 FRET and REES studies:

In case of fluorescence measurement for FRET experiment, the donor HSA was excited at 295 nm and emission spectra were recorded 310-580 nm wavelength range. For REES experiment, the Trp was excited at both 295 and 310 nm to investigate the REES effect. The value of ρ is defined as the difference of the emission maximum obtained for the excitation wavelength at 295 nm and 310 nm.

2.8 Measurement of Fluorescence Lifetime:

Fluorescence lifetimes were measured employing the time-correlated single-photon counting (TCSPC) method using Edinburgh Instrument Life-Spec II spectrometer. The samples (**7** and **7**+HSA) were excited at 390 nm keeping the emission wavelength at 438 nm using a pulsed diode laser. The fluorescence decays were analyzed by the re-convolution method using the FAST software provided by Edinburgh Instruments.

2.9 Competitive Drug Displacement Studies:

It has been well established that serum proteins are composed of three homologous α -helical domains (I–III) and each domain contains two sub domains. The principal ligand binding sites of HSA are located in hydrophobic cavities in sub domains IIA and IIIA, which are referred to as site I and site II according to the terminology. To identify **7** binding site on HSA, site marker competitive experiments were carried out using three site-specific drugs comprising warfarin (domain IIA), ibuprofen (domain IIIA) and salicylic acid (a site marker of subdomains IIA & IB).

2.10 Molecular Docking Studies:

Molecular docking was conducted to analyze the geometrically and energetically stable conformation upon binding of probe **7** to HSA. AutoDockTools-1.5.6 was used to generate a docked conformation of L1 with HSA by employing a Genetic Algorithm (GA) and a Lamarckian Genetic Algorithm. The binding free energies and binding sites of **7** within the active site of HSA were examined by this software. The crystal structure of HSA with four letter codes (1BM0) was retrieved from RCSB PDB (Sugio, S., Kashima, A., Mochizuki, S., Noda, M., Kobayashi, K. Protein Eng. 1999, 12, 439-446), and was subject to energy refinement, hydrogen additions and solvent removal through Swiss PDB Viewer v.4.1.0 to allow all the residues to adopt a correct and stable configuration. To define all binding sites, a grid box was generated with a spacing of 0.375 Å and dimensions of (60x60x60) points (.gpf file). The docking parameters were inserted as the number of GA runs: 25. The output is selected as Lamarckian GA (.dpf file), which was applied in AutoDockTools-1.5.6 to conduct docking simulations. Energy minimization and optimization of the probe **7** was also performed. In the end, analysis of docking result of the probe **7** was done using PyMOL viewer programs and the docking structure with the lowest binding energy calculated by AutoDockTools-1.5.6 was selected as the best binding conformation.

2.11 Crystallography:

The intensity data were collected using a Bruker SMART APEXII CCD diffractometer, equipped with a fine focus 1.75 kW sealed tube Mo-K α radiation ($\lambda = 0.71073 \text{ \AA}$) at 298(2) K, with increasing ω (width of 0.3° per frame) at a scan speed of 3s per frame. The SMART software was used for data acquisition. Data integration and reduction were performed with SAINT and XPREP^{2.7} software. Multi-scan empirical absorption corrections were applied to the data using the program SADABS.^{2.8} Structures were solved by direct methods using SHELXL-2016/6 and were refined by full-matrix least squares on F₂ using SHELXL-2016/6 program package.^{2.9,2.10} In the crystal structure, non-hydrogen atoms were refined aniso-tropically. Structural illustrations have been generated using MERCURY 2.3 for Windows.^{2.11} CCDC no: 2062591, Empirical formula: C₂₇ H₂₄ N₂ O, Mw: 392.48, T= 298(2) K, Triclinic, space group: P-1, a=8.3383(4) Å, b= 15.9039(8) Å, c=16.4937(9) Å, α =102.590(4), β =104.008(4), γ =92.454(4), V=2060.60(19) Å³, Z= 4, Dx(g/cm³)=1.265, F(000)=832, Reflections collected/unique=9344/ 5811, R₁=0.0700, wR₂= 0.203 [I>2 σ (I)], R₁=0.1104, wR₂=0.2520 (all data), GOF(F₂)=0.841.

2.12 AFM Imaging:

Transformations of **9/10**-aggregates due to hydrazine interaction were observed from a drop-cast

solution of **9** and **10** (10 μ M) in a 1:1 acetonitrile-water medium on glass cover slip using Asylum Research Cypher (Oxford Instruments) in non-contact mode.

2.13 Cytotoxic Assay:

The cytotoxic effect of compound **7**, **9** and **10** on cultured HeLa cells was ascertained by a standard MTT assay. MTT (3-(4,5-Dimethylthiazol-2-yl)-2,5-Diphenyltetrazolium Bromide) solution was procured from Sigma-Aldrich, USA. HeLa cells were initially propagated in 25 cm² tissue culture flask in Dulbecco's modified Eagle medium (DMEM) supplemented with 10% (v/v) fetal bovine serum (FBS), penicillin (100 μ g/mL) and streptomycin (100 μ g/mL) at 37 °C in a CO₂ incubator. Prior to MTT assay, cells were seeded onto 96-well tissue culture plates (approximately 10⁴ cells per well) and incubated in separate sets with various concentrations of compounds made in DMEM for a period of 24 h at 37 °C in a CO₂ incubator. The control sample consisting of untreated HeLa cells was also incubated in parallel under the same conditions. Following 24 h incubation, the media was aspirated and fresh DMEM containing MTT solution was added to the cells and incubated for 4 h at 37 °C in a CO₂ incubator. Following incubation, the MTT solution was removed and the insoluble and colored formazan product was solubilized in DMSO. The absorbance of the solution was then measured in a microtiter plate reader (Infinite M200, TECAN, Switzerland) at 570 nm against a reference of 640 nm. MTT assay for every sample was performed in six sets. The absorbance obtained for the untreated control samples represented 100% cell viability. The absorbance obtained for compound-treated cells was compared to the control to ascertain the % cell viability.

2.14 Cell Imaging Studies:

HeLa cells were initially propagated in 25 cm² tissue culture flask in Dulbecco's modified Eagle medium (DMEM) supplemented with 10% (v/v) fetal bovine serum (FBS), penicillin (100 μ g/mL) and streptomycin (100 μ g/mL) at 37 °C in a CO₂ incubator. Prior to cell imaging studies, HeLa cells were seeded into confocal dish (20 mm diameter) and grown in DMEM medium at 37 °C in a CO₂ incubator to achieve nearly 75% confluency. Subsequently the cells were incubated in separate sets with 10 equiv. hydrazine in DMEM at 37 °C for 10 min in a CO₂ incubator. DMEM medium was then aspirated and the cells were gently washed with sterile PBS in order to remove excess hydrazine and to each set, the AIEgens **9** and **10** (2.5 μ M each) were added separately in DMEM and the cells were further incubated at 37 °C for 10 min in a CO₂ incubator. The cells were washed again with sterile PBS to remove excess ligand and their images were captured using a confocal microscope (Zeiss LSM 880, Germany). The excitation wavelength used for the lasers

encompassed 488 nm for green emission, 405 nm for blue emission and 561 nm for red emission. Images for HeLa cells incubated with either **9** or **10** alone was also captured.

2.15 DFT studies:

Density Functional Theory (DFT) Study: DFT optimizations of respective compounds were carried out with the RB3LYP/ 6-31G method basis set using the Gaussian 09 program where and the results are given in the Table A2.1.

References

- 2.1 S. J. Moore, C. J. E. Haynes, J. Gonzalez, J. L. Sutton, S. J. Brooks, M. E. Light, J. Herniman, G. J. Langley, V. Sottocerrato, R. Perez-Tomas, I. Marques, P. J. Costa, V. Felix and P. A. Gale, *Chem. Sci.*, 2013, **4**, 103-117.
- 2.2 U. Manna, R. Chutia and G. Das, *Cryst. Growth Des.*, 2016, **16**, 2893-2903.
- 2.3 U. Manna, R. Chutia and G. Das, *Cryst. Growth Des.*, 2018, **18**, 6801-6815.
- 2.4 B. Nayak, U. Manna, G. Das, *ChemistrySelect*, 2018, **1**, 1-8.
- 2.5 A.M.Z. Slawin, J. Lawson, J.M.D. Storey and W.T.A. Harrison, *Acta Crystallogr., Sect. E: Crystallogr. Commun.*, 2007, **63**, o2925–o2927.
- 2.6 S.A. Kadam, K. Martin, K. Haav, L. Toom, C. Mayeux, A. Pung, P.A. Gale, J.R. Hiscock, S.J. Brooks and I.L. Kirby, *Chem. Eur. J.*, 2015, **21**, 5145-5160.
- 2.7 G.M. Sheldrick, SAINT and XPREP, 5.1 ed., Siemens Industrial Automation Inc., Madison, WI, 1995.
- 2.8 G.M. Sheldrick, SADABS: Software for Empirical Absorption Correction, University of Gottingen, Institute fur Anorganische Chemieder Universitat, Tammanstrasse 4, D-3400 Gottingen, Germany, 1999-2003.
- 2.9 G.M. Sheldrick, SHELXS-97, University of Gottingen, Germany, 1997.
- 2.10 G.M. Sheldrick, SHELXL-97, Program for Crystal Structure Refinement, University of Gottingen, Germany, 1997.
- 2.11 Mercury 1.3 Supplied with Cambridge Structural Database, CCDC, Cambridge, U.K., 2003-2004.

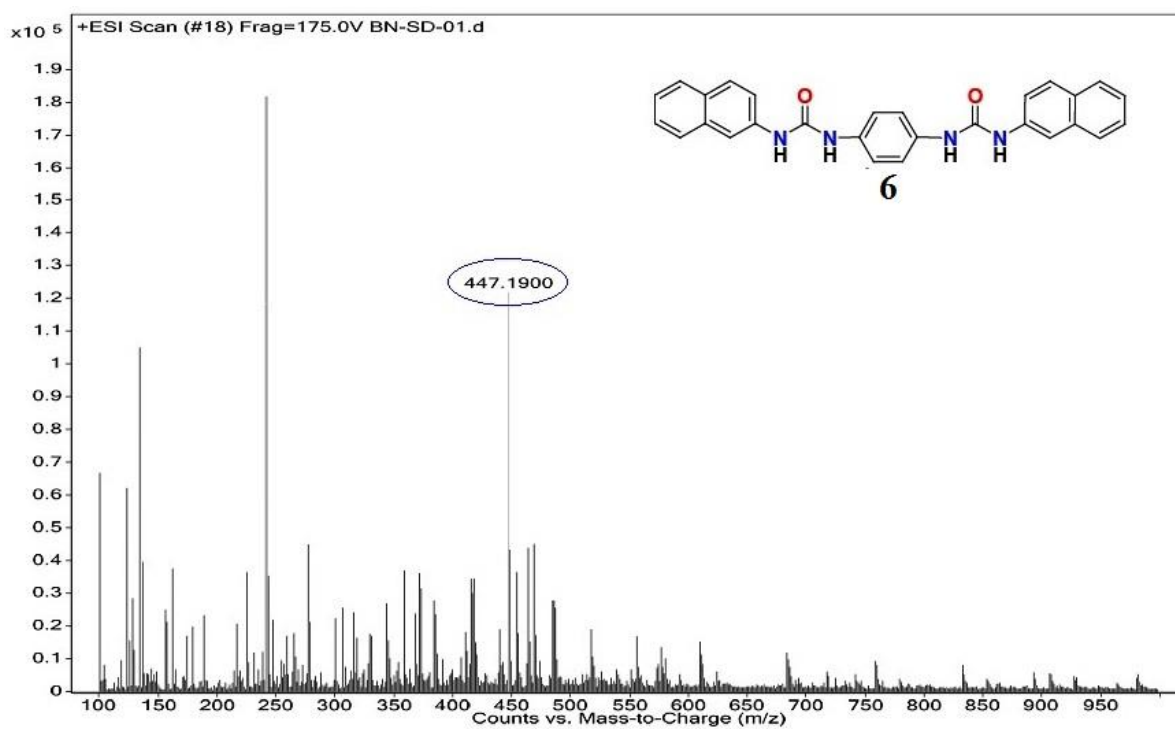
Appendix-Chapter 2

Figure A2.1 Mass spectrum of **6**.

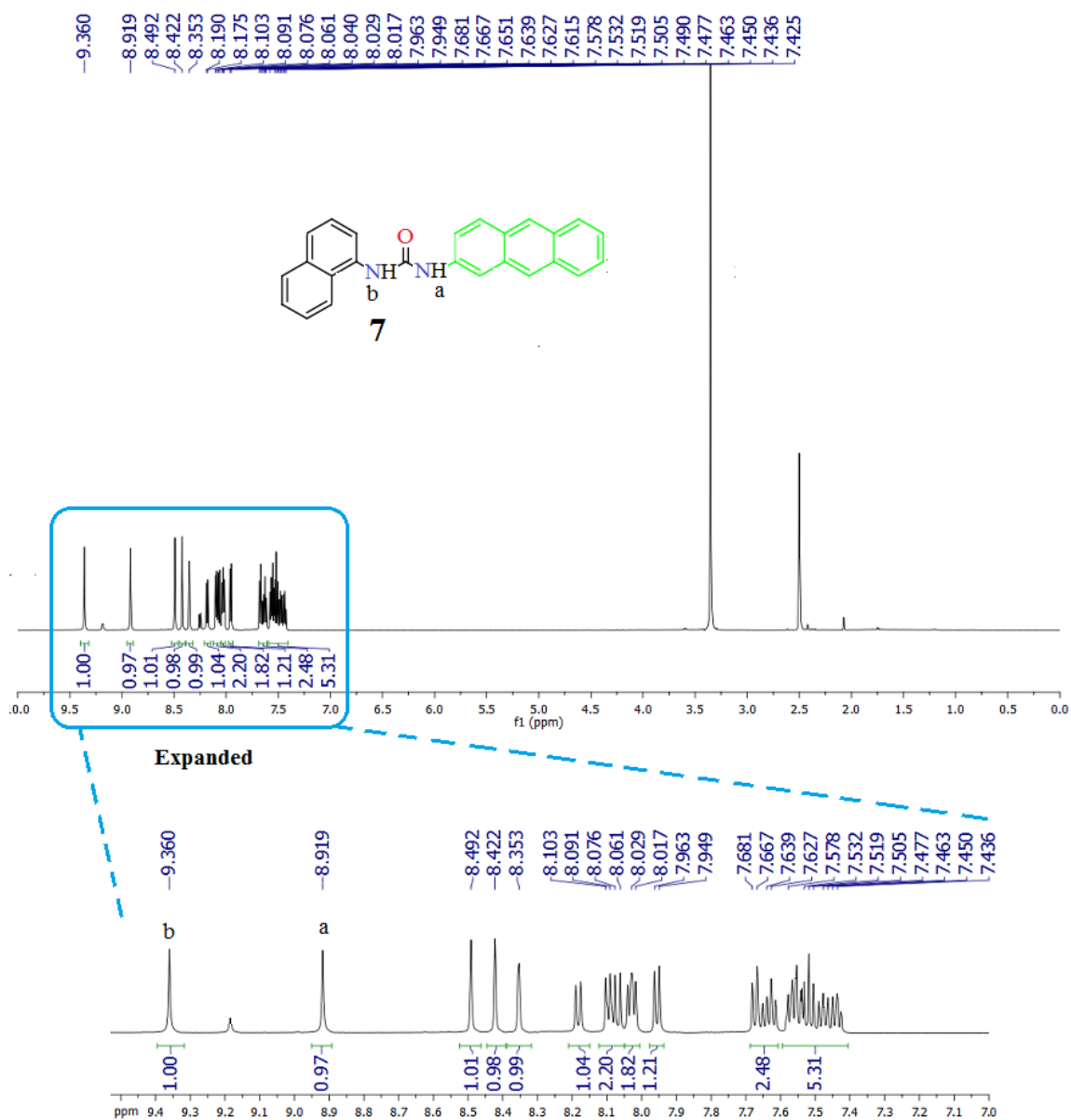


Figure A2.2 $^1\text{H-NMR}$ spectra of **7** in DMSO-d_6 .

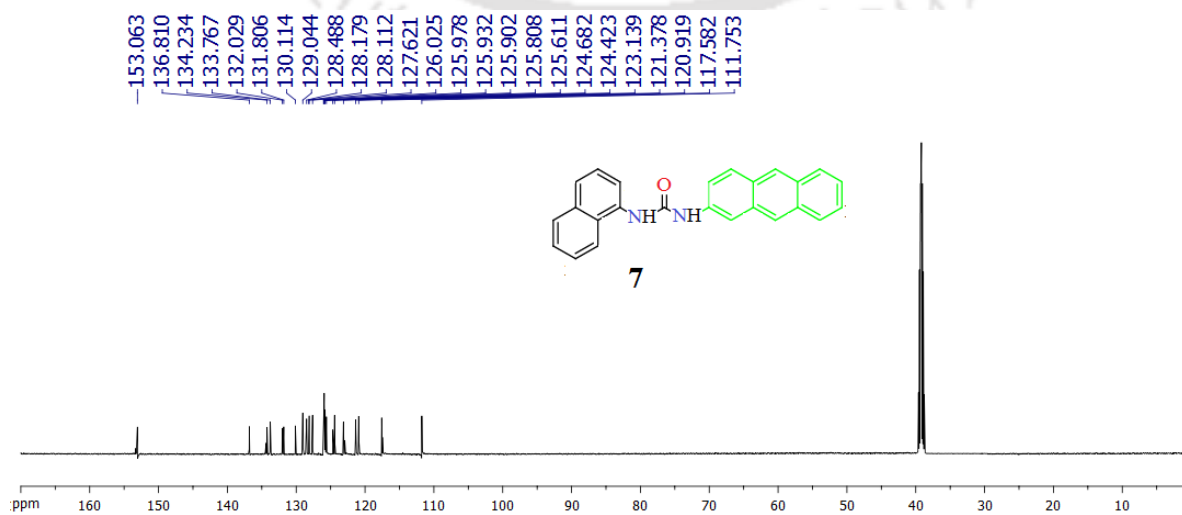


Figure A2.3 $^{13}\text{C-NMR}$ spectra of **7** in DMSO-d_6 .

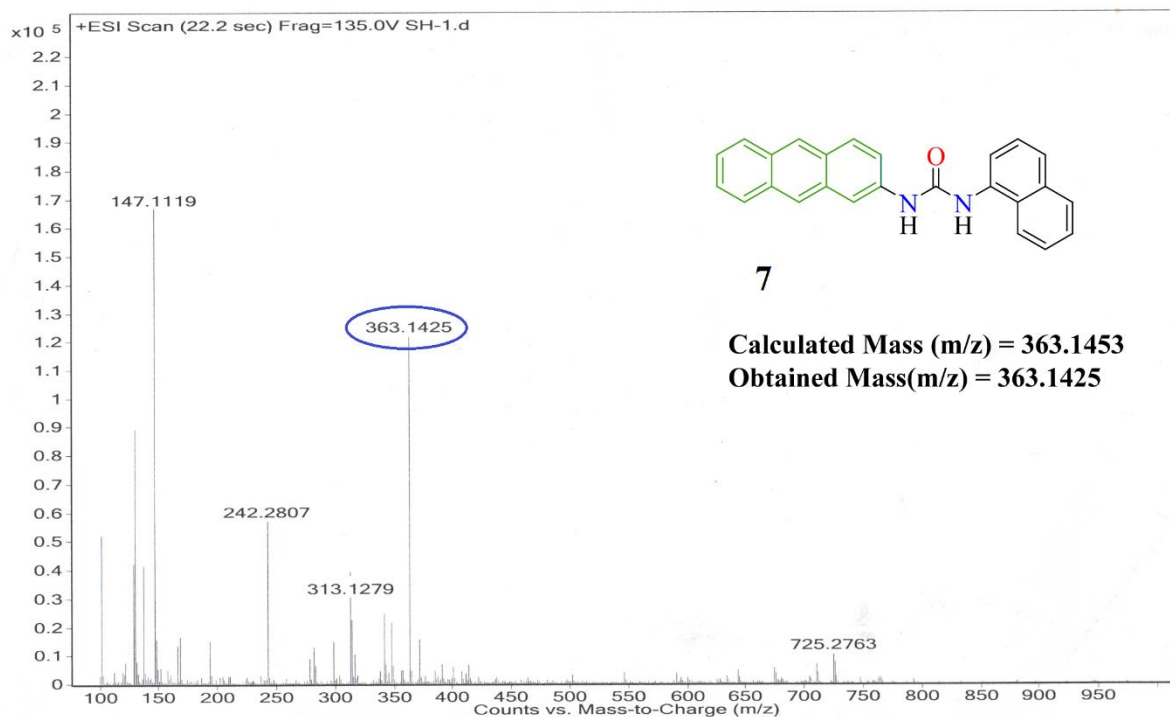


Figure A2.4 Mass spectrum of 7.

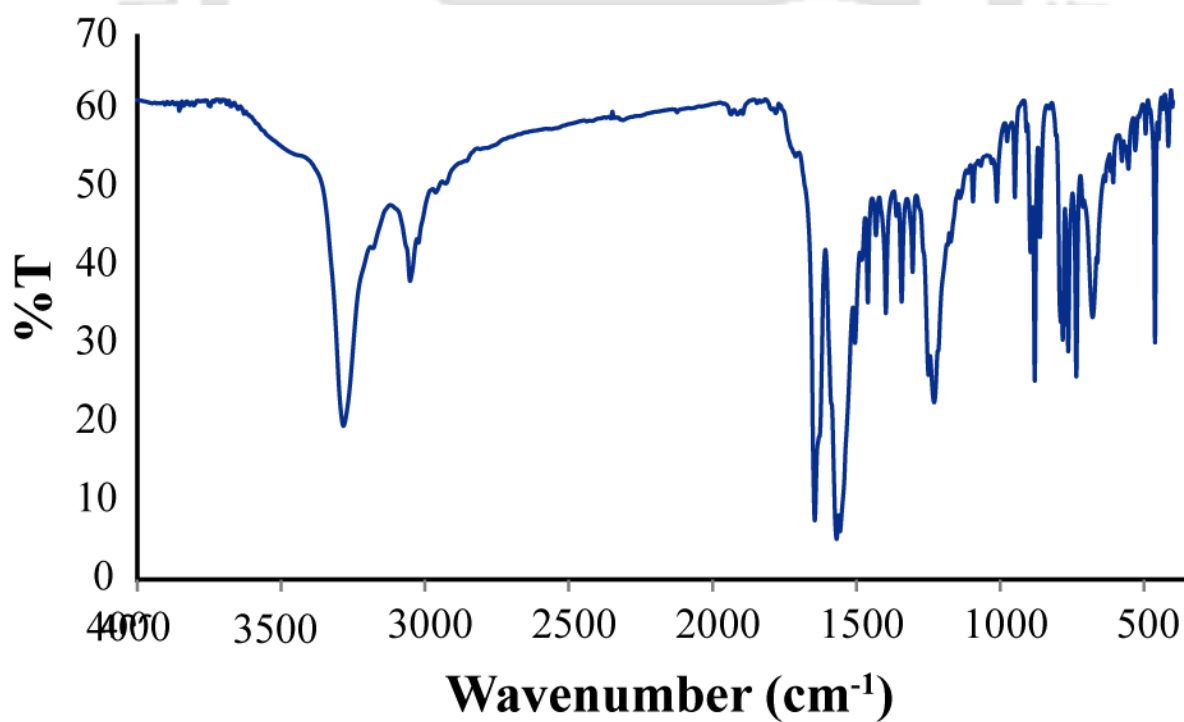


Figure A2.5 FT-IR spectrum of 7 recorded in KBr pellet at 25°C

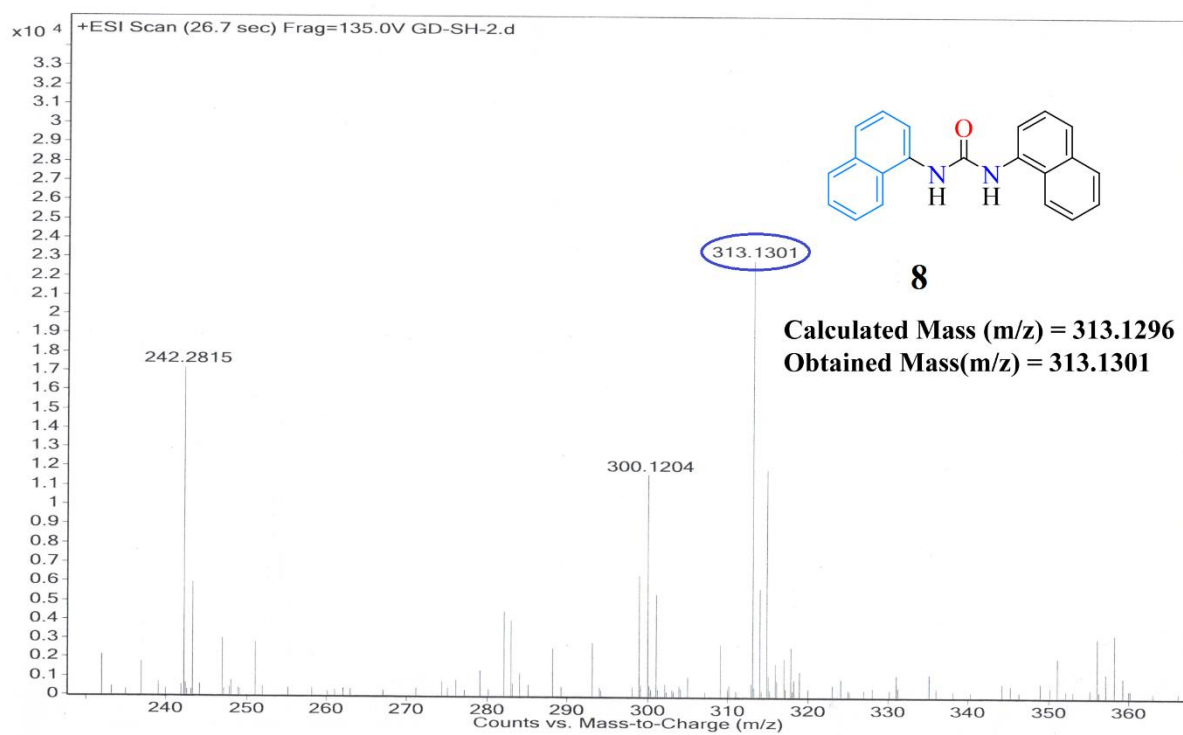


Figure A2.6 Mass spectrum of 8.

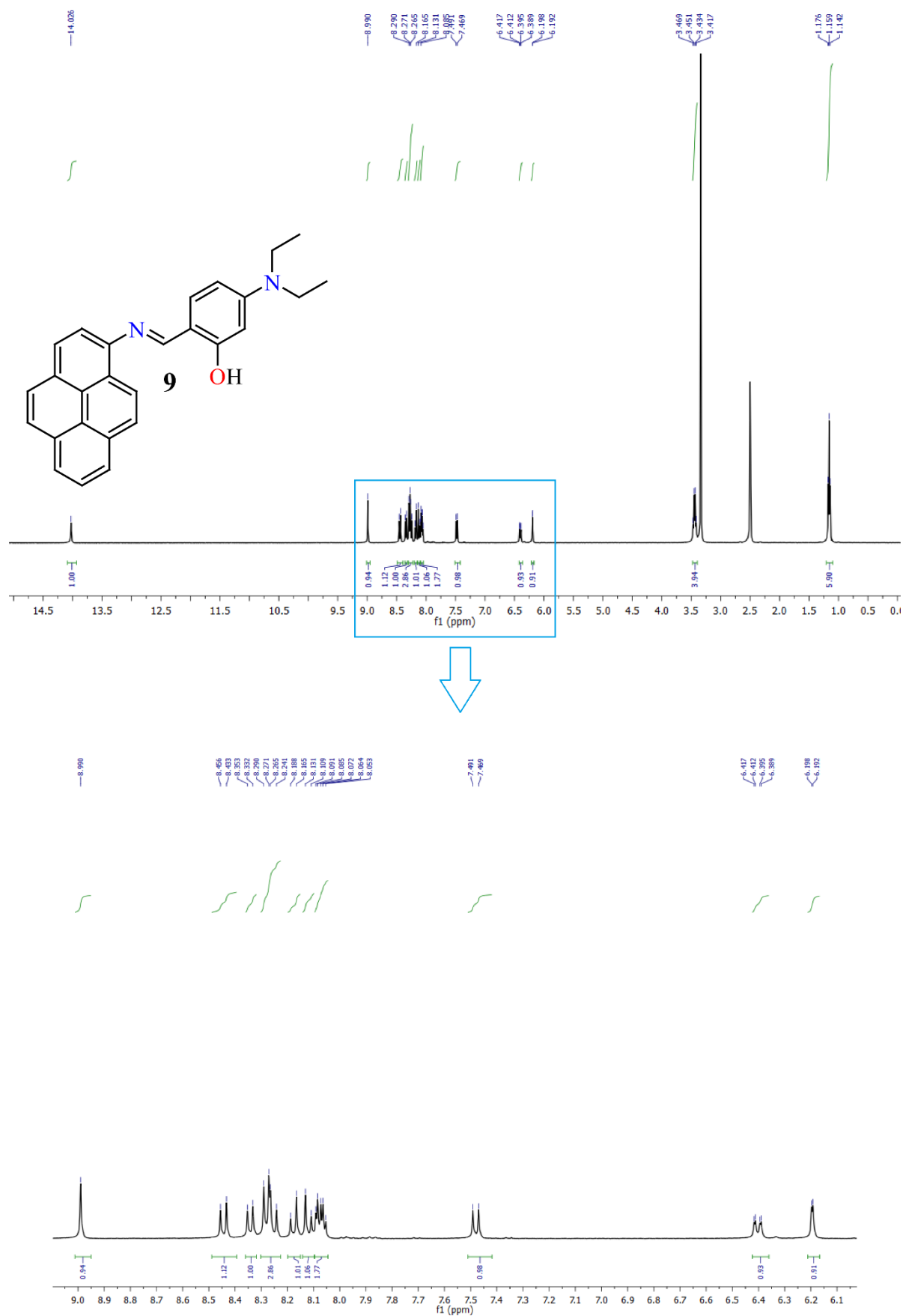


Figure A2.7 $^1\text{H-NMR}$ spectra of **9** in DMSO-d_6 .

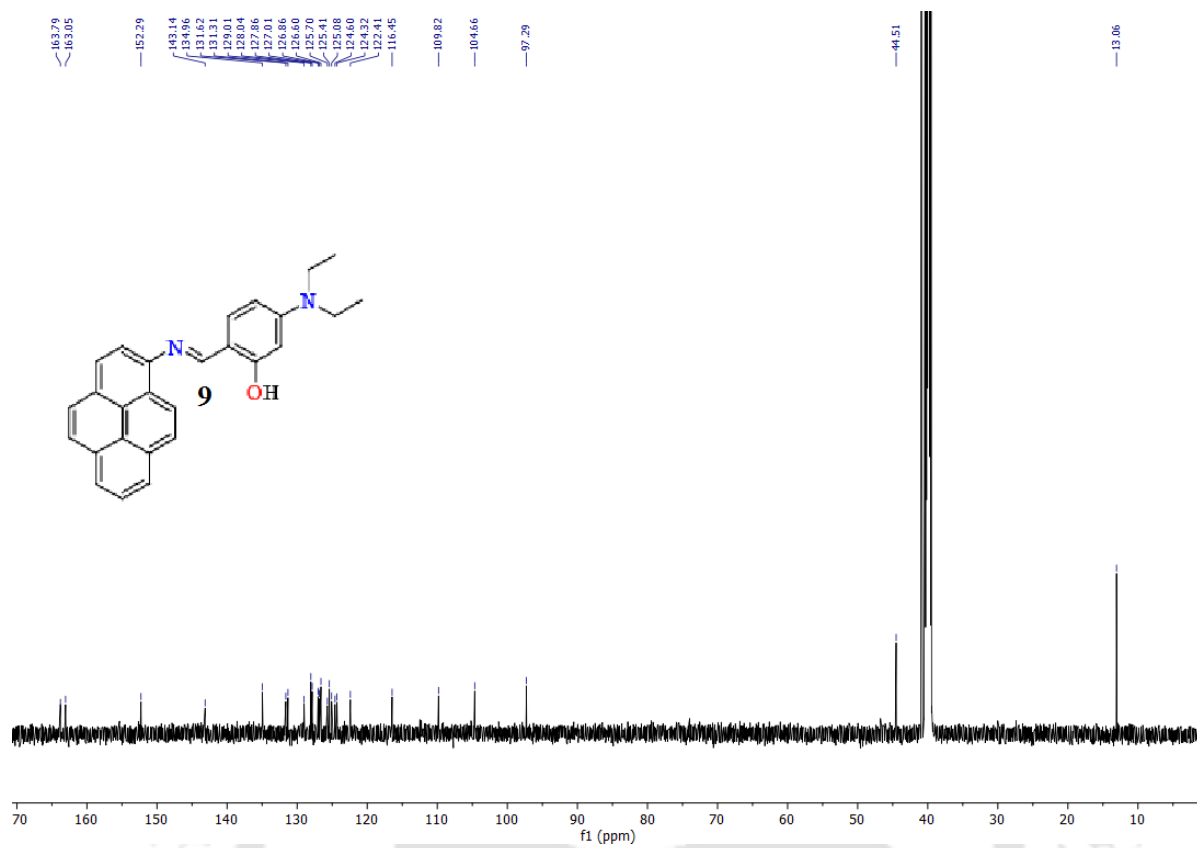


Figure A2.8 ^{13}C -NMR spectra of **9** in DMSO- d_6 .

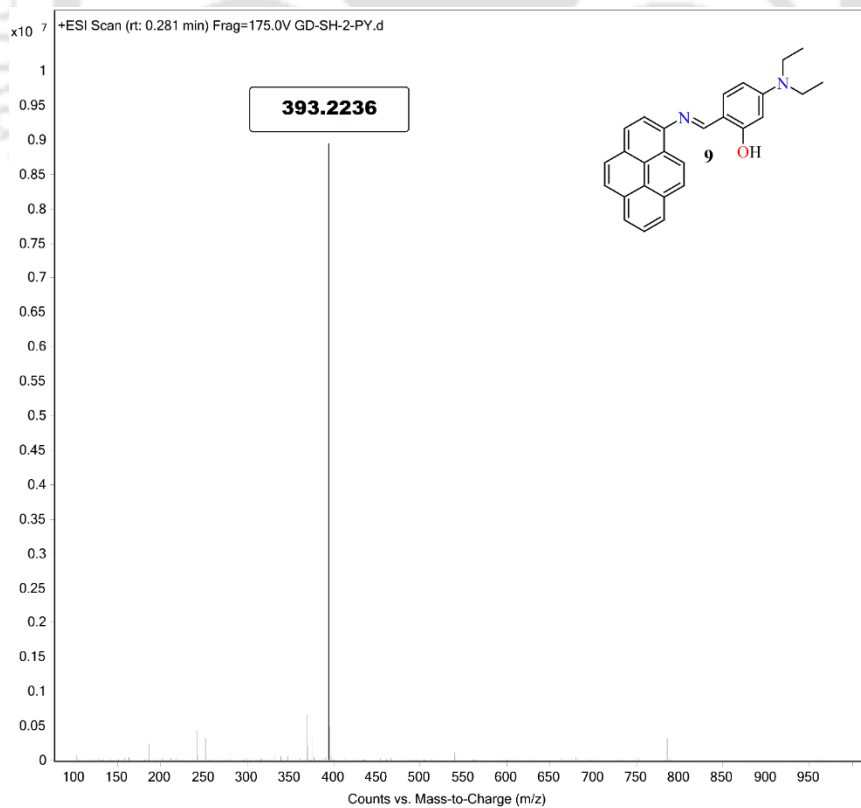


Figure A2.9 Mass spectrum of **9** (Calculated: 393.1922; Obtained: 393.2236).

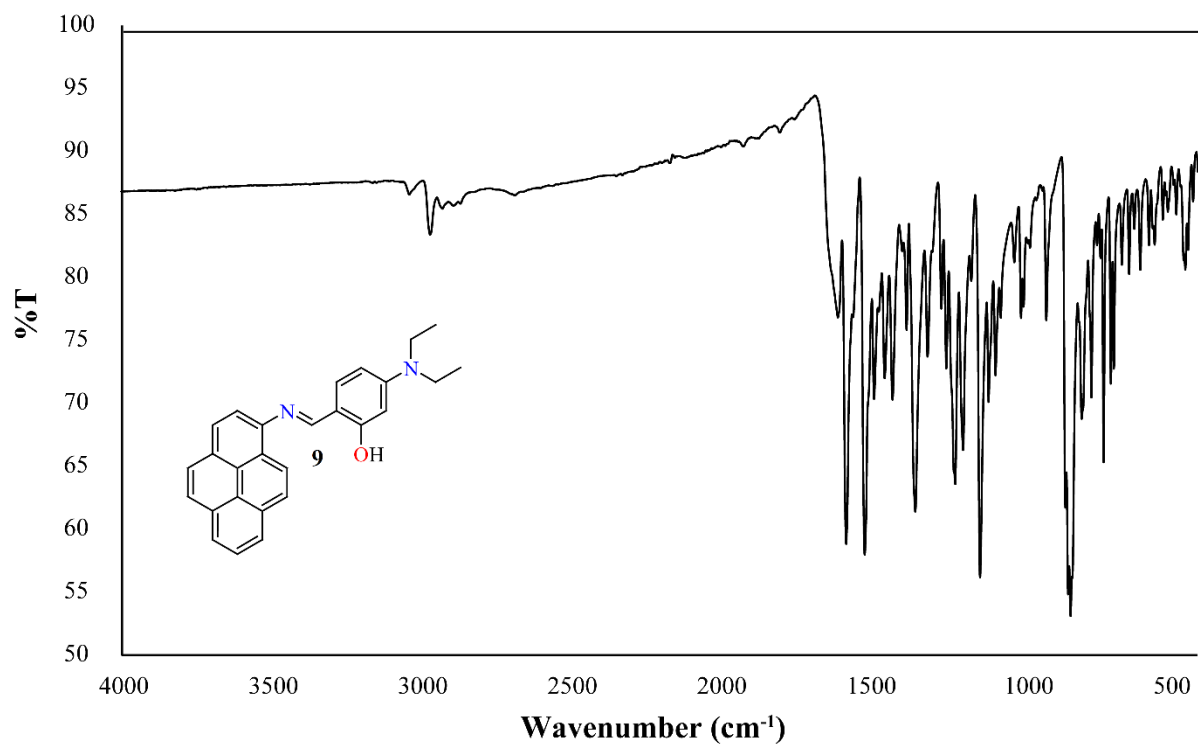
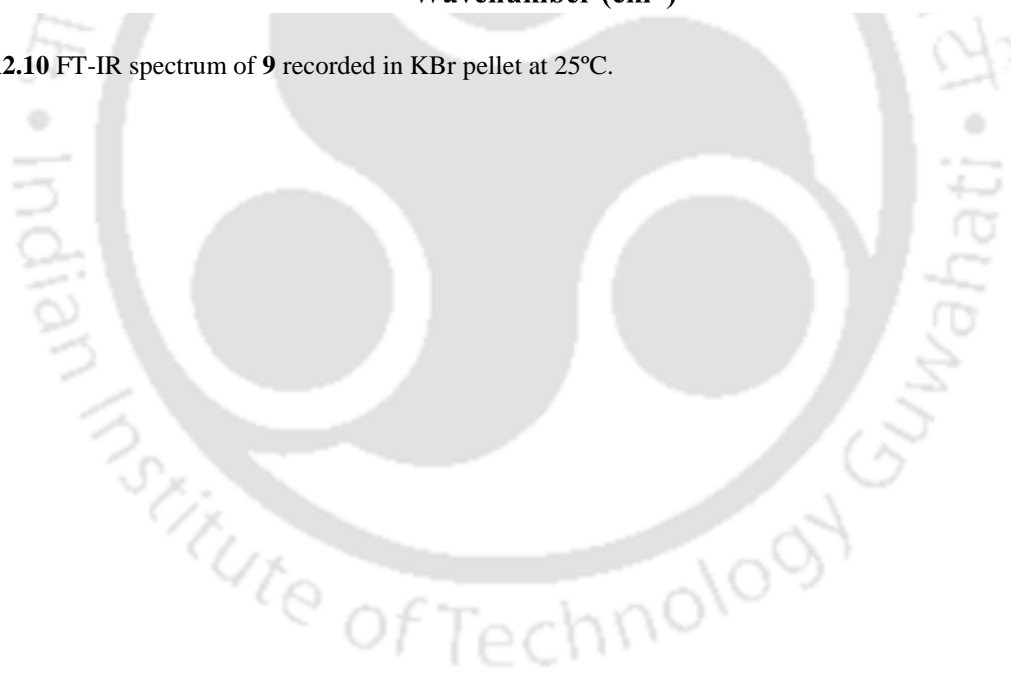


Figure A2.10 FT-IR spectrum of **9** recorded in KBr pellet at 25°C.



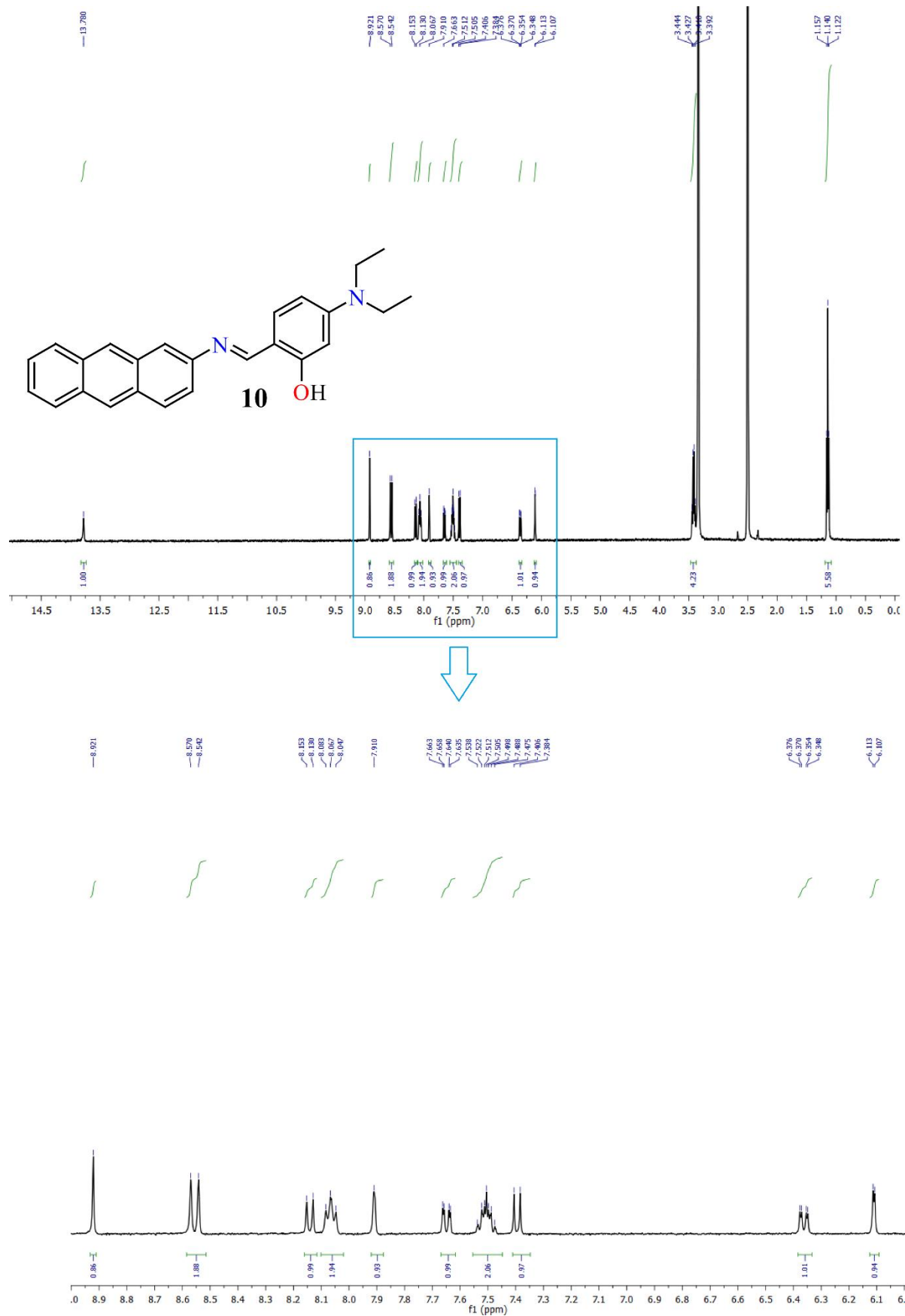


Figure A2.11 $^1\text{H-NMR}$ spectra of **10** in DMSO-d_6 .

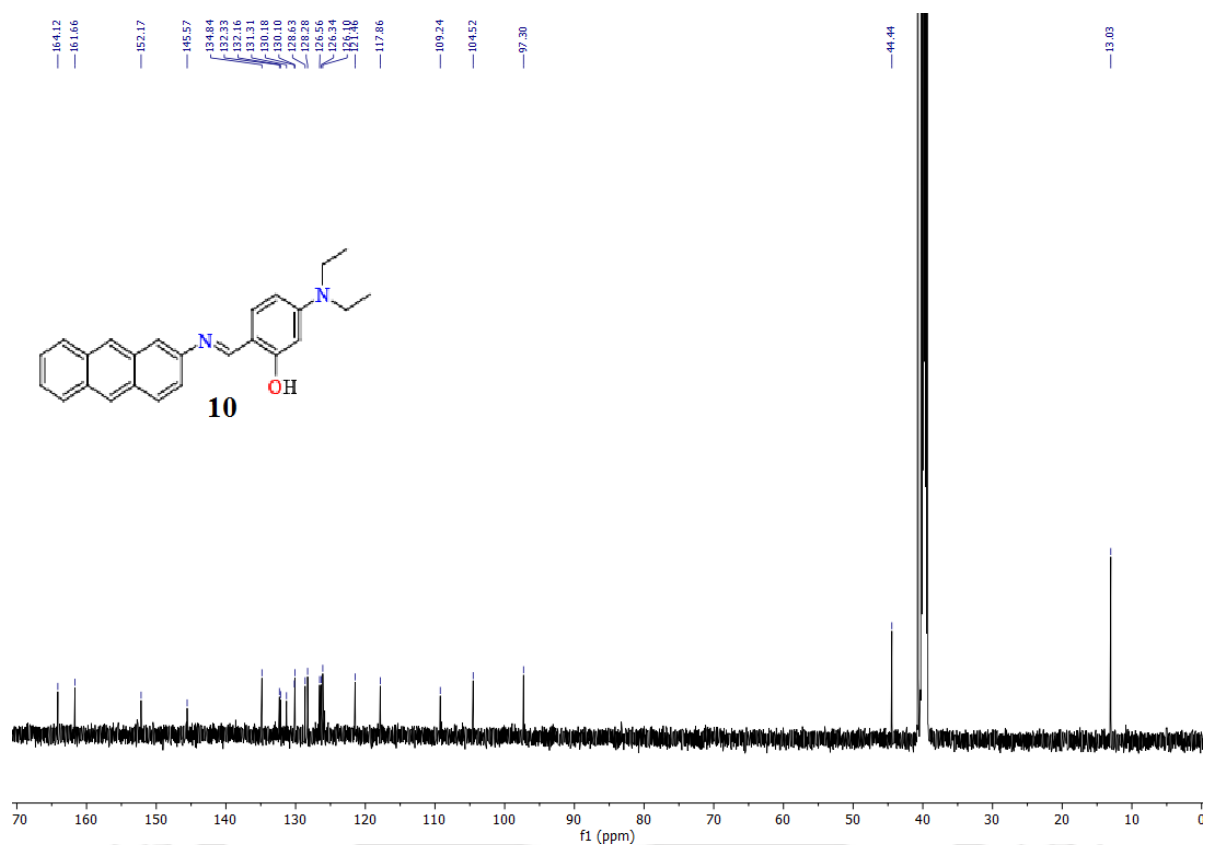


Figure A2.12 $^{13}\text{C-NMR}$ spectra of **10** in DMSO- d_6 .

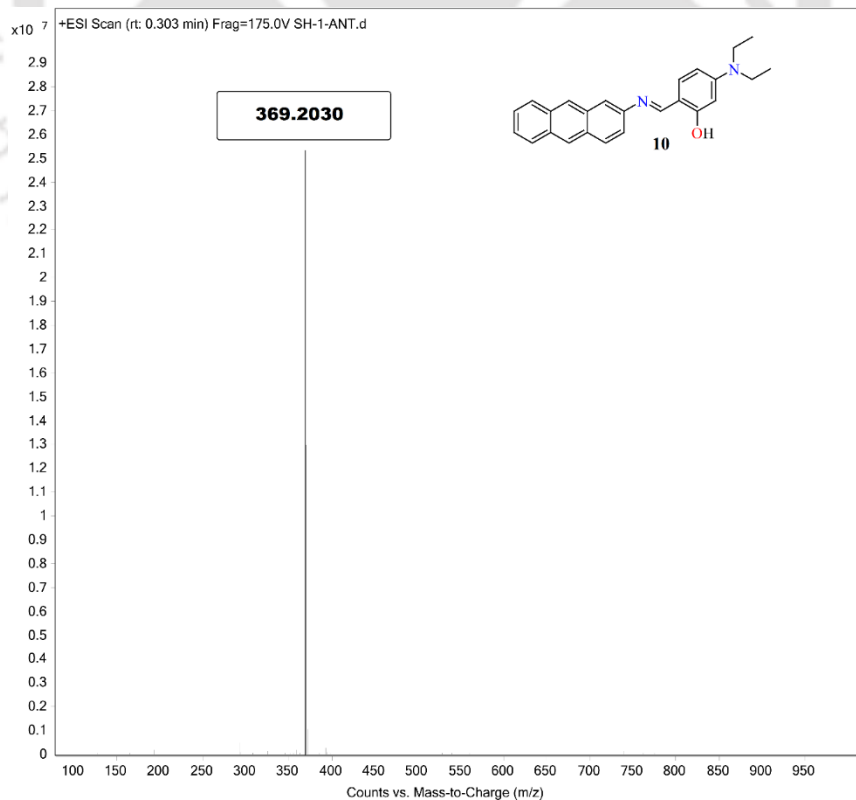


Figure A2.13 Mass spectrum of **10** (Calculated: 369.1922; Obtained: 369.2030).

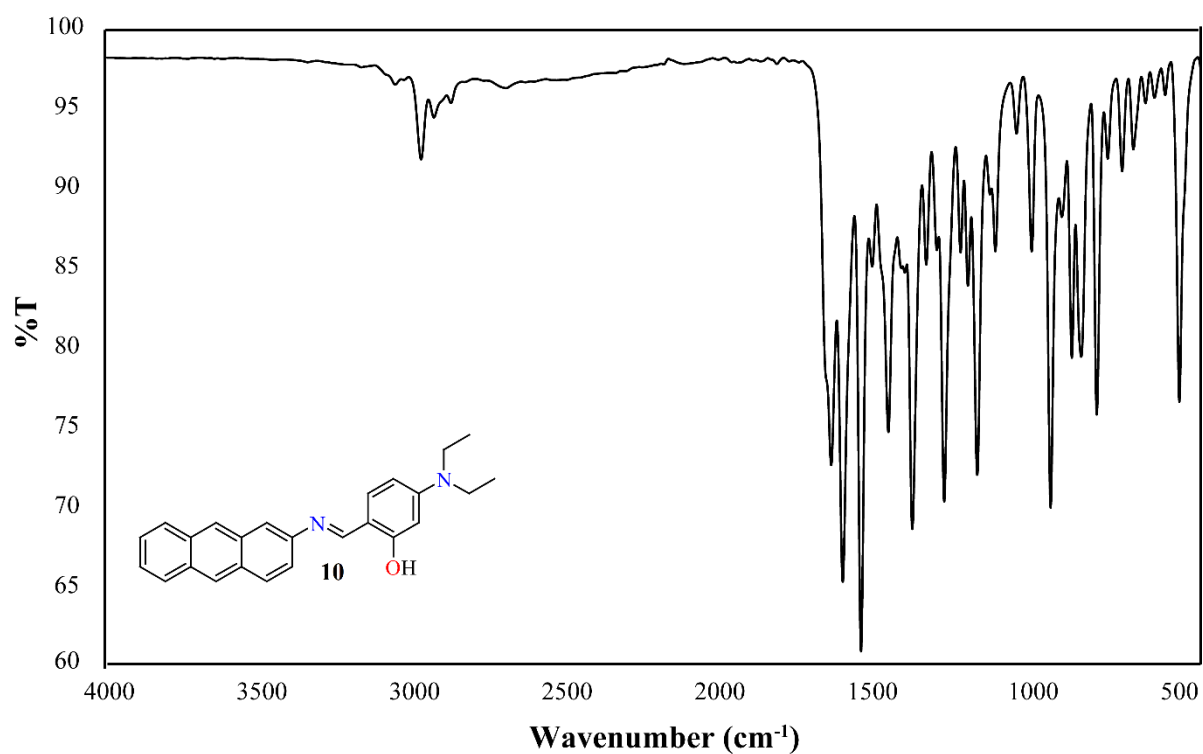


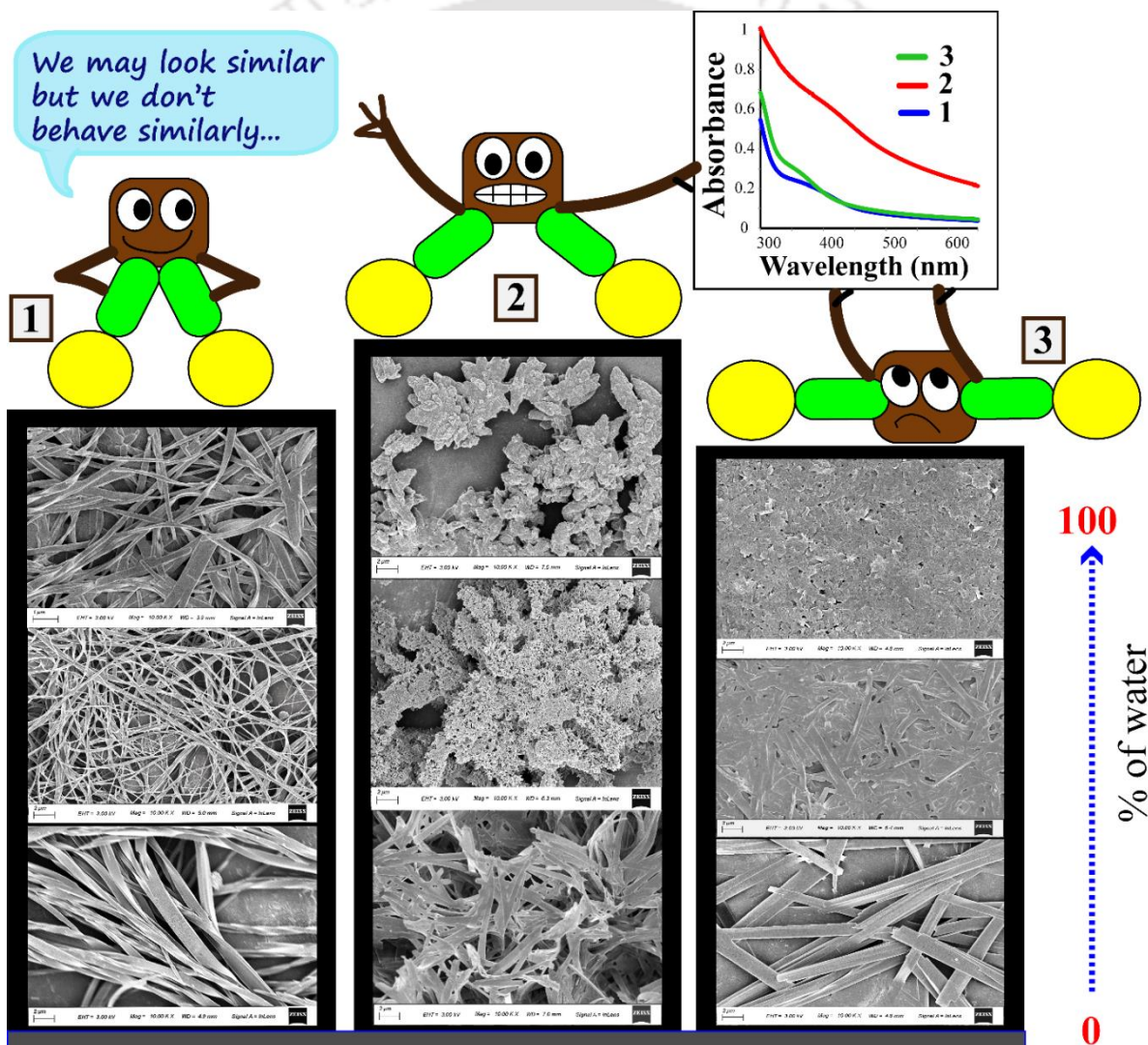
Figure A2.14 FT-IR spectrum of **10** recorded in KBr pellet at 25°C.

Table A2.1: DFT results.

Compound	Total Energy (a.u)	HOMO Energy (eV)	LUMO Energy (eV)	ΔE (eV)
1	-1551.013	-0.2451	-0.1171	0.1280
2	-1551.006	-0.2436	-0.1168	0.1268
3	-1551.006	-0.2402	-0.1190	0.1212
7	-1148.255	-0.30217	-0.22023	0.0819
9	-1228.032	-0.17819	-0.05761	0.1205
10	-1151.543	-0.17332	-0.04900	0.1243

CHAPTER 3

Tuning the Aggregation Performance of Neutral Bis-Urea Derivatives with Varying the Aromatic Core: Influence of External Factors



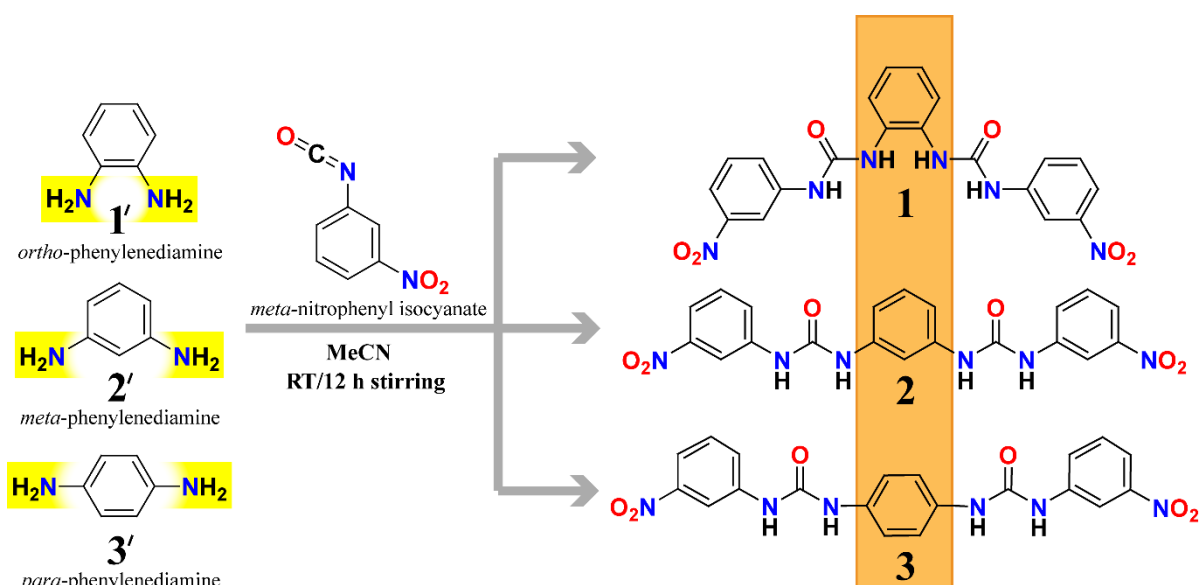
Chapter 3

3.1 Objective of the Chapter

In view of recent developments, studying the positional isomeric effect on the aggregation behavior of small molecules has become of acute interest as it links the changes in the characteristic properties with small changes in the structures, providing particulars on their working principle, which further helps to improve the performances of these functionalized materials via the structural modification.^{3.1-3.5} Self-assembly via π - π interaction and H-bonding interaction has attracted much attention due to the strong organizing capability and directional properties of these interactions in the formation of supramolecular architectures.^{3.6-3.8} Therefore, a π -conjugated molecule furnished with a H-bond donor and/or an acceptor provides the ideal prospect for the building blocks of supramolecular assemblies. However precise control over these interactions for ensuring desired functions still remains a major challenge.^{3.9} Although there is sufficient evidence from the recent advancement of molecular self-assembly in the case of naturally occurring materials, peptides, and amphiphiles, still the role of self-assembly of small molecules in revealing the natural process in aspects of chemistry remains very complicated and has been little explored. Among small molecules currently, urea and its derivatives are in high demand and gaining special scientific attention among researchers around the world for constituting multi-dimensional frameworks due to their vast applicability in chemical and biological studies.^{3.10,3.11} In this context, we focused our intention on examining the effect of substituent position on the aggregation behavior of a three already reported urea derivatives.^{3.12-3.14}

3.2 Outline of the Chapter

A set of three neutral bis-urea derivatives has been purposefully chosen to investigate the consequences of positional isomers on the aggregation performance. The comparative analysis based on the spectral study proved that all three isomers **1**, **2** and **3** exhibit substantial aggregation behavior while compound **2** is more potent in the formation and stabilization of aggregates. Variation in the aromatic core changes the directional property and steric effect, which causes diversity in the morphology of aggregated species of **1**, **2** and **3**, and this is further validated by FESEM images and a theoretical approach. Additional studies were also conducted to assess the influence of temperature, salt (NaCl), urea and pH on the aggregation properties to gain a deeper understanding of the relative aggregation aptitude and the results indicate the strong hydrogen bonding responsible for the aggregation phenomenon.



Scheme 3.1 Schematic representation of synthetic strategy of **1**, **2** and **3**.

3.3 Structural aspiration of **1**, **2** and **3**

The compounds **1**, **2** and **3** (Scheme 3.1) were purposely chosen based on the following contemplations: (i) the simultaneous presence of the urea subunit within the molecule can play the role for H-bonding interactions to give directional property, (ii) the electron rich core and the electron deficient terminal can offer the possibility of π - π stacking in the system and (iii) the change in aromatic core will revise their molecular orientation by increasing the distance between the two terminal substituted-arms to alter their aggregation nature. So it is obvious that change in aromatic core simply driven us to create the positional isomers and to check their substituent induced aggregation property individually.

3.4 Aggregation outcome of **1**, **2** and **3**

The photophysical properties of **1**, **2** and **3** (10 μ M) were explicated by UV-Vis spectra in mixed solvent system. The UV-Vis spectra displayed well defined absorbance band in 100% acetonitrile medium in all three cases in the wavelength region 300-400 nm. The absorption spectra of the three analogous compounds were examined by varying water fraction in acetonitrile-water mixture (Figure 3.1A). There was slight change in absorption spectra during addition of lower water fraction, but the gradual addition of water to the acetonitrile medium not only led to broadening of the absorption bands but also uplifted baseline in the tail of UV-Vis spectra along with simultaneous bathochromic shift in the absorbance maxima. The spectral responses varied obviously with the type of the isomers, and the overall results have validated the possible formation of aggregates of each compound with decreasing solubility in aqueous medium. The

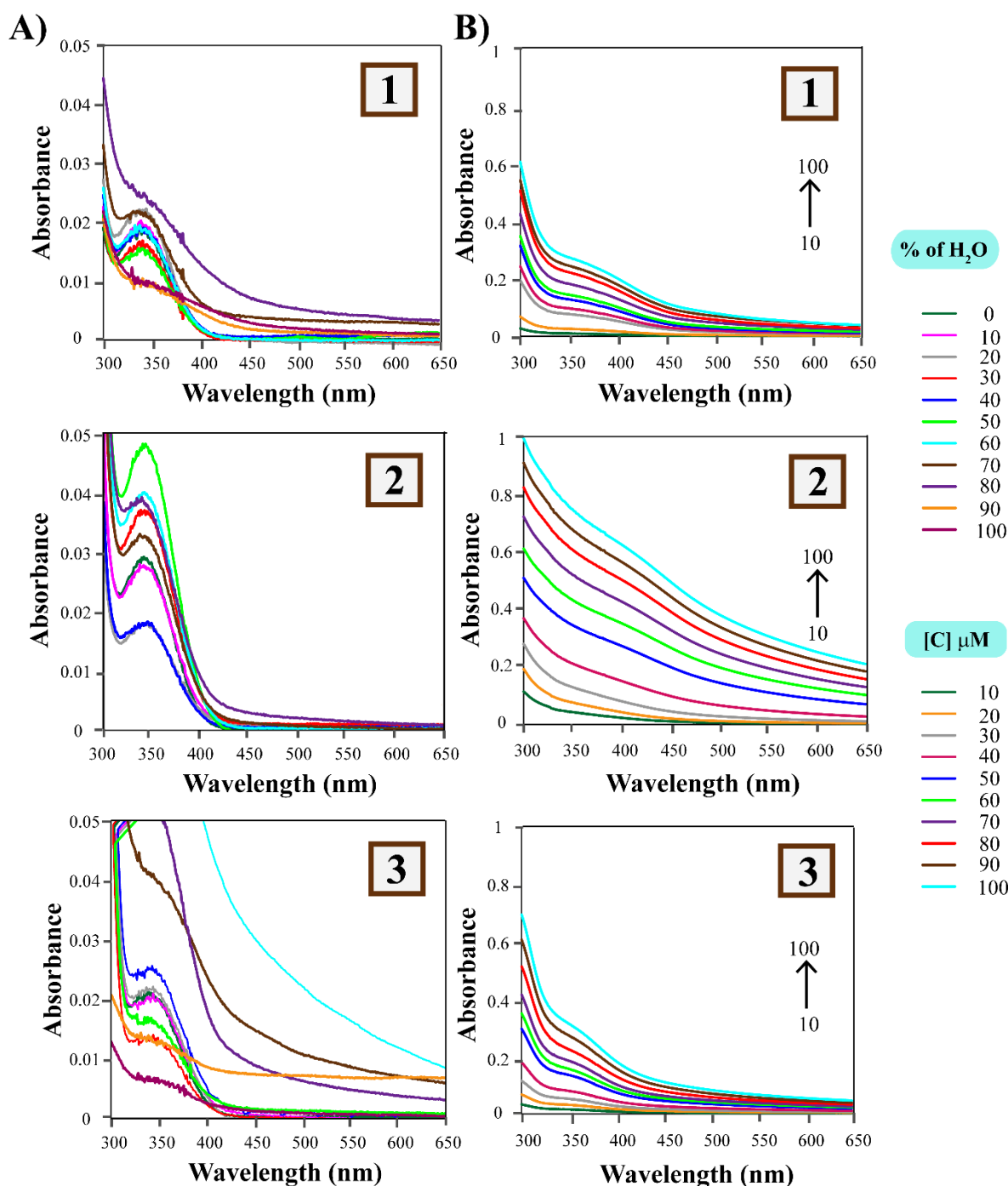


Figure 3.1 A) UV-Vis spectra of **1**, **2** and **3** in mixed solvent system by varying solvent fraction; B) UV-Vis spectra of **1**, **2** and **3** in aqueous medium by varying concentration of respective compound.

scattering contribution increases accordingly as the particles aggregate to a greater extent at higher concentration of compounds and provides a well resolution of the broadening of the bands with the bathochromic shift of the absorption maxima and the elevation of baseline (Figure A3.1). To gain a deeper understanding of their relative aggregation aptitude the absorption spectra were also recorded in aqueous medium for three compounds separately with the incremental addition of the respective compound (Figure 3.1B). It results in obvious systematic growth in the absorbance value accompanied by the visible change in the baseline in the tail of UV-Vis spectra for all three

compounds, which confirmed their ability to self-aggregate in aqueous medium. And this variation in absorption spectra is more prominent in case of meta-isomer suggesting the noteworthy isomeric effect on their aggregation performance. Hence, it was primarily proven that each of the compounds **1**, **2** and **3** possess aggregation properties. But all three compounds exhibit very poor fluorescence response in the aqueous medium (Figure A3.2).

DLS experiment of **1**, **2** and **3** in a mixed solvent system was performed to confirm the aggregation phenomenon. The average Particle size increased for all three cases due to the accumulation of particles to form larger aggregates with the increase in water content of the medium up to a certain limit. Thus the DLS results suggest the formation of aggregates by all three compounds in presence of water in acetonitrile medium (Figure A3.3) and are in good agreement with UV-Vis spectral studies in mixed solvent system.

In order to investigate the interactions responsible during aggregation, FT-IR spectroscopic study was conducted for three compounds and their aggregated form separately using KBr pellet at room

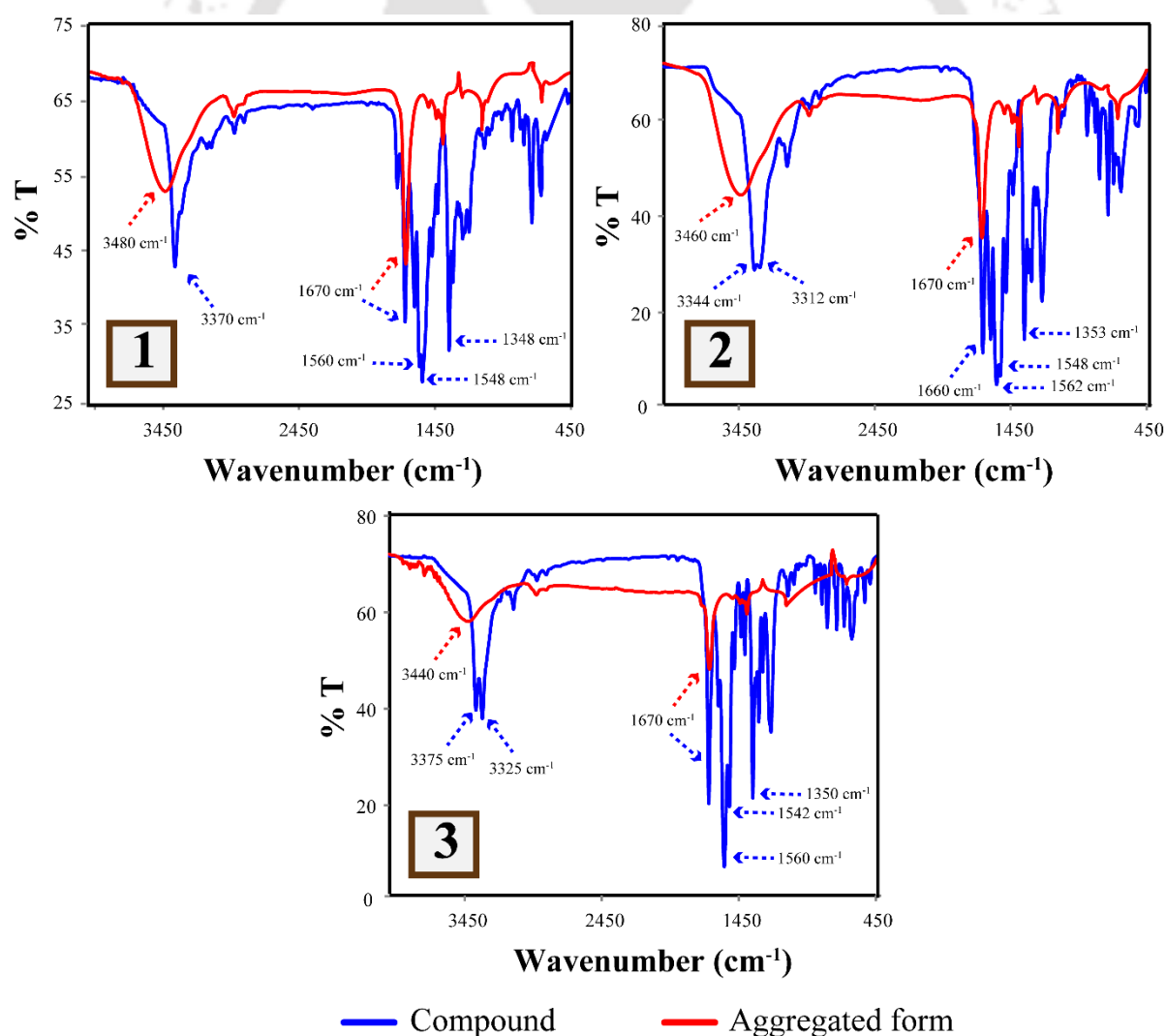


Figure 3.2 FT-IR spectra of **1**, **2** and **3** in compound and aggregated form using KBr pellet.

temperature (Figure 3.2). And the obtained FT-IR spectra can easily distinguish between the free compounds and their aggregated form based on stretching and bending frequency values of functional group of the respective compound (Figure A3.4). The sharp peak observed at 3375-3312 cm^{-1} for all three cases are due to N-H stretching which became broaden and shifted to higher wavenumber side in the aggregated form. This result suggests the contribution of strong H-bonding interaction during aggregation phenomenon. The sharp C=O signals detected at 1670, 1660, 1670 cm^{-1} for **1**, **2** and **3** respectively became moderate in aggregated form of all three compounds and got shifted only for **2**. The sharp peak encountered at 1560 and 1348 (**1**), 1562 and 1353 (**2**), 1560 and 1350 (**3**) cm^{-1} due to N-O stretching and 1548 (**1**), 1548 (**2**), 1542 (**3**) cm^{-1} due to N-H bending. But surprisingly in aggregated structure the peaks for N-O stretching and N-H bending got almost disappeared. Thus the shifts and variation in intensity of stretching and bending frequencies of functional groups in the compounds and their aggregated form confirmed the H-bonding interactions as major force operating during aggregation as well as the significant effect of substituents in tuning their aggregation behavior.

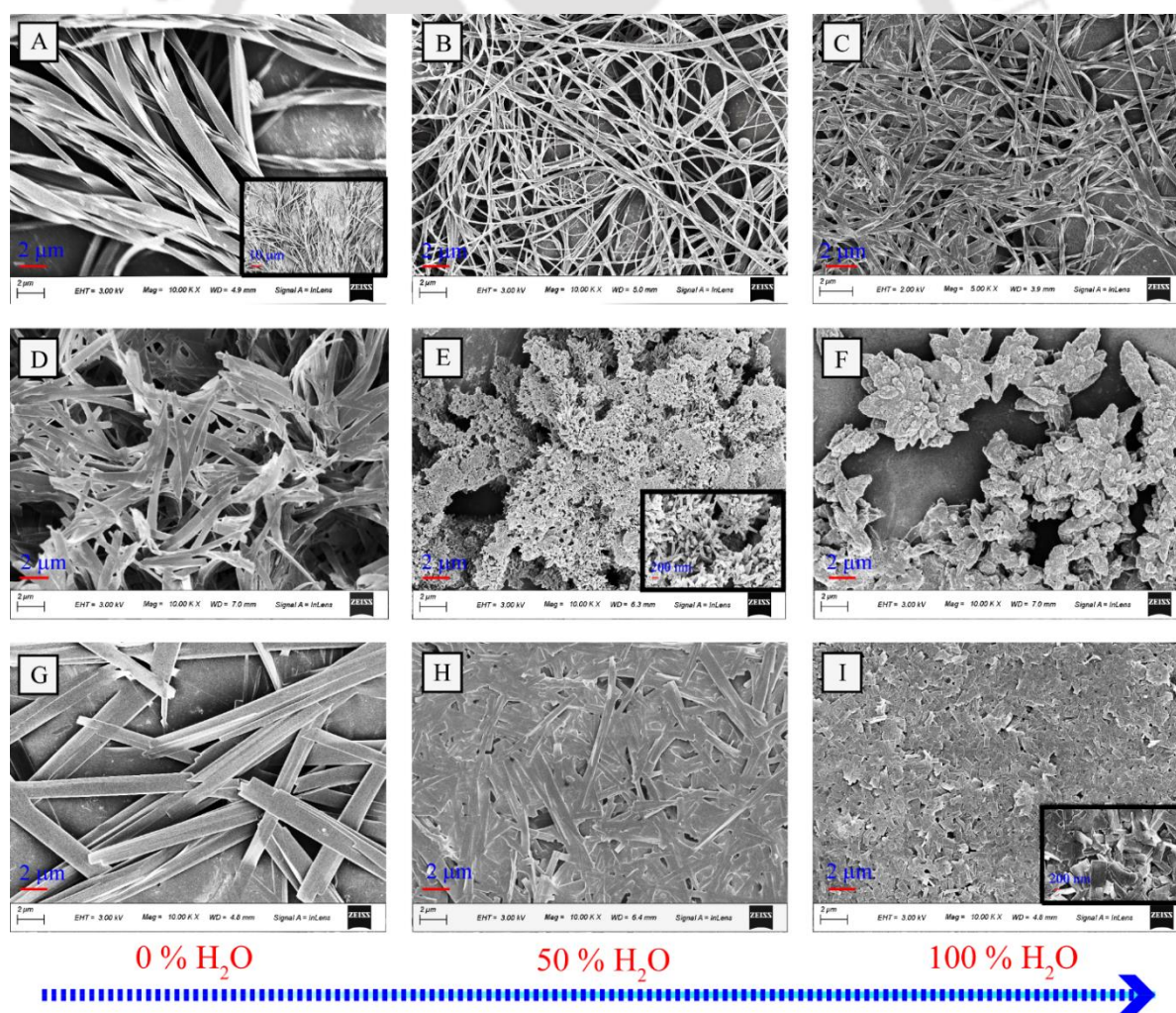


Figure 3.3 FESEM images of the **1**(A-C), **2** (D-F) and **3** (G-I) by varying the solvent fraction in mixed solvent system.

For further validation, the aggregation of three compounds fabricated by solution drop-casting was observed with FESEM as represented in Figure 3.3. It depicts that **1** in 100% acetonitrile medium exhibits flexible micro-fibrils with average width in micrometer range, but with increase in water content the average width falls to nanometer range. For **3**, the micro-sheets like structure were obtained which get densely packed with increase in water fraction with noticeable change in morphology whereas for **2** the change in morphology is highest by switching the solvent. In 100% acetonitrile medium the aggregates of **2** is embodied some shape in micrometer range but in 100% aqueous medium it forms worm-shaped particles with very large size and different 3D values. The above results indicate that a minor change in substituent position would have major effects in the arrangement of aggregated structures. Thus the positional isomers that possess different orientations may initiate the molecular aggregation in different ways giving rise to different molecular superstructures.

3.5 Influence of external stimuli on aggregation behavior

To gain a deeper insight on their relative aggregation characteristics, additional studies were also conducted to assess the effect of external factors on their aggregated arrangement.^{3.15-3.17} The absorption spectra of **1**, **2** and **3** in aqueous medium were recorded at two different temperatures 40 and 80 °C and the change in the spectra due to temperature difference are clearly visible for all cases (Figure A3.5). But the effect of temperature on the aggregation of **2** is maximum as shown in Figure 3.5A. To verify this, DLS experiments were also pursued at those two temperatures for three compounds in aqueous medium. A representative plot depicting the temperature dependence of the aggregates and their size distribution by intensity is given in Figure 3.4A. With the increase in temperature the particle size kept increasing progressively for all three cases but this progress was in a systematic way for **2**. The average particle size increased to 1293 nm from 537 nm for **2** with the increase in temperature from room temperature to 80 °C, which strongly suggests the formation of aggregates boosted by high temperature. FESEM images at high temperature (at 80 °C) are also corroborating the DLS results. The morphology got fully reformed (feather like structure) in case of **2** at higher temperature in comparison with room temperature but for other two cases the high temperature could not able to induce huge morphological change in their aggregated structure (Figure 3.4B).

The spectral properties of **1**, **2** and **3** were analyzed in presence of sodium chloride (NaCl) in order to gain some knowledge about possible changes in the structural characteristics of the aggregates of all compounds due to effect of salt (Figure A3.6). With the gradual increase in the NaCl concentration, the absorption spectra changes through bathochromic shift in the absorbance

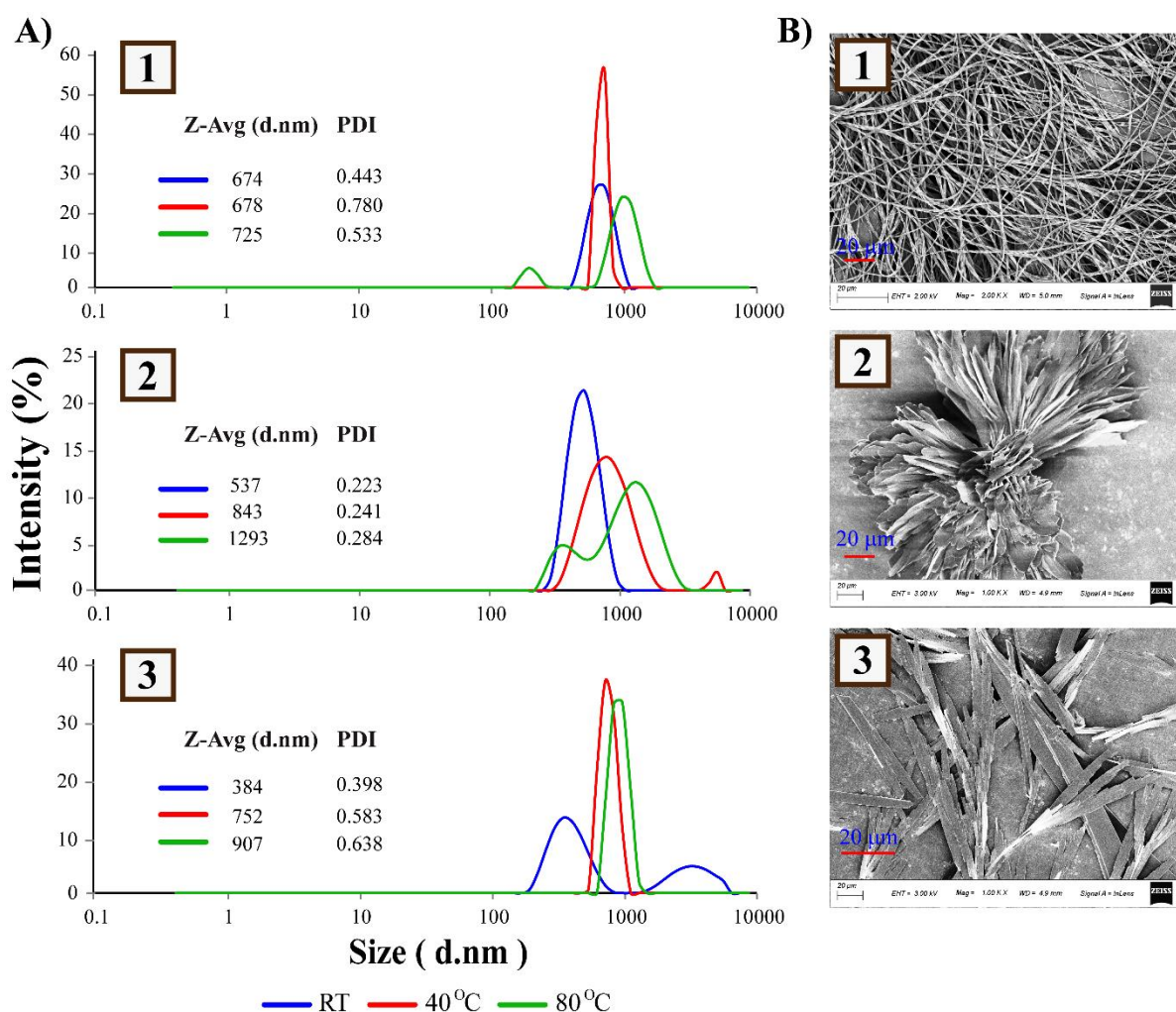


Figure 3.4 A) DLS-based particle size analysis of **1**, **2** and **3** in aqueous medium at different temperature. B) FESEM images of the **1**, **2** and **3** in aqueous solution at high temperature. (scale bar = 20µm).

maxima along with increase in the baseline in the tail of the UV-Vis spectra and the effect is more significant in case of **2** (Figure 3.5B). Thus the presence of salt facilitated the aggregation phenomenon which suggests that the high salt concentration favors the molecular aggregation by reducing the water molecules in the solutions.

Urea acts as an agent in the denaturation of proteins,^{3,18} mainly through hydrogen bonding interaction. Hence UV-Vis spectral studies were also conducted for all three compounds to examine the interaction between the compound and the urea molecule and the effects were monitored by evaluating the changes in their absorbance spectra at a fixed concentration of urea with respect to time (Figure A3.7). It is interesting to note that with the progress of time the aggregation was developing as the absorption maxima red-shifted along with elevation of the baseline in presence of urea up to 12 hrs. This interaction is higher in case of **2** (Figure 3.5C). This study proved that the hydrogen bonding interaction is the main force acting between the molecules for aggregation and it is also important to mention here that the hydrogen bonding interactions are

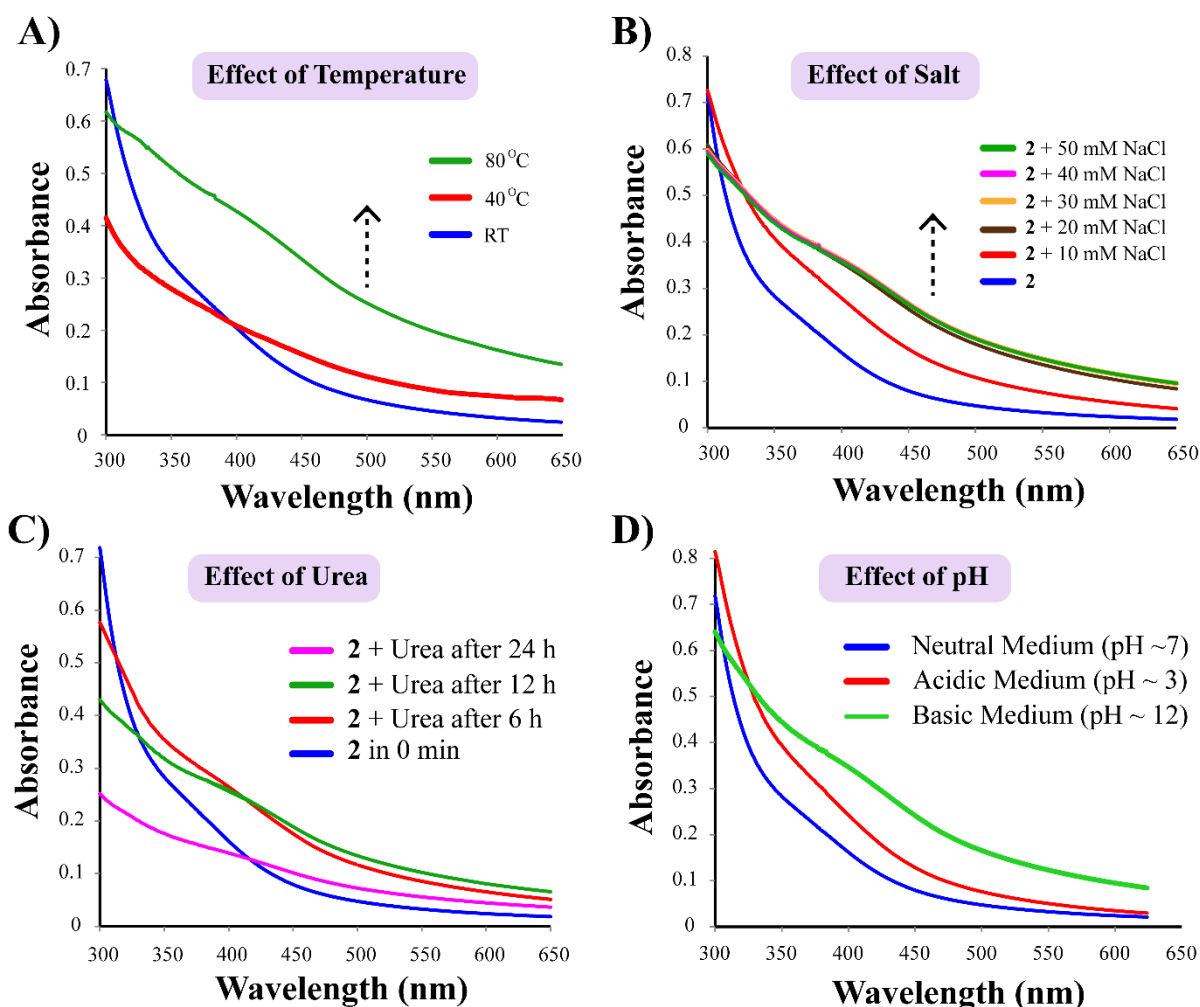


Figure 3.5 The effect of temperature (A), ionic strength (B), urea (C) and pH (D) in aggregation behavior of **2**.

much stronger than the protein molecules that the presence of urea molecule could not able to destroy the aggregated arrangement. On the contrary, the urea molecule acted as an inducing agent for the aggregation of all three compounds.

The stability of aggregates of **1**, **2** and **3** were also scrutinized at different pH by the changes in their UV-Vis spectral behavior (Figure A3.8). It may be noted that the change in the pH of the medium had a noticeable impact in case of **2** in comparison to **1** and **3**. All the compounds responded accordingly with the pH variation in spite of being neutral. But for compound **2**, the basic medium stabilizes the aggregated arrangement most. All these results indicate that neither temperature and salt concentration nor urea and pH lead to disaggregation of the compounds, instead all the factors stimulated the aggregation process by stabilizing the aggregates and this stabilization is more prominent in case of compound **2**.

3.6 Theoretical approach

To support their aggregation and to find out the plausible explanation behind the interesting

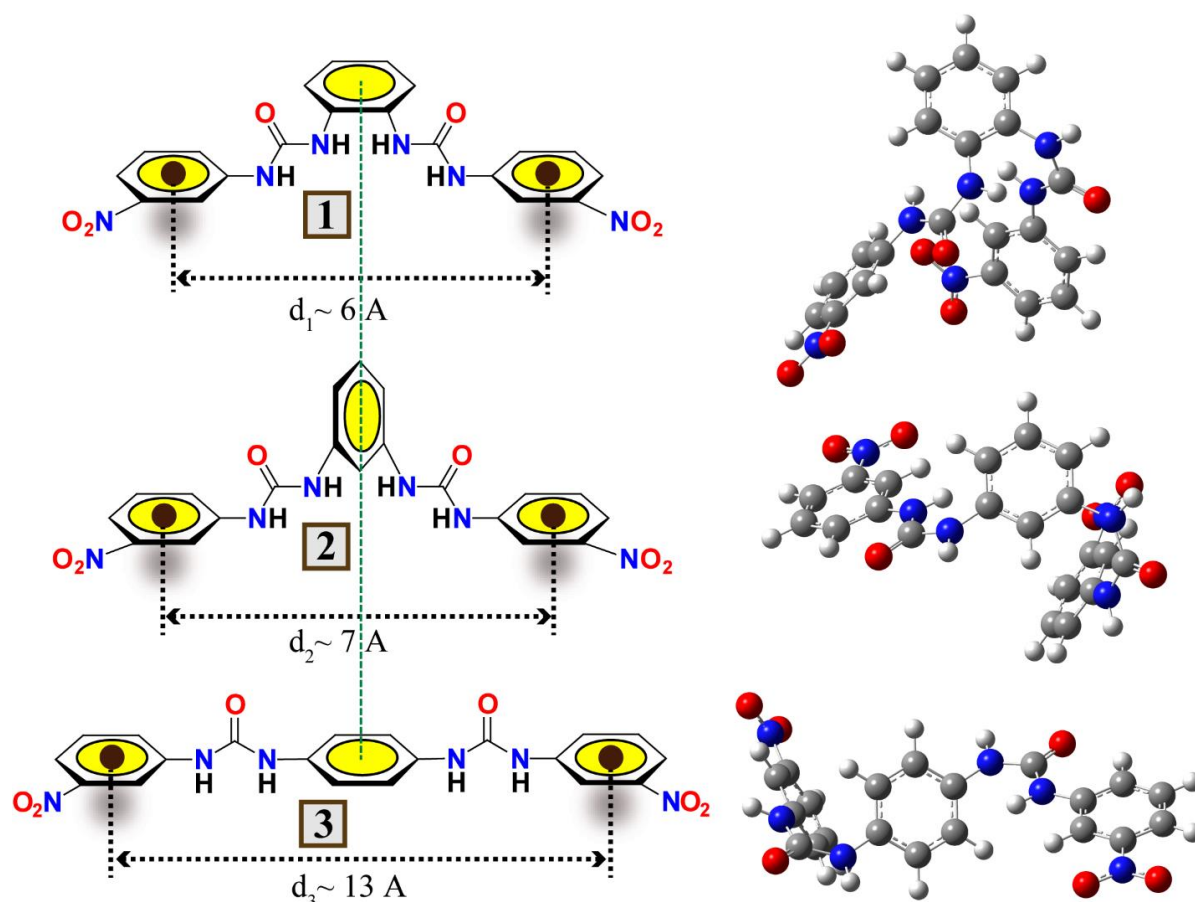


Figure 3.6. Geometry Optimized structures of **1**, **2** and **3** using RB3LYP/ 6-31G (d) as implemented on Gaussian 09.

aggregation behavior of **2**, density functional theory (DFT) calculations were performed to obtain the theoretical aspects of the observed spectral changes due to the positional isomeric effect. DFT optimizations of **1**, **2** and **3** were carried out with the B3LYP/6-31G basis set (no specific solvent model was used) using the Gaussian 09 program (Table A3.1) and HOMO and LUMO molecular orbital plots are shown in Figure A3.9. The optimized structures are presented in Figure 3.6, which demonstrates that as we move from compound **1** to **3**, steric influences decreases and the pod distance between the two terminal substituted arms increases. For compound **2**, these two differing factors is optimized which is manifested by a better aggregation prospect and more stability in aggregated form even in presence of external factor.

3.7 Conclusion

To summarize, the present study was focused on the effect of positional isomerism on the aggregation behavior of a new set of three bis-urea derivatives on basis of spectral studies along with microscope imaging. Based on the results of this comparative analysis, it was concluded that all the three isomers exhibit substantial aggregation behavior in mixed solvent system while the outcome is more pronounced in case of **2**. The obvious differences

in morphology with the change in solvent fraction for three cases were exemplified by FESEM images which indicate that a minor variation in the chemical structure has a major influence on the aggregation properties. It was predicted that the hydrogen bonding interactions are playing the main role among the molecules during the aggregation process and that interactions are so strong that even temperature, treatment with NaCl solution and urea molecule, change in pH failed to interrupt the aggregation phenomenon. Moreover, compound **2** appeared more potent in the formation and stabilization of aggregates compared with other two in the aqueous medium and the fact was also supported with the help of theoretical approach. Thus, this set of three neutral bis-urea derivatives offer an exclusive scope of understanding the consequence of the substituent induced aggregation behavior of positional isomers in the aqueous or mixed aqueous medium and can be utilized to manufacture several functional materials with different application potential in various fields.

References

- 3.1 Y. Hu, K. Miao, B. Zha, L. Xu, X. Miao and W. Deng, *Phys. Chem. Chem. Phys.*, 2016, **18**, 624-634.
- 3.2 C. Niu, L. Zhao, T. Fang, X. Deng, H. Ma, J. Zhang, N. Na, J. Han and J. Ouyang, *Langmuir*, 2014, **30**, 2351-2359.
- 3.3 H. Tong, Y. Dong, Y. Hong, M. Haussler, J. W. Y. Lam, H. H.-Y. Sung, X. Yu, J. Sun, I. D. Williams, H. S. Kwok and B. Z. Tang, *J. Phys. Chem. C*, 2007, **111**, 2287-2294.
- 3.4 D. Chakraborty, S. Dinda, M. Chowdhury and P. K. Das, *J. Colloid Interface Sci.*, 2019, **539**, 414-424.
- 3.5 J. Hou, J. Du, Y. Hou, P. Shi, Y. Liu, Y. Duan and T. Han, *Spectrochim. Acta, Part A*, 2018, **205**, 1-11.
- 3.6 B. K. An, J. Gierschner and S. Y. Park, *Acc. Chem. Res.*, 2012, **45**, 544-554.
- 3.7 P. S. Corbin and S. C. Zimmerman, *J. Am. Chem. Soc.*, 1998, **120**, 9710-9711.
- 3.8 P. S. Corbin and S. C. Zimmerman, *J. Am. Chem. Soc.*, 2000, **122**, 3779-3780.
- 3.9 E. M. Furst, *Soft Matter*, 2013, **9**, 9039-9045.
- 3.10 L. S. Shimizu, S. R. Salpage and A. A. Koros, *Acc. Chem. Res.*, 2014, **47**, 2116-2127.
- 3.11 K. Yabuuchi, E. M. Owusu and T. Kato, *Org. Biomol. Chem.*, 2003, **1**, 3464-3469.
- 3.12 S. J. Moore, C. J. E. Haynes, J. Gonzalez, J. L. Sutton, S. J. Brooks, M. E. Light, J. Herniman, G. J. Langley, V. Sottocerrato, R. Perez-Tomas, I. Marques, P. J. Costa, V. Felix and P. A. Gale, *Chem. Sci.*, 2013, **4**, 103-117.
- 3.13 U. Manna, R. Chutia and G. Das, *Cryst. Growth Des.*, 2016, **16**, 2893-2903.
- 3.14 U. Manna, R. Chutia and G. Das, *Cryst. Growth Des.*, 2018, **18**, 6801-6815.
- 3.15 N. Al-Manasir, K. Zhu, A. L. Kjoniksen, K. D. Knudsen, G. Karlsson and B. Nystrom, *J. Phys. Chem. B*, 2009, **113**, 11115-11123.
- 3.16 S. Pispas and N. Hadjichristidis, *Langmuir*, 2003, **19**, 48-54.
- 3.17 E. Lee, J. Kim and M. Lee, *Macromol. Rapid Commun.*, 2010, **31**, 975-979.
- 3.18 F. G. Hopkins, *Nature*, 1930, **126**, 328-330.

Appendix-Chapter 3

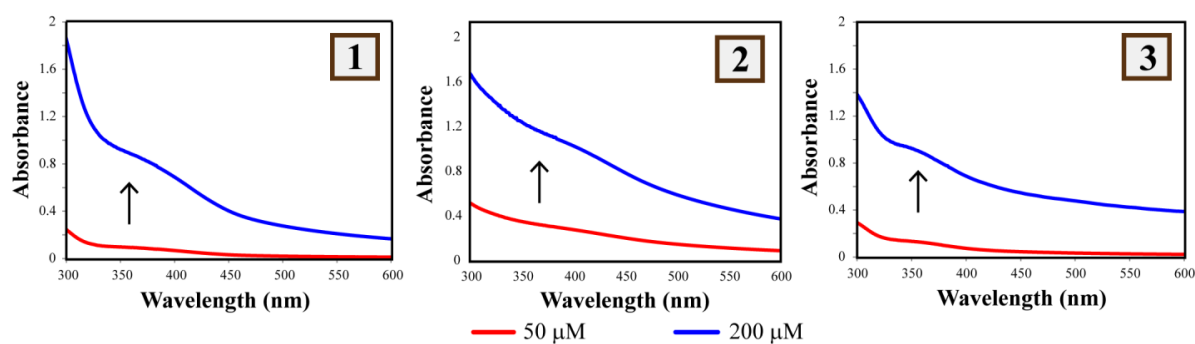


Figure A3.1 UV-Vis spectra of 1, 2 and 3 in aqueous medium at higher concentration.

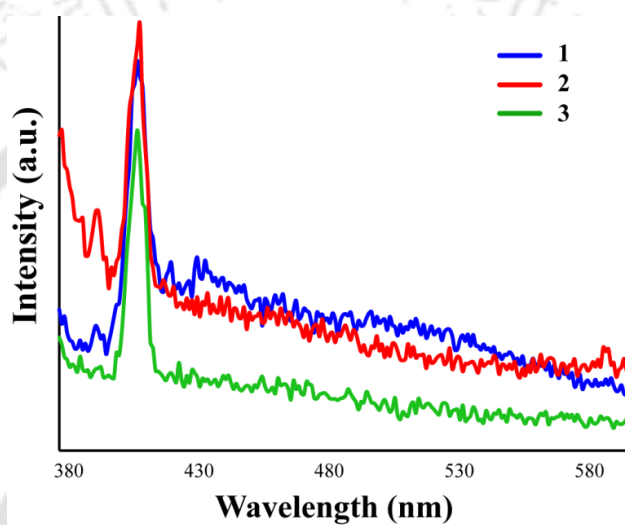


Figure A3.2 Fluorescence spectra of 1, 2 and 3 in aqueous medium.

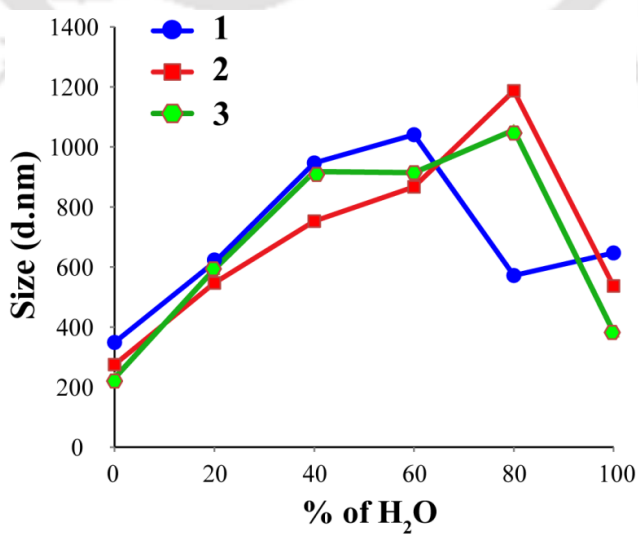


Figure A3.3 DLS-based particle size analysis of 1, 2 and 3 as the function of water fractions in mixed solvent system.

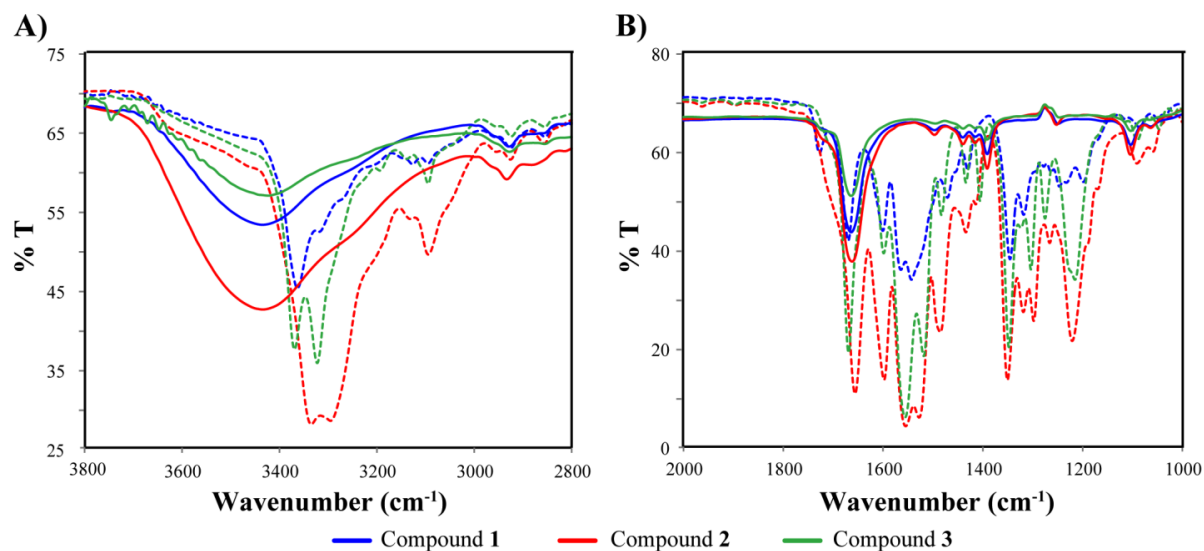


Figure A3.4 IR spectra of **1**, **2** and **3** and their aggregated form (A) region 3800-2800 cm^{-1} and (B) region 1000-2000 cm^{-1} (Dotted line - compound and Solid line - aggregated form).

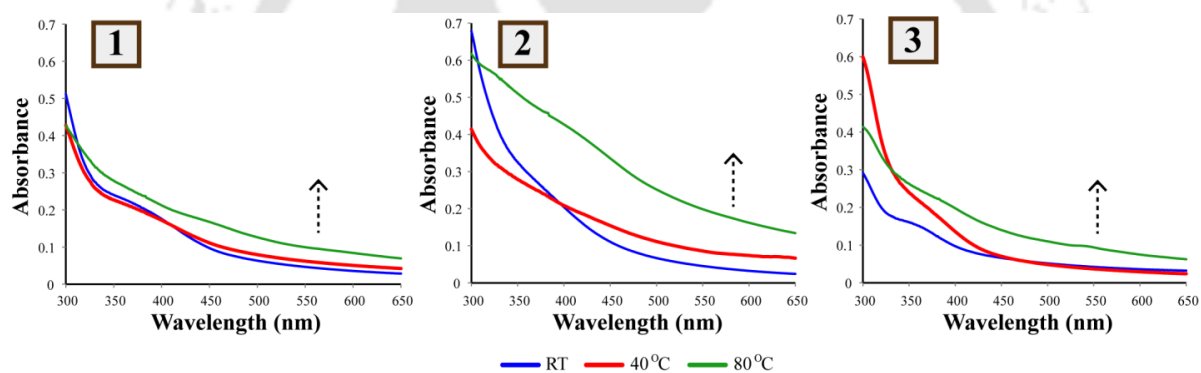


Figure A3.5 Effect of temperature on UV-Vis spectra of **1**, **2** and **3**.

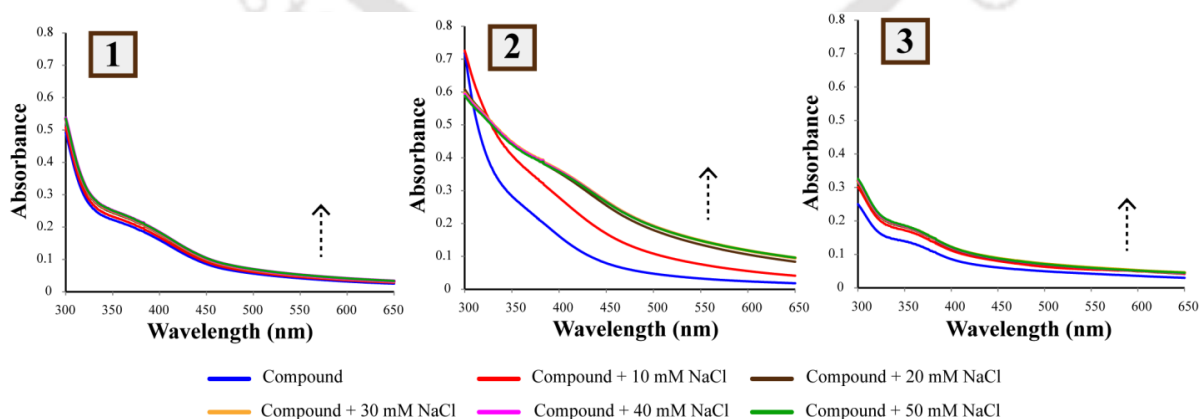


Figure A3.6 UV-Vis spectra of **1**, **2** and **3** in presence of salt (NaCl).

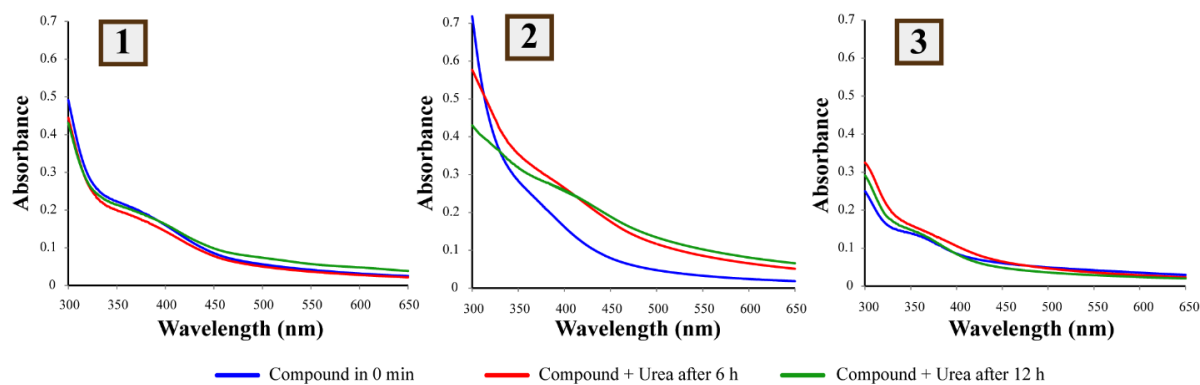


Figure A3.7 UV-Vis spectra of 1, 2 and 3 in presence of urea.

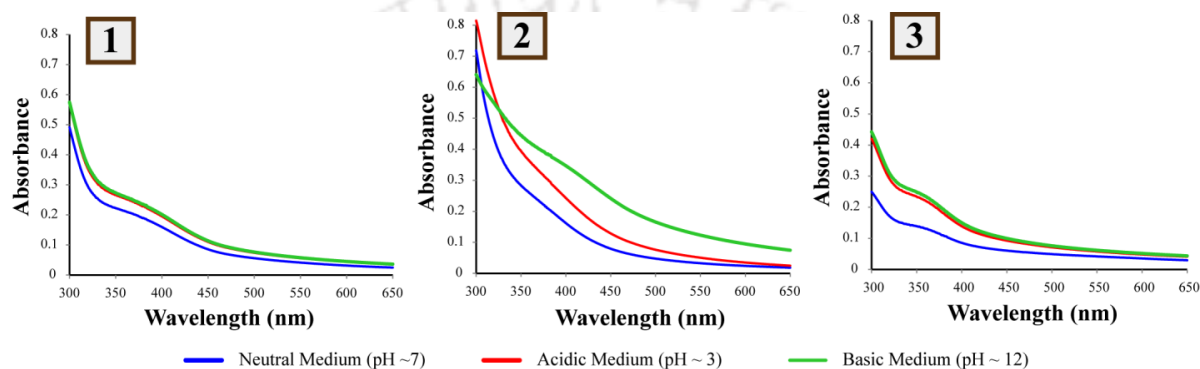


Figure A3.8 UV-Vis spectra of 1, 2 and 3 with the variation in pH of the medium.

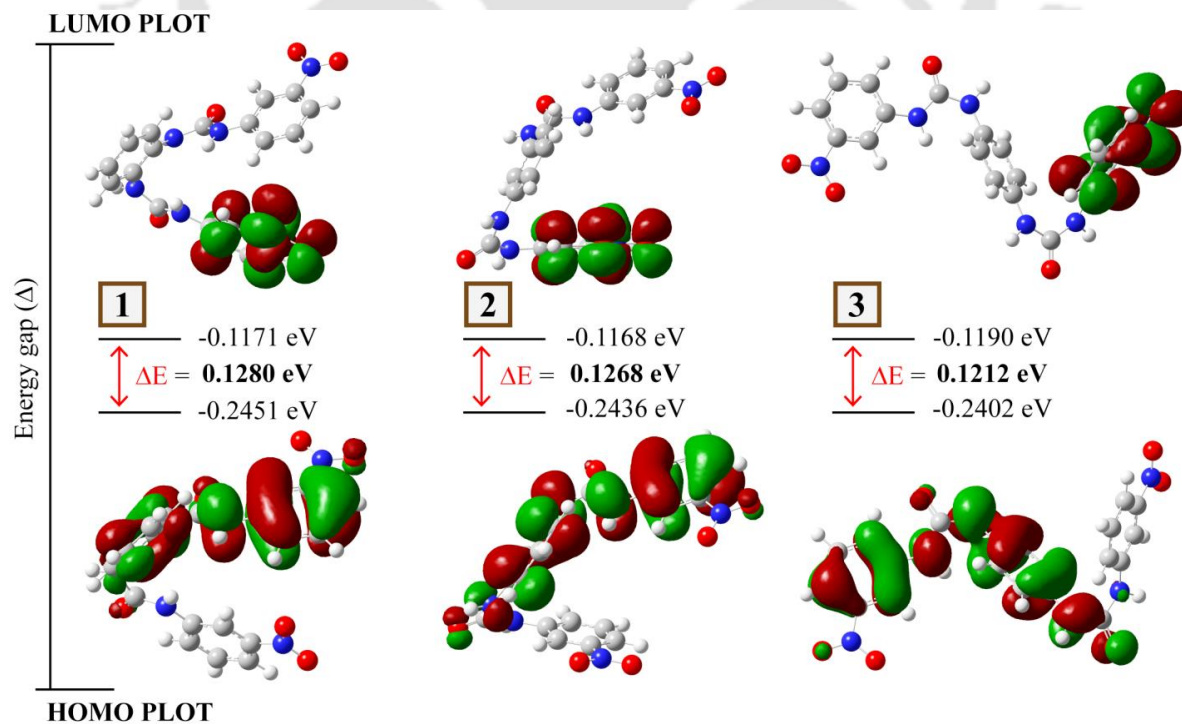


Figure A3.9 : Frontier molecular orbital plots of 1, 2 and 3 (ΔE = energy gap between HOMO and LUMO).

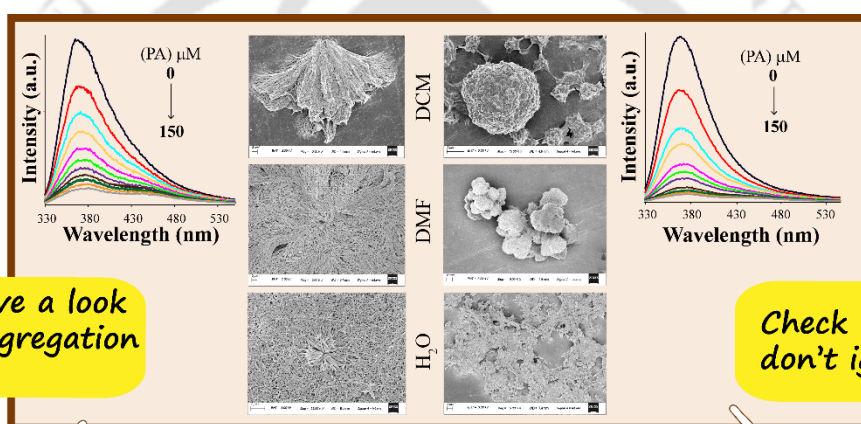
Table A3.1 Summary of DFT data.

	Total Energy (a.u)	HOMO Energy (eV)	LUMO Energy (eV)	ΔE (eV)
Compound 1	-1551.013	-0.2451	-0.1171	0.1280
Compound 2	-1551.006	-0.2436	-0.1168	0.1268
Compound 3	-1551.006	-0.2402	-0.1190	0.1212



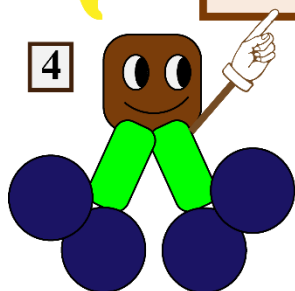
CHAPTER 4

Probing the Aggregation Aptitude of Neutral Naphthyl bis-Urea Series with Varying the Aromatic Core: Effect of Solvent-Tuning and Response towards Nitro-aromatics



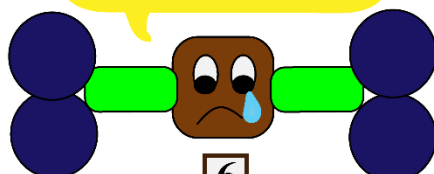
Please have a look on my aggregation ability...

4



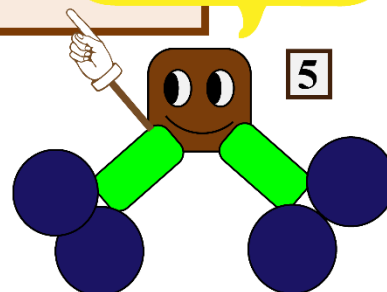
Oopps!!..But I think I am so useless..

6



Check mine too.. don't ignore...

5

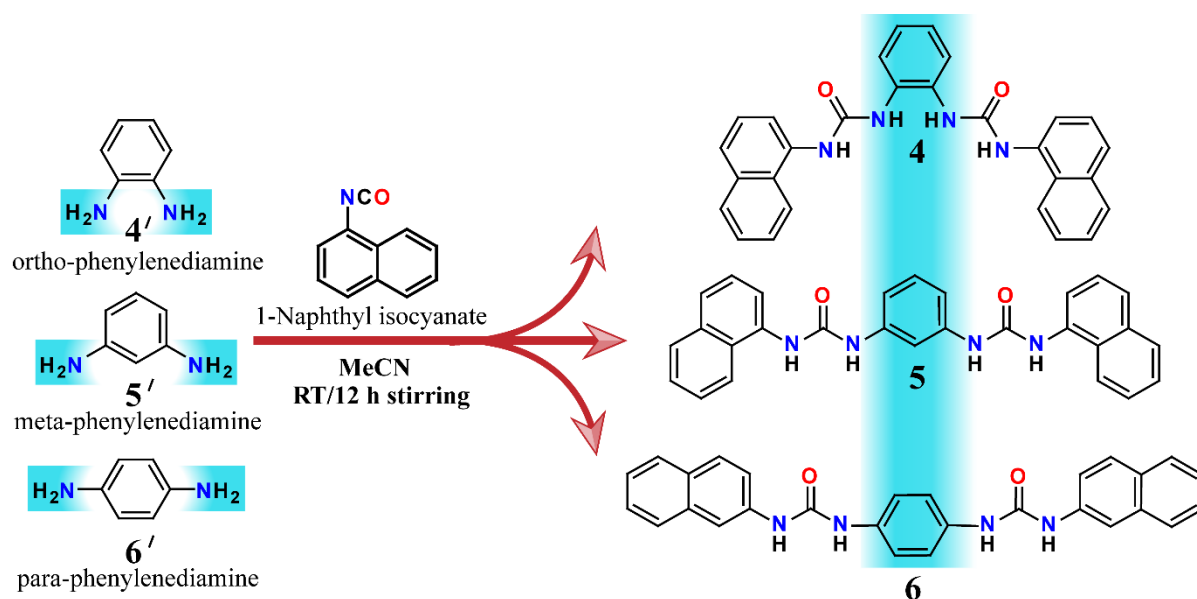


4.1 Objective of the Chapter

In previous chapter we realized that the position of the substituent group furnishing weak forces should be seriously considered in tuning the characteristics of self-aggregated system.^{4.1-4.3} But solvent being the second assembly partner, can play a vital role^{4.4,4.5} in manipulating those aggregation structures through variation of non-covalent interactions between solute-solvent molecules. Polarity, a key factor of solvent may perturb these non-covalent interactions and further fine-tune the morphology of the self-assembled framework.^{4.6-4.9} Therefore, methods for tuning self-assembled structures in a controlled way by varying the solvent properties become a challenging task, which opens up an alternative means for comprehending the association mechanism of the multi-dimensional molecular framework.^{4.10-4.12} In continuance of our interest in exploring the aggregation aptitude of small molecule, another set of naphthalene functionalized bis-urea derivatives^{4.13} with variations in the aromatic core (*ortho*-, *meta*- and *para*-position) has been examined to report their aggregation behavior by tuning the solvent nature. On the other hand, the fluorophores furnished with donor-acceptor groups may have sensitivity towards nitro-aromatics as the electron-deficiency nature of nitro-aromatics makes it readily interact with the electron-rich fluorophores through donor-acceptor (D-A) interactions.^{4.14} Hence, we further evaluated the interaction of nitro-aromatics with the isomers to elucidate other small aromatic molecules' influence on their aggregation aptitude.

4.2 Outline of the Chapter

The effect of core-substitution (*ortho*-, *meta*- and *para*- position) and solvent nature on the aggregation aptitude of three neutral naphthyl bis-urea derivatives **4**, **5** and **6**, is investigated here. Isomers **4** (*ortho*) and **5** (*meta*) exhibit substantial aggregation behavior, as verified by adequate spectroscopic studies. The ability of **4** and **5** to form a different type of micro/nano-structure in solvents with different polarity and H-bond donating capability was also explored with microscope imaging studies. Additionally, aggregated form of both compounds applied for studying the interaction with electron-deficient nitro-aromatics in pure aqueous medium to manipulate their aggregation outcome. And the systematic assessment encountered a significant effect in case of Picric Acid (PA) among the nitro-aromatics due to its strong electronic acceptor nature, which strikingly affects the electron transfer along with the donor-acceptor structure in the fluorophore skeleton.



Scheme 4.1 Schematic representation of synthetic strategy of **4**, **5** and **6**.

4.3 Structural aspects of **4**, **5** and **6**

We tried to explore the change in self-aggregation behavior by changing the core-substitution and solvent nature. The following vital factors simply motivated us to contemplate these set of positional isomers to study their aggregation property (i) the presence of the urea group within the molecule can offer both H-bonding donors as well as acceptor properties and also provide the directional feature to the aggregation processes, (ii) aromatic core can play a vital role in the π - π stacking arrangement which in turn help the aggregation processes, (iii) variation in the aromatic core will alter their molecular orientation as well as the distance between two substituted arms with a possibility to introduce contrasting nature in their aggregation property, and (iv) introduction of naphthalene moiety serving as a potential fluorophore unit to overcome the spectroscopic limitations of previous work. Hence, this comparative study was followed to recognize the effect of core substitution on their aggregation ability with the change in the solvent system.

4.4 Insights into the Aggregation Features

The photophysical properties of three compounds were studied by UV-Vis absorption and fluorescence emission study using acetonitrile/water solvent systems. The UV-vis spectra of **4**, **5** and **6** (10 μ M, respectively) in pure acetonitrile medium revealed sharp absorbance maximum around 300 nm (Fig. 4.1A) which led to a regular fall accompanied by a visible change in the baseline for all three cases with the incremental addition of water to their acetonitrile solutions. The spectrum profile changes with the type of the isomers, and the overall observation supports the existence of molecular aggregates in the mixed solvent

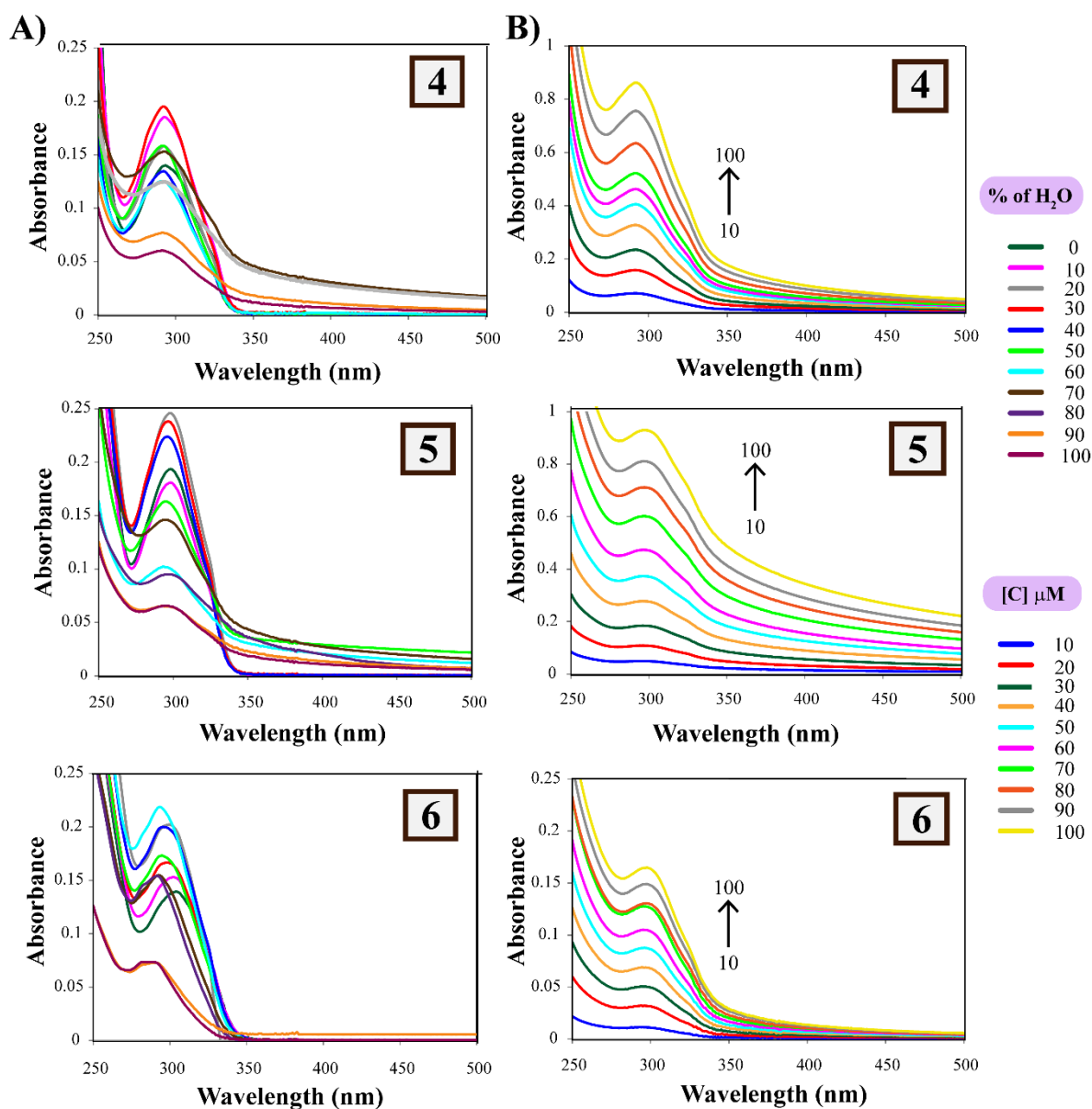


Figure 4.1 A) UV-Vis spectra of **4**, **5** and **6** in mixed solvent system by varying solvent fraction; B) UV-Vis spectra of **4**, **5** and **6** in aqueous medium by varying concentration.

system. But it is worth mentioning that this variation in absorption spectra is less prominent in the case of the *Para*-isomer suggesting the significant isomeric effect on their aggregation aptitude. Further analysis was carried out by recording the absorbance spectra (Fig. 4.1B) with the incremental addition of the respective compound separately in water to gain an insight into their comparative aggregation ability. And the results show a proper systematic growth in the absorbance value along with the elevated baseline in the tail region of UV-Vis spectra for all three compounds, which corroborated their possible self-aggregation properties in an aqueous medium. It is interesting to note that among the three compounds, *meta* isomer exhibited noteworthy spectral response (Figure A4.1A), which reaffirmed the occurrence of isomeric effect on their relative aggregation aptitude. Hence,

it was primarily anticipated that each of the isomers **4**, **5** and **6** exhibits aggregation features.

The fluorescence behavior of all three compounds was recorded in the mixed solvent system. Interestingly, *ortho* and *meta* isomers were found to be highly emissive in pure acetonitrile medium, whereas *para* isomer exhibits very poor fluorescence response. This strong emission intensity of **4** and **5** with zero water content underwent a gradual decrease with the incremental addition of water in acetonitrile medium with a significant red-shift in the case of *meta* isomer (Figure 4.2A). In 100% aqueous medium, the emission of the **4** and **5** become weak and red-shifted. This unprecedented downfall in their emission intensity strongly supported the aggregation phenomenon and proved that the change in

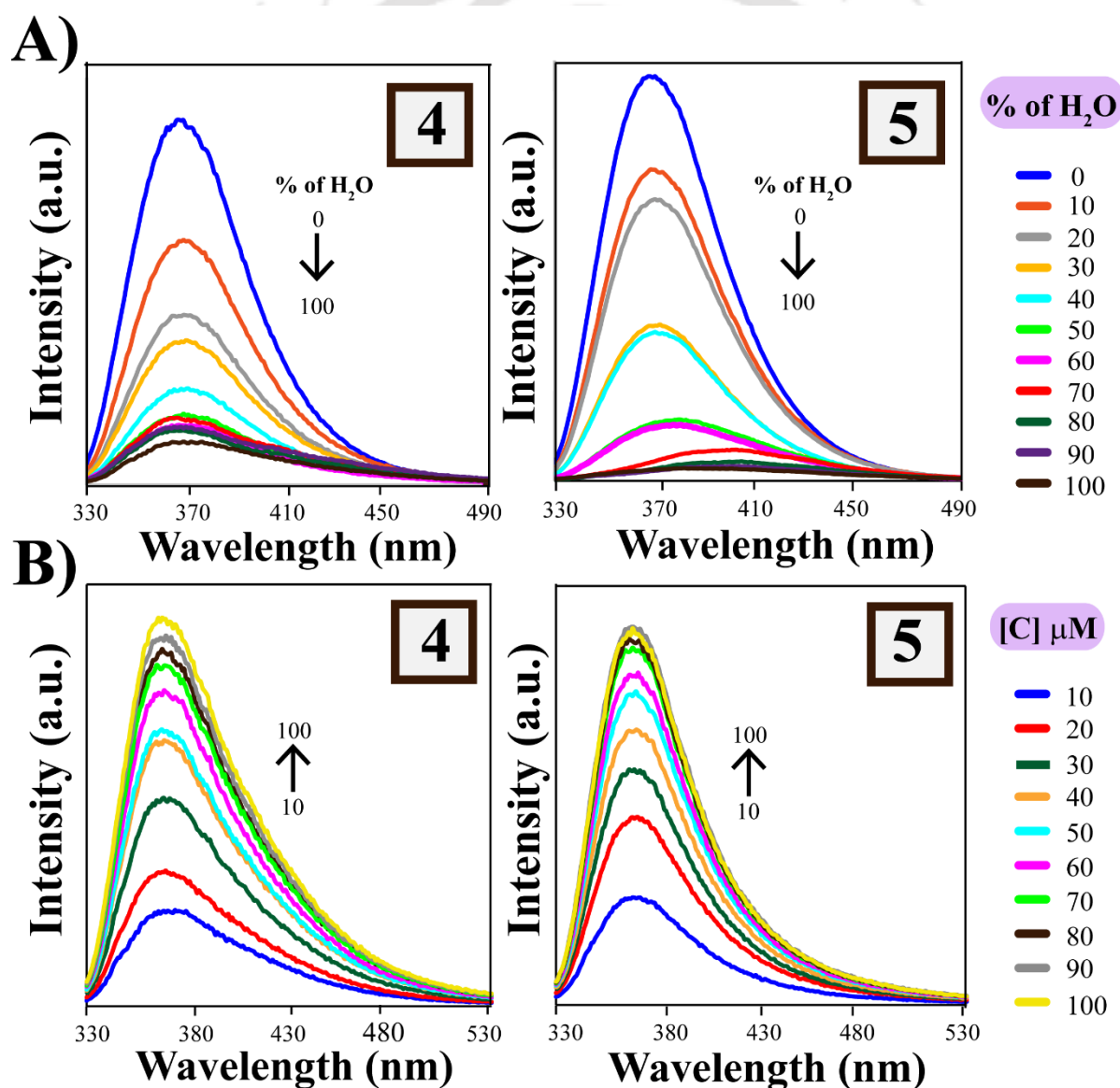


Figure 4.2. A) Fluorescence emission spectra of **4** and **5** in the mixed solvent system by varying solvent fraction; B) Fluorescence emission spectra of **4** and **5** in an aqueous medium by varying concentration.

solvent fraction could impressively affect the photoluminescence (PL) property of **4** and **5** by the introduction of induced restricted intramolecular rotational motions due to the molecular self-aggregations. But in the similar experimental condition, the *para* isomer did not display substantial spectral outcomes as **4** and **5** with the change in the solvent fraction. We also investigated the variation in emission intensity for **4** and **5** with the continual addition of the respective compound separately in water (Figure 4.2B) and it results in an obvious systematic enhancement in the emission maxima (Figure A4.1B) which strengthen the results obtained from UV-Vis study for self-aggregation. Moreover, solid-state fluorescence^{4.15,4.16} spectra of **4**, **5** and **6** also confirmed the aggregative nature of these compounds, which displayed strong fluorescence for **4** and **5** compared to **6** with different emission maxima, when excited at 310 nm (Figure A4.2). As the molecular aggregation in the solid state causes fluorescence quenching (ACQ) in general and there are very few dyes reported to display intensive fluorescence both in solution and solid state, it grows further interest to study their aggregation property in deep.

Besides, DLS experiments of **4**, **5** and **6** in a mixed solvent system also corroborate the aggregative-property of these compounds; as the average particle size increases for all due to the molecular aggregation to form larger assembly with the increase in the water content in the medium (Figure A4.3). Thus the entire spectral outcomes are in good agreement to validate the aggregation property of the compounds. However, compound **6** appeared to be less potent with regards to self-aggregation in the mixed solvent system as well as in aqueous medium may be due to its linear orientation.

4.5 Impact of the Solvent on Aggregation

The nature of the solvent and concentration can induce notable changes^{4.17-4.20} in the aggregation behavior of these types of compounds. Taking advantage of this observation, we attempted to study the aggregation behavior of **4** and **5** towards the solvent of different polarity as well as H-bonding interaction capabilities viz. toluene, DCM, DMF, and water. The absorption spectra of **4** and **5** in various solvents (Figure 4.3A) provide some primary knowledge about the likely changes in the structural characteristics of the aggregates. The variation in the spectra due to the combined effect of solvent polarity and H-bonding interactions is noticeable for all cases. The fluorescence emission spectra of **4** and **5** were also recorded (Figure 4.3B) in similar conditions to determine the solvent effect on the aggregation behavior. It is interesting to note that the change in emission spectra are strongly depended on the combined effect of solvent polarity as well as their H-bond donor properties.^{4.21,4.22} The results were also monitored by evaluating the changes in their

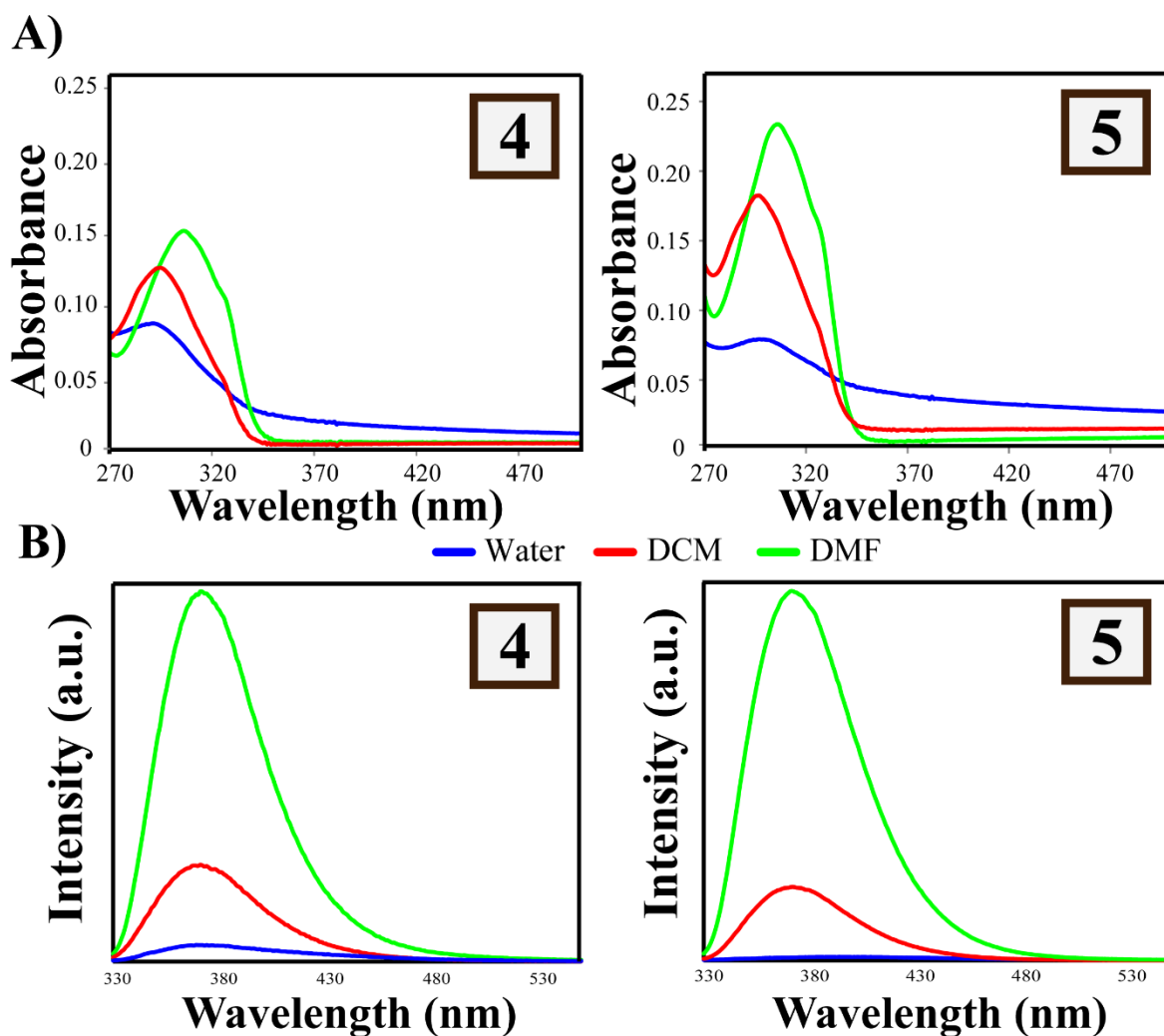


Figure 4.3 A) UV-Vis spectra of **4** and **5** (10 μM) in different polarity solvents. B) Fluorescence emission spectra of **4** and **5** (10 μM) in different polarity solvents.

emission spectra at a fixed concentration of the compound with respect to time (Figure A4.4). It is worth mentioning that with the progress of time, the dis-assembly took place, as the emission intensity decreases for up to 24 h, and this is higher in the case of DCM solvent (Figure 4.4A). Moreover, we also recorded the temperature dependent fluorescence response of **4** and **5** in various solvent to gain a close insight into this dis-assembly process (Figure 4.4B) and excitingly the results were strongly validated the role of thermal energy in aspect of their aggregation aptitude.

This study was also exemplified by the Fluorescence Microscope and FESEM images. The aggregation of the two compounds **4** and **5** fabricated by solution drop casting in different solvents were observed, as illustrated in Figure 4.5. And very interestingly, the morphology of the aggregative species revealed an observable sensitivity towards the respective solvents system. It represents that **4** in 100% DCM and 100% DMF exhibits micro flower kind structure with average width in the micrometre range, whereas **5** shows a globular kind of structure. But, switching the

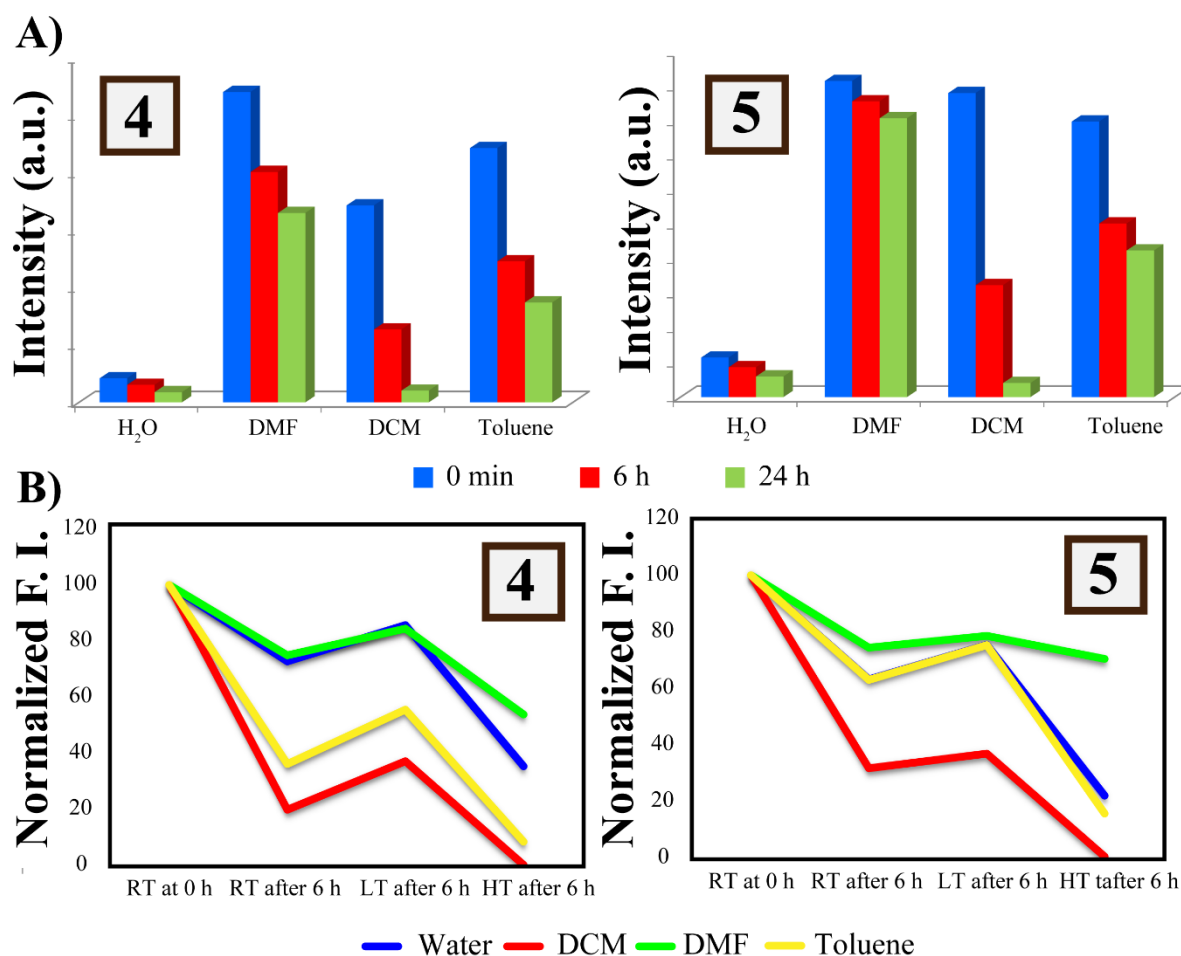


Figure 4.4 A) Fluorescence response of **4** and **5** as a function of time in different polarity solvents. B) Fluorescence response of **4** and **5** as a function of temperature in different polarity solvents.

solvent to water with an increase in water content, the morphology destroyed completely where the average width falls to the nanometer range. Even, the morphology gets further modified after 24 hrs in 100% aqueous medium (Figure A4.5). Thus the above results indicate that a minor change in substituent position would have significant effects in the arrangement of aggregated structures^{4.23,4.24} considering the interaction with solvents. Thus the positional isomers with different orientations may induce the molecular aggregation in the presence of the different solvent systems in diverse ways giving rise to contrasting molecular superstructures. Additionally, fluorescence microscopy revealed remarkable fluorescence in changing the solvent system at various excitation range (Figure A4.6), a feature which could be useful in probing self-aggregation strategy of small molecule.^{4.25} This multicolour emission capability of **4** and **5** as a solo discrete chromophore simply motivated us to check if the overlapping of images of blue, green and red emissions could produce the white coloured emission. And it was exciting to observe that the overlay of blue, green and red emission produces bluish white colour, as the formation of pure white is dictated by purity of the primary colours (RGB) among other factors. In DFT optimized data and structures^{4.26} of **4** and **5** can also be employed in support of their contrasting aggregation

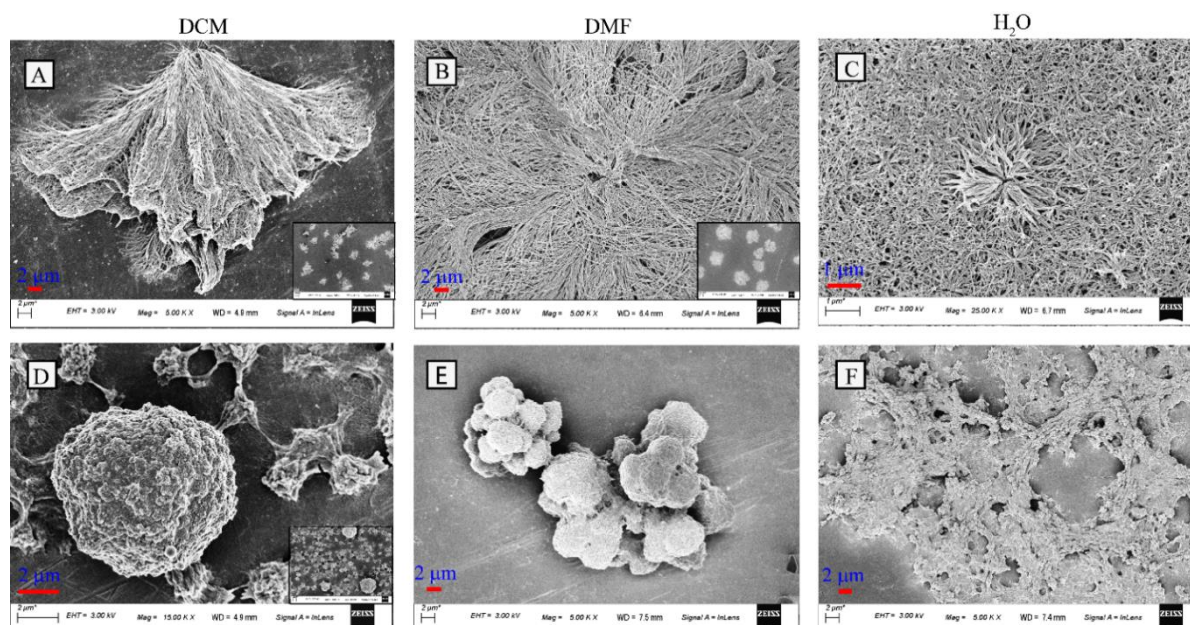


Figure 4.5 FESEM images of the **4** (A-C) and **5** (D-F) by varying the solvent.

behaviour.

4.6 Interactions with nitro-aromatics

The compound **4** and **5** were next applied for studying the interaction with nitro aromatics, specially nitro phenols such as 2-nitrophenol, 3-nitrophenol, 4-nitrophenol, 2,4-dinitrophenol and picric acid (PA) in the aqueous medium. Being electron deficient molecule, nitro-phenols are likely to quench the emission via PET and consequent non-radiative electron decay processes. Among the nitro-phenols, PA being most electron-deficient,^{4.27-4.29} can interact effectively with an electron-rich fluorophore and subsequently affect the emission properties. Herein we have investigated the interaction of the electron-rich **4** and **5** in the presence of the electron-deficient nitro-phenols. Among the various tested nitro-phenols, PA showed the highest quenching in the fluorescence intensity of **4** and **5** at 370 nm (Figure 4.6A). However, the addition of other nitro-phenols results in noticeable spectral changes but less than PA under similar conditions. The quenching of **4** and **5** upon addition of PA and other nitro-phenols could be attributed to the hydrogen bonding between the phenolic –OH group of PA and the urea unit of compounds. Further, the overlapping of the absorption spectrum of PA with the emission spectrum of **4** and **5** (Figure A4.7) proposes that the energy transfer process may also be involved in the quenching process. The quantitative behaviour of the compound **4** and **5** was also evaluated by adding different concentrations of the PA under the optimized conditions. The fluorescence quenching of **4** and **5** was depended on the concentrations of PA. Upon successive incremental addition of PA, the fluorescence spectrum of two compounds showed a gradual decrease at 370 nm, along with a

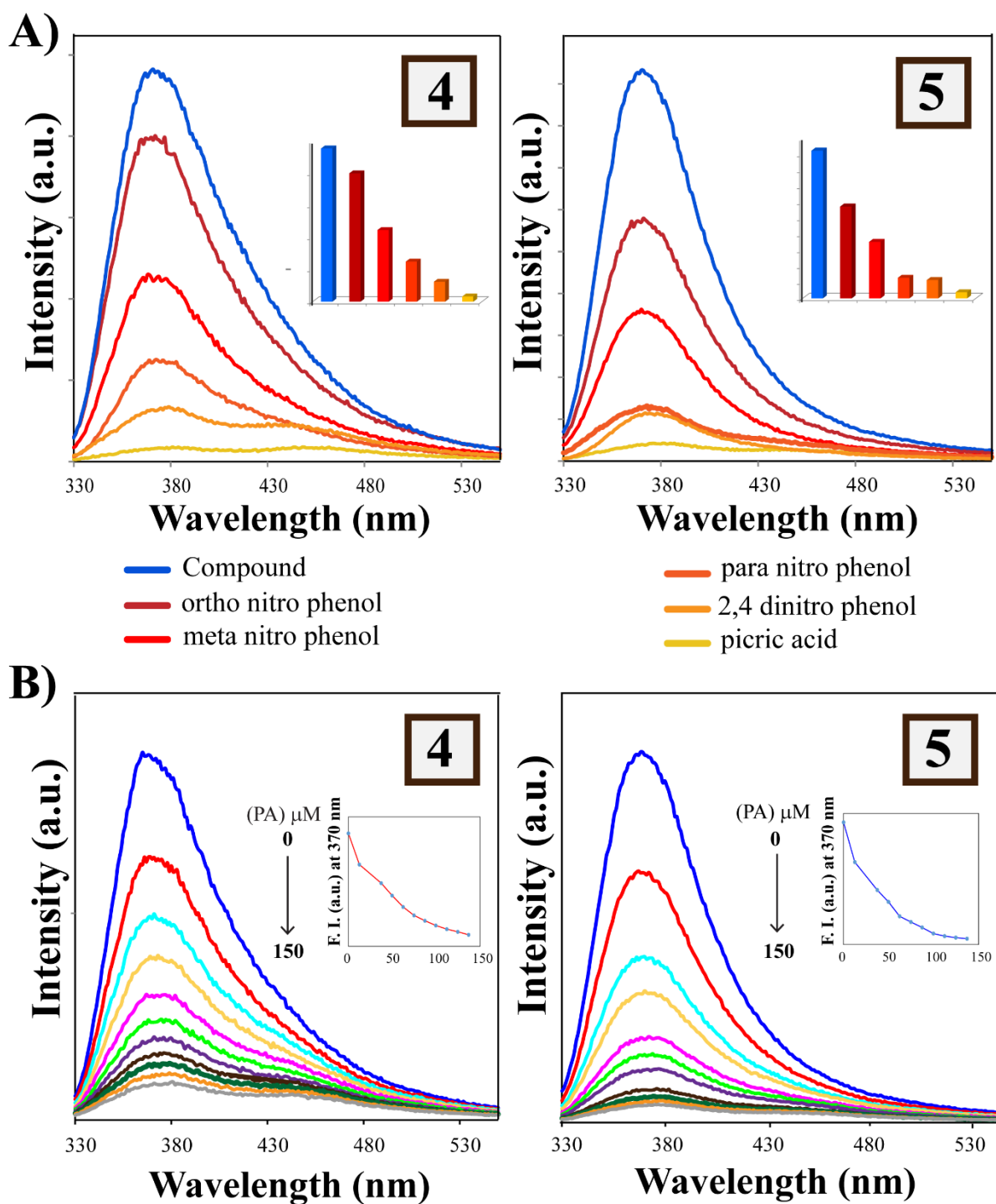


Figure 4.6 A) Fluorescence spectral change of **4** and **5** at 370 nm upon interaction with various nitrophenols; INSET: bar graph representations; B) Fluorescence spectra of **4** and **5** (50 μM) in the presence of a varying concentration of PA (12.5 μM); INSET: changes in fluorescence intensity at 370 nm with PA concentration.

slight red shift (Figure 4.6B). Thus, the molecular aggregation was completely disturbed by the introduction of PA and as a net result fluorescence quenched.

This disaggregation process was also supported by DLS experiment of **4** and **5** in absence and presence of PA in aqueous medium (Figure 4.7A). The average Particle size decreased for both the cases due to the addition of PA which breaks the molecular aggregation to the smaller particles

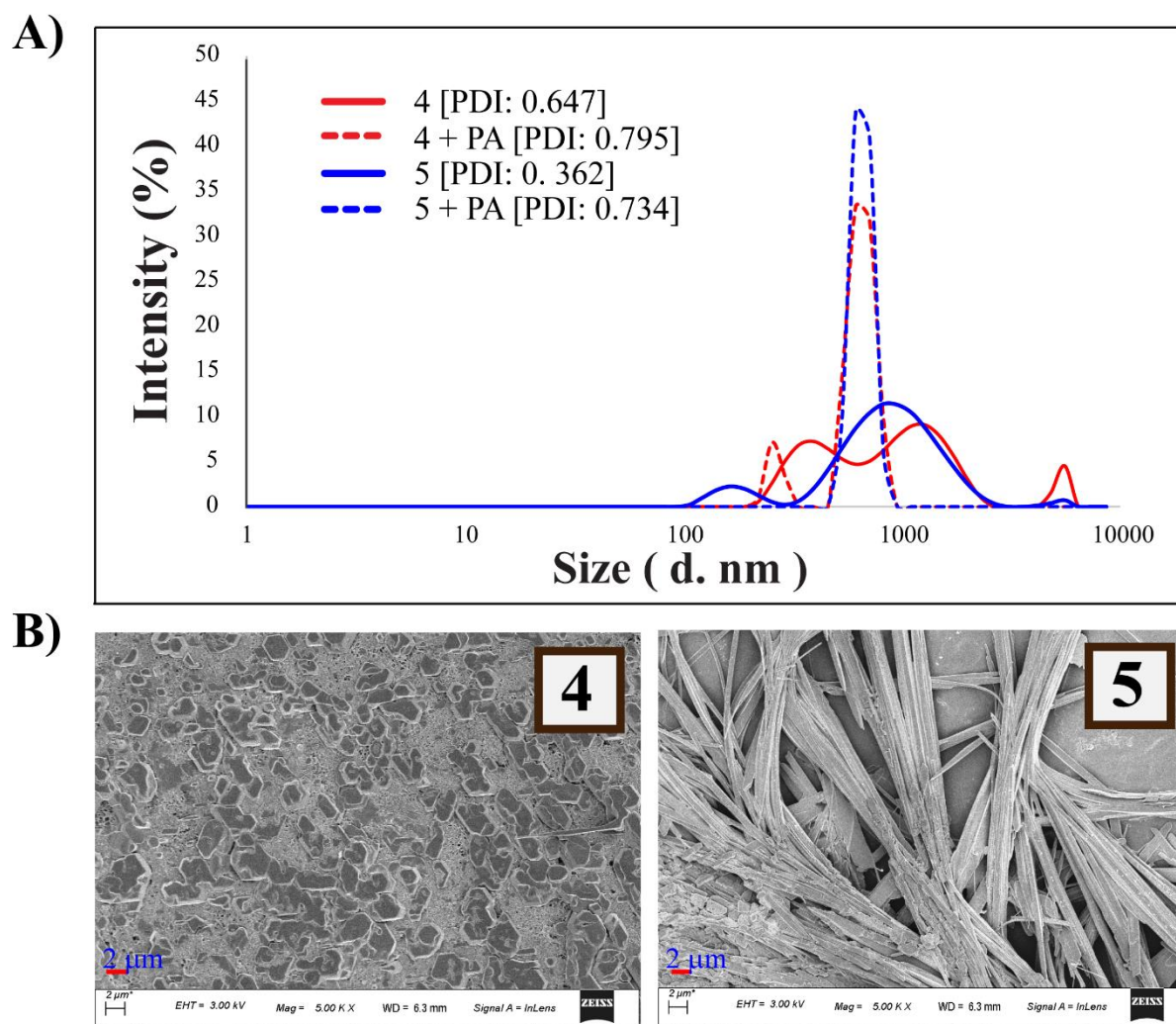


Figure 4.7 A) DLS-based particle size analysis of **4** and **5** in absence and presence of PA. B) FESEM images of **4** and **5** after the addition of PA in the aqueous medium.

and thus the DLS results are in good agreement. FESEM images of **4** and **5** in the presence of PA are also corroborating the interaction study. The morphology got fully reformed (tiles like structure for **4** and needle-like structure for **5** in both the cases after the addition of PA in an aqueous medium (Figure 4.7B), which confirmed the substantial morphological modification in their aggregated structure due to the interaction with electron-deficient molecules.

4.7 Conclusion

In summary, we have methodically studied the consequences of positional isomerism on the aggregation properties of another set of three naphthyl bis-urea derivatives with the help of spectral studies along with microscope imaging. We also developed a solvent dependent approach by changing the solvent system to investigate the effect of core-substitution on their aggregation behavior. And based on the outcomes of this comparative analysis, it can be concluded that the solvent nature can control their aggregation pattern, and the morphology can also be tuned by

altering the solvent system as confirmed from the FESEM images. Thus the entire results are in reasonable settlement to support the aggregation property of the compounds while compound **6** appeared to be less pronounced in the development of aggregates compared to the other two in the mixed solvent system as well as in aqueous medium. Moreover, we checked the interaction with the electron-deficient nitro-phenols for the aggregated form of the compound **4** and **5** in the aqueous medium to investigate the self-aggregation tactic of small molecules in depth. Hence, this work contributes a rationale between the molecular framework and their photophysical properties and deals with a substantial prospect for monitoring the consequence of solvent-tunable aggregation behavior of positional isomers. This effort can be applied in the manufacturing of several functional assemblies by taking account of the interaction with the solvents with different application potential in various fields.

References

- 4.1 J. Han, Y. Li, J. Yuan, Z. Li, R. Zhao, T. Han and T. Han, *Sens. Actuators B Chem.*, 2018, **258**, 373-380.
- 4.2 Y. Hou, J. Du, J. Hou, P. Shi, T. Han and Y. Duan, *J. Lumin.*, 2018, **204**, 221-229.
- 4.3 A.C.B. Rodrigues, J. Pina and J.S.S de Melo, *J. Mol. Liq.*, 2020, **317**, 113966.
- 4.4 T.L. Greaves, A. Weerawardena, C.J. Drummond, *Phys. Chem. Chem. Phys.*, 2011, **13**, 9180-9186.
- 4.5 T. Han, W. Wei, J. Yuan, Y. Duan, Y. Li, L. Hu and Y. Dong, *Talanta*, 2016, **150**, 104-112.
- 4.6 J. Wang, K. Liu, L. Yan, A. Wang, S. Bai and X. Yan, *ACS Nano*, 2016, **10**, 2138-2143.
- 4.7 T.N. Gao, T. Wang, W. Wu, Y. Liu, Q. Huo, Z.A. Qiao and S. Dai, *Adv. Mater.*, 2019, **31**, 1806254.
- 4.8 J. Huang, Y. Chen, P. Zhao, Y. Yu, S. Zhang and Z. Gu, *Regen. Biomater.* 2018, **5**, 275-282.
- 4.9 Y. Zhang, P. Xing, M. Yang, Y. Wang, B. Wang, A. Hao and M. Ma, *RSC Adv.* 2016, **6**, 71963- 71969.
- 4.10 L.L. Zhang, K.C. Liang, L.C. Dong, P.P. Yang, Y.Y. Li, X. Feng, J.G. Zhi, J.B. Shi, B. Tong and Y.P. Dong, *New J. Chem.*, 2017, **41**, 8877-8884.
- 4.11 L.F. Peng, Y.N. Chen, Y.Q. Dong, C.C. He and H.L. Wang, *J. Mater. Chem. C*, 2017, **5**, 557-565.
- 4.12 J. Wang, J. Mei, R.R. Hu, J.Z. Sun, A.J. Qin and B.Z. Tang, *J. Am. Chem. Soc.*, 2012, **134**, 9956-9966.
- 4.13 B. Nayak, U. Manna, G. Das, *ChemistrySelect*, 2018, **1**, 1-8.
- 4.14 M.S. Meaney and V.L. McGuffin, *Anal. Chim. Acta*, 2008, **610**, 57-67.
- 4.15 L. Bu, M. Sun, D. Zhang, W. Liu, Y. Wang, M. Zheng, S. Xue and W. Yang, *J. Mater. Chem. C*, 2013, **1**, 2028-2035.
- 4.16 F. Zhao, Z. Chen, C. Fan, G. Liu and S. Pu, *Dyes Pigm.*, 2019, **164**, 390-397.
- 4.17 Y. Hu, S. Xu, K. Miao, X. Miao and W. Deng, *Phys. Chem. Chem. Phys.*, 2018, **20**, 17367-17379.
- 4.18 V.D. Singh, R.S. Singh, R.P. Paitandi, B.K. Dwivedi, B. Maiti and D.S. Pandey, *J. Phys. Chem. C*, 2018, **122**, 5178-5187.
- 4.19 S. Wang and G.C. Bazan, *Chem. Commun.*, 2004, 2508-2509.
- 4.20 L. Wisniewski, I. Deperasinska, B. Zurowska and A. Szemik-Hojniak, *J. Photochem. Photobiol. A: Chem.*, 2011, **224**, 62-67.
- 4.21 A. Nandi, R. Ghosh and D.K. Palit, *J. Photochem. Photobiol. A*, 2016, **321**, 171-179.

- 4.22 M. Seo, J. Park, S.Y. Kim, *Org. Biomol. Chem.*, 2012, **10**, 5332-5342.
- 4.23 D. Wang, S.M. Li, Y.F. Li, X.J. Zheng and L.P. Jin, *Dalton Trans.*, 2016, 45, 8316-8319.
- 4.24 J. Hou, J. Du, Y. Hou, P. Shi, Y. Liu, Y. Duan and T. Han, *Spectrochim. Acta A*, 2018, **205**, 1-11.
- 4.25 G. Kastias, C.A. Kastias, B.K. Kirca and C.C. Ersanli, *J. Mol. Struct.*, 2020, **1200**, 127109.
- 4.26 D. Thiagarajan, S. Goswami, C. Kar, G. Das and A. Ramesh, *Chem. Commun.*, 2014, **50**, 7434-7436.
- 4.27 V. Bertolasi, P. Gilli and G. Gilli, *Cryst. Growth Des.*, 2011, **11**, 2724-2735.
- 4.28 M.K. Tiwari and S. Saha, *Spectrochim. Acta A*, 2021, **245**, 118930.
- 4.29 T. Rasheed, F. Nabeel, S. Shafi, M. Bilal and K. Rizwan, *J. Mol. Liq.*, 2019, **296**, 11196.

Appendix-Chapter 4

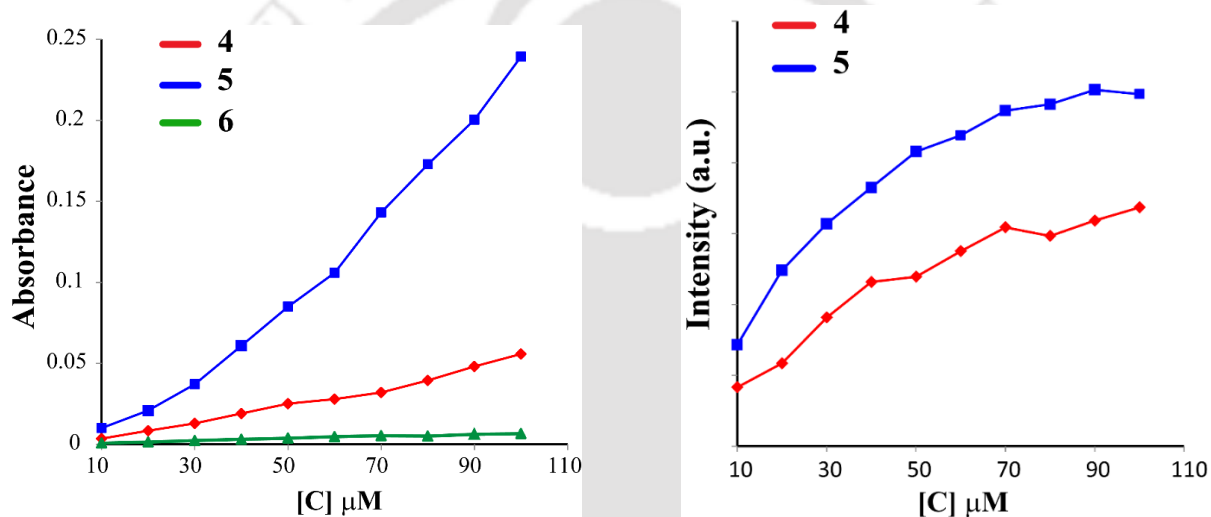


Figure A4.1 A) Change in absorbance value as a function of concentration of **4**, **5** and **6** in aqueous medium. B) Change in Fluorescence intensity at 370 nm of **4** and **5** as a function of concentration in aqueous medium.

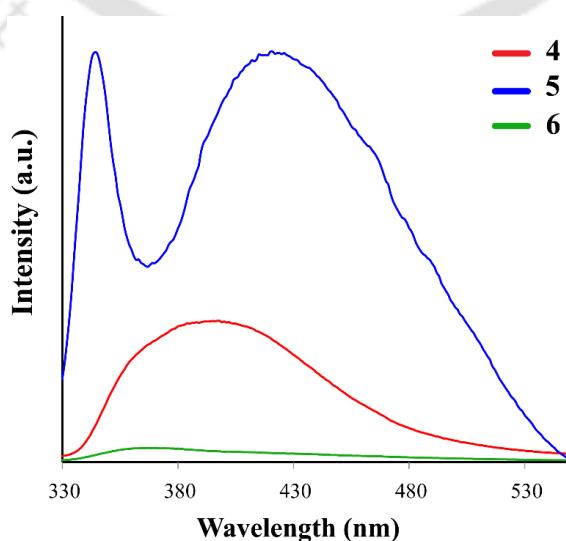


Figure A4.2 Solid state fluorescence spectra of **4**, **5** and **6**.

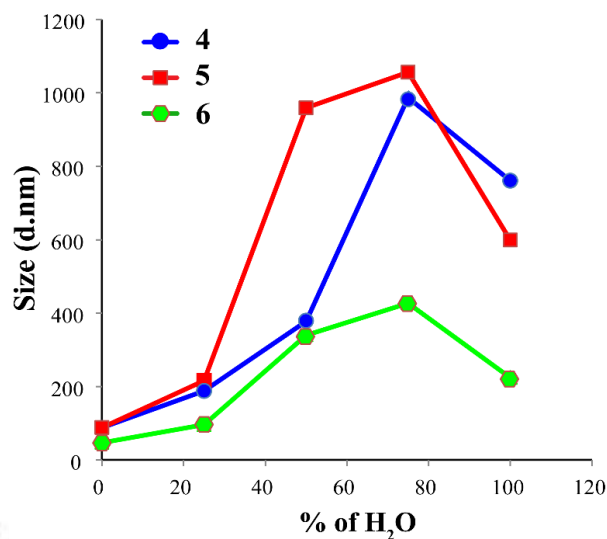


Figure A4.3 DLS-based particle size analysis of **4**, **5** and **6** as the function of water fractions in mixed solvent system.

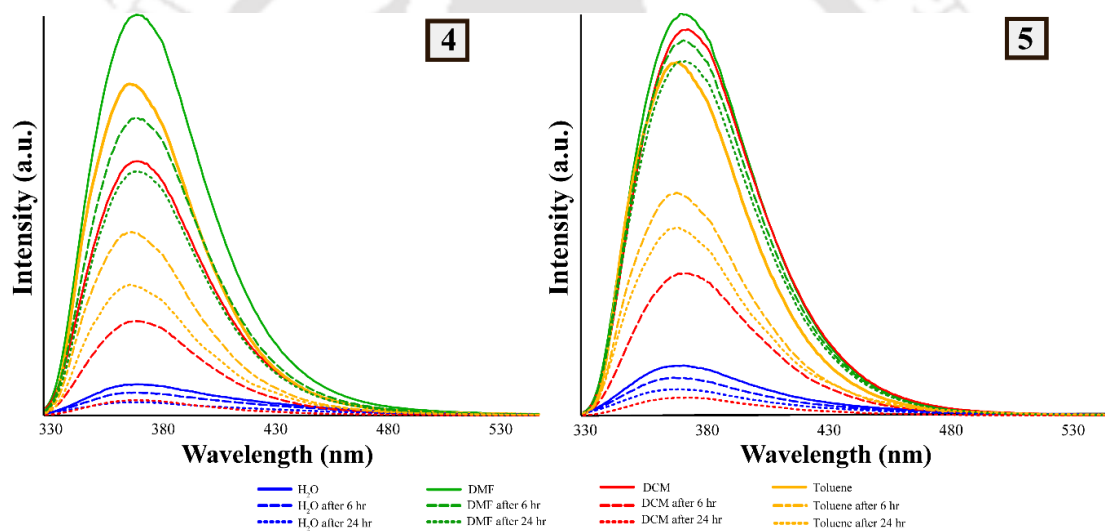


Figure A4.4 Changes in the emission spectra of **4** and **5** at a fixed concentration of the compound with respect to time in various solvents.

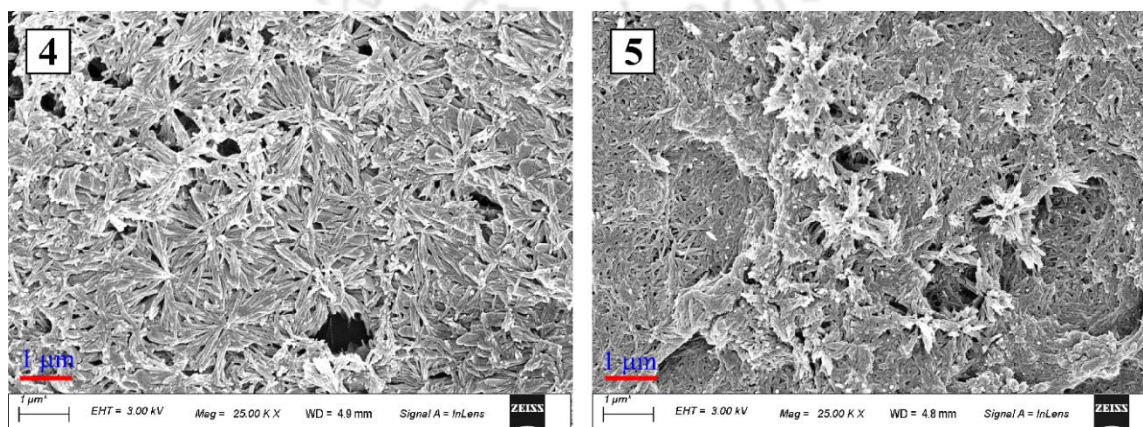


Figure A4.5 FESEM images of the **4** and **5** after 24 h in aqueous medium.

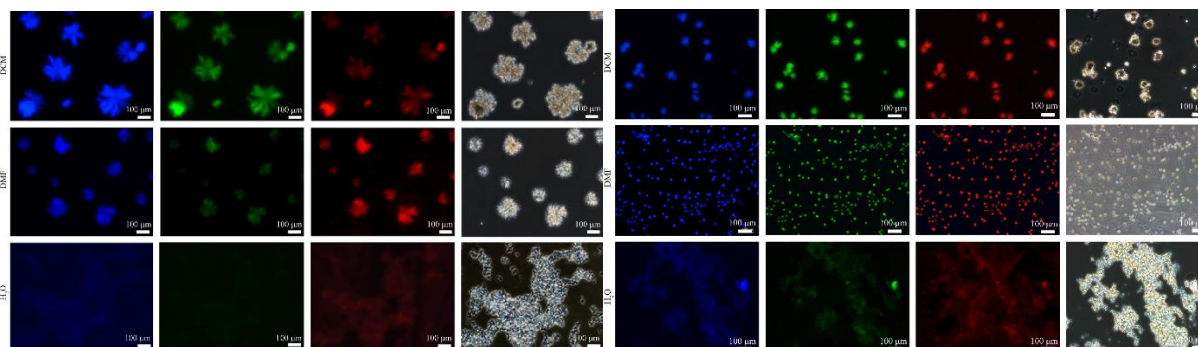


Figure A4.6 Fluorescence microscope images of **4** (left) and **5** (right) at different excitation range in a different solvent.

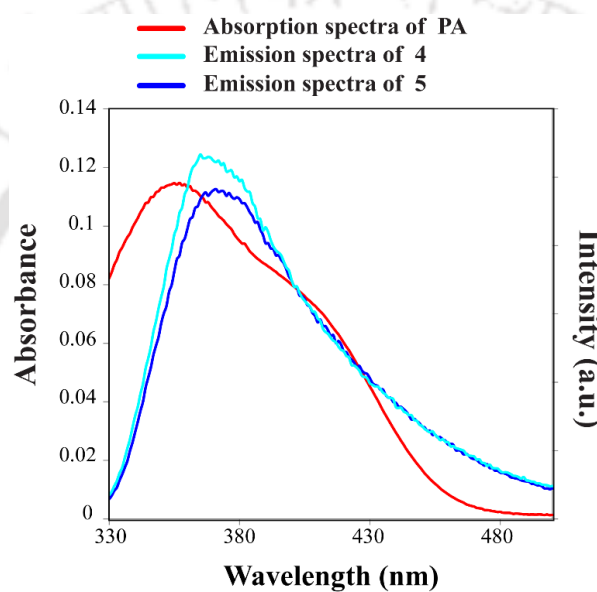


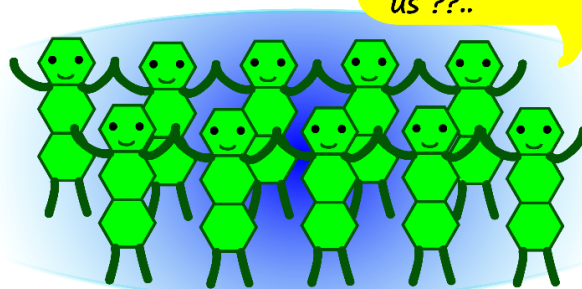
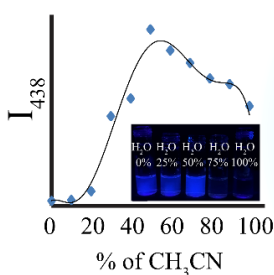
Figure A4.7 Spectral overlap of absorption spectra of PA and emission spectra of **4** and **5**.

CHAPTER 5

Exploring the Aggregation Potential of two Urea based-Luminogens by Varying the Fluorophore Unit: AIE Activity and Interaction with Human Serum Albumin

Aggregation-Induced Emission

Strongly Emissive



Aggregated- **7**

Hey, can you exhibit AIE like us ??..



8

It seems difficult for me...

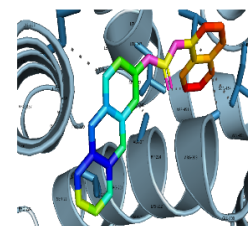
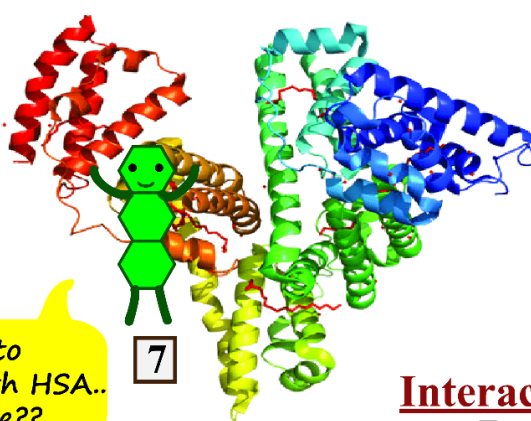
Sorry.. Not interested..



8

I am going to interact with HSA.. Wanna come??

7



Interaction with HSA

Turn-On Response

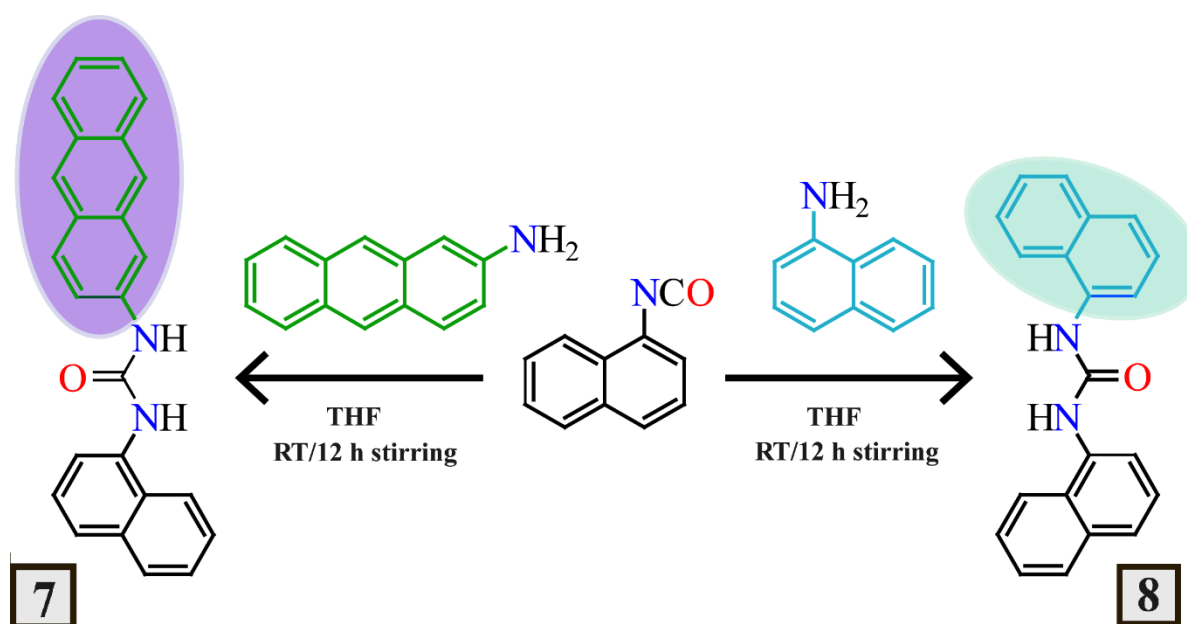
Chapter 5

5.1 Objective of the Chapter

The interaction of proteins with a broad variety of ligands and drugs continues to be of prime importance owing to their extensive and useful applications in industrial, biological, medical and cosmetic domains.^{5.1-5.5}. Thus, the development of efficient biosensors to selectively detect proteins with high sensitivity and good binding linearity remains a task of imminent prominence.^{5.6} Of these, selective detection of Human Serum Albumin (HSA), a major and versatile protein in the human body, deserves special mention. Its role in controlling plasma colloid osmotic pressure and performance as a physiological carrier for various endogenous and exogenous substances in the circulatory system in the human body underlines its marked significance in the execution of normal bodily functions.^{5.7-5.10} HSA is a polypeptide chain containing three α -helical domains (I–III), which are further divided into two subdomains (A and B).^{5.11} According to its crystal structure, the hydrophobic cavities located in subdomains IIA and IIIA are the main ligand-binding sites in the albumin.^{5.12} The use of HSA as a model protein in studying the various types of hydrophobic, hydrophilic and electrostatic interactions within the protein environment in the presence or absence of small molecules emerged as an active field of biochemical research. Of the variety of available biosensors for HSA, the ones based on AIE active small molecular system have drawn considerable attention.^{5.13-5.15} So, in this chapter we tried to recognize the the role of planar fluorophores with different sizes and π -electron clouds in the aggregation aptitude of the small AIE active molecules and subsequent interaction with HSA.

5.2 Outline of the Chapter

A urea derivative **7** exhibits Aggregation-Induced Emission (AIE) activity in acetonitrile-water mixed solvent. The aggregation phenomenon has been corroborated by microscopy and light scattering studies. It is worth mentioning that merely increasing the water content of the solvent mixture resulted in an exhibition of the much desired AIE characteristic of the fluorophore probe without the need for application of any external stimuli or analyte. **7** can also display a selective turn-on fluorescence response towards human serum albumin (HSA) over various other comparable proteins/enzymes and distinctly distinguish HSA from Bovine Serum Albumin (BSA) through individual fluorescence responses in 100% aqueous medium. Weakly emissive probe **7** showed a substantial increase in emission intensity upon binding with HSA through electrostatic interactions. The good linear relationship between the fluorescence enhancement ($I/I_0 - 1$) and the concentration of HSA provided the scope to attain an impressive detection limit as low as 5 μg



Scheme 5.1 Synthesis of Ligand **7** and **8**.

mL^{-1} . A drug displacement experiment and molecular docking study were employed to ascertain the likely protein (HSA)–ligand binding interactions. **7** also holds good practical utility by responding to HSA in bio-fluidic samples as well as in artificial urine. In addition, a previously reported probe **8** was also synthesized^{5,16,5.17} and studied to further understand the principles underlying the AIE behavior of **7**.

5.3 Design rationale of **7** and **8**

The ligand was judiciously designed taking into consideration several important factors. As depicted in Scheme 5.1, the designed probe **7** contains two different potential fluorophore units (anthracene and naphthalene) which are connected through a urea linkage. A previously reported probe **8** was also synthesized as a control compound, wherein the same fluorophore units (naphthalene) are connected through the urea linkage, unlike the probe **7**. This comparative design was followed to realize the role of planar fluorophores with different sizes and π -electron clouds in the aggregation aptitude of the fluorescent probes. In both the probes, the simultaneous presence of the H-bond donor and the acceptor in the urea subunit is deemed to be capable of aligning in a π – π stacking arrangement. Additionally, the urea subunit works as a suitable binding site for a variety of analytes encompassing different domains.

5.4 AIE activity of **7** and **8**

The photophysical properties of **7** and **8** were studied by UV-Vis absorption and fluorescence

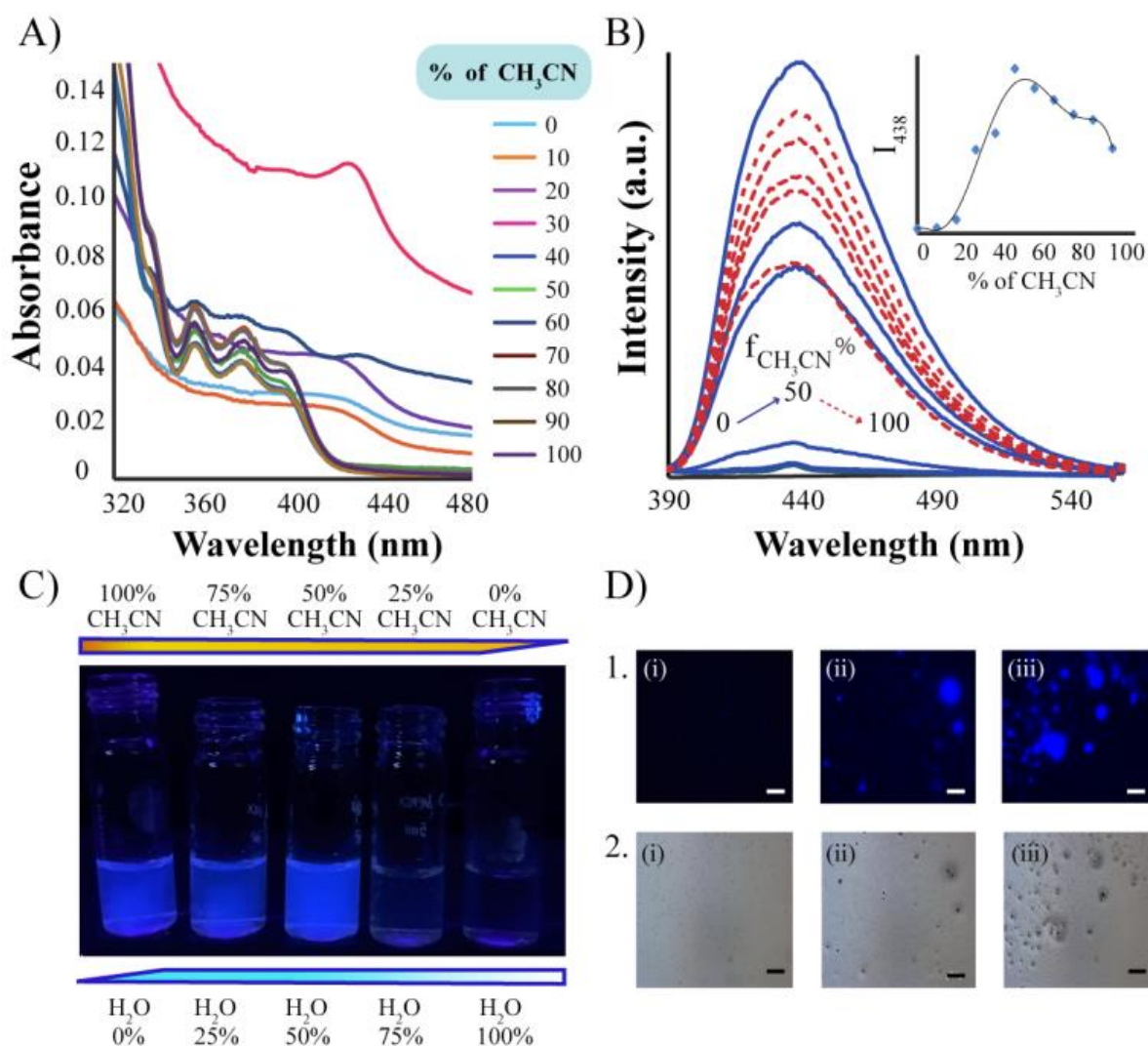


Figure 5.1 (A) UV-Vis spectra of **7** in the mixed solvent system by varying solvent fraction; (B) fluorescence spectra of **7** in the mixed solvent system by varying solvent fraction ($\lambda_{\text{ex}} = 380 \text{ nm}$); inset: fluorescence intensity at 438 nm as a function of acetonitrile fractions; (C) visual changes in fluorescence of **7** in the mixed solvent system under UV light; (D) fluorescence microscopy images of **7** in the mixed solvent system with water fractions (i) 0% (ii) 25% (iii) 50%.

emission studies in acetonitrile-water solvent systems. The UV-Vis spectra of **7** (10 μM) revealed a well-defined typical anthracene absorbance band in 100% acetonitrile medium in the wavelength region of 350–400 nm but broadened in 100% aqueous medium whereas **8** gave the absorption maximum at 305 nm in both acetonitrile and aqueous media (Figure A5.1). The change in the absorption spectra of **7** in the mixed solvent system is depicted in Figure 5.1A. The absorption spectra remained virtually unchanged when a low water fraction was added to the acetonitrile solution. But in a relatively high water fraction ($>50\%$), the absorption spectrum of **7** changed significantly. A simultaneous bathochromic shift in the absorbance maxima, accompanied by the obvious increase in the baseline in the tail of UV-Vis spectra of **7**, was observed upon increasing the water fraction. This clearly indicated the possible aggregation of the probe with decreasing

solubility. However, under similar experimental conditions, no such prominent changes were observed in the absorption spectra of **8** (Figure A5.2A). Hence, subsequent fluorescence studies were pursued to understand the aggregation behavior of **7**. The fluorescence behavior of **7** was studied in pure/mixed solvent systems. **7** reveals a reasonable fluorescence intensity in 100% acetonitrile medium. Interestingly, in a mixed aqueous solvent ($\text{CH}_3\text{CN}/\text{H}_2\text{O}$) system the fluorescence intensity of **7** altered significantly upon changing the water fractions. To investigate this in detail, the emission intensity of **7** was recorded with increasing water fraction in the mixed ($\text{CH}_3\text{CN}/\text{H}_2\text{O}$) solvent system (Figure 5.1B). The continuous addition of water to the solution of **7** in acetonitrile by maintaining the ligand concentration constant at $2 \mu\text{M}$ resulted in the simultaneous increase in the emission intensity at $\sim 438 \text{ nm}$ until it reached the maximum at the 50% acetonitrile content. So, the probe emitted much brighter fluorescence in the 1:1 ($\text{CH}_3\text{CN}/\text{H}_2\text{O}$) mixed solvent compared to that in pure acetonitrile. The subsequent further increment of the water fraction exhibited a top-to-bottom trend in the emission intensity change (Figure 5.1B, inset) and finally, in 100% aqueous medium, the emission intensity of **7** becomes very weak. Thus the change in the solvent fraction can greatly affect the emission behavior of **7** and the visual changes were also noticeable (Figure 5.1C). The fluorescence microscopy images

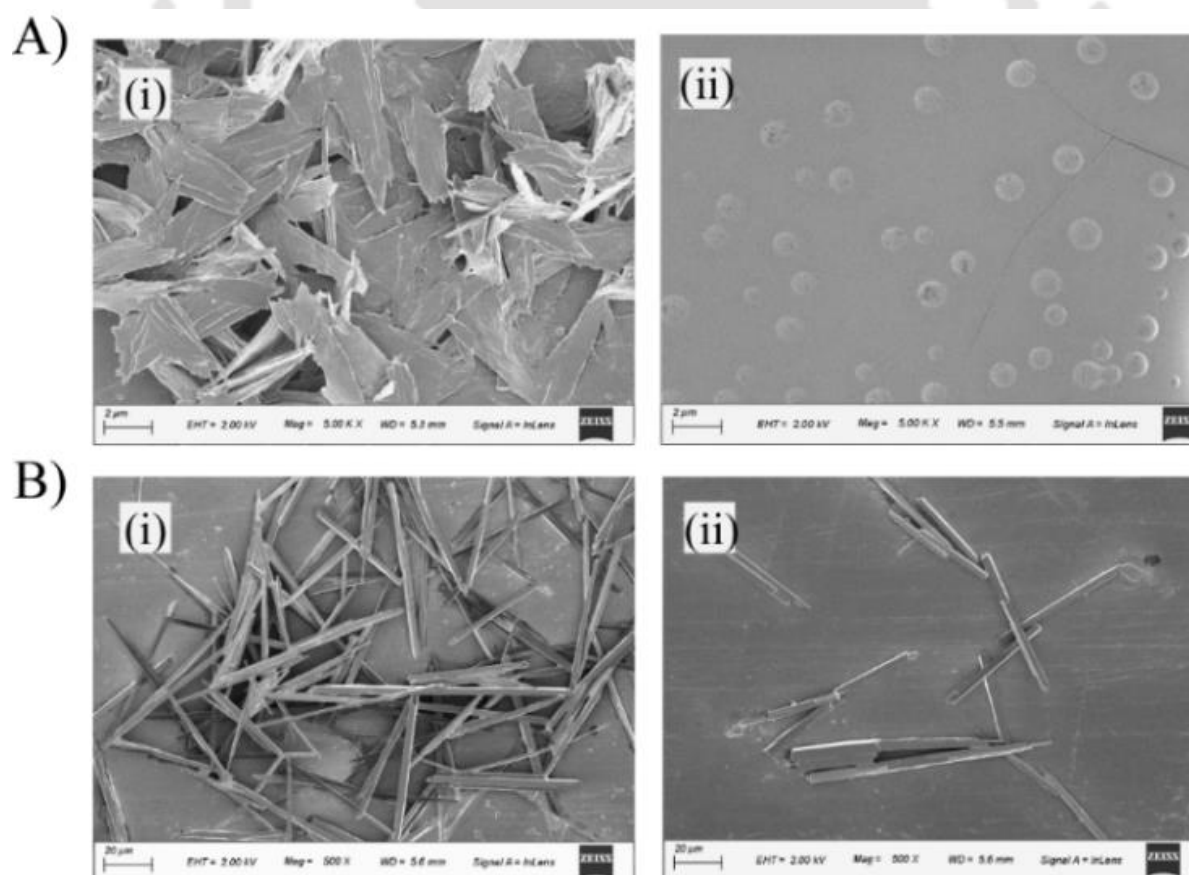


Figure 5.2 FESEM images of (A) **7** in (i) 50% $\text{CH}_3\text{CN}-\text{H}_2\text{O}$ and (ii) 100% H_2O [scale bar = 2 μm] and (B) **8** in (i) 50% $\text{CH}_3\text{CN}-\text{H}_2\text{O}$ and (ii) 100% H_2O [scale bar = 20 μm].

also suggested that almost non-fluorescent **7** can display a strong blue fluorescence upon increasing the water fraction in the mixed solvent system (Figure 5.1D). Hence, the probe has probable aggregation induced emission properties which resulted in the aggregation triggered enhancement in fluorescence by restricted intramolecular rotational motions of the molecule. However, similar studies with **8** displayed a negligible change in the emission intensity with changing water fraction (Figure A5.2B).

Interestingly, there was a significant change in the morphology of the aggregative species of **7** and **8** by varying the solvent fraction and the difference in morphology can be well depicted by FESEM (Figure 5.2). FESEM images of **7** in 50% acetonitrile reveal the formation of flake type aggregates, which become spherical in 0% acetonitrile or 100% water whereas the micro-rod kind of structure for **8** remained thinly distributed in 100% aqueous medium. In addition, DLS studies (Figure 5.3A)

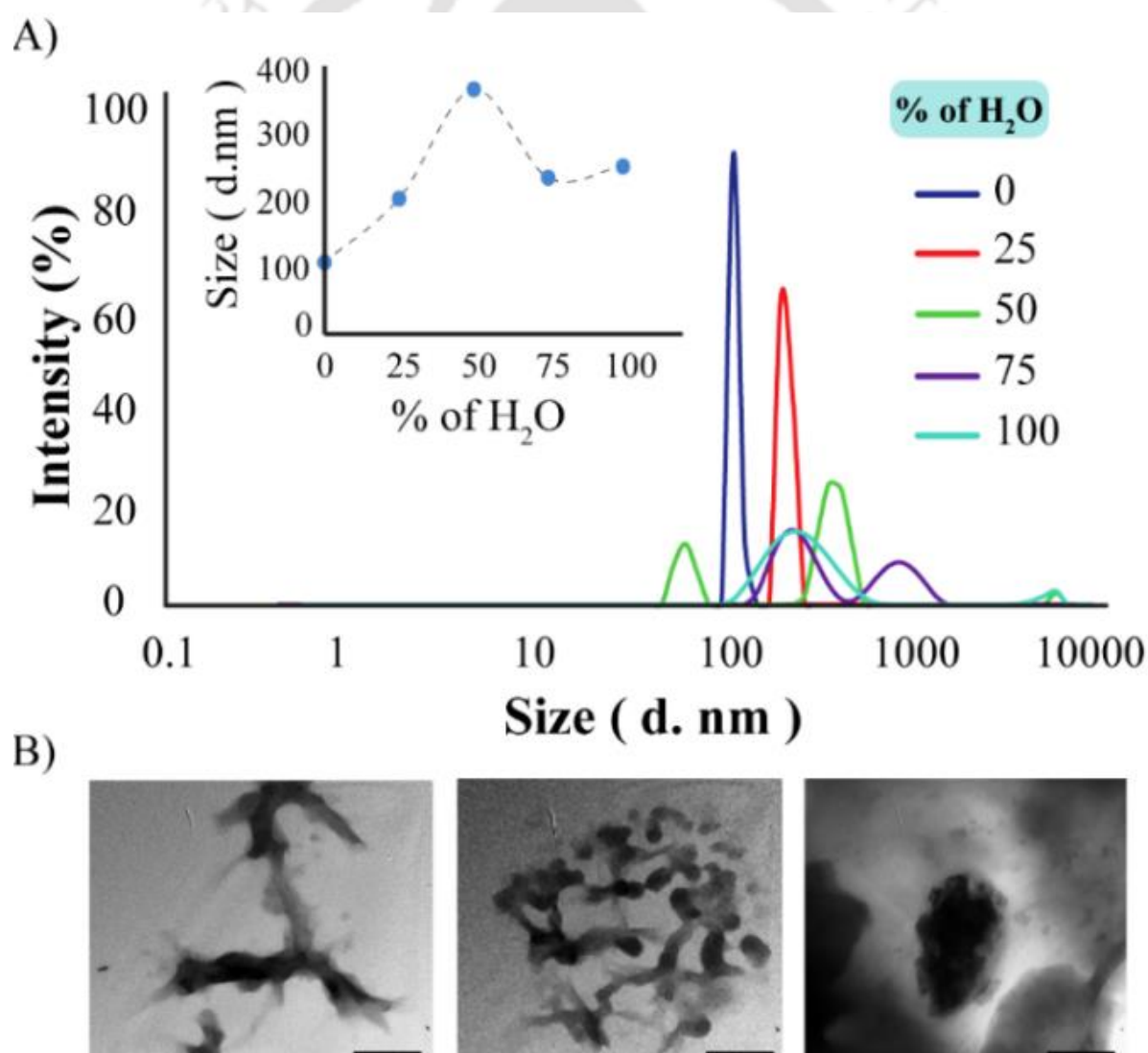


Figure 5.3 (A) DLS-based particle size analysis of **7** in the mixed solvent system by varying solvent fractions; inset: particle size of **7**-aggregates as a function of water fractions; (B) TEM images of the **7**-aggregates in the 1 : 1 mixed solvent system (scale bar = 0.2 μm).

of **7** in a mixed solvent system suggested that the average particle size increased to 358 nm from 102 nm with the increasing water content of the medium up to 50%. These results strongly suggest the formation of aggregates by **7** in the presence of water in acetonitrile. For further evidence of aggregate formation, TEM experiments were also pursued (Figure 5.3B), which also supported the aggregation behavior of **7**. To gain a close insight into the structure of **7**, DFT studies (Figure A5.3) and corresponding HOMO-LUMO energy calculations (Figure A5.4) were performed following the B3LYP/6-31G basis set. A close look at the DFT simulated structure thus obtained suggested the possibility of the molecule to exist in aggregated patterns. UV-Vis spectra of **7** were also calculated using the TDDFT method (no specific solvent model was used) with the same RB3LYP/6-31G basis set. The calculated absorption peak (392 nm) of **7** was found to match impressively with the experimentally observed peak (395 nm).

5.5 Interaction study of **7** with HSA

The UV-Vis spectra of **7** (2 μ M) in aqueous medium exhibited a broad absorbance peak around 350–400 nm. It was interesting to note that among the various tested proteins and bioanalytes only the addition of an excess amount of HSA to this solution resulted in a slightly red-shifted absorbance maximum along with the enhancement in absorbance value (Figure A5.5). This result prompted us to study the detailed sensing performance of the probe **7** towards various biomacromolecules. The selectivity experiment of **7** was performed in 100% aqueous medium using common ions and various bio-macromolecules including DNA, DNase, cysteine, pepsin, trypsin, lysozyme, HSA and BSA. But none of these bioanalytes exhibited significant changes in fluorescence behaviour except for HSA and BSA (Figure 5.4A). Upon interaction with HSA, the emission intensity of **7** at 438 nm showed about 50% more enhancement than with BSA. Furthermore, we checked the interference of various other proteins like BSA, β -lactoglobulin, ovalbumin, pepsin, trypsin, pancreatin, cysteine, DNase and lysozyme in the HSA sensing aptitude of **7**, which clearly asserted the strong selectivity of **7** towards HSA even in the presence of the mentioned biomolecules (Figure A5.6). It should be noted that all the interaction studies with different bio-analytes are preferred in 100% aqueous medium over other media as confirmed by the comparative solvent dependent study of the fluorescence responses (Figure A5.7). Interestingly, **8** shows no fluorescence spectral change when interacting with HSA/BSA (Figure A5.8), which ensures the specific selectivity of the probe **7** towards HSA/BSA.

Moreover, to determine the possible influence of the interaction process on the secondary structure of the proteins, CD measurements were performed. The vivid change in the characteristic peaks of HSA (208 and 222 nm) in the CD spectra in the presence of **7** (Figure 5.4B) suggests that there

was an obvious variation in the local physiological environment of HSA. Hence, the addition of **7** to the HSA solution in 100% aqueous medium induced some conformational changes in the protein structure but the secondary structure of HSA remains predominantly α -helix. This selective turn-on fluorescence response of **7** towards HSA was also verified by fluorescence microscopy imaging studies (Figure A5.9). A prominent blue fluorescence could be detected upon addition of HSA to the weakly emissive **7** using fluorescence microscopy. Aqueous solutions of HSA+**7** were also examined under TEM and the morphology is completely different from that of the aggregated-**7** species (Figure A5.10). Thus the TEM images are in good support for the interaction of **7** with HSA and cancelled out the probability of AIE response towards HSA. The DLS experiment also reaffirmed about the interaction between **7** and HSA. From the DLS data it is clear that the overall particle size of **7** i.e. $Z_{\text{average}} = 235$ nm decreased to $Z_{\text{average}} = 158$ nm upon interaction with HSA in an aqueous medium (Figure A5.11). The observation may suggest that

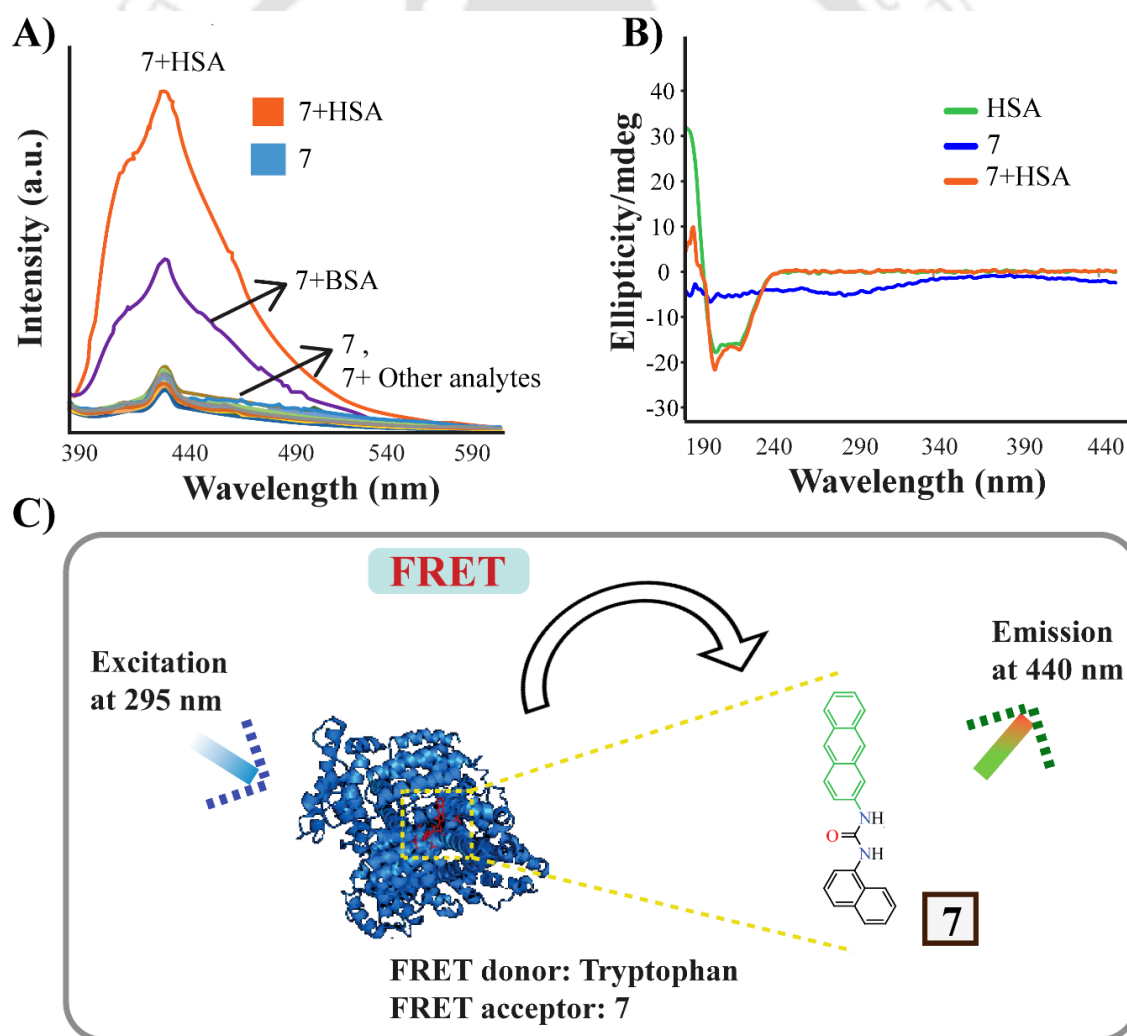


Figure 5.4 (A) Fluorescence spectra of **7** ($2 \mu\text{M}$) in 100% aqueous solution in the presence of an excess (10 equivalents) of various proteins and bio-analytes; (B) CD spectra of HSA ($15 \mu\text{g mL}^{-1}$) in the presence or absence of **7** ($0.02 \mu\text{M}$). (C) Plausible FRET mechanism between **7** and HSA.

HSA detection by **7** is not an outcome of the AIE phenomenon. The intrinsic fluorescence of HSA is mainly due to the tryptophan residue in domain II of HSA (Trp-214). As the absorption spectrum of **7** partially overlaps with the emission spectrum of HSA (Figure A5.12A), we investigated the FRET process between the tryptophan residue of HSA and the bound **7**.^{18,19} Upon irradiation at 295 nm, tryptophan emission maxima at 350 nm were obtained, which were found to be enhanced further upon addition of **7** in an aqueous medium and a new strong emissive peak at ~440 nm appears (Figure A5.12B). As there was no observable absorption at 295 nm for **7**, it is obvious that the appearance of the new emission maxima of **7** as explained above can only be responsible due to FRET from tryptophan to the bound **7** (Figure 5.4C). The FRET results corroborate that the probe binding site is very near to the tryptophan in the subdomain IIA of the protein HSA. REES, the shifting of the emission maxima of the ligand to the red side upon red-shifting the excitation wavelength of fluorescence, can be used as a tool for monitoring motions around the Trp residues in protein studies.^{5,20,5,21} In the present investigation, we chose to excite the Trp at both 295 and 310 nm to observe the REES effect (Figure A5.13). The value of $\Delta\lambda_{\max}$ is defined as the difference in the emission maximum obtained for the excitation wavelength at 295 nm and 310 nm, respectively. As shown in Table A5.1 in the presence of **7**, the REES value of HSA increased to 5 nm and it increases more with the further addition of HSA to **7**, indicating that **7** had an obvious impact on the mobility of the Trp microenvironment with the motional restriction. Hence, the present sensing platform constitutes unique features like the involvement of FRET and REES processes which introduce advanced analytical aspects to the sensing system compared to the other similar methods. In order to investigate the excited state behavior of **7**, we have performed time-resolved fluorescence measurements of **7** in the absence and presence of HSA in aqueous medium.^{5,22} A satisfactory data fit of four exponential decays with a χ^2 value close to 1.00 was obtained. Nanosecond time-resolved fluorescence analysis (Figure A5.14) showed that **7** alone exhibited a bi-exponential decay with an average lifetime ($\langle\tau\rangle$) of 2.206 ns at an emission wavelength of 435 nm, whereas in the presence of HSA there was a noteworthy increase in the average lifetime ($\langle\tau\rangle$) to 11.749 ns (Table A5.2). This increment in lifetime along with the REES observation advocates the regional rigidity of the probe within the protein interior and turn-on response towards HSA.

To further realize the appropriate binding sites of HSA for **7**, a competitive assay to displace **7** (2 μM) from HSA (150 $\mu\text{g mL}^{-1}$) was conducted with three site-specific drugs including warfarin (a site marker of subdomain IIA), ibuprofen (a site marker of subdomain IIIA), and salicylic acid (a site marker of subdomains IIA & IB).^{5,23,5,24} The displacement experiment clearly demonstrated that only salicylic acid exhibited a concentration dependent displacement of **7** and about 50% of

the ligand was displaced by 1 mM of salicylic acid, while both warfarin and ibuprofen showed almost no significant change in the fluorescence intensity (Figure A5.15). These studies clearly indicate that the fluorescence turn-on response of **7** is due to its specific binding to the domain IIA and IB of HSA. Furthermore, MTT-based cytotoxicity assay was carried out in the HeLa cell line (human cervical-carcinoma cells) to establish the cytotoxic potential of **7**. Interestingly, even at high concentrations of the probe or the probe in the presence of HSA (80 μM), the viability of the cells was as high as above 70% (Figure A5.16) which is another encouraging aspect for the practical efficacy of the probe.

5.6 HSA quantitation

Considering the specific selectivity of the probe for HSA, the following investigation was performed for quantitation of HSA (Figure 5.5). It was exciting to observe that the probe **7** could detect the HSA concentration as low as 5 $\mu\text{g mL}^{-1}$ which is much lower compared to the concentration of HSA in urine and blood serum (Figure A5.17). It might be mentioned here that the probe **7** offers better sensitivity compared to several other recently reported probes for albumin proteins (Table A5.3). The plot of $(I/I_0 - 1)$ as a function of HSA concentration was shown to be a linear curve, which had a wider range and better linearity in the concentration range of 0-0.8 mg mL^{-1} with a linear correlation coefficient $R^2 = 0.987$, where I and I_0 are the fluorescence signals of the probe in the presence and absence of HSA, respectively (Figure 5.5, INSET). The time-dependent fluorescence study

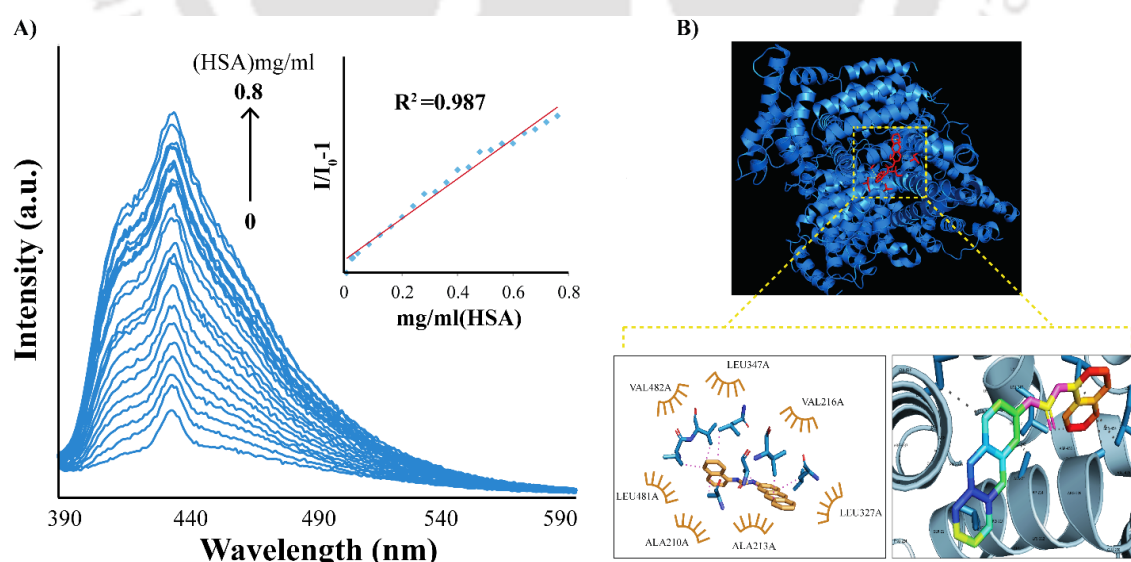


Figure 5.5 (A) Fluorescence spectra of **7** (2 μM) in the presence of varying concentrations of HSA; inset: changes in fluorescence intensity at 438 nm with HSA concentration. (B) Docking conformation of **7**/HSA with the lowest binding free energy.

of **7** with and without HSA was also carried out for monitoring the response time (Figure A5.18). The growth in the fluorescence intensity of **7** upon addition of HSA was observable almost instantaneously and continued until 15 minutes after the addition. Therefore, the AIE active molecule, **7**, can be employed as an efficient real-time sensor for efficient detection and sufficient low limit quantitation of HSA in 100% aqueous medium.

5.7 Binding studies from docking results

Another challenging aspect of bio-analyte detection by a simple molecule is the elucidation of appropriate binding sites of the molecule in the biomolecule moiety. In this respect, a molecular docking study between probe **7** and HSA was conducted using the molecular docking technique.^{5.25,5.26} The best binding structure between the probe **7** and HSA with the lowest binding energy ($-8.81 \text{ kcal mol}^{-1}$) is illustrated in Figure 5.5B. This negative and low binding energy suggests that the binding of the probe to HSA should be a spontaneous and energetically favourable process. It is noticeable that residues ALA210A, ALA213A, LEU327A, LEU347A, LEU481A, VAL216A and VAL482A are stabilized by the hydrophobic parts of the probe **7** via hydrophobic interactions (Figure A5.21). These interactions enhanced the conformational rigidity of **7**, which consequently resulted in **7** being more emissive in the bound form.

5.8 Interaction of **7** with HSA in bio-fluids and artificial urine samples

Another important aspect pertaining to the practical applicability of **7** was its capability to be employed for bio-fluidic samples for HSA detection in real life samples. The broad gauge of sensing for HSA by **7** was very well elucidated by the fact that **7** was able to detect HSA in the artificial body fluid (pH ~ 7.4) and under very low pH conditions (gastric fluid) or high pH conditions (intestinal fluid) (Figure A5.19). Artificial body fluid, gastric fluid and intestinal fluid were supplied by the Department of Biosciences and Bioengineering, IIT Guwahati. To further challenge the feasibility of **7** for HSA detection, artificial urine samples were tested as well. The artificial urine sample was prepared following the literature procedure^{5.27} in our laboratory. It was pleasant to note that **7** proved its efficient clinical utility in analytical prospects by responding to HSA in artificial urine samples as well (Figure A5.20)

5.9 Conclusion

In summary, we have designed and synthesized a simple disubstituted urea probe **7** which is capable of displaying interesting AIE characteristics. In addition, AIE active **7** can produce a significant rapid change in the fluorescence behavior in real time through a

selective turn-on response towards HSA over other proteins and bio-analytes in 100% aqueous medium with a very low detection limit ($5 \mu\text{g mL}^{-1}$). The interaction between HSA and **7** is mainly hydrophobic in nature and has been well supported by various spectroscopic methods and the molecular docking approach. Based on the drug displacement experiment, the detection of HSA by **7** can be attributed to the site-specific binding of **7** to the domain IIA and IB of HSA. A recent literature study stated that molecules possessing higher affinity for serum albumin and binding at site II were found to exhibit efficient photodynamic therapeutic (PDT) applications.^{5,28} In addition, **7** can successfully detect HSA in various bio-fluidic samples and in artificial urine.

References

- 5.1 M.N. Jones, *Chem. Soc. Rev.*, 1992, **21**, 127-136.
- 5.2 N.J. Turro, X.G. Lei, K.P. Ananthapadmanabhan and M. Aronson, *Langmuir*, 1995, **11**, 2525-2533.
- 5.3 D. Kelley and D.J. McClements, *Food Hydrocolloids*, 2003, **17**, 73-86.
- 5.4 T.J. Peters, *All About Albumin Biochemistry, Genetics and Medical Applications*, Academic Press, San Diego, CA, 1996.
- 5.5 J.F. Foster, in *Albumin Structure, Function and Uses*, ed. V.M. Rosenoer, M. Oratz and M.A. Rothschild, Pergamon Press Inc., Oxford, U.K., 1977.
- 5.6 X. Zhang, B. Yao, Q. Hu, Y. Hong, A. Wallace, K. Reynolds, C. Ramsey, A. Maeder, R. Reeda and Y. Tang, *Mater. Chem. Front.*, 2020, **4**, 2548.
- 5.7 T. Peters Jr., *Adv. Protein Chem.*, 1985, **37**, 161-245.
- 5.8 J.R. Simard, P.A. Zunszain, J.A. Hamilton and S. Curry, *J. Mol. Biol.*, 2006, **361**, 336-351.
- 5.9 F.P. Nicoletti, B.D. Howes, M. Fittipaldi, G. Fanali, M. Fasano, P. Ascenzi and G. Smulevich, *J. Am. Chem. Soc.*, 2008, **130**, 11677-11688.
- 5.10 O.K. Abou-Zied and O.I.K. Al-Shihi, *J. Am. Chem. Soc.*, 2008, **130**, 10793-10801.
- 5.11 X.M. He and D.C. Carter, *Nature*, 1992, **358**, 209-215.
- 5.12 G. Sudlow, D.J. Birkett and D.N. Wade, *Mol. Pharmacol.*, 1975, **11**, 824-832.
- 5.13 M.T. Gabr and F.C. Pigge, *Dalton Trans.*, 2017, **46**, 15040-15047.
- 5.14 Y. Hong, C. Feng, Y. Yu, J. Liu, J.W.Y. Lam, K.Q. Luo and B.Z. Tang, *Anal. Chem.*, 2010, **82**, 7035-7043.
- 5.15 Y. Tu, Y. Yu, Z. Zhou, S. Xie, B. Yao, S. Guan, B. Situ, Y. Liu, R. T. Kwok, J. W. Lam and S. Chen, *ACS Appl. Mater. Interfaces*, 2019, **11**, 29619-29629.
- 5.16 A.M.Z. Slawin, J. Lawson, J.M.D. Storey and W.T.A. Harrison, *Acta Crystallogr., Sect. E: Crystallogr. Commun.*, 2007, **63**, o2925-o2927.
- 5.17 S.A. Kadam, K. Martin, K. Haav, L. Toom, C. Mayeux, A. Pung, P.A. Gale, J.R. Hiscock, S.J. Brooks and I.L. Kirby, *Chem. Eur. J.*, 2015, **21**, 5145-5160.
- 5.18 S. Jana, S. Dalapati, S. Ghosh and N. Guchhait, *J. Photochem. Photobiol. A*, 2012, **231**, 19-27.
- 5.19 P.S. Sardar, S. Samanta, S.S. Maity, S. Dasgupta and S. Ghosh, *J. Phys. Chem. B*, 2008, **112**, 3451-3461.
- 5.20 S. Haldar and A. Chattopadhyay, *J. Phys. Chem. B*, 2007, **111**, 14436-14439.
- 5.21 L. Shang, Y. Wang, J. Jiang and S. Dong, *Langmuir*, 2007, **23**, 2714-2721.
- 5.22 Y. Moriyama, D. Ohta, K. Hachiya, Y. Mitsui and K. Takeda, *J. Protein Chem.*, 1996, **15**, 265-272.

- 5.23 F.F. Tian, F.L. Jiang, X.L. Han, C. Xiang, Y.S. Ge, J.H. Li, Y. Zhang, R. Li, X. L. Ding and Y. Liu, *J. Phys. Chem. B*, 2010, **114**, 14842-14853.
- 5.24 G. Zhang, N. Zhao and L. Wang, *J. Lumin.*, 2011, **131**, 2716-2724.
- 5.25 G.M. Morris, D.S. Goodsell, R.S. Halliday, R. Huey, W.E. Hart, R.K. Belew and A.J. Olson, *J. Comput. Chem.*, 1998, **19**, 1639-1662.
- 5.26 M.F. Sanner, *J. Mol. Graphics Modell.*, 1999, **17**, 57-61.
- 5.27 T. Brooks and C. W. Keevil, *Lett. Appl. Microbiol.*, 1997, **24**, 203-206.
- 5.28 K. Szacilowski, W. Macyk, A. Drzewiecka-Matuszek, M. Brindell and G. Stochel, *Chem. Rev.*, 2005, **105**, 2647-2694.

Appendix-Chapter 5

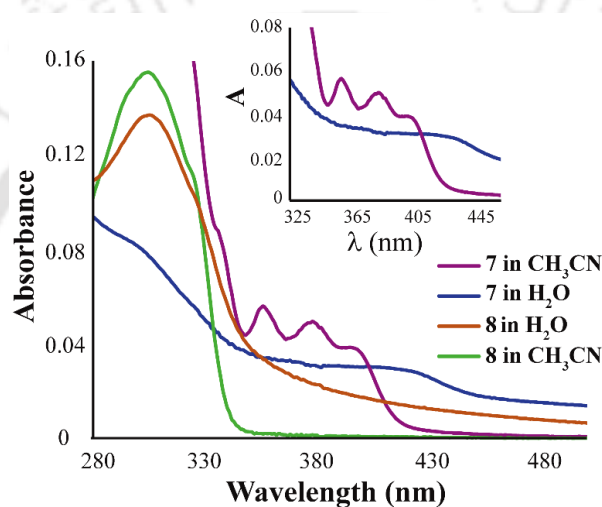


Figure A5.1 UV-Vis changes of 7 and 8 (10 μM) in various solvents at room temperature. INSET: Expanded region of the spectra in the wavelength region 325nm - 500 nm.

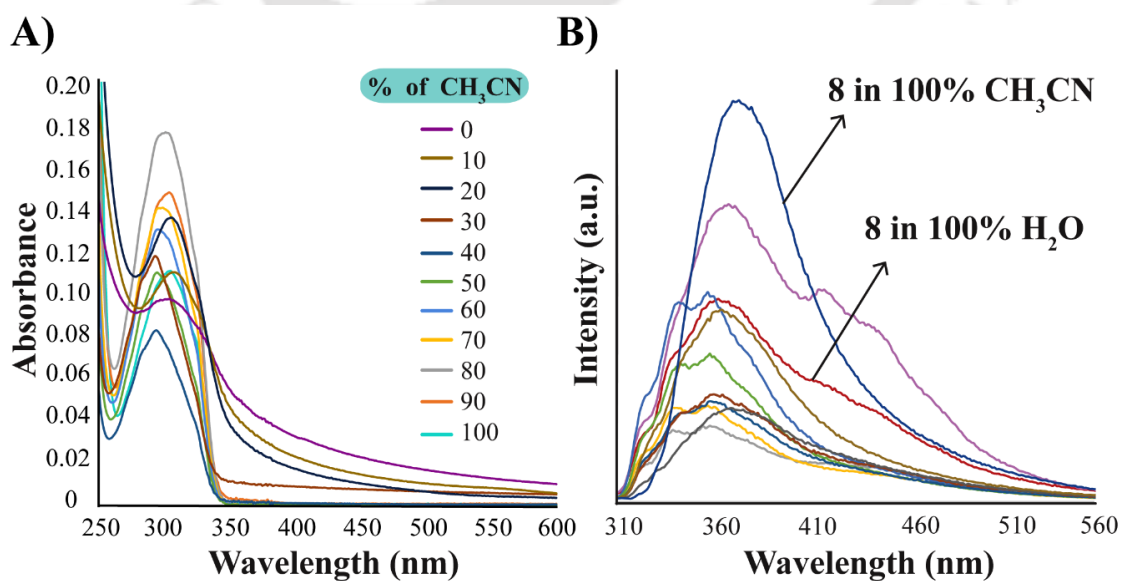


Figure A5.2 (A) UV Visible spectra of 8 (10 μM) in CH_3CN - H_2O with different CH_3CN fractions; B) Fluorescence spectra of 8 (2 μM) in CH_3CN - H_2O with different CH_3CN fractions ($\lambda_{\text{ex}} = 300 \text{ nm}$);

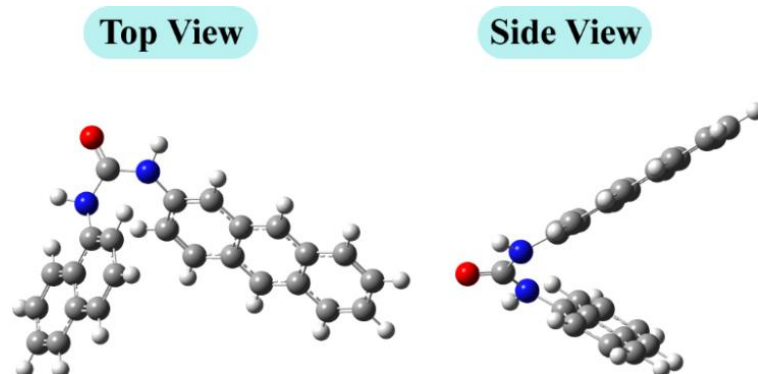


Figure A5.3. Geometry Optimized structures of **7** using RB3LYP/ 6-31G (d) as implemented on Gaussian 09.

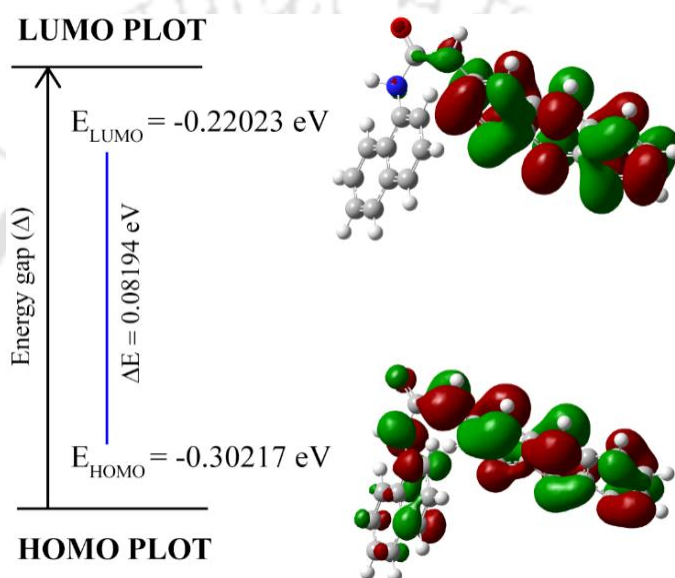


Figure A5.4 Frontier molecular orbital plots of **7** (ΔE = energy gap between HOMO and LUMO).

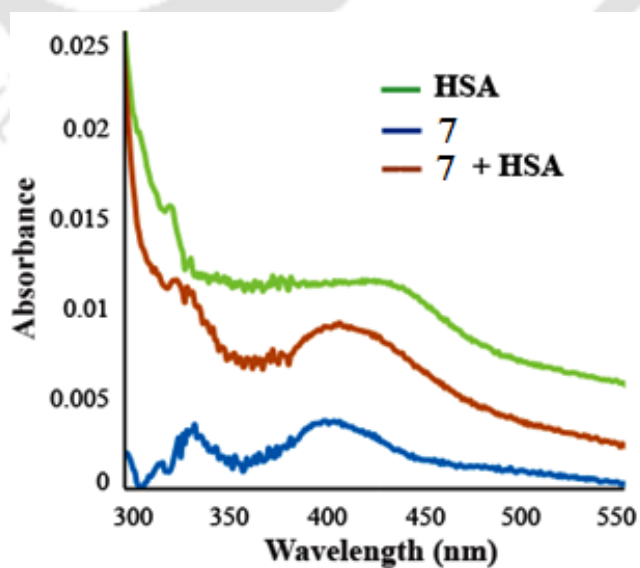


Figure A5.5 UV-visible spectra of **7** (2 μM) in aqueous medium in presence HSA (150 $\mu\text{g/mL}$).

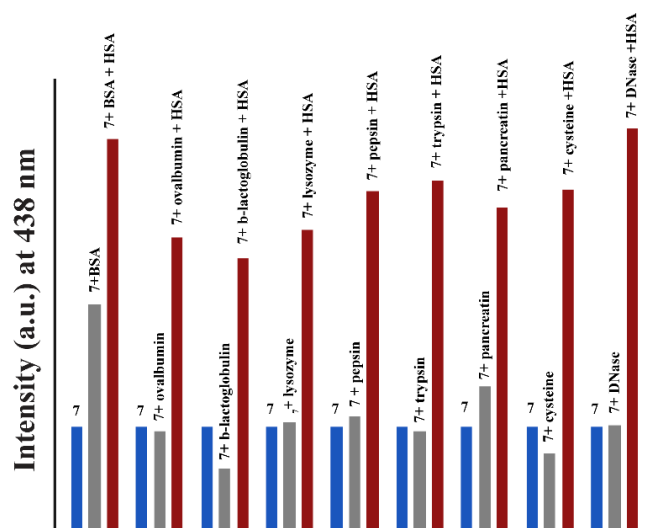


Figure A5.6 selectivity of **7** ($2 \mu\text{M}$) at 438 nm in 100% aqueous solution in the presence of an excess (10 equivalents) of various proteins and bio-analytes; [1-HSA, 2-BSA, 3-ovalbumin, 4- β -lactoglobulin, 5-lysozyme, 6-pepsin, 7-trypsin, 8-pancreatin, 9-cysteine, 10-DNase];

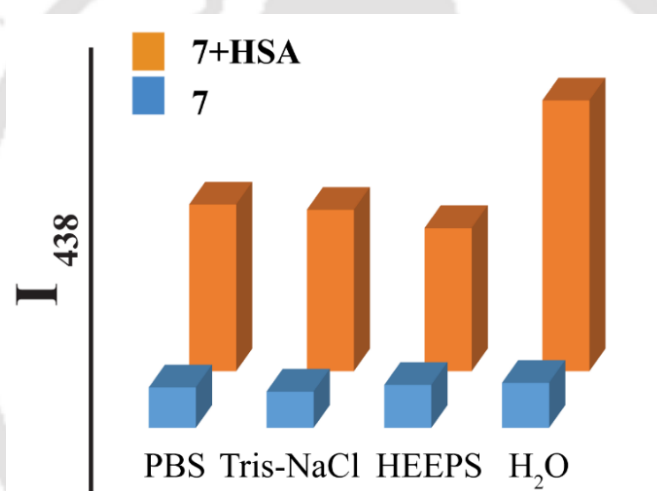


Figure A5.7 Fluorescence response of **7** ($2 \mu\text{M}$) at 438 nm upon interaction with HSA ($150 \mu\text{g/mL}$) in different medium

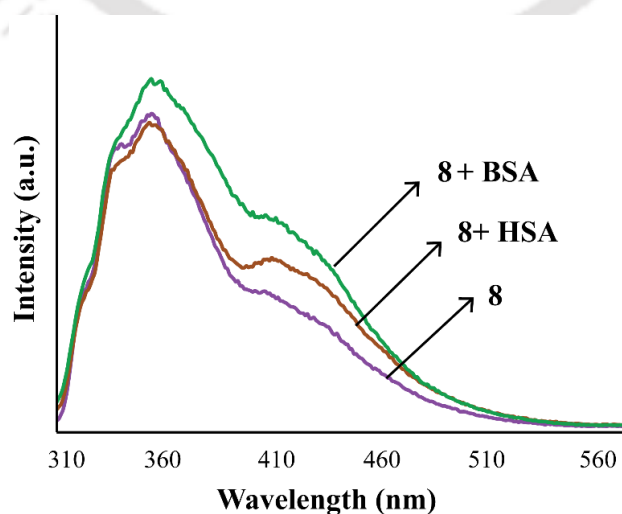


Figure A5.8 Fluorescence spectra of **8** ($2 \mu\text{M}$) in aqueous medium in presence of HSA and BSA($150 \mu\text{g/mL}$).

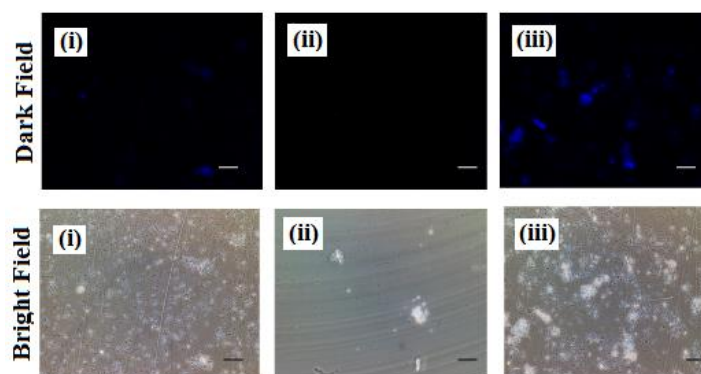


Figure A5.9 Epifluorescence microscopy images in 100% aqueous solution of (i) only **7** (ii) only HSA (iii) **7** in presence of HSA.



Figure A5.10 TEM images of the **7** in presence of HSA in 100% aqueous solution (scale bar = 200 nm).

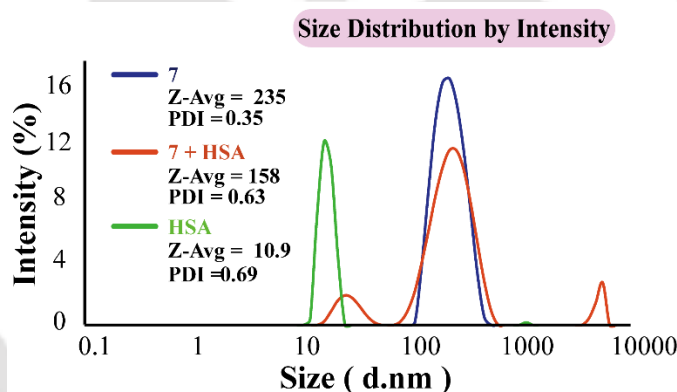


Figure A5.11 DLS-based particle size analysis; change in particle size of **7** (2 μM) in aqueous medium upon interaction with HSA (150 $\mu\text{g/mL}$).

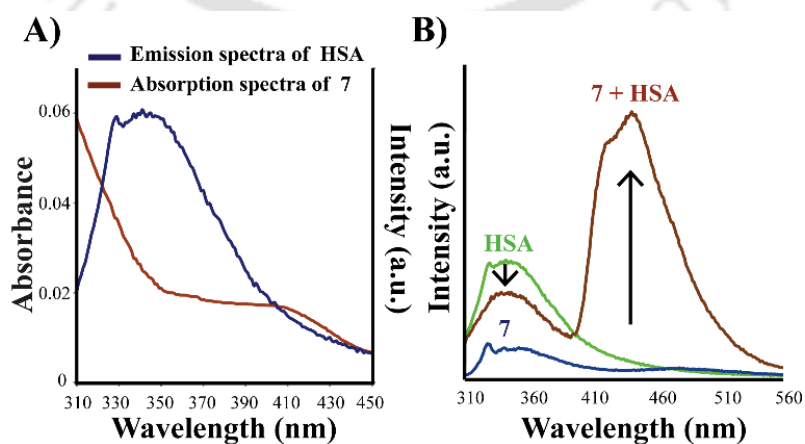


Figure A5.12 A) Spectral overlap of emission spectra of HSA and absorption spectra of **7**; B) The occurrence of FRET with addition of **7** (2 μM) to HSA (150 $\mu\text{g/mL}$) in aqueous medium.

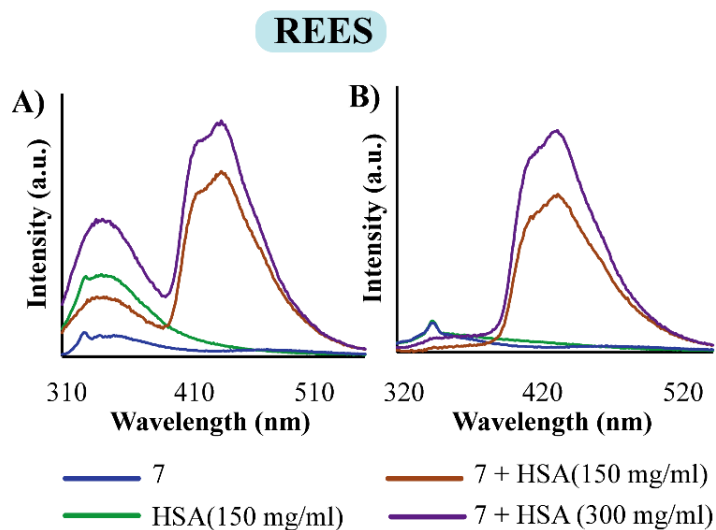


Figure A5.13 Red edge excitation shift effects at A) λ_{ex} 295 nm and B) λ_{ex} 310 nm.

Table A5.1 Red edge excitation shift effects at λ_{ex} 295 nm and at λ_{ex} 310 nm.

	$\lambda_{\text{em}}^{\text{max}}$		$\Delta\lambda_{\text{em}}^{\text{max}}$
Sample	λ_{ex} 295 nm	λ_{ex} 310 nm	REES (nm)
7	346	346	0
7+HSA (150 $\mu\text{g}/\text{mL}$)	344	349	5
7+HSA (300 $\mu\text{g}/\text{mL}$)	344	354	10

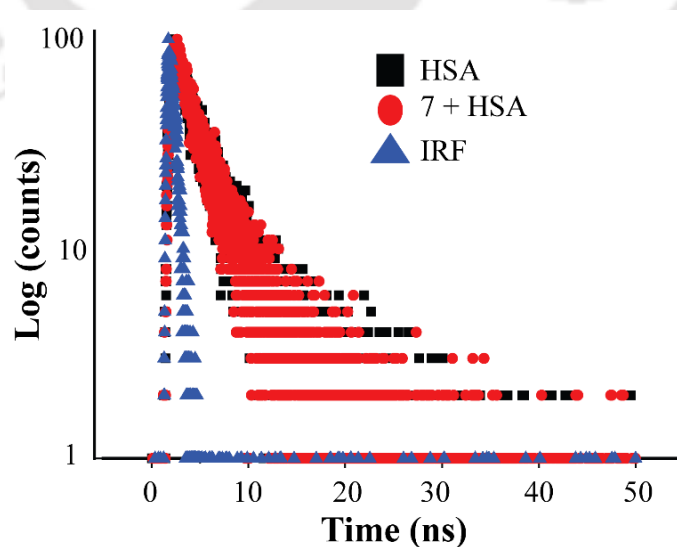
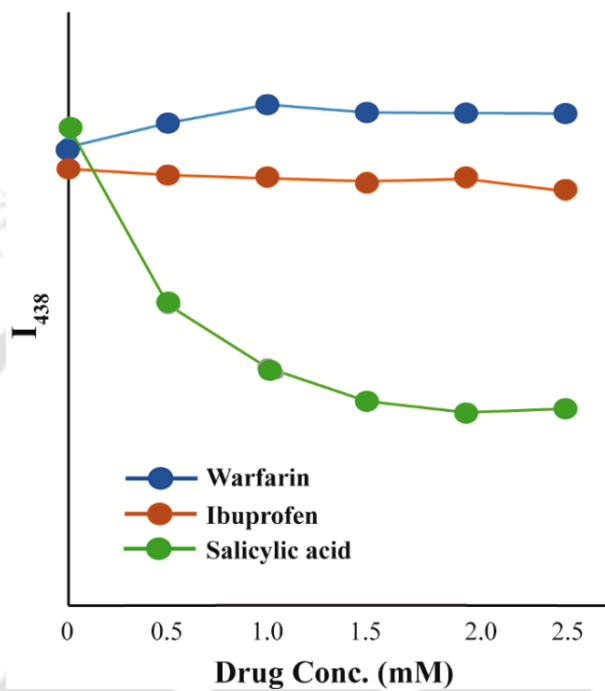
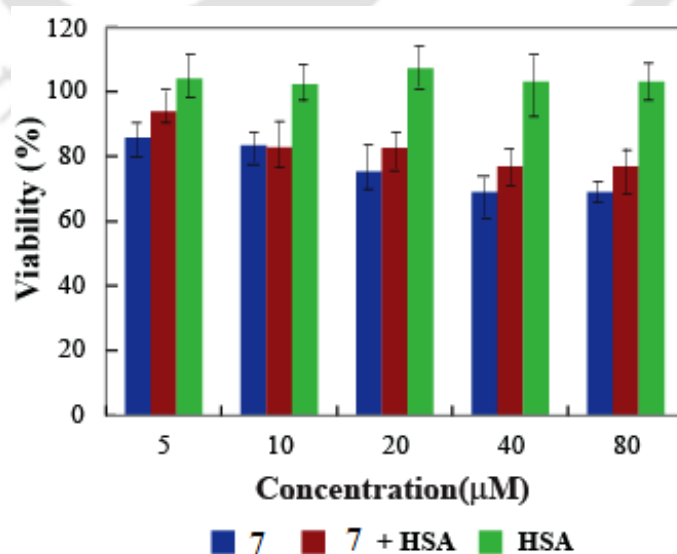


Figure A5.14 Fluorescence lifetime decay profiles of 7 (2 μM) in absence and in presence of HSA (150 $\mu\text{g}/\text{mL}$) in aqueous medium.

Table A5.2 Lifetime of **7** A) in the absence and B) in presence of HSA where $\langle\tau\rangle = a_1\tau_1 + a_2\tau_2$

Sample	B ₁	B ₂	a ₁	a ₂	τ_1	τ_2	$\langle\tau\rangle$	χ^2
7	0.055	0.001	0.719	0.281	0.442	6.721	2.206	0.935
7+HSA	0.008	0.004	0.198	0.801	1.528	14.290	11.749	1.233

**Figure A5.15** Changes in the emission intensity of **7** (2 μM) in presence of HSA (150 $\mu\text{g/mL}$) at 438 nm upon addition of various site specific drugs; $\lambda_{\text{ex}}=380$ nm.**Figure A5.16** MTT based cytotoxicity assay for (A) probe **7**, **7**/HSA ensemble and (B) only HSA.

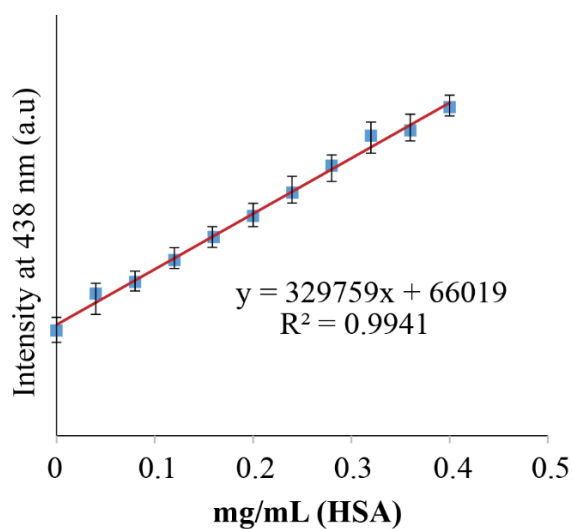


Figure A5.17 Fluorescence intensity (at 438 nm) vs. concentration of HSA plot for determination of detection limit.

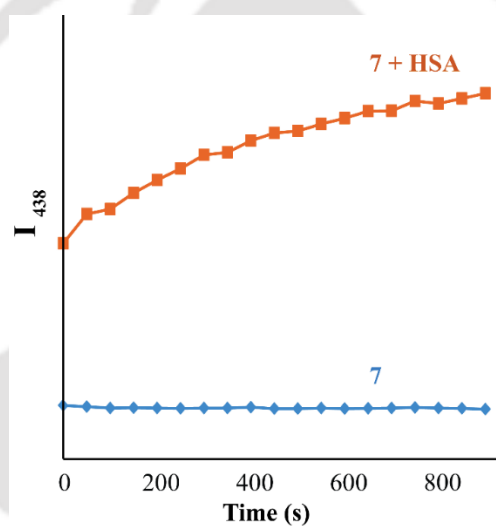


Figure A5.18 Changes in the emission intensity of 7 (2 μM) at 438 nm with time upon interaction with HSA (150 $\mu\text{g/mL}$); $\lambda_{\text{ex}}=380$ nm.

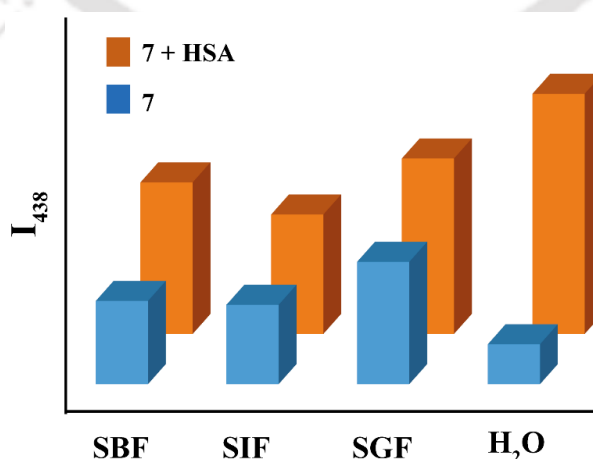


Figure A5.19 Changes in the emission intensity of 7 (2 μM) at 438 nm in presence of HSA (150 $\mu\text{g/mL}$) in bio-fluidic samples [SBF- Simulated Body Fluid (pH~7.4), SIF- Simulated Gastric Fluid (pH~2.0) and SGF- Simulated Intestinal Fluid (pH~8.0)].

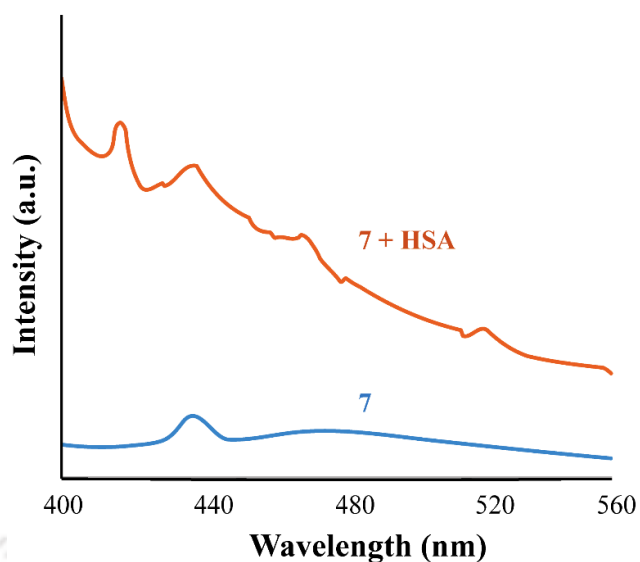


Figure A5.20 Fluorescence spectra of **7** (2 μM) in presence of HSA (150 $\mu\text{g/mL}$) in artificial urine sample.

Hydrophobic Interactions ---

Index	Residue	AA	Distance	Ligand Atom	Protein Atom
1	210A	ALA	3.26	11277	2029
2	213A	ALA	3.01	11264	2060
3	216A	VAL	3.32	11262	2090
4	327A	LEU	3.42	11261	3134
5	347A	LEU	3.62	11284	3343
6	481A	LEU	3.34	11280	4646
7	482A	VAL	3.10	11280	4654

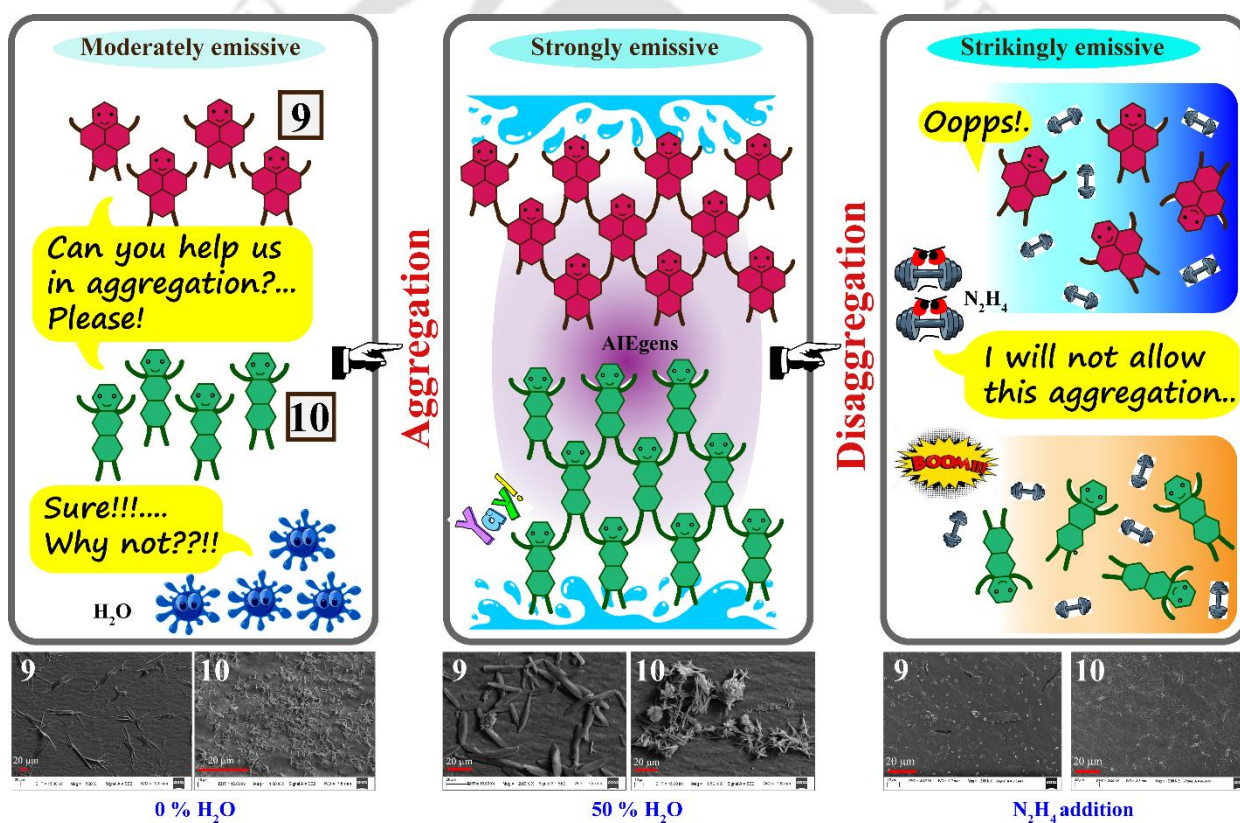
Figure A5.21 Interactions encountered in the Docking conformation of HSA/**7** with the lowest binding free energy obtained from Protein-Ligand Interaction Profiler.

Table A5.3 Recent progress in the field of HSA sensing, a comparative study.

Sl. No.	Reference	Fluorophoric Receptor type	Solvent system	Detection limit	Analytes detected
1.	Analyst, 2014 , 139, 581–584	Supramolecular aggregates of a cyanine dye	Tris–HCl buffer	Not Reported	Human Serum Albumin
4.	Chem. Commun., 2016 , 52, 6064--6067	2-dicyanomethylene-3-cyano-4,5,5-trimethyl-2,5-dihydrofuran (TCF) derivative	PBS (pH 8)	2.5 mg L ⁻¹	Human albumin
1.	Sens. Actuators B Chem., 2017 , 243, 831–837	AIE active amphiphilic molecule	Tris-HCl buffer	0.58 g/mL	Human serum albumin and chitosan
3.	Chem. Commun., 2017 , 53, 6432--6435	Coumarin derivative with dioxaborine unit	PBS buffer	0.21 mg/mL	HSA and BSA
6.	Dyes and Pigments, 2018 , 152,60–66	Three fluorescent chalcone-based dyes CD1-3	PBS buffer	0.57 mg/L	Human Serum Albumin
	J. Lumin., 2018 , 197, 193–199	Two NIR fluorescence probes, BI-FPI and NTPS-FPI	PBS buffer	0.66 mg/L 2.04 mg/L	Human Serum Albumin and Bovine Serum Albumin
7.	Talanta, 2018 , 185, 568–572	Probe XYQ based on the quinoline ring and indole ring	PBS buffer	0.0033 g/L	Human Serum Albumin (site I binding)
8.	Present Work	Di-substituted Urea	Water	5 µg/mL	Human Serum Albumin

CHAPTER 6

Directing the Aggregation Prospective of Schiff Base-Luminogen with Varying the Fluorophore: From Classic AIEgen to Efficient Hydrazine Sensor in their Aggregated State



Chapter 6

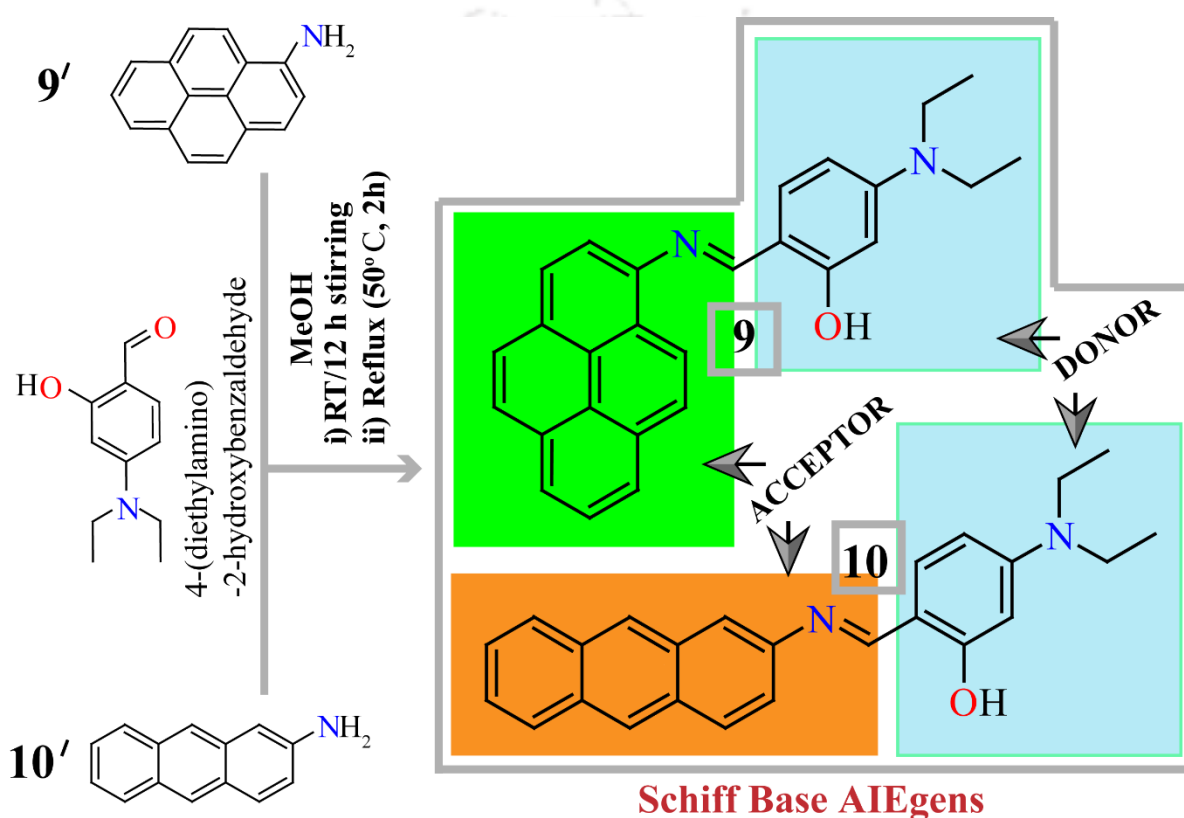
6.1 Objective of the Chapter

The idea of using functional aggregates of small molecules as fluorescent sensors for the detection and imaging of important analytes and small molecules has attracted considerable attention nowadays.^{6.1-6.4} In view of the latest advancement, the involvement of AIE-active small molecule assembly in modern sensing techniques is rapidly emerging as a functional tool for fabricating diverse supramolecular architecture for effective applications in sensing, imaging, optoelectronics, and therapeutic studies. Moreover, in comparison with conventional fluorescent sensors, AIE-active fluorescent sensors possess distinct advantages due to their bright emission with high fluorescent quantum yields, easy fabrication and broad application scope in water/high water content medium. In search of AIE-active building block, compared to other conjugated polymers, Schiff base compounds can be a good alternative and more advantageous due to their synthetic feasibility, structural tunability, better solubility and superior AIE activity owing to CN isomerization and the intramolecular hydrogen bonding capability.^{6.5-6.8} Hydrazine is a highly reactive base, which plays numerous roles as a synthetic precursor in a plethora of applications and can cause adverse effects to ecology and human health.^{6.9-6.11} Several traditional analytical techniques^{6.12-6.16} are commonly used for hydrazine detection. But complicated protocols, tedious procedure and instrumentation and sophisticated experimental conditions limit their application in most of the cases. Although a number of fluorescent sensors for hydrazine have been reported,^{6.17,6.18} still up-gradation in fluorescence methods for rapid detection of hydrazine with good sensitivity and selectivity in environmental and biological samples is a significant concern. So, it has been really challenging to achieve most of the qualities for an efficient bio-sensor in a single small molecular framework by bypassing the drawbacks encountered in the already reported hydrazine sensors. Till date, literature reports describe a variety of AIE-active hydrazine sensor in near-perfect aqueous media^{6.19-6.22} but none of them report their sensitivity towards hydrazine in their aggregation state. In this study, we have successfully leveraged the molecular assembly of AIEgens **9** and **10** into a reliable hydrazine sensor based on disaggregation approach.

6.2 Outline of the Chapter

In this study, we present two small fluorogenic Schiff base molecules **9** and **10** encompassing both donor and acceptor moiety in the single-molecule to trigger the AIE activity and report their aggregation behavior through in-depth spectroscopic and microscopic analysis. **9** and **10** are not only capable of acting as a potential AIE luminogen and display morphological variation during

aggregate formation by tuning the water content of the acetonitrile medium, but can also sense hydrazine efficiently in their aggregated state by exhibiting remarkable selective turn-on fluorescence response towards hydrazine in 1:1 acetonitrile-water medium. The detection limits (LODs) for hydrazine were calculated to be 0.5 ppb and 0.4 ppb for **9** and **10**, respectively. The sensing phenomenon can be attributed to the hydrogen bonding induced disaggregation phenomenon of AIEGen aggregates. Moreover, the sensing aptitude of AIEgens **9** and **10** to discriminate hydrazine in the vapor phase and various water samples and fluorescence bio-imaging studies highlights the analytical merit of the AIEgens in practical applications.



Scheme 6.1 Design and synthesis of Schiff base AIEgens **9** and **10**.

6.3 Design Principle of **9** and **10**

Our prime objective was to synthesize rationally designed Schiff base ligands that could potentially act as an AIEGen and simultaneously sense small molecules. To achieve this objective, we have synthesized **9** and **10** (Scheme 6.1), taking into consideration the following vital factors: (i) the use of two different potential fluorophore pyrene and anthracene as the aromatic core for strong fluorescence response and contrasting photophysical properties. Moreover, a high planarity in structure can promote π - π interaction, which in turn boosts charge transfer to yield extraordinary optical properties including AIE, (ii) the existence of the Schiff base linkage for better AIE prospective via

CN isomerization and the intramolecular hydrogen bonding capability, (iii) incorporation of both donor and acceptor site in a single molecule by the presence of diethylamino moiety for crafting ICT prospect. Thus, this comparative study was undertaken to distinguish the effect of aromatic core substitution on their aggregation ability and furthermore to employ that aggregated system as a sensing tool.

6.4 Crystallographic evidence

The suitable crystal for single-crystal X-ray analysis of free receptor was obtained from DMF solutions of receptor **9**, and it crystallized in the triclinic space group $P-1$. Structural elucidation revealed the existence of two symmetrically distinct receptors in the asymmetric unit ($Z = 2$). One of the receptor interacts with the symmetrically identical receptor unit via $\pi \cdots \pi$ interactions between the pyrene rings having an average distance of 3.600 \AA . Additionally, the receptor is stabilized by several weak $\text{C-H} \cdots \pi$ and $\text{C-H} \cdots \text{O}$ interactions (Figure 6.1 and Table A6.1). The other symmetrically distinct receptor interacts with the identical receptor unit via two weak $\text{C-H} \cdots \pi$ interactions having average bond distance of 2.806 \AA and one $\text{C-H} \cdots \pi$ interaction from another symmetrically distinct receptor unit having bond distance 2.721 \AA . Additionally, there is intramolecular H-bonding between the OH group and Nitrogen atom.

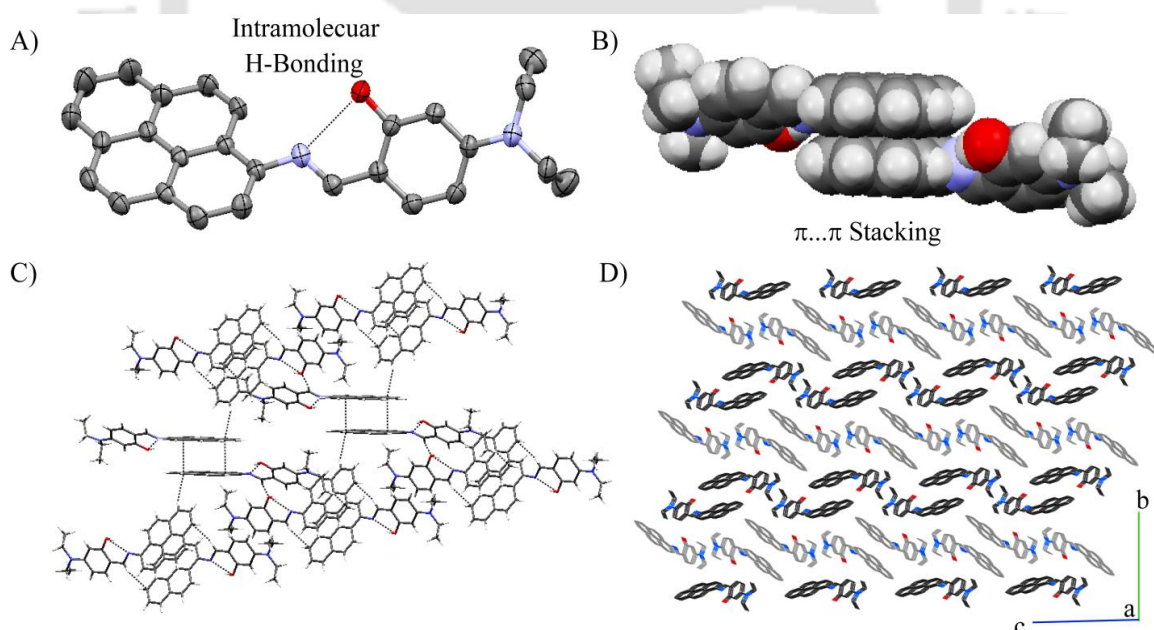


Figure 6.1 A) Ellipsoid structure of **9** showing intramolecular H-Bonding, B) spacefill view of **9** viewing $\pi \cdots \pi$ stacking among the pyrene moiety, (C) showing all the H-bonding contacts of **9** and D) packing diagram of **9** as seen along the crystallographic a-axis.

6.5 Aggregation Prospective

The presence of both donor and acceptor units in **9** and **10** automatically focused our attention on the possibility of a typical solvatochromism^{6.23,6.24} in both the compounds. In UV-Vis spectra, **9**

exhibited a sharp absorbance maximum around 400 nm in hexane, and it gradually shifted to 420 nm in DMSO, a high polarity solvent (Figure 6.2A). Similarly, for **10** there were well-separated absorbance bands around 350/400 nm in hexane, but in DMSO, these bands appeared at longer wavelengths (Figure 6.2B). The increase in solvent polarity significantly affects the energy gap via geometry relaxation and results in a longer absorption wavelength. This type of polarity dependent redshift of the absorption spectra undoubtedly confirmed the ICT along D- π -A track in **9** and **10** both. Next, the aggregation of **9** and **10** were investigated via UV-Vis absorption and fluorescence emission using acetonitrile-water solvent systems. In pure acetonitrile medium, there was a well-defined absorbance maximum around 400 nm for **9**, whereas **10** revealed two absorbance bands around 350/400 nm. But, the spectrum profile deviated during the gradual addition of water to the acetonitrile solutions, which led to the broadening of spectra and a prominent upsurge in the baseline in the tail region for both the cases (Figure 6.2C and 6.2D). This primary observation indicated the possibility of aggregate formation in the mixed solvent

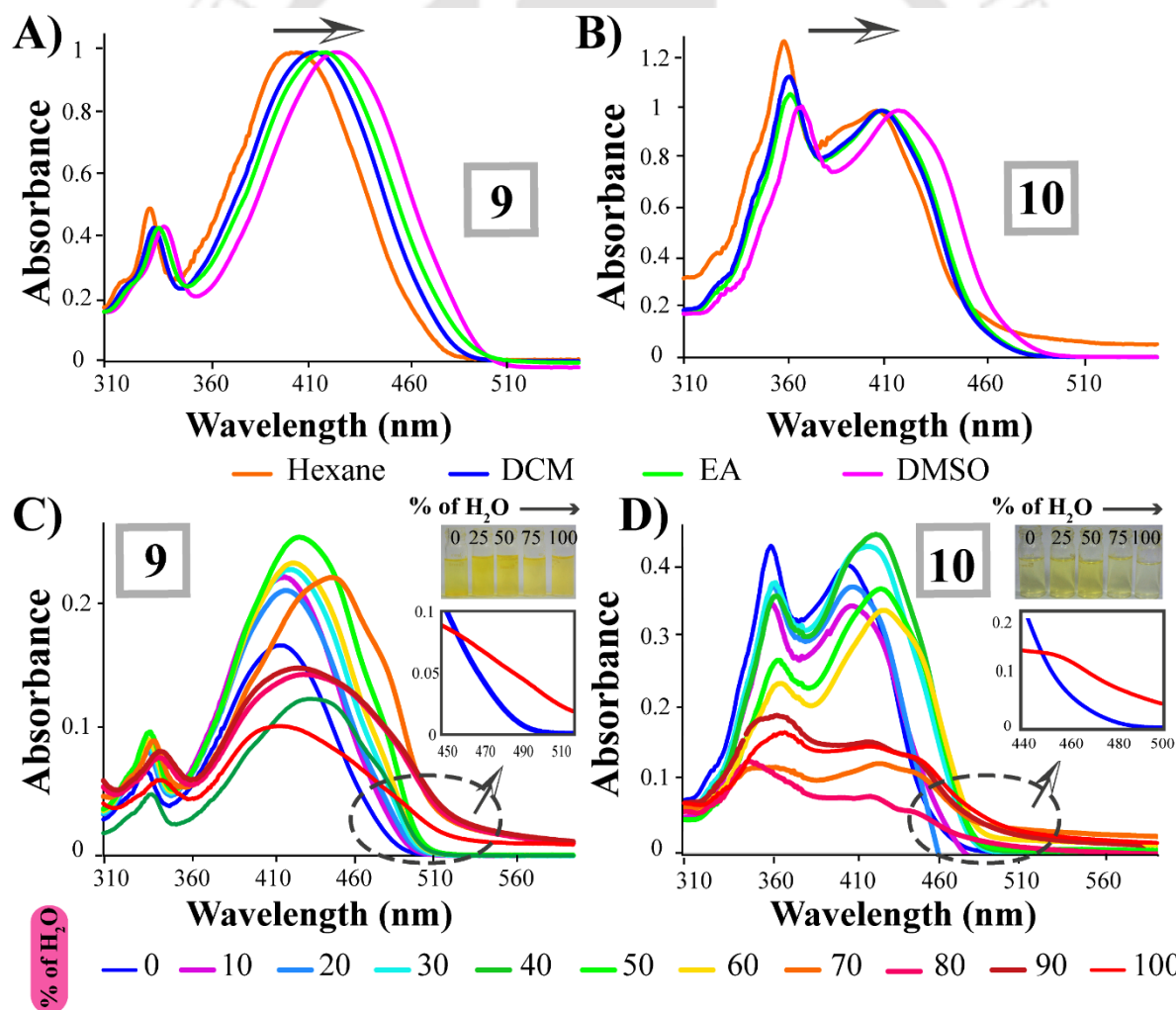


Figure 6.2 Normalized UV-Vis spectra of **9** (A) and **10** (B) in solvents with different polarities. UV-Vis spectra of **9** (C) and **10** (D) in the mixed solvent system by varying solvent fraction.

system. Hence further verification was carried out by recording their solvent dependent fluorescence emission spectra (Figure 6.3A-C). Both **9** and **10** were found to be moderately emissive in the pure acetonitrile medium, when excited at 380 nm and 420 nm, respectively. Interestingly, **9** exhibited two well-defined emission maxima at ~425 nm (peak 1, high intensity and may be ascribed to the excimer formation owing to the presence of a pyrene moiety) and at ~500 nm (peak 2, very low intensity), whereas there was only one emission peak for **10** at ~485 nm. But, it was observed that upon incremental addition of water to 10 μ M ligand in acetonitrile medium, a systematic growth in the intensity for peak 2 was observed in case of **9**, which suggested an increased aggregation of the compound. Further, an overall strong fluorescence emission along with a noticeable bathochromic shift in the emission maxima for each case substantiated the aggregation phenomenon. The emission intensity enhanced up to 60% water content for both the compounds, and the successive further addition of water resulted in a downward trend of the emission intensity. Finally, when the water fraction reached 100%, the emission intensity of **9** and **10** dropped down quite remarkably, likely due to the solvent effect. Furthermore, as observed in Table A6.2, the Φ values of 0.002 and 0.018 for **9** and **10** in 1:1 acetonitrile-water medium was achieved with considerable fluorescence enhancements, respectively. Comparative aggregation behavior of **9** and **10** were also reflected in their corresponding intensity vs. water fraction plots (Figure 6.3A, 6.3B, 6.3C, inset) and the variation in the AIE aptitude of **9** and **10** depends mainly on their conformational flexibility and vibrational amplitude. As the molecular structure of both **9** and **10** consist of donor and acceptor units, the increase in emission intensity can be attributed to the formation of aggregates with the stabilized ICT effect^{6.25,6.26} in higher water fractions. The red-shifted UV-Vis/fluorescence emission peaks were a clear indication of a favorable AIE with J-type aggregation^{6.27,6.28} due to the π - π stacking interactions. Moreover, the restriction in intramolecular motion in **9** and **10** also resulted in a more planar structure, which might stimulate the transfer of a proton from the -OH group to the N_{imine} atom upon photo-excitation. Hence, it may be anticipated that this ESIPT mechanism^{6.29,6.30} perhaps induced a significant effect on the restriction of intramolecular rotation, which is manifested as a gradual red shift in the band maxima (peak 2) upon an increase in the water fraction. Thus, the alteration in the solvent fraction can significantly interfere with both the compounds' emission behavior, which strongly suggested probable aggregation triggered fluorescence enhancement via Restriction of Intramolecular Motion (RIM).^{6.31} Additionally, as evident from the chromaticity diagram, the fluorescence spectra of **9** with water contents of 0%, 20%, 40% 60%, 80% and 100% represented respective light emission (Figure 6.3D). However, among these, the coordinates (0.20, 0.23) of emission spectrum of **9** with $f_w=60\%$ in acetonitrile-

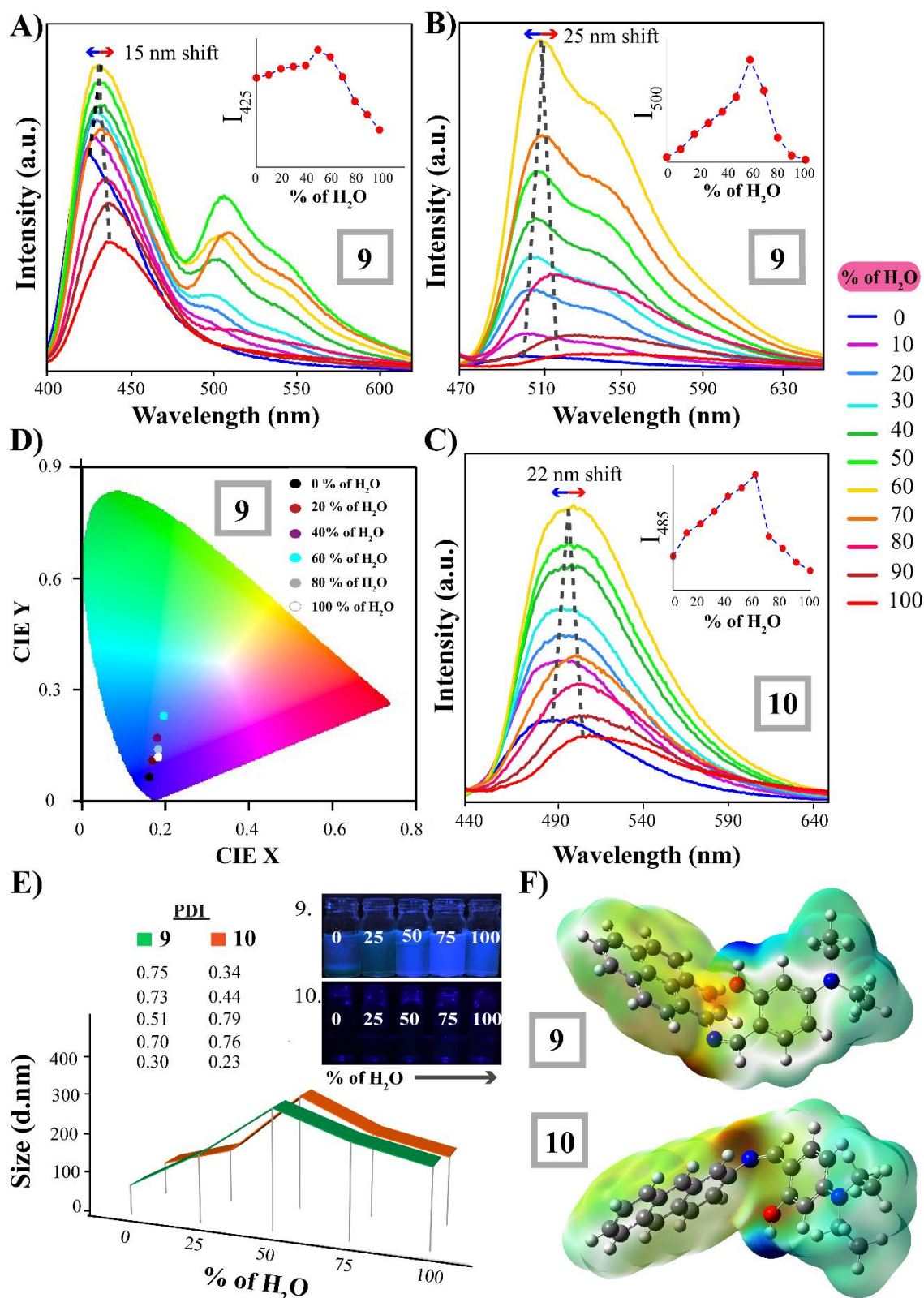


Figure 6.3 Fluorescence emission spectra of **9** [A ($\lambda_{ex} = 380$ nm) and B ($\lambda_{ex} = 450$ nm)] and **10** [C ($\lambda_{ex} = 420$ nm)] in the acetonitrile-water medium by varying solvent fraction; inset: change in fluorescence intensity as a function of water fractions; D) CIE chromaticity diagrams of the spectra of **9** in different water fractions. E) DLS-based particle size analysis of aggregated **9** and **10** as a function of water fractions; inset: visual changes in fluorescence of **9** and **10** in the acetonitrile-water medium under UV light. F) Molecular electronic potential diagrams of **9** and **10** as obtained by density functional theory (DFT) calculation using B3LYP/6-31G as the basis set on Gaussian 09.

water mixture is closer to the pure white light emission coordinates (0.33, 0.33). Thus for **9**, it can be fair to anticipate that AIE phenomenon coupled with the combined ICT+ESIPT effect is responsible for corresponding bluish white-light emission by varying the solvent fraction. The change in fluorescence emission for **10** in different water fractions was hard to decipher with the naked eye. In contrast, for **9**, visible fluorescence changes were observed from weak to strong bluish-white light emissions upon increasing the water fraction of the medium (Figure 6.3E, inset). Further elucidation of aggregation was corroborated by DLS studies (Figure 6.3E). The average particle size of **9** increased from 85 nm to 337 nm upon increasing the water fractions from 0–50% in acetonitrile medium. A similar effect was encountered in the case of **10**, where the average particle size increased to 326 nm ($f_w=0\%$) from 93 nm ($f_w=50\%$). This increase in particle size undoubtedly supports particle assembly in association with the solvent molecules, which led to formation of larger aggregates of AIEgens up to a specific limit of water fraction.

However, the observed AIE activity of **9** and **10** was also corroborated via a theoretical approach. Optimization of the structures and HOMO LUMO energy calculations were performed via DFT (density functional theory) studies following the RB3LYP/6-31G basis set and the results are illustrated in Figure A6.1. The calculated HOMO and LUMO energy gaps of **9** and **10** are 0.120 and 0.124 eV, respectively. The **9** has a lower HOMO–LUMO energy gap than the **10** because of higher π -conjugated system present in **9**. A close look at DFT simulated structure and pictorial representation of HOMO LUMO electron clouds thus obtained support the occurrence of aggregation phenomenon of the two molecules. However, it is hard to guess the direction of electron transfer. Hence, the molecular electronic potential (MEP) diagrams of **9** and **10** were employed to understand the electronic distribution in the molecular surfaces. As evidenced in Figure 6.3F, the electron-deficient reddish color surfaces were mainly positioned on the imine bond along with the aromatic ring, and the electron-rich bluish color surfaces were spread over the rest of the molecule. Therefore, it could be easily summarized that the electron transfer will occur from the 4-(N,N-diethylamino)salicylaldehyde moiety to aromatic ring through imine bond.

In order to acquire morphological evidence for formation of aggregates of **9** and **10**, FESEM imaging and fluorescence microscope analysis was performed by a solution drop-casting method. As depicted in Figure 6.4, FESEM imaging studies indicated that the diversity in topography of both aggregative species displayed apparent sensitivity towards the respective solvent fraction changes. **9** assembled into a thin micro-rod structure in 100% acetonitrile medium and turned into micro-sheets in $f_w=50\%$ followed by closely packed micro-tiles when $f_w=100\%$. In contrast, we found broken star-shaped particles in the micrometer meter range for **10** in 100% acetonitrile medium. The morphology of **10** was further modified for $f_w=50\%$, and finally, in 100% aqueous

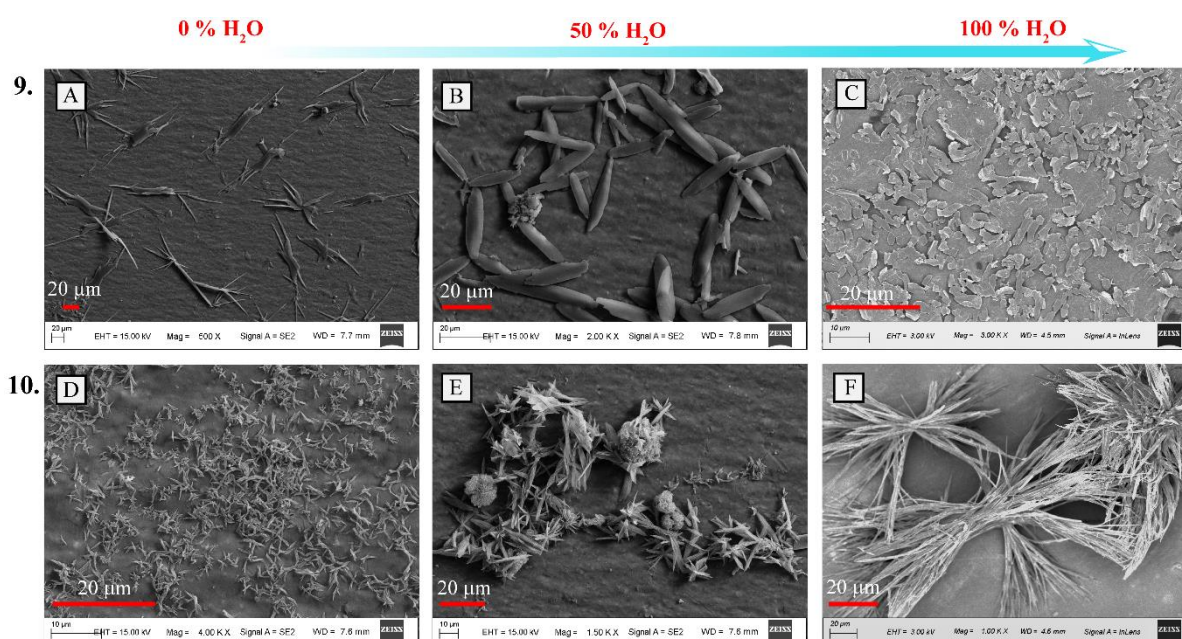


Figure 6.4 FESEM images of **9** (A-C) and **10** (D-F) by varying the solvent fraction [scale bar = 20 µm].

medium, it appeared as a bunch of straws with a considerable increase in size. Thus the morphology of the two AIEgens can be controlled typically with the alteration in the solvent fraction. It may be mentioned here that owing to inherent difference in the aromatic core, the AIEgens likely display heterogeneity in molecular arrangement and assembly in presence of varying solvent fraction. Additionally, fluorescence microscope images revealed distinctive multichannel emission for **9** by changing the solvent fraction at various excitation ranges (Figure A6.2). This also suggested that it may be worthwhile to probe and ascertain whether the overlapping images of UV, blue and green emission could produce white-colored emission. It is worth mentioning the observation of bluish-white light emission in the merged images of fluorescence microscopy. Hence, considering the solid-state emission behavior, **9** can be categorized as an example of classic AIEgen among the very few single small molecule multicolor luminogen reported in the literature. Fluorescence microscope analysis also suggested that in contrast to **9**, the response of AIEgen **10** was different. We encountered that almost non-fluorescent **10** can exhibit a blue fluorescence upon increasing the water fraction 50% in the mixed solvent system (Figure A6.3). Thus, fluorescence microscopy images can offer an additional means for featuring the aggregation strategy of AIEgens **9** and **10** in the aspect of multicolor emission behavior. Therefore the entire spectral outcomes and microscope studies are in good accordance to validate the aggregation characteristics of the AIEgens **9** and **10**. However, AIEgen **9** appeared fascinating in its way, which encouraged us to continue this study further.

6.6 Sensing Performance

Further analysis was commenced to probe the subsequent sensing potential of both the

AIEgens in their aggregated state in the case of hydrazine detection and its impact on the aggregation aptitude of **9** and **10**. As it has been already established, both the AIEgens **9** and **10** undergo ICT from donor to acceptor, hence, it was conceived that a chemical analyte approaching the respective donor (D) and/or acceptor (A) units may affect their optical properties. This motivated us to monitor the absorbance spectra of **9** and **10** in the presence of hydrazine. Interestingly, the addition of hydrazine to the solution of **9** and **10** in 1:1 acetonitrile-water medium produced a prominent reduction in the absorption intensity at 400 nm. Further, the intensity of the band around ~350 nm increased and became well defined for both the case and blue-shifted only in case of **10**. We have also recorded the absorption spectra for other reactant molecules in 1:1 acetonitrile-water medium, and none of them resembled the absorption spectra obtained upon hydrazine addition. This negated the possibility of hydrolysis or degradation of AIEgens **9** and **10** in the presence of water and strong reducing agent hydrazine (Figure A6.4). On the contrary, this result validated the tenet that AIEgens **9** and **10** can act as a selective and rapid sensor for hydrazine. This observation also prompted us to determine the fluorescence selectivity of AIEgens **9** and **10** for hydrazine over other competitive amine-based compounds, including hydroxylamine, ethylenediamine, phenyl-hydrazine, benzylamine, diphenylamine, triethylamine, aniline, pyridine, NH₃ solution, urea, and thiourea in 1:1 water-acetonitrile medium. As shown in Figures 6.5A and 6.5B, under identical testing conditions, only hydrazine (10 equiv.) induced an outstanding fluorescence turn-on response among the other amine-based analytes. It was observed that the addition of hydrazine in **9** and **10** led to about seven and five-times increase in the fluorescence intensity, respectively. Interestingly, a distinct color change of **9** and **10** upon interaction with hydrazine also enabled naked-eye detection (Figure 6.5A-6.5B, inset). This hydrazine responsive selective turn-on fluorescence response of **9** and **10** can be ascribed to the weakened AIE effect due to the H-bond formation between imine nitrogen atoms and hydrogen atoms of hydrazine.^{6,32} Such hydrogen bonding played a crucial role in this sensing process by hindering the PET process, resulting in a significant emission enhancement. The fluorescence selectivity experiment in a similar experimental condition was also carried out in the presence of various metal ions and anions along with other representative amines-based compounds, but surprisingly none of them were found to interfere with the hydrazine sensing ability of **9** and **10**, which clearly emphasized the rapid selectivity and strong sensitivity of **9** and **10** towards hydrazine even in the presence of other mentioned analytes (Figure A6.5).

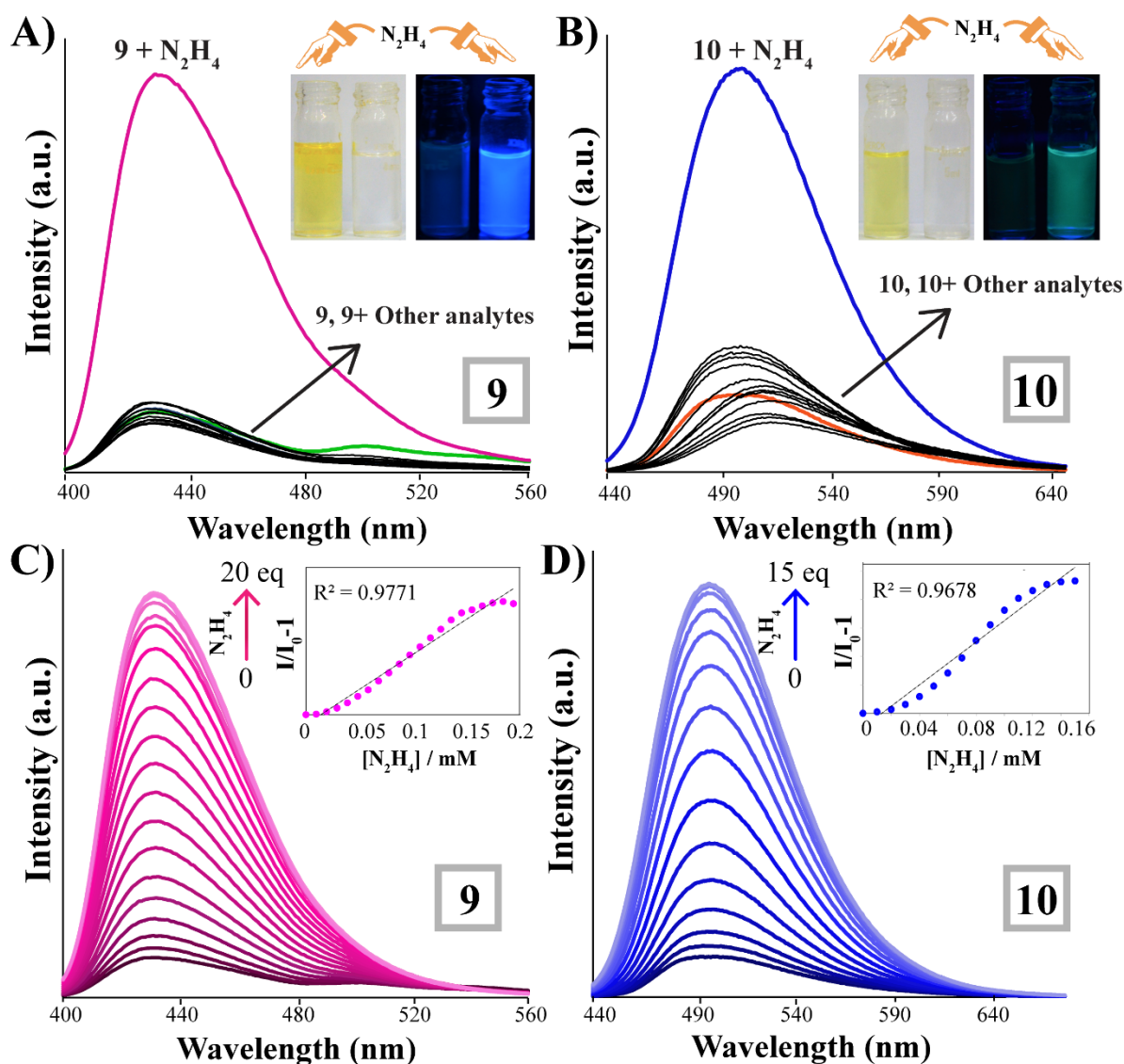


Figure 6.5. Fluorescence spectra of **9** and **10** (10 μM) in 1:1 acetonitrile-water medium in the presence of an excess (10 equivalents) of various amine based compounds [A ($\lambda_{\text{ex}} = 380 \text{ nm}$) and B ($\lambda_{\text{ex}} = 420 \text{ nm}$)]; inset: visual changes in the fluorescence of **9** and **10** in the presence of hydrazine. Fluorescence spectra of **9** (C) and **10** (D) (10 μM) in the presence of varying concentrations of hydrazine; inset: changes in fluorescence intensity with hydrazine concentration.

However, to realize the turn-on fluorescence response of AIEgens **9** and **10** toward hydrazine in detail, a fluorescence titration experiment was performed for a quantitative appraisal of the interaction between hydrazine and AIEgens **9** and **10** in 1:1 acetonitrile-water medium (Figure 6.5C and 6.5D). It was exciting to note that with increasing hydrazine concentration to the solution of **9** and **10**, the fluorescence intensity increased gradually and then leveled off for both cases. The titration data implies that the 20 and 15 equiv. of hydrazine is required respectively for **9** and **10** to reach saturation. A linear relationship was obtained from the plot of $(I/I_0 - 1)$ as a function of hydrazine concentration with a linear correlation coefficient $R^2 = 0.9771$ and $R^2 = 0.9678$ for **9** and **10**, respectively, where I and I_0 are the fluorescence signals of the respective AIEgen in the presence and

absence of hydrazine (Figure 6.5C and 6.5D, inset). Accordingly, a possible quantitative determination was done through the Job's plot analysis (Figure A6.6). The detection limits (LODs) were also calculated through standard deviations and linear fittings, as evidenced in Figure A6.7. It was inspiring to observe that the AIEgens **9** and **10** could detect the hydrazine concentration as low as 0.5 ppb and 0.4 ppb, respectively, which is much less than the TLV limit set by the USEPA. It should be stated here that all the fluorescence spectra were recorded in similar experimental conditions within 1 min of the addition of the analytes to AIEgens **9** and **10** and therefore confirmed its rapid nature in hydrazine detection. Moreover, to realize the response time, fluorescence-kinetic studies of both AIEgens were performed in the absence and presence of hydrazine and resulted in a fast increase in the emission intensity, which reached saturation within minutes after the addition of hydrazine to AIEgens solutions (Figure A6.8). Furthermore, the effect of pH on the AIEgens and their fluorescence response towards hydrazine was also evaluated to confirm the better selectivity of **9** and **10** towards realistic hydrazine detection (Figure A6.9). The efficacy of AIEgens was also assessed by recording its temperature-dependent emission spectra (Figure A6.10). No notable changes were observed for both the AIEgens by altering the temperature. In contrast, the emission intensity recorded at room temperature (RT) within 1 min of hydrazine addition increased more after keeping the solution for 5 mins at RT as disaggregation occurs with time. But cooling down the temperature to 5° C immediately after hydrazine addition slows down the disaggregation and as a result, there was a negligible increase in emission intensity. In contrast, heating to 60° C accelerates the disaggregation process as the upsurge in emission intensity is higher than the emission intensity at RT after 5 mins. Thus temperature did not cause any abnormal effect on the sensing system. It should be added here that both the AIEgens possess high photosensitivity as irradiation of **9** and **10** in 1:1 acetonitrile-water medium with 100W bulb for 2 hrs could not induce any notable changes in their emission behavior (Figure A6.11). We would also like to mention here that the AIEgens **9** and **10** offers better scope and superior efficacy in hydrazine sensing compared to recently reported other probes as hydrazine sensors in the aspect of synthetic feasibility, cost-effectiveness, simple experimental condition, very low detection limit, and realistic multifunctional applicability as evident from Table A6.3.

This selective interaction of **9** and **10** with hydrazine was also well supported by DLS and AFM imaging studies. Interestingly, according to DLS data, the **9/10-N₂H₄** adduct led to disaggregation of the aggregative species of **9** and **10** AIEgens in 1:1 water acetonitrile

mixture (Figure 6.6A). The overall particle size of **9** and **10** reduced considerably upon interaction with hydrazine. Similarly, in the aspect of AFM images, Figure 6.6B reaffirms the transformation of aggregates into much smaller particles with an average diameter in the nanometer range due to hydrazine addition obtained from a drop-cast solution of **9/10** in a 1:1 acetonitrile–water medium. This outcome clearly validates the interaction between **9/10** AIEgens and hydrazine, which triggers the disaggregation of aggregates. The hydrazine interaction was also scrutinized under an optical microscope (Figure A6.12) and FESEM (Figure A6.13), which revealed that the morphology is entirely different from that of the aggregated-**9/10** species. Thus the microscope imaging studies provided additional evidence of the interaction of **9/10** with hydrazine aptly. For further corroboration, we recorded and compared the $^1\text{H-NMR}$ spectra of the **9** and **10** in the presence and absence of hydrazine in DMSO- d_6 (Figure A6.14). It was noticeable that the formation of hydrogen bonds results in shifting of all proton signals to the lower δ values to free **9** and **10** for both

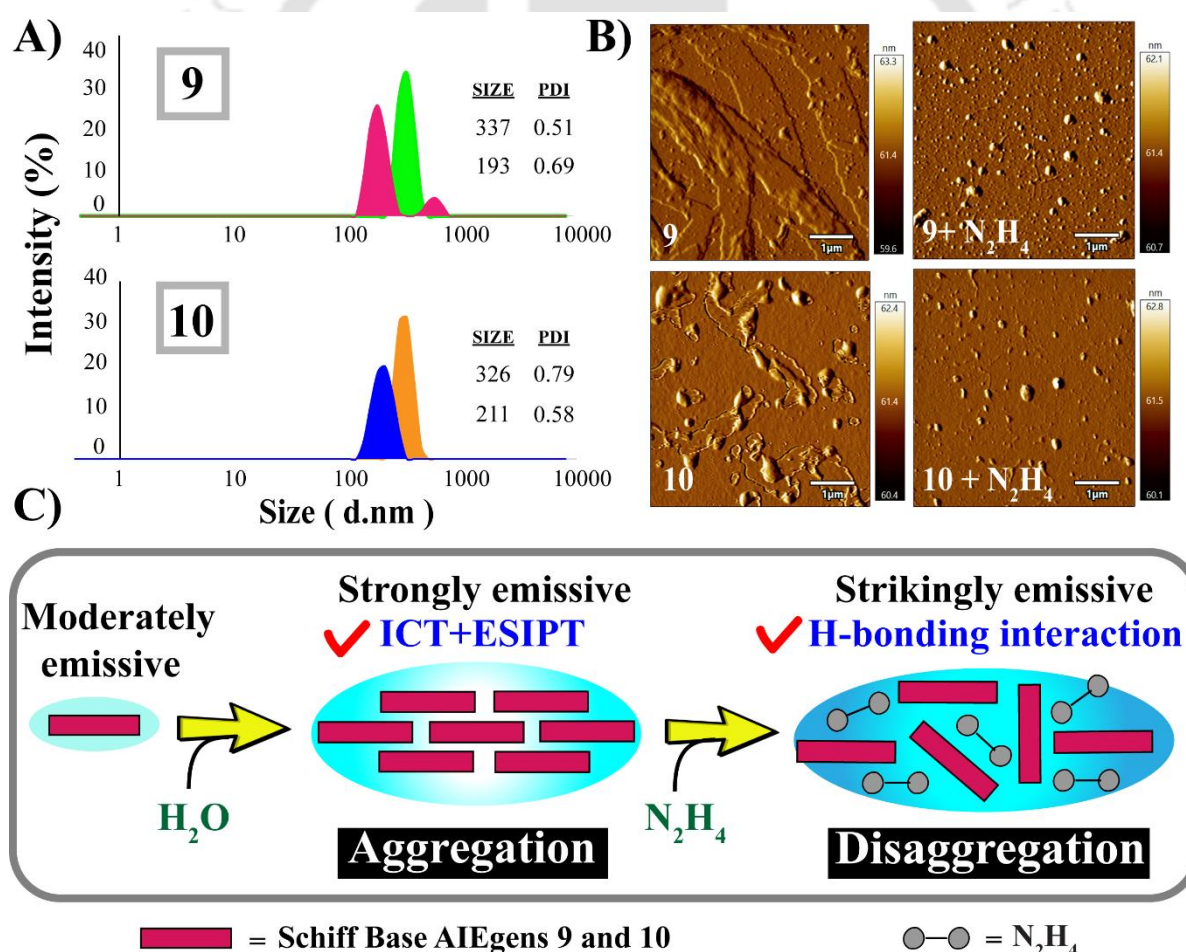


Figure 6.6 A) DLS based comparative particle size analysis of AIEgens **9** and **10** in the absence and presence of excess hydrazine in 1:1 acetonitrile–water medium. B) AFM images of the aggregates upon interaction with hydrazine with AIE gens **9** and **10** in a 1:1 acetonitrile–water medium [Scale-1 μm]. C) Pictorial representation of the plausible mechanism of aggregation due to solvent fraction alteration and disaggregation due to hydrazine interaction with AIEgens **9** and **10**.

cases. Again, a new peak that appeared at ~6 ppm may correspond to the signal of hydrogen of hydrazine. This observation certainly validates the hydrogen bond-driven sensing mechanism of the **9** and **10** AIEgens. Thus the reported sensing process does not involve any complicated mechanism and sophisticated experimental conditions and simply works based on disaggregation approach via H-bonding interaction to give selective turn-on response towards hydrazine. Most of the probes reported for hydrazine detection works either through reaction-based approaches such as hydrazone formation, deprotection, substitution-cyclization or using expensive nano-particles.^{6,17,6.18} However, there is a handful of hydrogen bonding-induced sensing mechanisms reported in the literature for hydrazine. The plausible aggregation by solvent fraction variation and consecutive disaggregation due to hydrazine interaction of two AIEgen is pictorially exemplified in Figure 6.6C.

6.7 Analytical Aptitude

The high selectivity and fast response of **9** and **10** AIEgens towards hydrazine encouraged us to evaluate its analytical prospect in real-life application. As demonstrated, test kits prepared by coating the TLC plate with the 1:1 acetonitrile-water solution of **9** and **10** can be employed in detecting hydrazine effectively (Figure 6.7A). Again, the test kits dipped into AIEgen solution (1:1 acetonitrile-water) were dried and exposed to hydrazine vapor for 30 mins and surprisingly, the color of the TLC plate changed from yellow to colorless, which indicates that **9** and **10** could successfully sense hydrazine in vapor phase too (Figure 6.7B). It is also impressive to note that **9** and **10** AIEgens could detect hydrazine even in water samples collected from different sources and in artificial urine samples (Figure 6.7C). Appreciable fluorescence turn-on responses were recorded for both **9** and **10** towards hydrazine in each real-life sample, which unquestionably demonstrated the practical feasibility of the AIEgens as an effective hydrazine sensor. Lake water was collected from the IIT Guwahati Lake, whereas industrial wastewater was supplied by the Department of Chemical Engineering, IIT Guwahati. The reported literature procedure^{6.33} was followed for the preparation of the artificial urine sample. To further demonstrate the imaging application of AIEgens, fluorescence imaging of hydrazine in plants was accompanied. The root section of 15 days old tomato plant was incubated with the hydrazine solution for 3 hrs separately and then divided into two groups. One group was again incubated with the solution of **9** and **10** for another 3 hrs followed by fluorescence imaging. The hair root fragments stained by AIEgen solution (1:1 acetonitrile-water)

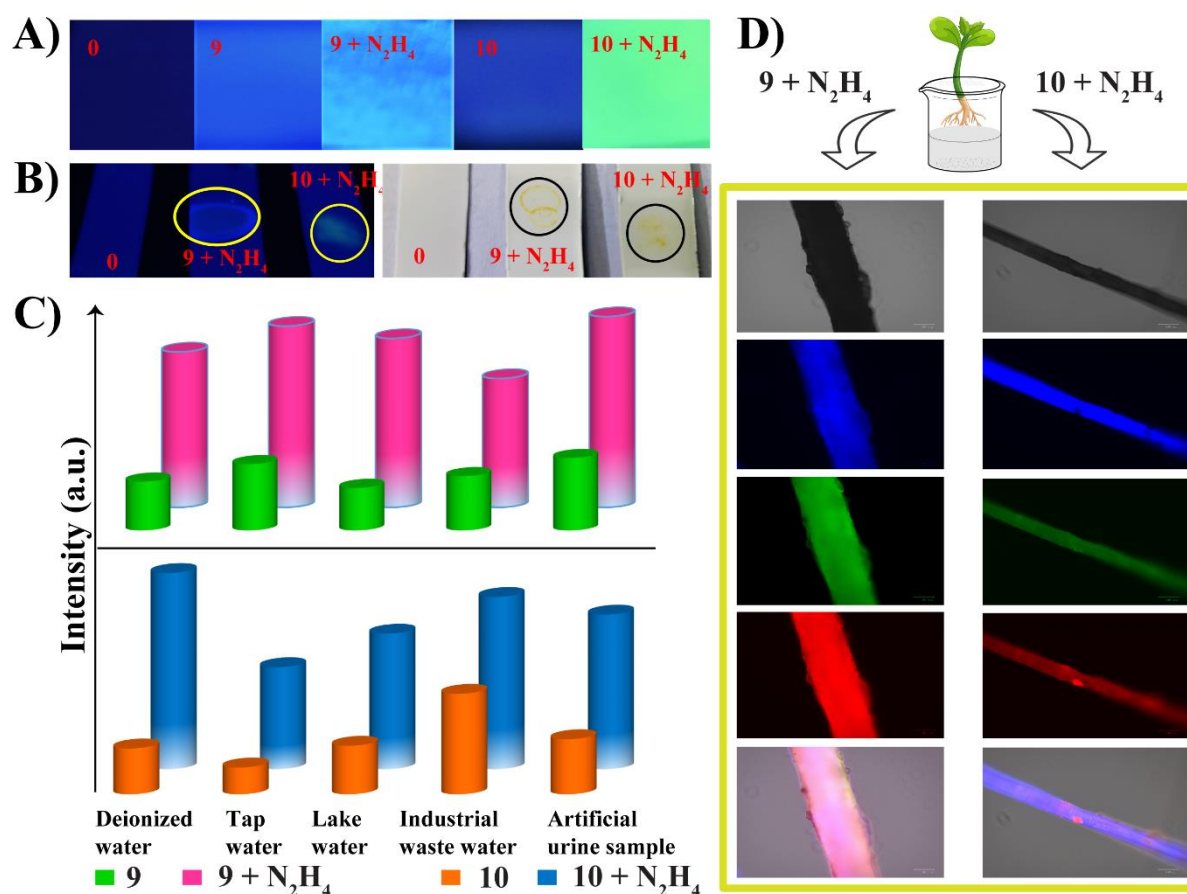


Figure 6.7 A) Photographs of the test kits coated with AIEgens **9** and **10** for detecting hydrazine in 1:1 acetonitrile-water medium B) Change in color of the TLC plate coated with AIEgens **9** and **10** in the presence of hydrazine vapour. C) Changes in the emission intensity of AIEgens **9** and **10** in the presence of hydrazine in different water samples D) The fluorescence images of root segments (Indian tomato plant) incubated with AIEgens and hydrazine solution (Left Column: AIEgen **9**; Right Column: AIEgen **10**).

exhibited an intense fluorescence in all channels, whereas the other group, which were only incubated with hydrazine solution, displayed no emission. Figure 6.7D visibly portrays the efficacy of both the AIEgens for bio-imaging applications. Encouraged by these results, our next endeavor was to ascertain the potential of the AIEgens **9** and **10** to sense hydrazine in mammalian cells. To this end, the cytotoxic potential of the AIEgens was initially assessed against HeLa cells by a standard MTT assay (Figure A6.15). The results suggested that both **9** and **10** were essentially non-toxic to cultured HeLa cells (cell viability in excess of 85%) at concentrations ranging from 2.5 μ M–20 μ M. Subsequently, fluorescence-based cell imaging studies were performed with **9** and **10** (2.5 μ M each in DMEM medium) for intracellular sensing of hydrazine in live HeLa cells (Figure A6.16). Confocal microscopy revealed that upon incubation with the AIEgen **9** for 10 min, a notable blue fluorescence was observed in the cytoplasm of HeLa cells whereas upon excitation in the other channels, a faint green and red fluorescence emanating from the cells could also be captured. These

results suggested that the AIEgen **9** could readily traverse across the cell membrane rapidly and localize in the perinuclear region of HeLa cells. Interestingly, when hydrazine (10 equiv.) was first added to HeLa cells and incubated for 10 min and then followed by addition of **9**, the blue fluorescence observed in the cytoplasm of HeLa cells was again detected. In addition, a marginal increase in the intensity of red fluorescence in the cells was evident. This suggested that the AIEgen **9** could readily sense intracellular hydrazine. In case of the AIEgen **10**, a strong blue fluorescence was evident in the cytoplasm of HeLa cells, upon incubation with the probe alone. However, in this case, green and red fluorescence originating from the cells could not be detected upon excitation in the other channels. Thus, akin to **9**, the AIEgen **10** could also perfuse through the cell and localize in the perinuclear region of HeLa cells. In the context of intracellular hydrazine (10 equiv.) sensing by **10**, it was observed that there was a decrease in intensity of blue fluorescence observed in the cytoplasm of HeLa cells. Interestingly, in this case, a remarkable turn-on green fluorescence could be detected in HeLa cells. This observation was in agreement with solution-based hydrazine detection by **10** and illustrated that the AIEgen **10** rendered facile sensing of hydrazine in live cells. Based on the aforementioned results, both the AIEgens hold significant analytical prospect for hydrazine detection in real-life samples and in cell imaging studies.

6.8 Conclusion

So, it can be concluded that our in-depth studies lead to the development of two rationally designed Schiff base molecules, which are not only capable of displaying fascinating AIE characteristics through solvent fraction tuning but also can selectively sense hydrazine both in solution and vapour phase in their aggregated state over other amines with a detection limit of 0.5 ppb (**9**) and 0.4 ppb (**10**). Both the AIEgen molecules **9** and **10** contain traditional aromatic core with schiff base linkage and endows ICT scope. The AIE activity of the two molecules can be attributed to the RIM, including ICT+ESIPT effect, and well supported by spectroscopic and microscopic analysis. The interaction between the aggregated AIEgens and hydrazine is mainly responsible for the hydrogen bonding phenomenon, which eventually results in the disaggregation induced remarkable turn-on fluorescence response and has been well supported by various spectroscopic methods and microscope imaging. Moreover, AIEgen aggregates can show good sensitivity towards hydrazine in multiple water samples and artificial urine. Even this sensing ability was also applied in the fluorescence imaging experiment to track hydrazine in plant roots and mammalian cells as well. Hence, the overall findings highlight the design strategy for

developing functional-assembly of AIE active small molecular system, enabling reliable hydrazine sensors with the ability to employ in real-life application. Hopefully, this work may inspire further exploration of interesting photophysical characteristics and morphology study and sensing endeavors with this type of small molecule moiety.

References

- 6.1 I. Kaur, V. Sharma, S. M. Mobin, P. Kaur and K. Singh, *Sens. Actuators: B Chem.*, 2019, **281**, 613-622.
- 6.2 J. Han, Y. Li, J. Yuan,; Z. Li, R. Zhao, T. Han and T. Han, *Sens. Actuators B Chem.*, 2018, **258**, 373380.
- 6.3 X. Wen and Z. Fan, *Sens. Actuators B Chem.*, 2017, **247**, 655-663.
- 6.4 Qi. Wang, X. Wen and Z. Fan, *J. Photochem. Photobiol. A*, 2018, **358**, 92-99.
- 6.5 S. Densil, C.H. Chang, C.L. Chen, A. Mathavan, A. Ramdass, V. Sathish, P. Thanasekaran, W.S. Li and S. Rajagopal, *Luminescence.*, 2018, **33**, 780-789.
- 6.6 L. McDonald, J. Wang, N. Alexander, H. Li, T. Liu and Yi. Pang, *J. Phys. Chem. B*, 2016, **120**, 766-772.
- 6.7 B. Liu, H. Zhou, B. Yang and X. Hu, *Sens. Actuators B Chem.*, 2017, **246**, 554-562.
- 6.8 T. Simon, M. Shellaiah, V. Srinivasadesikan, C.-C. Lin, F.-H. Ko, K. W. Sun and M.-C. Lin, *Sens. Actuators B Chem.*, 2016, **231**, 18-29.
- 6.9 E. H. Vernot, J. D. MacEwen, R. H. Bruner, C. C. Haus and E. R. Kinkead, *Appl. Toxicol.* 1985, **5**, 1050-1064.
- 6.10 R. F. Kimball, *Mutat. Res. Rev. Genet. Toxicol.*, 1977, **39**, 111-126.
- 6.11 G. Choudhary and H. Hanse, *Chemosphere*, 1998, **37**, 801-843.
- 6.12 J.S. Pinter, K.L. Brown, P.A. DeYoung and G.F. Peaslee, *Talanta* 2007, **71**, 1219-1225.
- 6.13 P. Bravoa, F. Isaacsa, G. Ram´ıreza, I. Az´ocara, E. Trollunda and M. J. Aguirrea, *J. Coord. Chem.* 2007, **60**, 2499-2507.
- 6.14 A. Umar, M.M. Rahman, S.H. Kim and Y.B. Hahn, *Chem. Commun.* 2008, 166-168.
- 6.15 X. Gu and J. Camden, *Anal. Chem.* 2015, **87**, 6460-6464.
- 6.16 G. Elias and W.F. Bauer, *J. Sep. Sci.* 2006, **29**, 460-464.
- 6.17 X.-Y. Zhang, Y.-S. Yang, W. Wang, Q.-C. Jiao and H.-L. Zhu, *Coord. Chem. Rev.*, 2020, **417**, 213367.
- 6.18 B. Roy and S. Bandyopadhyay, *Anal. Methods*, 2018, **10**, 1117-1139.
- 6.19 K. Siddharth, P. Alam,; Md D. Hossain, N. Xie,; G. S. Nambafu, F. Rehman, J. W.Y. Lam, G. Chen, J. Cheng, Z. Luo, G. Chen, B. Z. Tang and M. Shao, *J. Am. Chem. Soc.*, (<https://dx.doi.org/10.1021/jacs.0c13178>).
- 6.20 J. Zhu, H. Zhang, Y. Liao, J.-J. Liu, Z. Quan and X. Wang, *Dyes Pigm.*, 2020, **175**, 108111.
- 6.21 P. Yin, Q. Niu, T. Li, T. Wei, J. Chen and X. Qin, *J. Mol. Liq.*, 2020, **316**, 113845.
- 6.22 H. Wu, Y. Wang, W.-N. Wu, Z.-Q. Xu, Z.-H. Xu, X.-L. Zhao and Y.-C. Fan, *Spectrochim. Acta A*, 2019, **222**, 117272
- 6.23 K. Anandhan, M. Ceron, V. Perumal, P. Ceballos, P. Gordillo-Guerra, E. Perez-Gutierrez, A. E. Castillo, S. Thamotharanb and M. J. Percino, *RSC Adv.*, 2019, **9**, 12085-12096.
- 6.24 Y. Niko, Y. Cho, S. Kawauchia and G. Konishi, *RSC Adv.*, 2014, **4**, 36480-36484.
- 6.25 L. Bu, J. Chen, X. Wei, Xin. Li, H. Ågren and Y. Xie, *Dyes pigm.*, 2017, **136**, 724-731.

- 6.26 J. Xu, X. Liu, J. Lv, M. Zhu, C. Huang, W. Zhou, X. Yin, H. Liu, Y. Li and J. Ye, *Langmuir*, 2008, **24**, 4231-4237.
- 6.27 F. Wurthner, *Angew.Chem. Int. Ed.* 2020, **59**, 14192-14196.
- 6.28 Z. Ma, C. Liu, N. Niu, Z. Chen, S. Li, S. Liu and J. Li, *ACS Sustainable Chem. Eng.*, 2018, **6**, 3169-3175.
- 6.29 L. Peng, S. Xu, X. Zheng, X. Cheng, R. Zhang, J. Liu, B. Liu and A. Tong, *Anal. Chem.*, 2017, **89**, 3162-3168.
- 6.30 Y. Chen, Y. Fang, H. Gu, J. Qiang, H. Li, J. Fan, J. Cao, F. Wang, S. Lu and X. Chen, *ACS Appl. Mater. Interfaces*, 2020, **12**, 55094-55106.
- 6.31 N. L. C. Leung, N. Xie, W. Yuan, Y. Liu, Q. Wu, Q. Peng, Q. Miao, J. W. Y. Lam and B. Z. Tang, *Chem. Eur. J.*, 2014, **20**, 15349-15353.
- 6.32 A. Ghorai, J. Mondal, S. Bhattacharya and G. K. Patra, *Anal. Methods*, 2015, **7**, 10385-10393.
- 6.33 T. Brooks and C. W. Keevil, *Lett. Appl. Microbiol.*, 1997, **24**, 203-206.

Appendix-Chapter 6

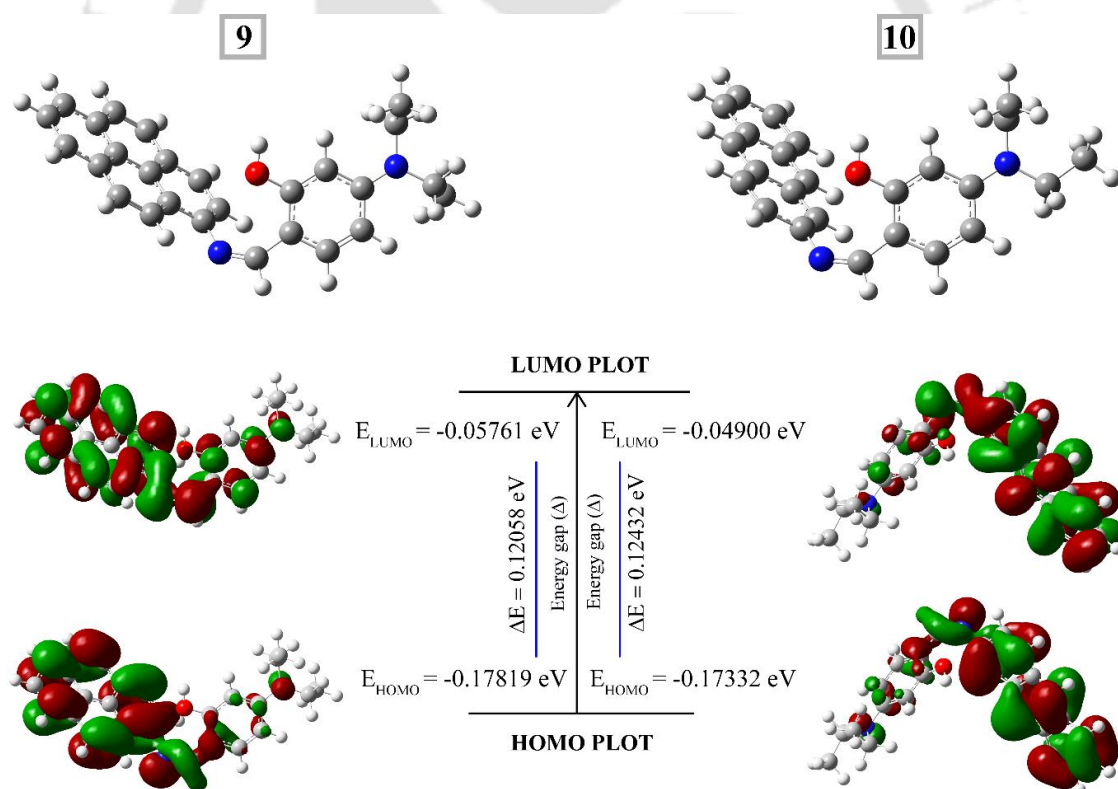


Figure A6.1 Geometry optimized structures and Frontier molecular orbital plots (ΔE = energy gap between HOMO and LUMO) of **9** (left) and **10** (right) using RB3LYP/6-31G as implemented on Gaussian 09.

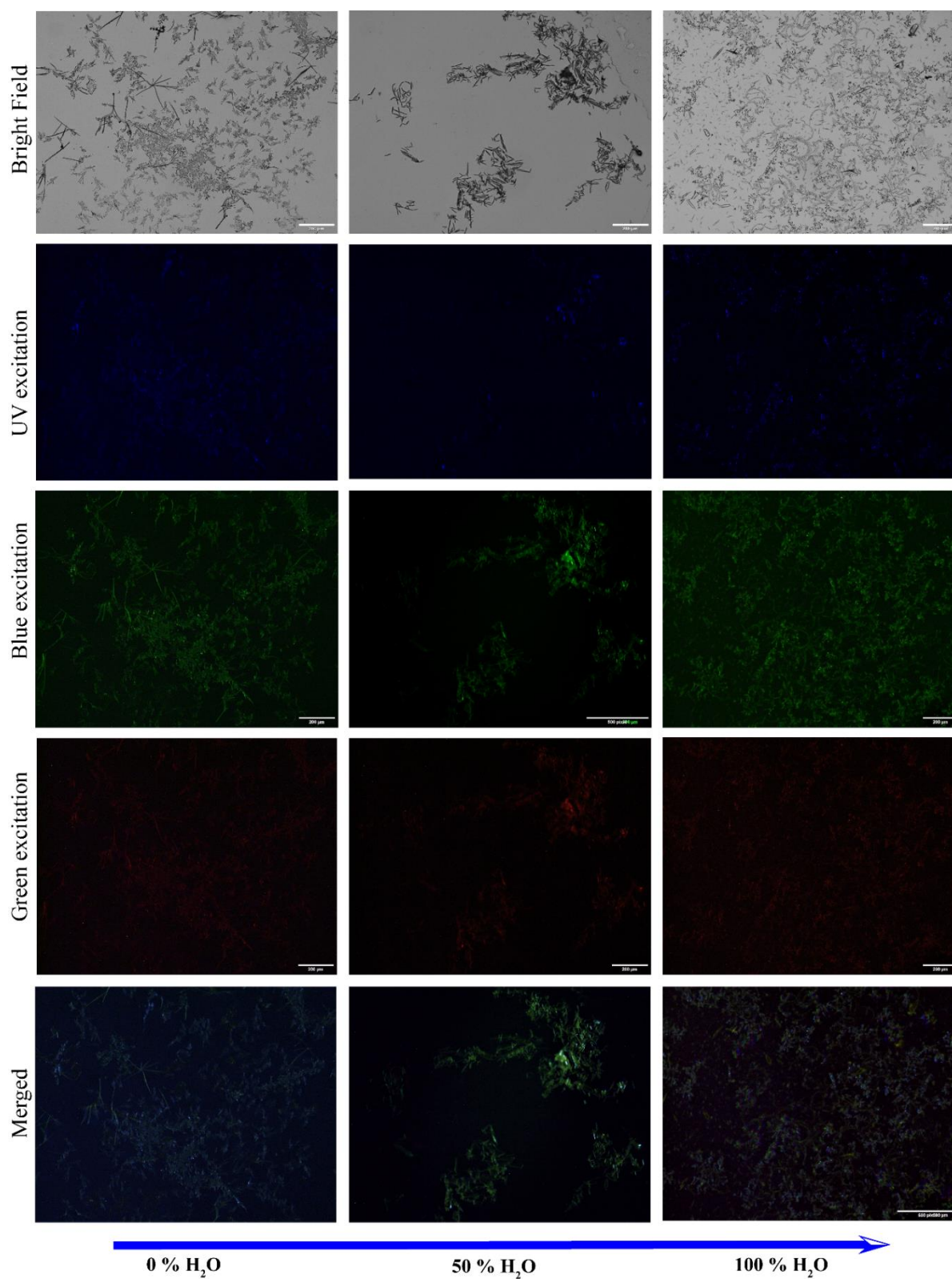


Figure A6.2 Fluorescence microscope images of **9** at different excitation range by varying the solvent fraction. [Bright field, UV channel ($\lambda_{\text{ex}}=404.1$ nm, $\lambda_{\text{em}} = 425\text{--}475$ nm) blue channel ($\lambda_{\text{ex}}=488$ nm, $\lambda_{\text{em}} = 500\text{--}530$ nm), green channel ($\lambda_{\text{ex}}=543.5$ nm, $\lambda_{\text{em}} = 553\text{--}618$ nm) and merged, scale bar = 200 μm].

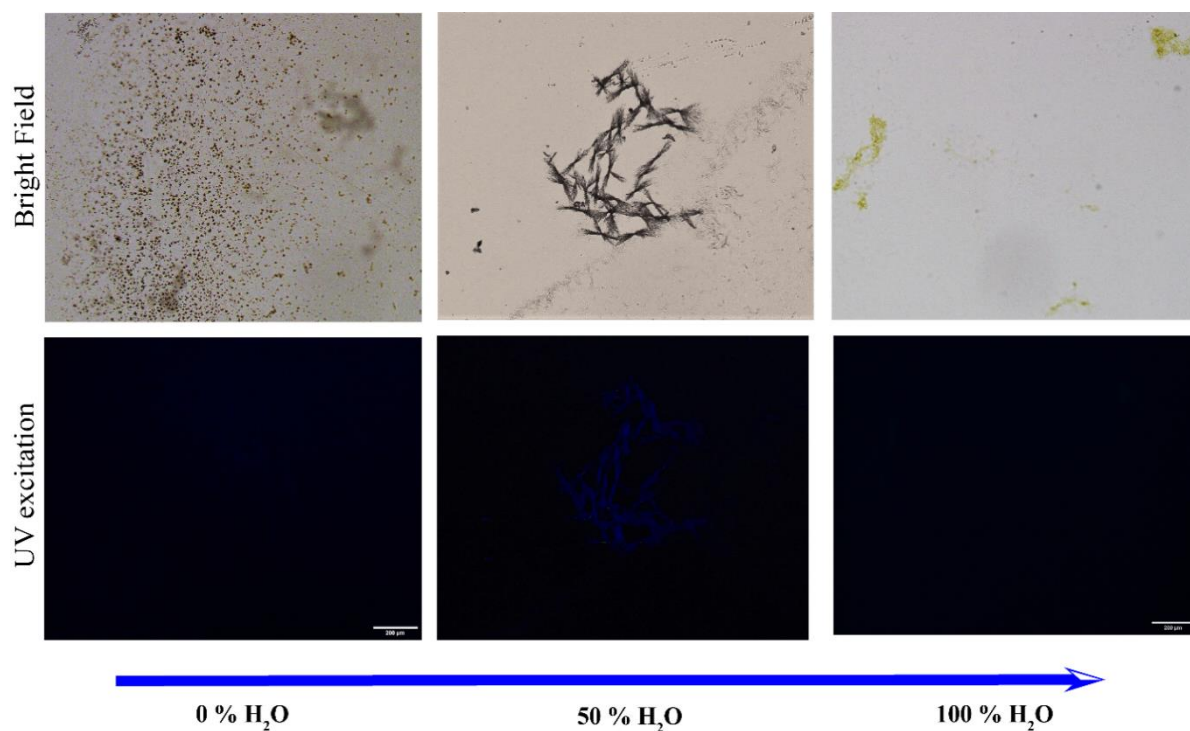


Figure A6.3 Fluorescence microscope images of **10** by varying the solvent fraction. [Bright field, UV channel ($\lambda_{\text{ex}}=404.1$ nm, $\lambda_{\text{em}} = 425\text{--}475$ nm), scale bar = 200 μm].

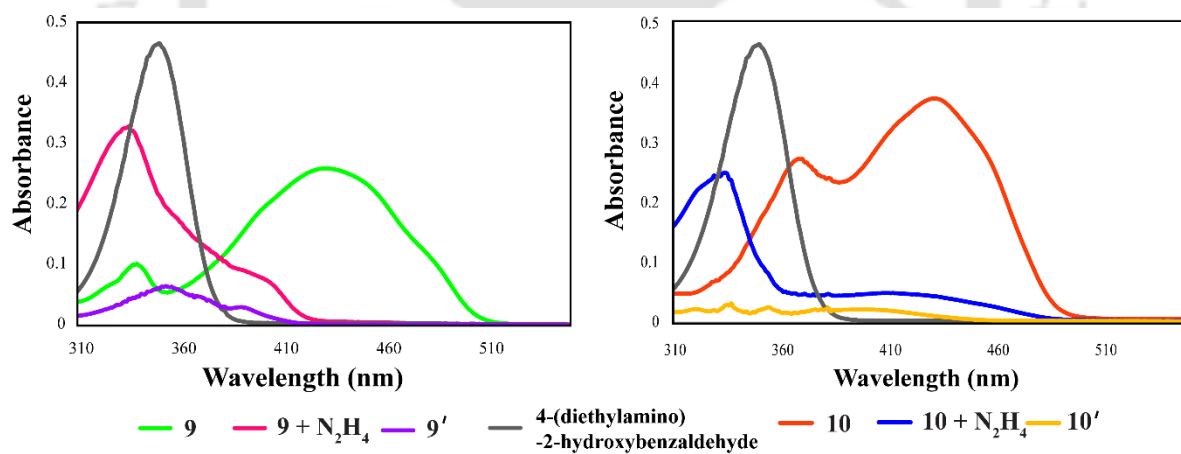


Figure A6.4 Comparative UV-visible spectra of **9** and **10** in absence and presence of excess hydrazine (10 equiv.) as well as their starting material in 1:1 acetonitrile-water medium.

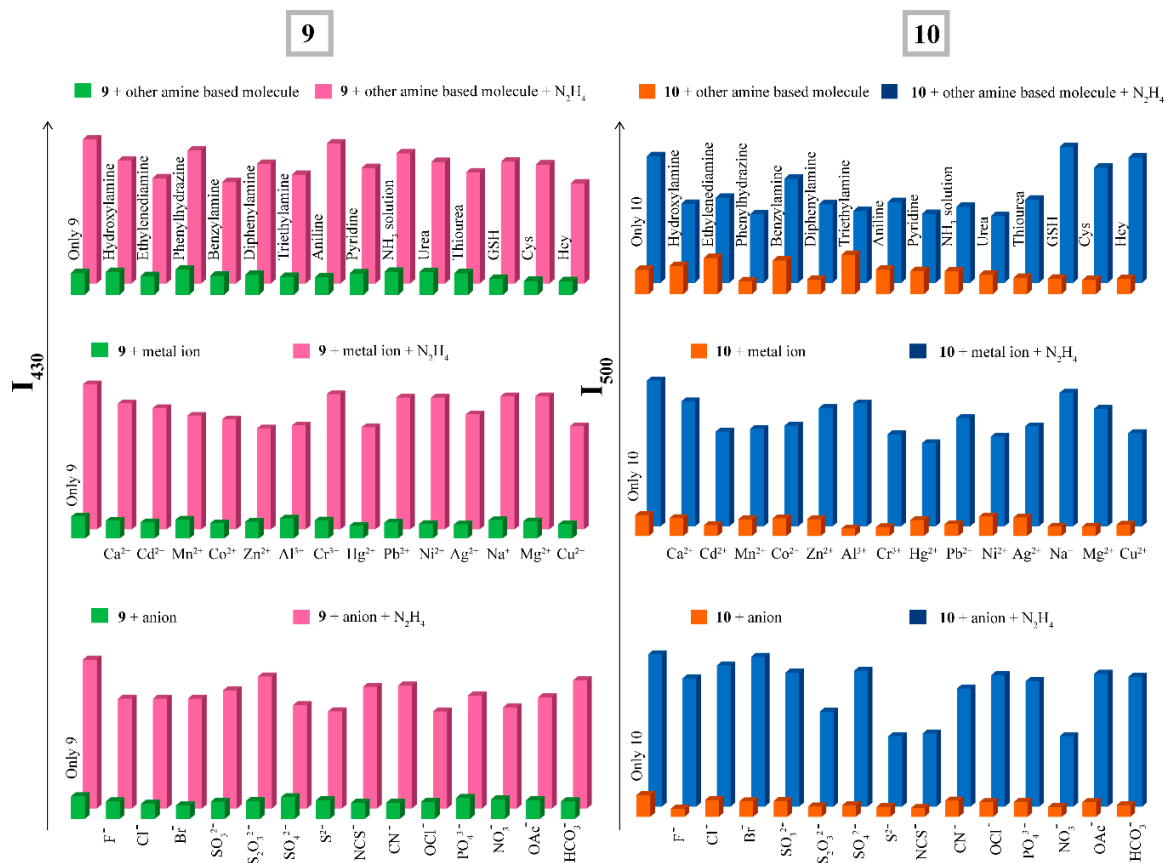


Figure A6.5 Selectivity of **9** and **10** (10 μ M) in 1:1 acetonitrile-water medium in the presence of an excess (10 equivalents) of various amine based compounds, metal ions and anions.

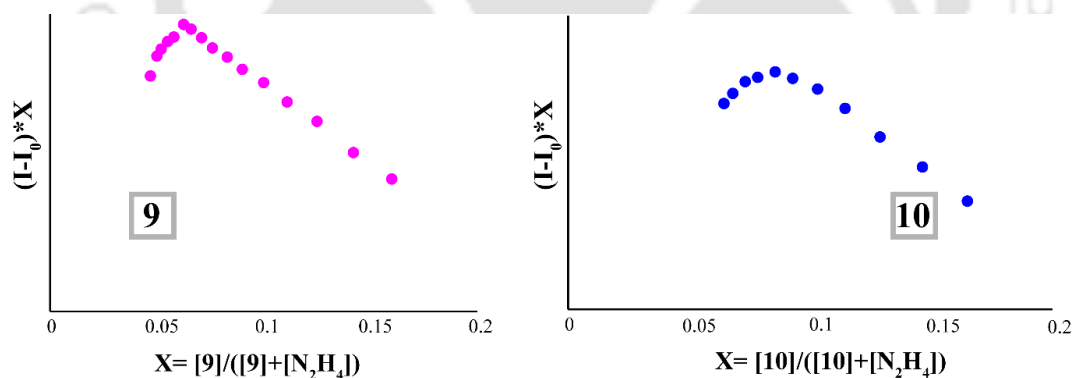


Figure A6.6 Job's plot obtained from the fluorescence titration experiment of **9** and **10**.

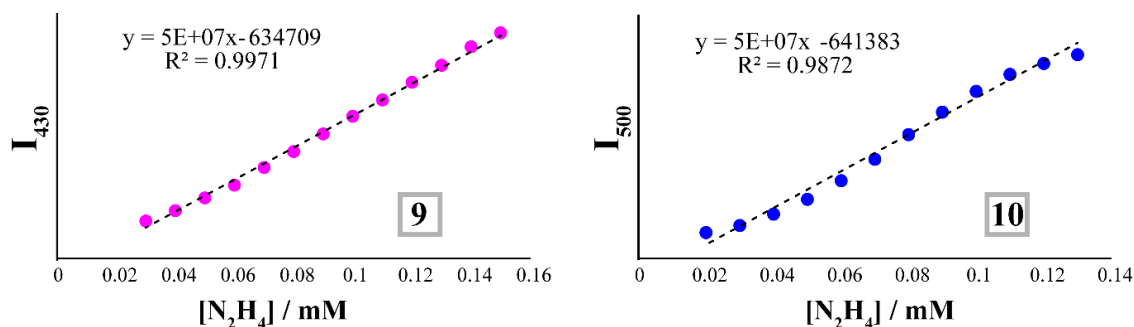


Figure A6.7 Fluorescence intensity vs. concentration of HSA plot for determination of detection limit.

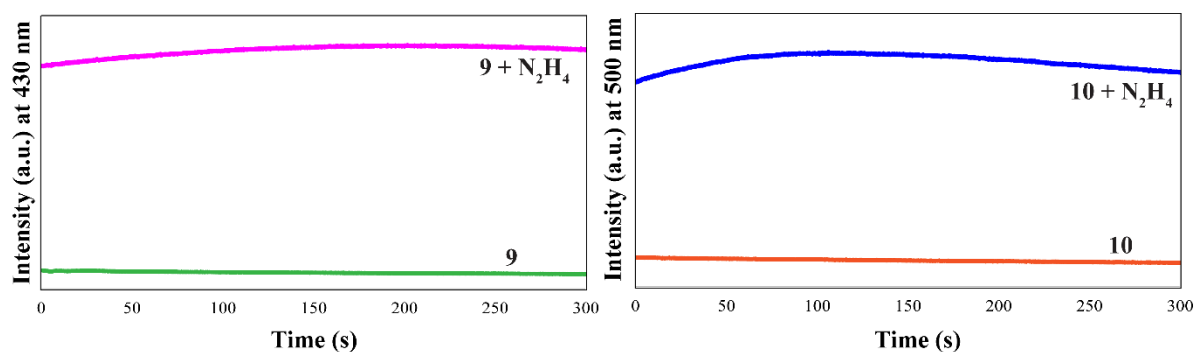


Figure A6.8: Changes in the emission intensity of **9** and **10** with time upon interaction with hydrazine.

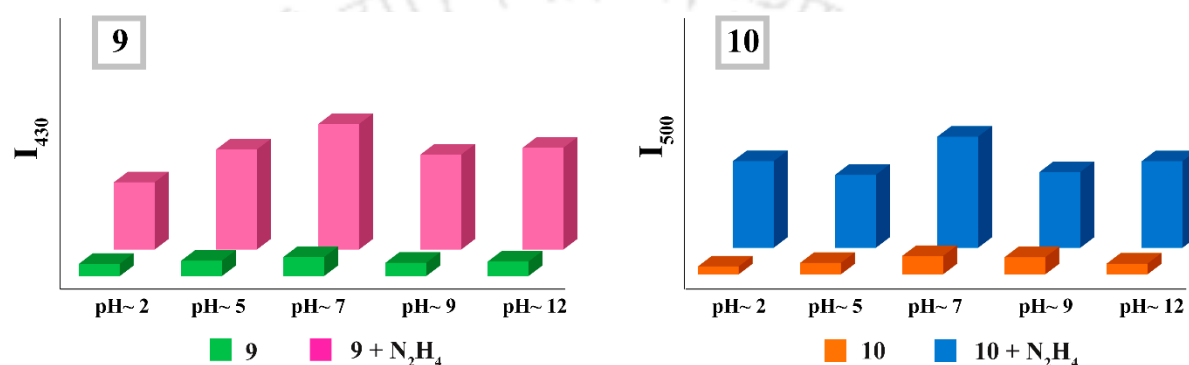


Figure A6.9 Fluorescence intensity of **9/10** and **9/10-N₂H₄** adduct at low and high pH values at room temperature.

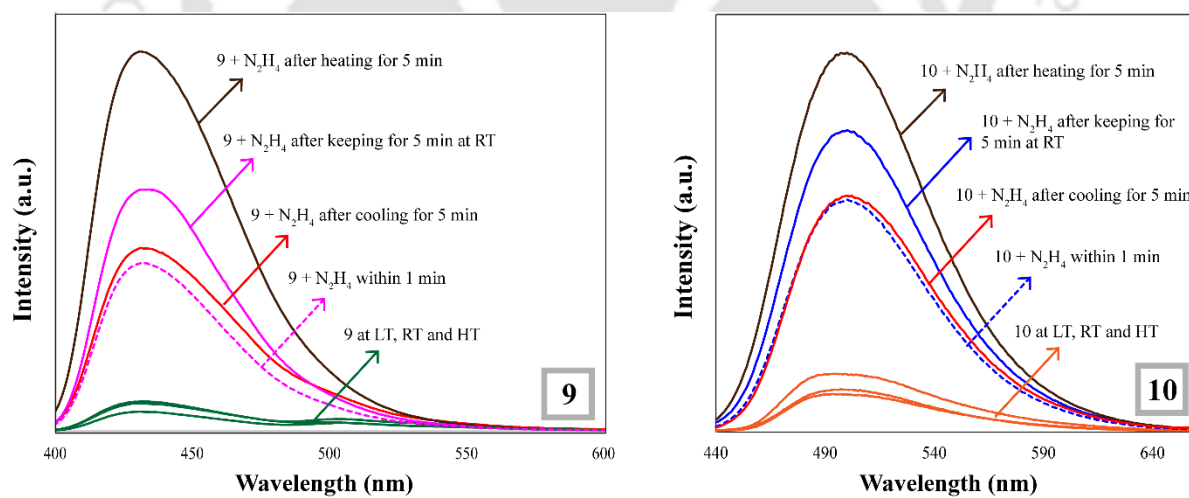


Figure A6.10: Effect of temperature on emission intensity of **9/10** and **9/10-N₂H₄** adduct.

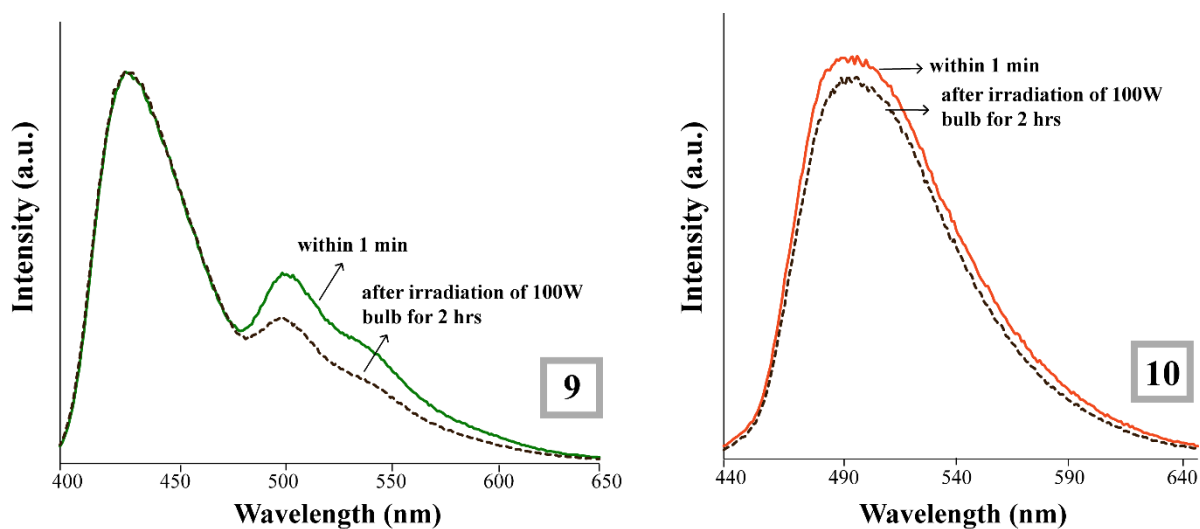


Figure A6.11: Fluorescence spectra of AIEgens **9** and **10** ($10 \mu\text{M}$) before and after the irradiation of a 100W bulb for 2 hrs in 1:1 acetonitrile-water medium.

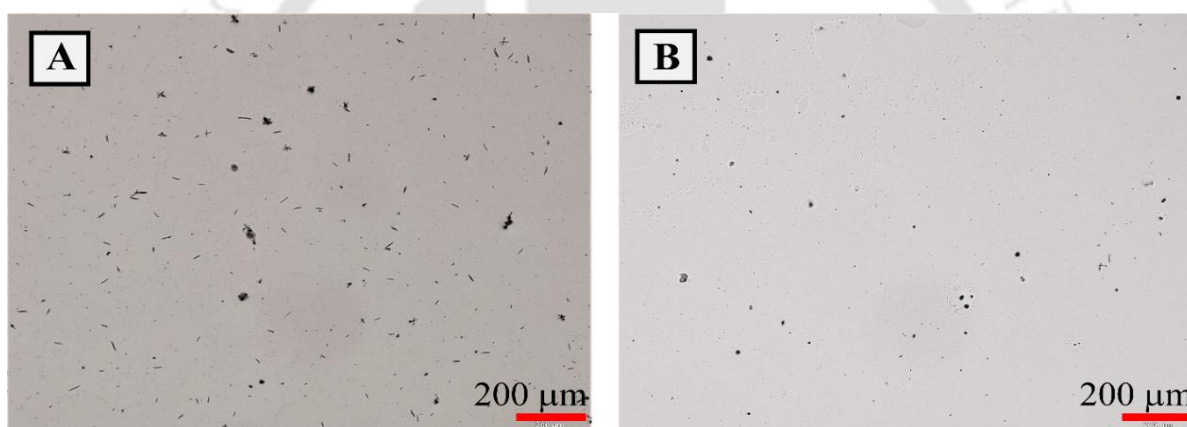


Figure A6.12 Optical microscope images of AIEgens **9** and **10** after hydrazine addition [Scale bar: $200 \mu\text{m}$].

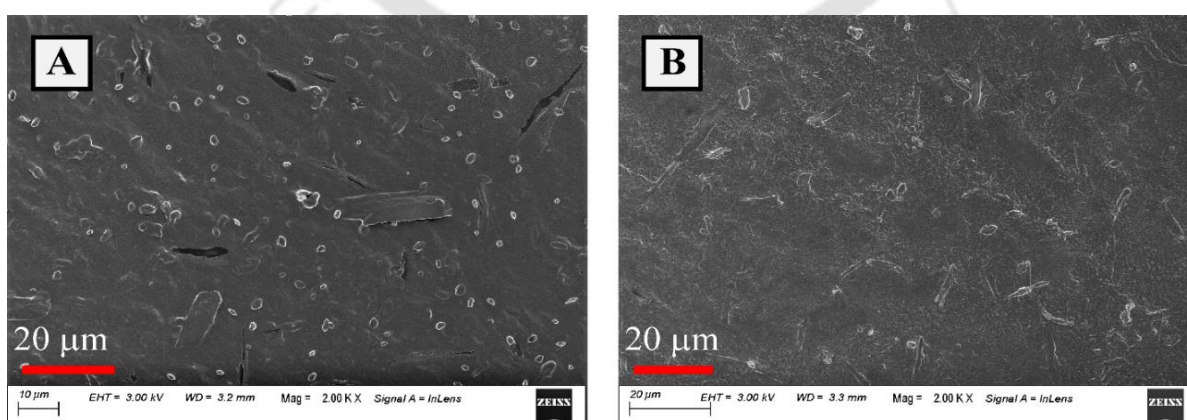


Figure A6.13 FESEM images of AIEgens **1** and **2** after hydrazine addition [Scale bar: $20 \mu\text{m}$].

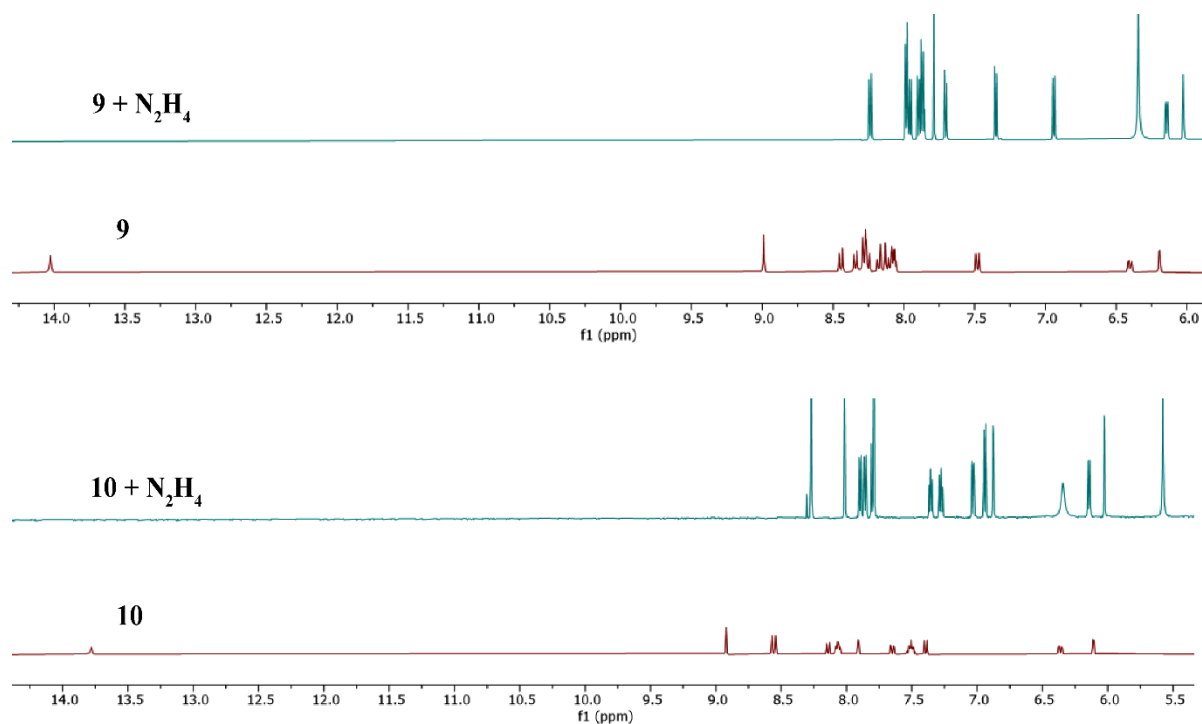


Figure A6.14 ^1H NMR spectra of the **9** and **10** and its N_2H_4 adduct in DMSO-d_6 .

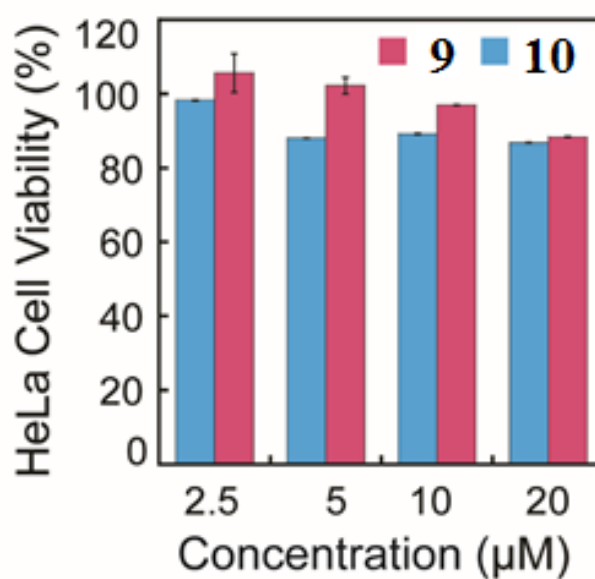


Figure A6.15 MTT assay to ascertain the cytotoxic effect of the AIEgens **1** and **2** against HeLa cells. Each data point represent mean \pm standard deviation from six samples.

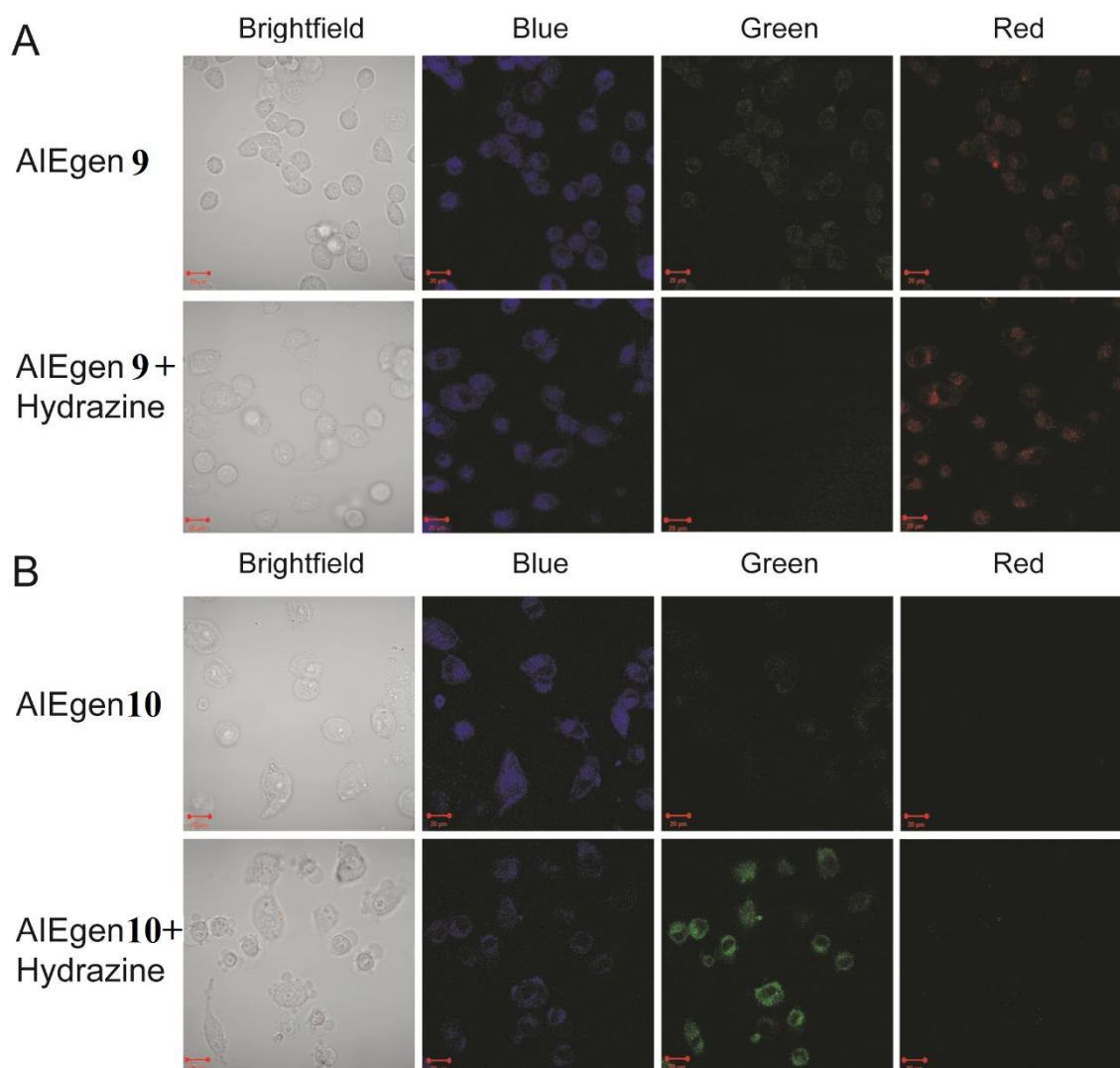


Figure A6.16 Confocal microscope-based cell imaging analysis for hydrazine sensing in HeLa cells in presence of (A) AIEgen 9 and (B) AIEgen 10. Scale bar for the images is 20 μm .

Table A6.1 Hydrogen bonding table of **9**.

Ligand	D-H...A	d(D...H)/Å	d(H...A)/Å	d(D...A)/Å	<D-H...A/°	Symmetry codes
	O1-H1...N1	0.82	1.87	2.608(3)	149	x, y, z
	O2-H2...N3	0.82	1.88	2.612(4)	148	x, y, z
	C8-H8...N1	0.93	2.53	2.842(4)	100	x, y, z
	C38-H38...N3	0.93	2.55	2.857(4)	100	x, y, z
	C44-H44...O1	0.93	2.60	3.516(4)	170	x, y, z

Table A6.2 Quantum yields (Φ) values of **9** and **10** in different water fractions.

Sample	Quantum Yield (Φ)
9 ($f_w = 0\%$)	0.0009
9 ($f_w = 50\%$)	0.002
9 ($f_w = 100\%$)	0.006
10 ($f_w = 0\%$)	0.005
10 ($f_w = 50\%$)	0.018
10 ($f_w = 100\%$)	0.004

Table A6.3 Comparative study on the recent progress in the field of hydrazine sensing.

Sl. No.	Reference	Fluorophore involved and sensing mode	Solvent system	Detection limit	Application
1.	Dyes Pigm., 2020 , 174, 108056	Naphthalene OFF-ON/-	DMSO	1.1×10^{-7} M	Test strips
2.	Dyes Pigm., 2020 , 175, 108111	Coumarin OFF-ON/ICT, AIE	PBS/DMSO (2/3)	1.29 ppb M	solid state lighting
3.	ACS Sustain. Chem. Eng. 2020 , 8, 4457	Naphthofluorescein OFF-ON	aqueous medium	~47 nM	eco-friendly test strip, bioimaging
4.	ACS Sens. 2019 , 4, 441	orthomethoxy-methyl-ether OFF-ON	DI H ₂ O	0.035 ppb	spray-based sensing, soil analysis, and bioimaging in tissue samples
5.	Sens. Actuators B Chem., 2019 , 285, 368–374	1, 8-Naphthalimide ratiometric	PBS/DMSO (1:1)	2.03×10^{-7}	Filter paper strips, HepG-2 cells
6.	Org. Biomol. Chem., 2019 , 17, 6975–6979	Schaap's Adamantylidene-dioxetane OFF-ON/Chemiluminescent	PBS/DMSO (7:3)	9.3×10^{-7} M	water samples/HeLa cells
7.	Int. J. Environ. Anal. Chem., 2019 , 1–13	Imidazo [1,5-a] pyridin OFF-ON/ESIPT	PBS/DMSO (10:1)	2.56 ppb	test strips, HeLa cells
8.	Sens. Actuators B Chem., 2018 , 272. 479–484	Triphenylamine ON-OFF/self-assemble	PBS buffer	-	Hela cells
9.	Anal. Chem. 2017 , 89, 10625	1-Pyrenecarboxaldehyde and 9-anthraldehyde OFF-ON/-	H ₂ O/CH ₃ OH(4:1)	5.4, 7.7 ppb	Drosophila larvae, paper test strips, MCF-7 cells
10.	Present Work	Pyrene and anthracene based Schiff base OFF-ON/hydrogen bonding	ACN/H ₂ O (1:1)	0.5, 0.4 ppb	test strips, water samples, plant imaging

Conclusion and Future Perspective

So, it can be concluded that this thesis exemplifies the significant consequences in realization of aggregation prospective of certain urea and Schiff base derivatives and their response towards other biologically and environmentally relevant analytes. The progressive studies during the research period provides some interesting findings in aspect of small molecule aggregation and insightful route in morphological evolution regarding design, synthesis and characterization of small molecule with contrasting aggregation prospect in developing supramolecular organization for high-tech application in various fields.

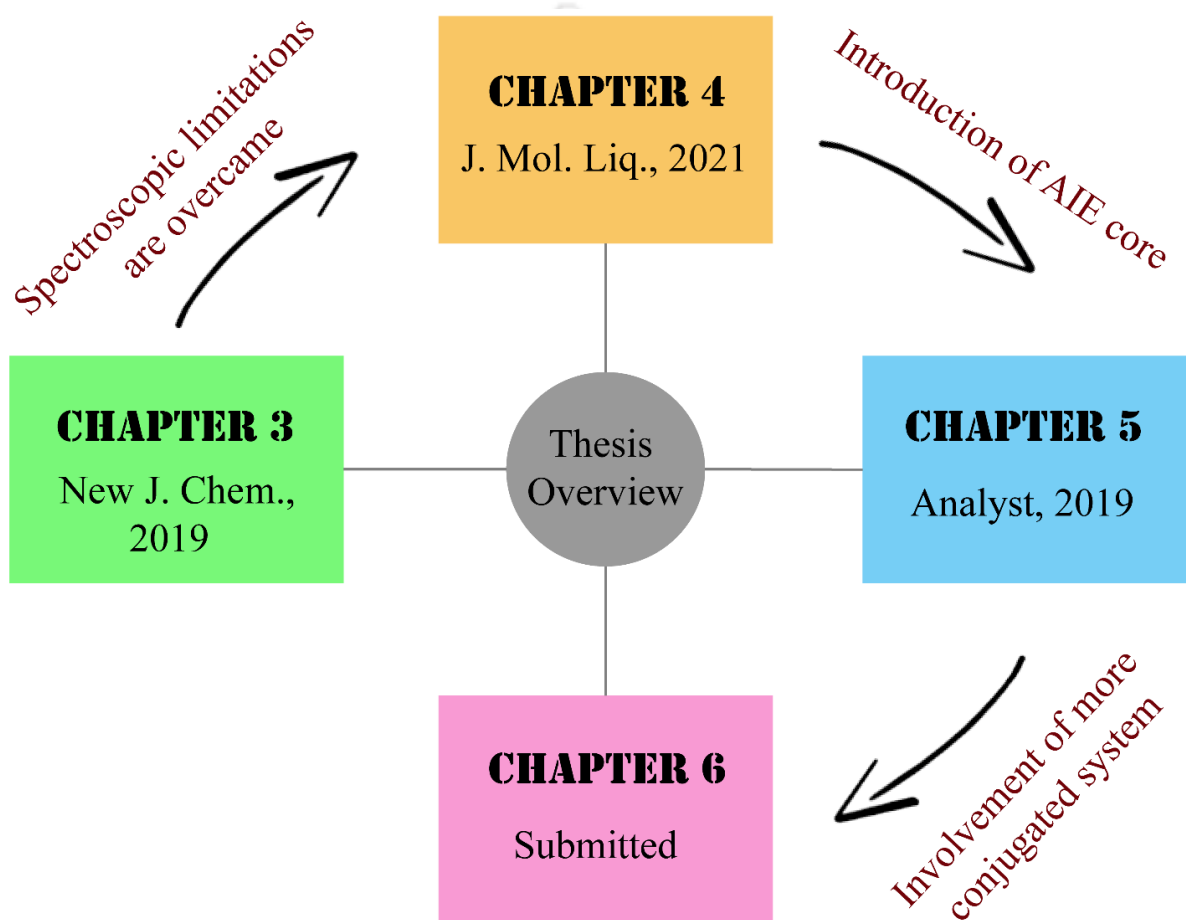
In short, during the research endeavor, we started with the purposely chosen compounds **1**, **2** and **3**, and the change in their aromatic core simply driven us to create the positional isomers and subsequent spectroscopic investigation of substituent induced aggregation property individually. Variation in the aromatic core changes the directional property and steric effect, which causes diversity in the morphology of aggregated species of **1**, **2** and **3**, and this is further validated by FESEM images and a theoretical approach. To gain a deeper insight on their relative aggregation characteristics, additional studies were also conducted to assess the effect of external factors on their aggregated arrangement and we found that the outcome is more pronounced in case of **2**. However, to overcome the spectroscopic limitations, we continued our survey with another series of neutral naphthyl bis-urea derivatives **4**, **5** and **6** which were employed to recognize the effect of core substitution on their aggregation ability with the change in the solvent nature. The variation in the photophysical behaviour due to the combined effect of solvent polarity and H-bonding interactions is noticeable for all three cases but **6** appeared less potent among them. Further examination of the interaction of nitro-aromatics with three isomers to elucidate the influence of other small aromatic molecules on their aggregation aptitude properties. Among the nitro-aromatics, PA being most electron-deficient, interacted effectively with the electron-rich **4** and **5** to subsequently affect the emission properties. Thus, this two works offer an exclusive scope of understanding the consequence of the substituent induced aggregation behavior of positional isomers in the aqueous, mixed aqueous or non-aqueous medium in absence and presence of external stimuli and can be utilized for monitoring the functional integration of a range of small molecules in the aspect of the self-assembly phenomenon. Keeping in mind the bonus advantage of introduction of AIE core, next we attempted to recognize the the role of planar fluorophores with different sizes and π -electron clouds in the aggregation aptitude of the small fluorescent molecules. Interestingly, simple disubstituted urea probe **7** is capable of displaying interesting AIE characteristics and a selective turn-on fluorescence response towards HSA over other proteins and bio-analytes in 100% aqueous medium with a very low detection limit. But **8** displayed

negligible change in emission intensity with change in water fraction and remain silent when interacted with HSA/BSA. In addition, significant change in the morphology of the aggregative species of **7** and **8** by varying the solvent fraction were well depicted by microscopic evidences. Thus change in fluorophore from naphthalene to anthracene imposed a noticeable control over aggregation characteristics. Proceeding on the same lines, this work was further challenged by replacing the anthracene moiety by more conjugated pyrene moiety along with crafting ICT prospect in two Schiff base derivatives **9** and **10**, which furthermore open up an attractive scope for realizing the effect of fluorophore substitution in the aggregation aptitude. It is worth mentioning that simply regulating the water content of the medium leads to in an exhibition of the already anticipated AIE properties of the two compounds without the presence of any external stimuli. It is important to note that **9** and **10** can selectively sense Hydrazine both in solution and vapour phase in their aggregated state over other amines with a very impressive detection limit. Thus, the last two comparative studies was strategized to distinguish the effect of aromatic core substitution on their aggregation ability and furthermore to employ that aggregated system as a sensing tool for real life analytical application. Further challenge on the design and development of simple AIE active fluorogenic molecules and to study their aggregation behavior and interaction with other analytes and biomolecules using the spectroscopic strategy with morphological validation are desirable.

Hence, the overall findings in the thesis revise the design strategy for developing functional-assembly of small molecular system and successfully established the some of the various fundamental concepts of small molecule aggregation through sequential approach of spectroscopic and microscopic studies. The results of our continuous effort portrays a systematic details of structural alteration within molecular framework in the field of small molecule aggregation. In essence, we believe that this thesis would find meaningful contribution to both analytical chemistry and supramolecular chemistry community for enhancing cognizance and development in the particular field of research. Hopefully, this thesis may inspire further exploration of interesting photophysical characteristics along with morphology study and sensing endeavor with this type of small molecule moiety with aggregative nature.



THESIS OVERVIEW



checkCIF/PLATON report

Structure factors have been supplied for datablock(s) SH_Pyrene

THIS REPORT IS FOR GUIDANCE ONLY. IF USED AS PART OF A REVIEW PROCEDURE FOR PUBLICATION, IT SHOULD NOT REPLACE THE EXPERTISE OF AN EXPERIENCED CRYSTALLOGRAPHIC REFEREE.

No syntax errors found. [CIF dictionary](#) [Interpreting this report](#)

Datablock: SH_Pyrene

Bond precision: C-C = 0.0045 Å Wavelength=0.71073

Cell: a=8.3383(4) b=15.9039(8) c=16.4937(9)
alpha=102.590(4) beta=104.008(4) gamma=92.454(4)
Temperature: 298 K

	Calculated	Reported
Volume	2060.60(19)	2060.60(19)
Space group	P -1	P -1
Hall group	-P 1	-P 1
Moiety formula	C27 H24 N2 O	C27 H24 N2 O
Sum formula	C27 H24 N2 O	C27 H24 N2 O
Mr	392.48	392.48
Dx,g cm-3	1.265	1.265
Z	4	4
Mu (mm-1)	0.077	0.077
F000	832.0	832.0
F000'	832.31	
h,k,lmax	11,21,22	11,20,21
Nref	10783	9344
Tmin,Tmax	0.978,0.985	0.978,0.985
Tmin'	0.978	

Correction method= # Reported T Limits: Tmin=0.978 Tmax=0.985
AbsCorr = MULTI-SCAN

Data completeness= 0.867 Theta(max)= 28.813

R(reflections)= 0.0700(5811) wR2(reflections)= 0.2520(9344)

S = 0.841 Npar= 547

The following ALERTS were generated. Each ALERT has the format

test-name_ALERT_alert-type_alert-level.

Click on the hyperlinks for more details of the test.

Alert level B

PLAT230 ALERT 2 B Hirshfeld Test Diff for N4 --C51 . 17.6 s.u.

Alert level C

CRYSC01 ALERT 1 C The word below has not been recognised as a standard identifier.
deepbrown

CRYSC01 ALERT 1 C No recognised colour has been given for crystal colour.
PLAT220 ALERT 2 C NonSolvent Resd 2 C Ueq(max)/Ueq(min) Range 4.1 Ratio
PLAT222 ALERT 3 C NonSolvent Resd 2 H Uiso(max)/Uiso(min) Range 4.5 Ratio
PLAT242 ALERT 2 C Low 'MainMol' Ueq as Compared to Neighbors of C51 Check
PLAT340 ALERT 3 C Low Bond Precision on C-C Bonds 0.00446 Ang.
PLAT360 ALERT 2 C Short C(sp3)-C(sp3) Bond C51 - C52 . 1.35 Ang.
PLAT906 ALERT 3 C Large K Value in the Analysis of Variance 8.561 Check

Alert level G

PLAT007 ALERT 5 G Number of Unrefined Donor-H Atoms 2 Report
PLAT066 ALERT 1 G Predicted and Reported Tmin&Tmax Range Identical ? Check
PLAT154 ALERT 1 G The s.u.'s on the Cell Angles are Equal ..(Note) 0.004 Degree
PLAT883 ALERT 1 G No Info/Value for _atom_sites_solution_primary . Please Do !
PLAT910 ALERT 3 G Missing # of FCF Reflection(s) Below Theta(Min). 4 Note
PLAT912 ALERT 4 G Missing # of FCF Reflections Above STh/L= 0.600 1372 Note
PLAT941 ALERT 3 G Average HKL Measurement Multiplicity 1.8 Low
PLAT965 ALERT 2 G The SHELXL WEIGHT Optimisation has not Converged Please Check
PLAT978 ALERT 2 G Number C-C Bonds with Positive Residual Density. 5 Info

0 ALERT level A = Most likely a serious problem - resolve or explain
1 ALERT level B = A potentially serious problem, consider carefully
8 ALERT level C = Check. Ensure it is not caused by an omission or oversight
9 ALERT level G = General information/check it is not something unexpected

5 ALERT type 1 CIF construction/syntax error, inconsistent or missing data
6 ALERT type 2 Indicator that the structure model may be wrong or deficient
5 ALERT type 3 Indicator that the structure quality may be low
1 ALERT type 4 Improvement, methodology, query or suggestion
1 ALERT type 5 Informative message, check

Validation response form

Please find below a validation response form (VRF) that can be filled in and pasted into your CIF.

```
# start Validation Reply Form
_vrf_CRYSC01_SH_Pyrene
;
PROBLEM: The word below has not been recognised as a standard
RESPONSE: ...
;
_vrf_PLAT230_SH_Pyrene
;
PROBLEM: Hirshfeld Test Diff for N4 --C51 . 17.6 s.u.
RESPONSE: ...
;
_vrf_PLAT220_SH_Pyrene
;
PROBLEM: NonSolvent Resd 2 C Ueq(max)/Ueq(min) Range 4.1 Ratio
RESPONSE: ...
```

```

;
_vrf_PLAT222_SH_Pyrene
;
PROBLEM: NonSolvent Resd 2 H Uiso(max)/Uiso(min) Range 4.5 Ratio
RESPONSE: ...
;
_vrf_PLAT242_SH_Pyrene
;
PROBLEM: Low 'MainMol' Ueq as Compared to Neighbors of C51 Check
RESPONSE: ...
;
_vrf_PLAT340_SH_Pyrene
;
PROBLEM: Low Bond Precision on C-C Bonds ..... 0.00446 Ang.
RESPONSE: ...
;
_vrf_PLAT360_SH_Pyrene
;
PROBLEM: Short C(sp3)-C(sp3) Bond C51 - C52 1.35 Ang.
RESPONSE: ...
;
_vrf_PLAT906_SH_Pyrene
;
PROBLEM: Large K Value in the Analysis of Variance ..... 8.561 Check
RESPONSE: ...
;
# end Validation Reply Form

```

It is advisable to attempt to resolve as many as possible of the alerts in all categories. Often the minor alerts point to easily fixed oversights, errors and omissions in your CIF or refinement strategy, so attention to these fine details can be worthwhile. In order to resolve some of the more serious problems it may be necessary to carry out additional measurements or structure refinements. However, the purpose of your study may justify the reported deviations and the more serious of these should normally be commented upon in the discussion or experimental section of a paper or in the "special_details" fields of the CIF. checkCIF was carefully designed to identify outliers and unusual parameters, but every test has its limitations and alerts that are not important in a particular case may appear. Conversely, the absence of alerts does not guarantee there are no aspects of the results needing attention. It is up to the individual to critically assess their own results and, if necessary, seek expert advice.

Publication of your CIF in IUCr journals

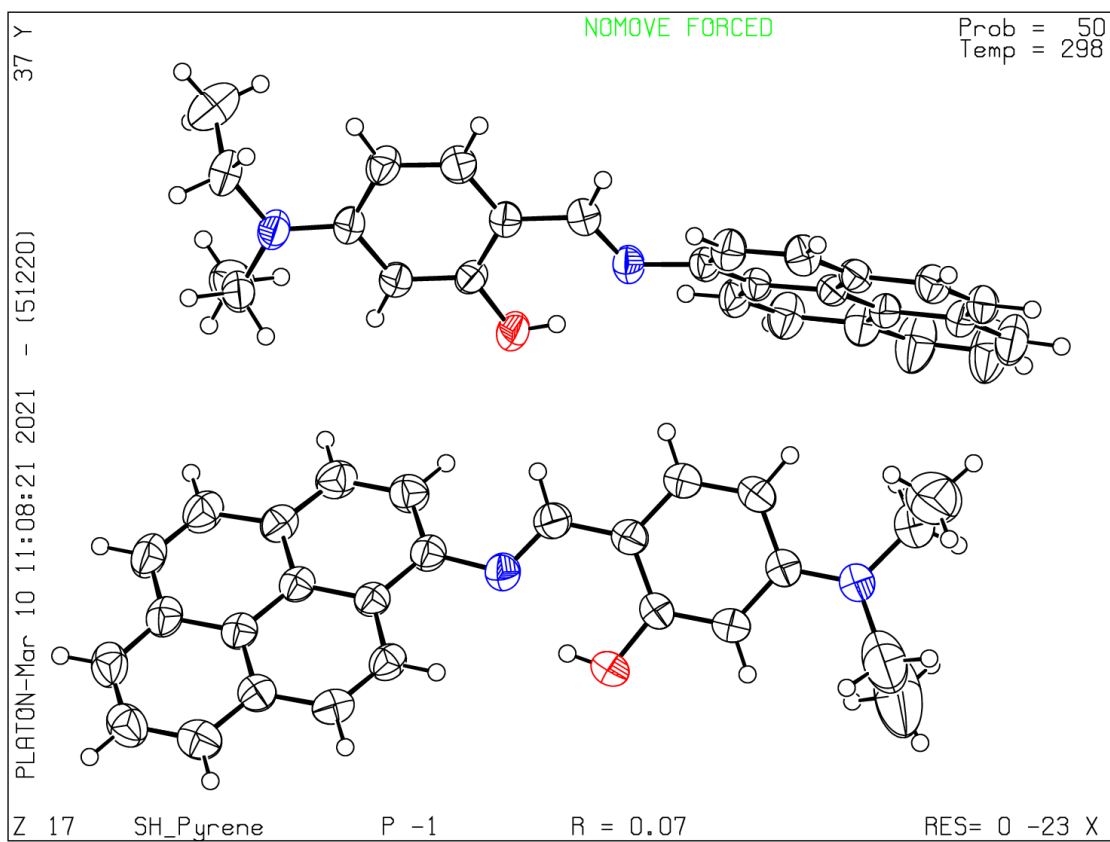
A basic structural check has been run on your CIF. These basic checks will be run on all CIFs submitted for publication in IUCr journals (*Acta Crystallographica*, *Journal of Applied Crystallography*, *Journal of Synchrotron Radiation*); however, if you intend to submit to *Acta Crystallographica Section C* or *E* or *IUCrData*, you should make sure that full publication checks are run on the final version of your CIF prior to submission.

Publication of your CIF in other journals

Please refer to the *Notes for Authors* of the relevant journal for any special instructions relating to CIF submission.

PLATON version of 05/12/2020; check.def file version of 05/12/2020

Datablock SH_Pyrene - ellipsoid plot



Senjuti Halder

Curriculum Vitae

Lab CHL-201, Department of Chemistry,
Indian Institute of Technology, Guwahati, India
✉ senjuti.halder@iitg.ac.in, chem.senju@gmail.com

Education

- 2016-present **Ph.D. student**, *Indian Institute of Technology Guwahati*, Guwahati, India.
- Thesis: *Comprehending the aggregation aptitude through structural variation within small molecular framework: Comparative analysis and interaction studies*
 - Supervisor: **Prof. Gopal Das**
 - GPA: 8.75/10.0
- 2014-2016 **M.Sc. in Chemistry**, *Indian Institute of Technology Madras*, Chennai, India.
- Dissertation: *Cobalt(II) and Iron(II/III) complexes with a tridentate Schiff-base ligand having a biphenyl append: Synthesis and characterizations*
 - Supervisor: **Prof. N.N. Murthy**
 - CGPA: 7.59/10.0
- 2011-2014 **B.Sc. (Hons.) in Chemistry**, *Asutosh College, University of Calcutta*, Kolkata, India.
- Percentage: 73.4%
- 2009-2011 **Higer Secondary, Class XII**, *Bidhannagar Govt. High School, WBCHSE*, Kolkata, India.
- Percentage: 88.4%
- 2009 **Secondary, Class X**, *Bethune Collegiate School, WBBSE*, Kolkata, India.
- Percentage: 89.1%

Research Interests

- Photo-physical and morphological study of molecular aggregates
- Exploration of sensing potential of self-assembled molecular building blocks
- Application of supramolecular assembly-disassembly approach
- Development of sensing system with AIE features
- Fluorescent probes for biologically and environmentally relevant analytes

- Luminescent systems for biological/medical/chemical applications
- Coordination chemistry for cations and anions

Experience

Indian Institute of Technology Guwahati

- 2018-2021 **Trained and authorized operator.**
Instrument: *Atomic Force Microscopy (Oxford, Cypher)*
- 2017-2020 **Co-supervised four M.Sc. final year students.**
Project: *Aggregation Studies of Synthetic Amphiphile*
- July-Nov, 2019 **Teaching Assistant (UG).**
Module: *Inorganic Tutorial Courses*
- July-Nov, 2018 **Teaching Assistant (PG).**
Module: *Inorganic Laboratory Courses*
- July-Nov, 2017 **Teaching Assistant (UG).**
Module: *Inorganic Tutorial Courses*

Achievements

- **CSIR-JRF 78** in JOINT CSIR-UGC NET (National Eligibility Test) 2016
- **AIR 849** in GATE (Graduate Aptitude Test in Engineering) 2016
- **UGC-JRF 94** in JOINT CSIR-UGC NET (National Eligibility Test) 2015
- **AIR 811** in JAM (Joint Admission Test for Masters) 2014

Journal Publications

Links: [Google Scholar](#), [ResearchGate](#)

In referred journals

1. **S. Halder**, B. Nayak, B. Bhattacharjee, R. Aiyagari and G. Das, **2021**, Insight into the aggregation prospective of Schiff base AlEgens enabling efficient hydrazine sensor in their aggregated state, *J. Mater. Chem. C*.
2. M. Basak, **S. Halder**, and G. Das, **2021**, Folic acid induced disassembly of self-assembled Fluorene-Naphthalene based receptor and contemporaneous detection of folic acid in aqueous medium, *J. Photochem. Photobiol. A*
3. **S. Halder**, B. Nayak, S. De and G. Das, **2021**, Probing the solvent-tunable aggregation aptitude of neutral naphthyl bis-urea series and their interactions with nitro-aromatics, *J. Mol. Liq.*
4. D. Paul, **S. Halder** and G. Das, **2020**, Whey protein directed in vitro vaterite biomineralization: Influence of external parameters on phase transformation, *Colloid Interfac. Sci. Comm.*
5. **S. Halder**, U. Manna and G. Das, **2019**, Tuning the aggregation performance by varying the substituent position: Comparative study of neutral bis-urea derivatives in aqueous medium, *New J. Chem.*

6. **S. Halder**, S. Samanta and G. Das, **2019**, Exploring the potential of a urea derivative: An AIE-Luminogen and its interaction with human serum albumin in aqueous medium, *Analyst*.
7. B. Nayak, **S. Halder** and G. Das, **2019**, Terminal substituent induced differential anion coordination and self-assembly: Case study of flexible linear bis-urea receptors, *Cryst. Growth Des.*
8. S. Samanta, **S. Halder** and G. Das, **2019**, Specific detection of hypochlorite: A cyanine based turn-on fluorescent sensor, *J. Chem. Sci.*
9. B. Nayak, **S. Halder**, S. De and G. Das, **2019**, Binding consistency of anions by the effect of aromatic meta-substitution of bis-urea receptors: Entrapment of hexafluorosilicate clusters, *Crys. Eng. Comm.*
10. U. Manna, **S. Halder** and G. Das, **2018**, Ice-like cyclic water hexamer trapped within a halide encapsulated hexameric neutral receptor core: First crystallographic evidence of a water cluster confined within a receptor-anion capsular assembly, *Cryst. Growth Des.*
11. S. Samanta, **S. Halder** and G. Das, **2018**, TICT-based TURN-ON fluorogenic nano-probe for realtime detection of serum albumin in physiological condition, *Anal. Chem.*
12. S. Samanta, **S. Halder**, U. Manna, P. Dey, A. Ramesh and G. Das, **2018**, Ratiometric fluorogenic probe for real-time detection of SO₃²⁻ in aqueous medium: Application in cellulose paper-based device and potential to sense in mitochondria, *Analyst*.

In preparation

13. S. De, **S. Halder** and G. Das, Impact of isomeric alteration in morphological pattern and aggregation aptitude of rigid tripodal urea series in binary solvents.

Conferences

1. Oral presentation in **ChemCYS 2020**, The Chemistry Conference for Young Scientists, Blankenberge, Belgium.
2. Poster presentation in **Modern Trends in Inorganic Chemistry (XVII) 2019**, Indian Institute of Technology Guwahati, India.
3. Poster presentation in **24th CRSI National Symposiums in Chemistry 2019**, CSIR-CLRI, Chennai, India.
4. Oral presentation in **Frontiers in Chemical Science 2018**, Indian Institute of Technology Guwahati, India.

Skills

Computer Microsoft office, Origin, Chemdraw, Gaussian 09, AutoDockTools 1.5.6, Adobe Illustrator

Lab Spectroscopic techniques (UV, Fluorescence, FT-IR, NMR, DLS, CD), Microscope imaging (AFM, FESEM, FETEM, Optical and Fluorescence microscopy)

References

- Dr. Gopal Das
Professor and Head
Department of Chemistry
Indian Institute of Technology Guwahati, India.
Phone: (+91-361)-258 2313
E-mail: gdas@iitg.ac.in
- Dr. Aiyagari Ramesh
Professor
Department of Biosciences and Bioengineering
Indian Institute of Technolgy Guwahati, India.
Phone: (+91-361)-258-2205
E-mail: aramesh@iitg.ac.in
- Dr. Ramesh L. Gardas
Professor
Department of Chemistry
Indian Institute of Technology Madras, India.
Phone: (+91-44)-2257-4248
E-mail: gardas@iitm.ac.in

